



Towards Automation Process of 3D Printing in Construction under Uncontrolled Environment

Xinrui Yang

► To cite this version:

Xinrui Yang. Towards Automation Process of 3D Printing in Construction under Uncontrolled Environment. Automatic. Université de Lille, 2023. English. NNT : . tel-04456444

HAL Id: tel-04456444

<https://hal.science/tel-04456444>

Submitted on 14 Feb 2024

HAL is a multi-disciplinary open access archive for the deposit and dissemination of scientific research documents, whether they are published or not. The documents may come from teaching and research institutions in France or abroad, or from public or private research centers.

L'archive ouverte pluridisciplinaire **HAL**, est destinée au dépôt et à la diffusion de documents scientifiques de niveau recherche, publiés ou non, émanant des établissements d'enseignement et de recherche français ou étrangers, des laboratoires publics ou privés.



Doctoral School: MADIS-631

Towards Automation Process of 3D Printing in Construction under Uncontrolled Environment

PhD THESIS

to obtain the degree of

Doctor of University of Lille

Speciality : ROBOTICS

Defended by

Xinrui YANG

prepared at

CRIStAL CNRS-UMR 9189

defended on November 30, 2023

at CRIStAL, Lille

Jury

<i>Reviewers :</i>	Pr. Mitra FOULADIRAD	- École Centrale de Marseille, France
	Pr. Taha BOUKHOBZA	- University of Lorraine, France
<i>President of jury :</i>	Pr. Sébastien RÉMOND	- University of Orléans, France
<i>Examiners :</i>	Pr. Abdelaziz BENALLEGUE	- University of Versailles Saint-Quentin-en-Yvelines, France
	Pr. Kamal YUCEF-TOUMI	- Massachusetts Institute of Technology, USA
	Dr. Aurélie DE BOISSIEU	- University of Liège, Belgium
<i>Supervisor :</i>	Pr. Rochdi MERZOUKI	- University of Lille, France
<i>Co-Supervisor :</i>	Dr. Othman LAKHAL	- University of Lille, France
<i>Guest:</i>	Dr. Agnès PETIT	- CEO, MOBBOT, Switzerland

Ecole Doctorale: MADIS-631

Vers un processus d'automatisation de l'impression 3D dans la construction en environnement non contrôlé

THÈSE

soumise à l'Université de Lille en vue de l'obtention de

Doctorat

Spécialité : ROBOTIQUE

par

Xinrui YANG

préparée au laboratoire
CRISAL CNRS-UMR 9189

soutenue le 30 Novembre 2023
à CRISAL

Jury

<i>Rapporteurs :</i>	Pr. Mitra FOULADIRAD	- École Centrale de Marseille, France
	Pr. Taha BOUKHOBZA	- Université de Lorraine, France
<i>Président du jury :</i>	Pr. Sébastien RÉMOND	- Université d'Orléans, France
<i>Examineurs :</i>	Pr. Abdelaziz BENALLEGUE	- Université de Versailles S.Q.Y, France
	Pr. Kamal YOUCEF-TOUMI	- Massachusetts Institute of Technology, USA
	Dr. Aurélie DE BOISSIEU	- Université de Liège, Belgique
<i>Directeur de thèse :</i>	Pr. Rochdi MERZOUKI	- Université de Lille, France
<i>Co-encadrant:</i>	Dr. Othman LAKHAL	- Université de Lille, France
<i>Invitée:</i>	Dr. Agnès PETIT	- CEO, MOBBOT, Suisse

Towards Automation Process of 3D Printing in Construction under Uncontrolled Environment

Abstract

Additive Manufacturing (AM) with concrete material, also known as 3D Concrete Printing (3DCP), has gained increasing attention in the construction industry as well as in academia across various research fields including material science, automatic control, and robotics. This technology enables the fabrication of designed 3D complex geometries in a layer-by-layer manner, using construction materials such as concrete that can come from recycled demolition wastes containing RFA (Recyclable Fine Aggregates). A robotic system guides a nozzle that deposits material along a defined trajectory. Most 3DCP technologies are performed under controlled environments without environmental disturbances. However, in uncontrolled environments, changes in temperature and humidity can significantly affect the rheological properties of the fresh concrete, thereby impacting print quality. Specifically, the material behavior changes, causing the width of the material filament to deviate from its desired value. To address the issue of printing process control under uncontrolled environments, this thesis work focuses on adaptive compensation for deviations in material filament width during deposition. The printing process involves a trade-off between two different dynamics: a rapid dynamic system, namely the robot, which is a mechatronic system, and a slow dynamic system, namely material pumping, which is a fluid mechanical system. Thus, the research question consists of: How to adapt the printing robot's velocity along the trajectory to maintain continuous and consistent material deposition, under the constraints of trajectory curvature, desired material filament width, and flow rate, while accounting for fluctuations in external temperature and humidity. For this purpose, an integrated approach has been proposed that covers the overall process: pre-printing, in-printing, and post-printing.

Keywords: Additive manufacturing, Adaptive estimation and compensation, Qualitative diagnosis, Serial robot, Uncontrolled environment, Quantitative diagnosis

Vers un processus d'automatisation de l'impression 3D dans la construction en environnement non contrôlé

Résumé

La fabrication additive à base des matériaux dérivés du béton, également connue sous le nom d'impression 3D en béton (3DCP), a gagné de plus en plus d'attention dans l'industrie de la construction ainsi que dans le monde académique dans divers domaines de recherche, y compris les sciences des matériaux, l'automatique et la robotique. Cette technologie permet la fabrication de géométries complexes 3D, conçues suivant un dépôt contenu couche par couche, en utilisant des matériaux de construction tels que le béton recyclé issu de déchets de démolition contenant des AFR (agrégats fins recyclables). Un système robotique est utilisé dans le processus d'impression pour guider une buse qui dépose du matériel le long d'une trajectoire définie. La plupart des technologies 3DCP sont effectuées dans des environnements contrôlés sans perturbations extérieures. Cependant, dans des environnements non contrôlés, des changements de température et d'humidité peuvent affecter considérablement les propriétés rhéologiques du béton frais, ce qui a un impact sur la qualité de l'impression. Plus précisément, le comportement du matériau change, ce qui fait dévier la largeur du filament du matériau de sa valeur souhaitée. Pour aborder le problème du contrôle/commande du processus d'impression 3D dans la construction dans des environnements non contrôlés, ce travail de thèse se concentre sur la compensation adaptative des écarts de largeur du filament de matériau pendant le dépôt. Le processus d'impression implique un compromis entre deux dynamiques différentes : un système dynamique rapide, à savoir le robot, qui est un système mécatronique, et un système dynamique lent, à savoir le pompage du matériel, qui est un système de mécanique des fluides. Ainsi, la question de recherche consiste à : Comment adapter la vitesse du robot d'impression le long de la trajectoire pour maintenir un dépôt de matériau continu et cohérent, sous les contraintes de courbure de la trajectoire, de largeur de filament de matériau souhaitée et de débit, tout en tenant compte des fluctuations de la température et de l'humidité externes. À cet effet, une approche intégrée a été proposée qui couvre l'ensemble du processus : pré-impression, impression et post-impression.

Mots clés: Fabrication additive, Estimation et compensation adaptative, Diagnostic qualitatif, Robot de guidage et de réparation, Environnement non contrôlé, Diagnostic quantitatif

*This thesis is dedicated to my parents, YANG Zuneng and BAI Zhiping,
for their love, endless support and everything they have given me.*

Acknowledgments

I would like to express my deepest appreciation to my supervisor, Prof. Rochdi Merzouki, for his continuous support and guidance over the past five years since my Master's studies. His immense knowledge, insightful suggestions, and expertise have been invaluable to my learning experience. I am endlessly inspired by his professionalism and attitude. His mentorship has been indispensable in realizing this research work.

I would like to express my sincere gratitude to my co-supervisor, Dr. Othman Lakhel, for his expertise and vast experience in this research field. His assistance and guidance have been invaluable throughout this work. I would also like to extend a special thanks to my colleague Mr. Abdelkader Belarouci, for his continuous help and insightful discussions about my research work.

I gratefully acknowledge the financial support from the EU CIRMAP project, without which this research would not have been possible.

My gratitude extends to my thesis reviewers: Prof. Mitra Fouladirad and Prof. Taha Boukhobza, and other jury members: Prof. Sébastien Rémond, Prof. Abdelaziz Benallegue, Prof. Kamal Youcef-Toumi, Dr. Aurélie De Boissieu and Dr. Agnès Petit, for their time and insightful comments to improve this work.

Many thanks to my colleagues and lab mates at CRISAL: Gérald Dherbomez, Mario Sanz Lopez, Maxime Duquesne, Mahdi Boukerdja, Steeve Kamga Mbakop, Rim Abdallah, Rabah Ouali, Braian Igreja De Freitas, Abbass Chreim, and Abdeslem Smahi. They have always been friendly and willing to help.

Special thanks to my friends in Lille: Xiaoqin Zhai, Jun Jiang, Yiwen Chen, Yibing Cui, Guangjie Li, Dongxue Jiang, Chenyang Pan, Bofan Wu, Yuyang Chang. You have provided me with wonderful times and emotional support during my stay in France. Your friendship has been precious.

Thank you to my cat Dingdang, who was born on my 26th birthday, for accompanying me through many tough times during my stay in France.

To my parents, your love and trust has been a constant source of strength for me. Thank you for always being there.

To my wife, Shuting Pan, your love, encouragement, and companionship have made all the difference. I couldn't have come so far without you.

Contents

1	Introduction	1
1.1	General introduction	1
1.2	Industrial Context for Automation of 3D Printing in Construction	3
1.3	Contractual context of the thesis	3
1.4	Scientific context of the thesis	4
1.5	Thesis objectives	5
1.6	Research problem statement	6
1.7	Thesis methodology	7
1.8	Main contributions	8
1.9	Contributions within CIRMAP framework	8
1.10	Disseminated results	9
1.11	Thesis organization	10
2	State of the Art on 3D Printing in Construction	12
2.1	Introduction	12
2.2	3D Printing in Construction using Recycled Materials	13
2.2.1	Selection of Recycled Materials	15
2.2.2	3D Printing Process	16
2.2.3	Finishing and Detailing	21
2.2.4	Post-Printing Quality Inspection	22
2.2.5	Advantages of 3D Printing in Construction using Recycled Materials	23
2.3	3D printing with environmental conditions	24
2.3.1	Controlled Environmental Conditions	25
2.3.2	Uncontrolled Environmental Conditions	31
2.4	Comparative 3D printing processes	37
2.5	Conclusion	39
3	Pre-printing of 3DCP process	40
3.1	Introduction	40
3.2	Robot pre-preparation	41
3.2.1	Printing workspace	42
3.2.2	Trajectory Generation	49
3.2.3	Implementing in Robot Control	54
3.2.4	Executing the Trajectory	56
3.3	Shape Pre-preparation	59
3.3.1	Curvature limitation	60

3.3.2	Shape reconstruction from the 3D robot printing	61
3.4	Material Pre-preparation	66
3.4.1	Material mixing	66
3.4.2	Material Quantity Estimation	66
3.5	Emulated Uncontrolled Environment	68
3.6	Conclusion	72
4	In-printing stage: Tracking of Filament Deposition	73
4.1	Introduction	73
4.2	Problem Statement	74
4.2.1	Material deposition parameters	75
4.2.2	Assumptions	77
4.3	Deep Learning-based filament width estimation	77
4.3.1	Filament segmentation	78
4.3.2	Camera calibration	79
4.3.3	Filament width estimation	79
4.4	Qualitative diagnosis approach	84
4.4.1	Pattern recognition for system diagnosis	84
4.4.2	Case study: CIRMAP printing session	85
4.4.3	Results and discussion	91
4.5	Quantitative Diagnosis approach	99
4.5.1	Diagnosis based on Analytical Redundancy	99
4.5.2	Case study: CIRMAP printing session	100
4.5.3	Real-time diagnosis in controlled environment	107
4.5.4	Real-time diagnosis in uncontrolled environment	112
4.5.5	Comparison study	114
4.5.6	Conclusion	115
5	In-printing stage: Adaptive estimation and compensation	118
5.1	Introduction	118
5.2	Problem statement	119
5.3	Adaptive compensation based on velocity estimation	120
5.3.1	Neural network based velocity estimation	120
5.3.2	Adaptive velocity compensation	122
5.4	Results and discussion	123
5.4.1	Compensation of filament width deviations during the in-printing stage	123
5.4.2	Evaluation in large scale printing	126
5.5	Conclusion	139

6	Post-printing stage: Preventive maintenance	141
6.1	Introduction	141
6.2	Predictive maintenance system	143
6.2.1	Description of the Flying 3D printing system	143
6.2.2	Operating principle description	145
6.3	Trajectory Generation : Crack Detection and Localization	145
6.3.1	Deep Learning for crack detection	145
6.3.2	Crack centerline extraction and localization	149
6.4	Model-based kinematic control of the soft arm	151
6.4.1	Modeling assumptions	152
6.4.2	Towards inverse kinematic model of the CBHA	154
6.4.3	Effort-based deformation of an inter-vertebra	159
6.5	Preventive maintenance: Crack repair	165
6.5.1	Soft-arm control strategy for crack repair	166
6.5.2	Relationship between material flow and input pressure	169
6.5.3	Experimental results	170
6.6	Discussion	171
6.7	Conclusion	173
7	Conclusion and Perspectives	175
7.1	General conclusions	175
7.2	Perspectives	178
7.2.1	Pre-printing	178
7.2.2	In-printing	179
7.2.3	Post-printing	181
	Appendices	182
A	CIRMAP printing system in emulated environment	184
A.1	CIARMAP printing system description	184
A.2	3D concrete printing dataset	185
A.3	Printing tests in the emulated environment	186
B	3D shapes printed in CIRMAP project	193
B.1	CIRMAP 3D Printing Campaign at Polytech Lille, June 2023	193
B.2	Printing session at Orléans, September 2023	197
	Acronyms	199
	Bibliography	201

List of Figures

1.1	The CIRMAP project.	4
2.1	Fresh state properties of 3DCP materials.	14
2.2	A typical process of 3D concrete printing in controlled or uncontrolled environment consisting of 3 stages. The environmental parameters (T: temperature, H: humidity, etc.) can affect the mixing (step 2) and deposition of material (step 3).	17
2.3	Building up a cylindrical structure layer by layer.	20
2.4	A post-printing offline layer deformation method combining DL and CV [Davtalab 2020].	23
2.5	Sika 3D printing gantry.	27
2.6	CyBe mobile 3D printer.	27
2.7	Apis Cor 3D printer machine.	28
2.8	MATRICE[Lakhal 2018] mobile 3D concrete printer. a) Application in printing process. b) Quality inspection of printed structures, the printer nozzle is replaced by a soft arm equipped with visual sensors.	28
2.9	BatiPrint3D developed by University of Nantes.	29
2.10	a) Winsun’s concrete printing machine. b) Winsun’s 3D printed office for Dubai Future Foundation.	30
2.11	The printer developed by XtreeE using an ABB industrial manipulator.	30
2.12	Conventional CV edge detectors have been used to determine filament size in AM of plastic based material [Wu 2021a] and food material [Ma 2023].	32
2.13	Conventional CV methods used in concrete 3D printing quality control. a) Otsu’s binarization is used to distinguish filament, the material extrusion rate is regulated in case of anomaly [Kazemian 2019]. b) Edge detector is used to distinguish filament, nozzle velocity is regulated in case of anomaly [Barjuei 2022].	33
2.14	Dedibot’s concept of flying 3D concrete printer.	35
2.15	Printing process concept employing teams of aerial robots, developed by the Imperial College London [Zhang 2022].	36
2.16	a) Concept of space construction through contour crafting by NASA. b) Automated Construction of Expeditionary Structures (ACES) by U.S. Army.	36

3.1	Robot preparation steps.	41
3.2	The Denavit-Hartenberg parameters and frame assignment of UR10e manipulator.	43
3.3	The global workspace of the UR10e robot without constraints (blue) and the sub workspace (red) under constraints for 3DCP.	47
3.4	The sub workspace under constraints.	47
3.5	3DCP process workspace limitation: the final workspace is represented by the shadowed area.	48
3.6	Slicing and tool path generation	52
3.7	A curved region approximated as a segment of a circle.	53
3.8	Slicing of a complex 3D shape for tool path planning of 3DCP process: 4 different selections of layer height and distance between points.	54
3.9	Different joint configurations for the same position: (1)-(6). (2) and (3) are two different configurations for the same position and orientation of end effector. (3) is the optimal configuration.	56
3.10	The sequence of poses of the nozzle tracking a circular toolpath.	57
3.11	Nozzle pose and velocity control of robot.	57
3.12	Curvature along trajectory	60
3.13	Printing a complex shape: toolpath generated by slicing and the final printed shape.	62
3.14	Circumcircle of $\triangle P_1P_2P_3$, the curvature at P_2 is given by the reciprocal of the circumradius.	62
3.15	The curvature distribution along a single layer in XOY plane.	64
3.16	Nozzle velocity and curvature along traveled distance by nozzle.	64
3.17	Representation in 3D, the blue arrows in XOY plane is the curvature, the red arrow along the third axis represents the velocity error Δv	65
3.18	The relationship between local curvature κ and actual nozzle velocity v given a reference velocity $v^d = 12 \text{ cm/s}$	65
3.19	Flow table test to determine the workability of fresh concrete.	67
3.20	External configuration of the emulated environment.	68
3.21	Internal configuration of the emulated environment.	69
3.22	3DCP tests conducted within the emulated environment. (a)(g) Printing objects of variable-curvature shape. (b)(d) Printing objects of constant-curvature (cylindrical) shape. (c) Control panel of the climatic chamber. e) Mortar mixer used for material preparation. f) The climate chamber.	70

3.23	Test example: outdoor ambient temperature $T_{ambient} = 19^{\circ}C$. a) Temperature of newly extruded material T_{fresh} and deposited material at a specific point T_{bottom} measured during printing. b) The evolution of temperature at the top (T_{top}) and bottom (T_{bottom}) of the printed object and temperature inside the climate chamber measured during the material drying process. c) Humidity inside the climate chamber H_{EE} during the material drying process.	71
4.1	3DCP SoS architecture	75
4.2	Continuous material deposition during in-printing stage.	76
4.3	Architecture of Mask RCNN	79
4.4	a) without undistortion step, $SSE \approx 73.3mm^2$; b) with undistortion step, $SSE \approx 0.39mm^2$	80
4.5	a) The contour and center line of the filament segment, extracted from the binary mask given by the instance segmentation model. b) The distance map of filament binary mask. c) The medial axis transform (MAT) of filament binary mask, defining the center line.	81
4.6	Filament center line in image frame. a). Local width values at two ends E1 and E2 should be ignored for width estimation. b). segmented filament from image captured by visual sensor.	81
4.7	Local width value distribution (pixel unit)	82
4.8	Overall filament width calculated in real dimension (35.5mm)	83
4.9	The overall workflow of filament width estimation algorithm.	83
4.10	Results of an automatic filament segmentation and width calculation. a). Automatic calculated width during the printing stage: 25.7mm b). measured width in post printing stage: 26mm.	84
4.11	Classifications and observation points in the feature space.	85
4.12	Continuous deposition operation points can be categorized into three classes. Normal: $w = w^d$; Abnormal 1: $w > w^d$; Abnormal 2: $w < w^d$	86
4.13	Three considered classes in the feature space formed by U , v , and Q	87
4.14	Qualitative diagnosis based on pattern recognition techniques.	88
4.15	Shape designs for printing test under different environments.	90
4.16	Cloud of operation points under $20^{\circ}C$	91
4.17	Classification of operating points under $T = 10^{\circ}C$, $H = 50\%$	93
4.18	Classification of operating points under $T = 20^{\circ}C$, $H = 50\%$	94
4.19	Classification of operating points under $T = 30^{\circ}C$, $H = 50\%$	95
4.20	Operation points of Normal class under three temperatures.	97

4.21	Operation points of Abnormal 1 class under three temperatures.	97
4.22	Operation points of Abnormal 2 class under three temperatures.	98
4.23	Accumulative flow (cm^3/s) under $T = 15^\circ\text{C}$ given different pump voltage control during the pumping of a same batch of material fresh mixture.	101
4.24	The flow rate Q and the pump voltage command conform to a linear relation under constant temperature $T = 15^\circ\text{C}$	101
4.25	The flow rate Q and the pump voltage in different temperatures.	102
4.26	a) Pump voltage command U ; b) Estimated flow rate \hat{Q} based on U and measured flow rate Q ; c) Estimation error.	103
4.27	Geometric model of material deposit filament during a normal printing process.	104
4.28	Layer height considered constant across the printed shape. . .	105
4.29	Complex shapes with variable curvature: nozzle paths given by slicing and final printed shapes. a) The toolpath and printed structure of Shape (A). b) The toolpath and printed structure of Shape (B).	108
4.30	Tracking of a layer of Shape (A). a) Nozzle velocity v . b) Nozzle velocity error Δv . c) Filament width w . d) Filament width error Δw . e) Residual r_1 . f) Residual r_2 . g) Path curvature. h) Sharp turn with large curvature.	109
4.31	Tracking of a layer of Shape (B). a) Nozzle velocity v . b) Nozzle velocity error Δv . c) Filament width w . d) Filament width error Δw . e) Residual r_1 . f) Residual r_2 . g) Path curvature. h) Sharp turn with large curvature.	110
4.32	$T = 10^\circ\text{C}$, detection of an over deposition (Abnormal 1). a) Filament width. b) Filament width error. c) d) Residuals r_1 and r_2	112
4.33	$T = 20^\circ\text{C}$, detection of over depositions (Abnormal 1). a) Filament width. b) Filament width error. c) d) Residuals r_1 and r_2	113
4.34	$T = 30^\circ\text{C}$, detection of over deposition (Abnormal 1) and under deposition (Abnormal 2). a) Filament width. b) Filament width error. c) d) Residuals r_1 and r_2	113
5.1	Neural network structure for velocity estimation.	121
5.2	Adaptive compensation mechanism.	123
5.3	Compensation: $T = 20^\circ\text{C}$. a) Estimated velocity \hat{v} and real velocity v . b) Velocity error Δv . c) Control input $K\Delta v$	125
5.4	Compensation: tracking of filament width error, $T = 20^\circ\text{C}$. . .	126

5.5	Compensation: $T = 10\text{ }^{\circ}\text{C}$. a) Estimated velocity \hat{v} and real velocity v . b) Velocity error Δv . c) Control input $K\Delta v$	127
5.6	Compensation: tracking of filament width error, $T = 10\text{ }^{\circ}\text{C}$. . .	127
5.7	Compensation: $T = 30\text{ }^{\circ}\text{C}$. a) Estimated velocity \hat{v} and real velocity v . b) Velocity error Δv . c) Control input $K\Delta v$. d) Width error Δw	128
5.8	a) Test shape in 3D view. b) Test shape view in XOY plane. . .	129
5.9	Test at $T=20^{\circ}\text{C}$, with compensation, compensation threshold is 10% of w^d . a) Material flow rate. b) Nozzle velocity measured during printing. c) Filament width.	131
5.10	Test at $T=20^{\circ}\text{C}$, with compensation, compensation threshold is 10% of w^d . a) Tracking of velocity error $\Delta v = \hat{v} - v$. b) Tracking of control input $K\Delta v$	132
5.11	Histogram of filament width error and printed shape. $T = 10\text{ }^{\circ}\text{C}$, without compensation.	134
5.12	Histogram of filament width error and printed shape. $T = 10\text{ }^{\circ}\text{C}$, with compensation given 15% of w^d as threshold.	134
5.13	Histogram of filament width error and printed shape. $T = 10\text{ }^{\circ}\text{C}$, with compensation given 10% of w^d as threshold.	135
5.14	Histogram of filament width error and printed shape. $T = 20\text{ }^{\circ}\text{C}$, without compensation.	135
5.15	Histogram of filament width error and printed shape. $T = 20\text{ }^{\circ}\text{C}$, with compensation given 15% of w^d as threshold.	136
5.16	Histogram of filament width error and printed shape. $T = 20\text{ }^{\circ}\text{C}$, with compensation given 10% of w^d as threshold.	136
5.17	Histogram of filament width error and printed shape. $T = 30\text{ }^{\circ}\text{C}$, without compensation.	137
5.18	Histogram of filament width error and printed shape. $T = 30\text{ }^{\circ}\text{C}$, with compensation given 15% of w^d as threshold.	137
5.19	Histogram of filament width error and printed shape. $T = 30\text{ }^{\circ}\text{C}$, with compensation given 10% of w^d as threshold.	138
6.1	Predictive Maintenance Robot System	143
6.2	Description of the CBHA soft arm	144
6.3	Functional scheme of automatic predictive maintenance for microscopic cracks	146
6.4	The architecture of Mask RCNN	148
6.5	Results of the segmentation model applied on different images of cracks	148
6.6	Crack shape reconstruction in image frame	149

6.7	Extraction of crack centerline in image coordinate system. (a) : Crack centerline; (b) : reconstruction of crack and centerline in image coordinate system	150
6.8	Crack centerline extraction and localization. (A) : Crack centerline in raw image; (B) : reconstruction of crack and centerline in image coordinate system (pixels); (C) : reconstruction of crack and centerline in real dimension (mm)	151
6.9	Schematic of an inter-vertebra modeled as parallel robot with 3 UPS-1 UP	153
6.10	Calculation of the Inverse Kinematic Step for the CBHA	155
6.11	Placement of Bishop frames on the CBHA's central curve	155
6.12	Geometric relationship of an inter-vertebra	157
6.13	Cross-section of the pressure propagation in each CBHA's tube allowing deformation.	160
6.14	Finite Element Method (FEM) Simulation for Studying Microscopic Deformations and Mechanical Behavior of CBHA Using ANSYS.	161
6.15	Results Generated by ANSYS for the Scenario Where All Tubes Are Simultaneously Supplied with the Same Pressure from 0 to 1.5 Bar	163
6.16	Results Generated by ANSYS for the Scenario with Simultaneous Pressurization of Two Tubes from 0 to 1.5 Bar	163
6.17	Results Generated by ANSYS for the Scenario with Only One Tube Supplied with Pressure from 0 to 1.5 Bar	164
6.18	Comparative Analysis of Displacement Variation with Pressure Across Single, Double, and Triple Tubes	164
6.19	Predictive maintenance robot system control scheme for crack repair	167
6.20	Associated frames of the robot system	168
6.21	Workspace of the soft arm (a) perspective view (b) z-y view (c) z-x view	168
6.22	Material Delivery System with Syringe	169
6.23	Neural Network architecture for modeling the material deposit pressure	170
6.24	Rear and forward movements for pressure estimation of deposited material	170
6.25	Trajectory of the tip of the arm during the reparation process of the crack 1. (A) 3D position tracking of the crack 1. (B) X-axis Error. (c) Y-axis Error. (D) Z-axis Error.	171

6.26	Trajectory of the tip of the arm during the reparation process of the crack 2. (A) 3D position tracking of the crack 2. (B) X-axis Error. (c) Y-axis Error. (D) Z-axis Error.	172
6.27	Repair steps for crack 1	173
7.1	Online measurement and data collection system for creating digital twin for 3D concrete printing.	179
7.2	Estimation of crack depth with depth (RGB-D) camera.	181
A.1	3D Concrete Printing system and available sensors.	184
A.2	Time-stamped image data sample captured during printing test under $T = 10^{\circ}C$. a) RGB images of freshly deposited filament from top-view captured by two cameras integrated on the nozzle. b) Thermal image captured by the thermal camera placed in front of the printed object.	186
A.3	Temperature and humidity set values and measured values inside climate chamber and outdoor ambient conditions in Lille, France during two testing days (19^{th} - 20^{th} July, 2022, these dates corresponded to an extreme heatwave in Lille, hence particularly high outdoor temperatures can be observed). The fluctuations were due to differences between outdoor ambient parameters and inside-climate chamber parameters when the door was opened.	187
A.4	The cylindrical shape with constant curvature designed for the printing test, the diameter is 30 cm.	188
A.5	The first layer of the cylindrical shape designed for manual calibration of the printing system parameters based on the measurement of layer widths.	188
A.6	Test example: outdoor ambient temperature $T_{ambient} = 39^{\circ}C$. a) Temperature of newly extruded material T_{fresh} and deposited material at a specific point T_{bottom} measured during printing. b) The evolution of temperature at the top (T_{top}) and bottom (T_{bottom}) of the printed object and temperature inside the climate chamber measured during the material drying process. c) Humidity inside the climate chamber H_{EE} during the material drying process.	191

A.7	Test example: outdoor ambient temperature $T_{ambient} = 21^{\circ}C$. a) Temperature of newly extruded material T_{fresh} and deposited material at a specific point T_{bottom} measured during printing. b) The evolution of temperature at the top (T_{top}) and bottom (T_{bottom}) of the printed object and temperature inside the climate chamber measured during the material drying process. c) Humidity inside the climate chamber H_{EE} during the material drying process.	192
B.1	Recycled sand sourced from different regions (Belgium, France, Germany, the Netherlands).	194
B.2	French design using French sand, 19-20 June, 2023.	194
B.3	Dutch design using Dutch sand, 22-23 June, 2023.	195
B.4	German design using German sand, 26-27 June, 2023.	195
B.5	German design using German sand, 26-27 June, 2023.	196
B.6	Belgian design using Belgian sand, 29-30 June, 2023.	196
B.7	Printing system setup, 27 September, 2023.	197
B.8	Equipment installed in-situ, 27 September, 2023.	198

List of Tables

2.1	Existing robot-based techniques for additive manufacturing in the construction	38
3.1	Denavit-Hartenberg parameters of UR10e manipulator.	43
3.2	Batching of Concrete Mix	66
4.1	Description of Parameters	76
4.2	Range of features: Normal	92
4.3	Range of features: Abnormal 1 (over deposition)	92
4.4	Range of features: Abnormal 2 (under deposition)	92
4.5	Fault Signature Matrix	107
4.6	Summary comparison between Pattern Recognition and Analytical Redundancy diagnosis approaches for 3DCP	116
5.1	The deviation length percentage (total print length $L_{total} = 50.4$ m) under different environment temperatures (T) given different threshold (15% and 10% of w^d).	134
6.1	Polynomial trend-line coefficients for the three different scenarios	165
A.1	3DCP dataset	185
A.2	Summary of results obtained through the printing tests. The set value of relative humidity of the climate chamber is fixed at $H^{env} = 50\%$. $H_{ambient}$: outdoor ambient humidity, $T_{ambient}$: outdoor ambient temperature, T_{EE} : set value of temperature in climate chamber, T_{dry}^{mat} : temperature of dry materials before mixing, Δt_{mix} : duration between the start of material mixing and the beginning of printing, T_{mix}^{mat} : temperature of mixed material at the beginning of printing, D : diameter of flow table test, U^{pump} : pump voltage control, v^{nozzle} : nozzle motion speed, N : number of layers reached (maximum 40), W : average width of material deposit filament.	189
B.1	CIRMAP partnters	193
B.2	Recycled sand from different countries.	194

Introduction

Contents

1.1	General introduction	1
1.2	Industrial Context for Automation of 3D Printing in Construction	3
1.3	Contractual context of the thesis	3
1.4	Scientific context of the thesis	4
1.5	Thesis objectives	5
1.6	Research problem statement	6
1.7	Thesis methodology	7
1.8	Main contributions	8
1.9	Contributions within CIRMAP framework	8
1.10	Disseminated results	9
1.11	Thesis organization	10

1.1 General introduction

The emergence of 3D Concrete Printing (3DCP) has gained considerable interest from the research community including diverse fields such as material science, automation, robotics, etc., and it has been broadly implemented in the construction industry. 3DCP concerns a mold-free fabrication process by depositing cementitious material layer by layer through a nozzle guided by a robot or a gantry system, forming a pre-designed geometry. In instances of large-scale construction, the employment of mass production techniques results in a reduction of construction duration at the expense of design complexity. 3DCP provides an alternative solution that enables the preservation of complex geometrical designs whilst simultaneously reducing construction time [Buswell 2018, Hossain 2020, Souza 2020]. This technology is particularly advantageous in the production of non-large-scale urban furniture, which requires highly customized designs that are context-specific.

In term of environmentally sustainable manufacturing, extensive research has proven the feasibility of utilizing recycled materials in 3DCP [Zou 2021, Ding 2020]. Although there exists also research focusing on optimized materials with more suitable behavior for 3DCP [Shahzad 2021], in the case of using recycled materials, the choice of material mix is limited by local conditions. An instance of this phenomenon can be observed in North West Europe, where approximately 65 million tons of Recycled Fine Aggregates (RFA) are produced annually through the crushing of concrete construction and demolition wastes, presenting a significant environmental hazard if not reused. However, as the production of RFA is typically localized, the properties and characteristics of the material can differ from one particular region to another, this variability poses a challenge for mass production using recycled materials and complicates the development of standardized procedures for incorporating RFA into the fabrication of urban furniture.

The quality of 3D Concrete Printing is subject to various factors, which can be broadly categorized into three main groups: material mixture, environmental conditions, and printing system parameter configurations. Each of these factors may significantly influence the behavior and characteristics of the material during deposition. Moreover, the shape design can also impact the quality of the printed structure.

Unlike 3D printing processes involving plastics and metals, where both material and environmental conditions are strictly controlled, a considerable fraction of 3D Concrete Printing tasks are executed outdoors, especially in on-site printing scenarios. For example, a mobile 3DCP platform that allows for on-site printing was developed in [Lakhal 2020], thus reducing the need for transportation and minimizing labor costs. However, this outdoor nature of 3DCP can have significant implications for the process, including the quality and properties of the printed structures. Additionally, studies investigating the control and optimization of the 3D Concrete Printing process have been limited to structured environments, single process stage or individual system components, therefore, an integrated approach considering the overall 3DCP process from pre-printing (trajectory generation), in-printing (robot motion and material pumping) to post-printing (quality control and maintenance), might contribute in addressing the aforementioned issues related to the overall process automation of 3D Concrete Printing. These constitute the main interest of the presented research work.

1.2 Industrial Context for Automation of 3D Printing in Construction

The automation of 3D printing in construction represents a significant advancement in the construction industry [Li 2019]. It accelerates the construction process and leads to faster project completion times, allowing for more projects to be undertaken. Automated systems follow digital models with high precision, minimizing human error. This ensures that the final structure closely matches the design specifications. Also, automation enables the construction of complex, non-standard geometries that may be challenging or impractical to achieve using traditional construction methods. This is one objective of this thesis work. To improve overall safety on construction sites, automated systems can operate in hazardous environments or perform tasks that may pose risks to human workers. Finally, the automation of 3D printing in construction offers a high degree of adaptability to different architectural styles and construction needs [Arnaud Perrot 2017]. While automation brings numerous advantages, there are limitations when trying to implement it in uncontrolled environments, such as outdoor construction sites that present challenges like temperature variations, humidity, wind, and dust. These factors can affect the performance of automated systems and may require additional adaptations. Also, uncontrolled environments often require dynamic adjustments to the construction process based on real-time conditions. For example, changes in weather can be more complex for automated system. These limitations are the main disturbances that are considered in the thesis work to perform the overall 3D printing process.

1.3 Contractual context of the thesis

This research work was conducted within the framework of the CIRMAP¹ (Circular economy via customizable furniture with Recycled Materials for public Places) project funded by the Interreg North-West Europe Program². The duration of the project is 36 months (April 2020 – March 2023). The thematic priorities of the project are resource and materials efficiency. The project involves partners with different background, including higher education institutes, public institutions, and companies from France, the UK, the Netherlands, Germany, and Belgium (see B). The overall objective of the project is to implement on-site 3D printing of various types of furniture, such

¹<https://www.nweurope.eu/projects/project-search/cirmap-circular-economy-via-customisable-furniture-with-recycled-materials-for-public-places/>

²<https://www.nweurope.eu/>

as urban, memorial, or garden furniture, by providing a new mixture proportion method for 3D printing mortars, a new design methodology for customized shapes, and an implementation of a new master control command. Five Local Public Authorities in North West Europe will provide public places that will be equipped with 3D printed customized furniture.

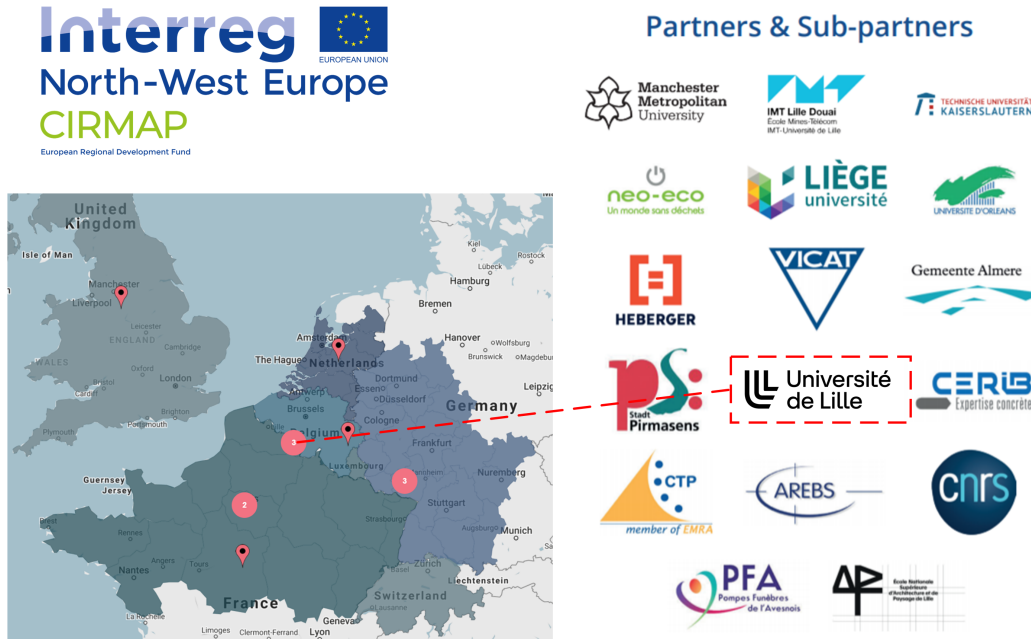


Figure 1.1: The CIRMAMP project.

The project is divided into a series of work packages (WPs), with activities allocated to different partners. The primary focus of this thesis falls within the following work packages:

- WP T2: Development of methodologies and process for the 3DP of mortars containing RFA. The involved activities include online monitoring and quality control of 3DP process.
- WP T3: Industrial feasibility. The involved activities include the development and demonstration of 3DP facilities on industrial scale. A robotized construction 3D printing and data collection system has been developed.

1.4 Scientific context of the thesis

This research work has been conducted at the Research Center in Computer Science, Signal and Automation of Lille (CRISAL UMR CNRS 9189) within

the SoftE (System of Systems Engineering) team³ of the ToPSyS (Tolerance Prognosis System of Systems) group⁴. The research team main topic is the automation of large scale systems, known with its class of system of system engineering. The aim of the thesis work is to address the scientific issues relating to the control of the overall **3D Concrete Printing** process, which can be easily affected by unstable material properties and environmental disturbances, as well as the complexity of object shapes. The scientific context concerns the following:

- Performing the automation of the overall 3D printing process in construction for highly customized complex shapes under uncontrolled environment.
- Investigating the links and relationships between different parameters of the printing process, based on large data set collected during printing experiments. This, with respect to a set of heterogeneous components, including robot, material and shape. The data set is shared with the project partners from different backgrounds.

The research has been carried out under the supervision of Prof. Rochdi Merzouki, Professor at the University of Lille and Dr. Othman Lakhal, Associate Professor at the University of Lille.

1.5 Thesis objectives

3D Concrete Printing has emerged as a significant research topic over recent decades, attracting increasing interest from the academic community and finding extensive applications within the construction industry. In contrast to 3D printing with thermoplastic materials such as PLA and ABS where the printer is an integrated system and factors such as material properties and printing environment are tightly controlled, **3D Concrete Printing** presents a more complex scenario. The concrete materials used can exhibit unstable properties during the printing process, and print quality can be influenced by environmental disturbances and inherent properties of the material. Additionally, **3D Concrete Printing** can be modeled as a system of systems (SoS), comprising several disparate components: the robot, the material, and the shape.

The thesis research work on the automation of 3D printing of recycled concrete material in uncontrolled environments aims to achieve several key objectives:

³<https://www.cristal.univ-lille.fr/equipes/softe/>

⁴<https://www.cristal.univ-lille.fr/gt/topsys/>

1. Identify the optimal printing parameters, including layer height, printing velocity, and material flow rate, for 3D printing with recycled concrete material. This helps achieve the best print quality and structural integrity.
2. Study the flow behavior of recycled concrete material during printing to ensure it can be extruded and layered effectively, after examining factors like viscosity, rheology, and workability.
3. Develop strategies and technologies to adapt the 3D printing process to uncontrolled environments, by addressing challenges related to temperature variations, humidity, luminescence, and other site-specific conditions.
4. Explore the integration of automation systems, such as robotic arms in a climate chamber used to emulate external environment, to enhance the efficiency and precision of the 3D printing process in uncontrolled environments.

1.6 Research problem statement

Let's consider a process of printing a complex shape with concrete material containing **RFA** in its fresh state (fluid) in uncontrolled environment. In pre-printing stage, trajectory generation defines the position and velocity of the nozzle, thereby determines the local curvatures κ along the trajectory. We assume that there is a continuous material flow at the printer nozzle. However, the flow rate Q describing the material behavior can vary under the impact of environmental disturbances, affecting the quality of deposited material filament. The goal of the fundamental research focuses on **enhancing the overall kinetic energy ($E_k(t)$) efficiency of 3DCP process which is linked to the velocity of the nozzle, taking into account various parameters**, including the curvature of the shape and material behavior variations during the continuous deposition. It also considers the compromise between two dynamic systems, a rapid dynamic system, namely robot, which is a mechatronic system and slow dynamic system, namely material pumping which is a fluid mechanical system.

Thus, the research question consists on: **How to adapt the printing robot's velocity in the trajectory to maintain continuous and consistent material deposit, under the constraints of trajectory curvature, material filament width and flow, with fluctuation of external temperature and humidity.** This problem can be therefore formulated as follows:

$$\begin{aligned}
& \text{minimize } E_k(t) = f(\kappa, w, Q(T, H)), \\
& \text{subject to :} \\
& 0 \leq \kappa \leq \kappa_{\max}, \\
& w_{\min} \leq w \leq w_{\max}, \\
& T_{\min} \leq T \leq T_{\max}, \\
& H_{\min} \leq H \leq H_{\max}, \\
& \varepsilon_{\min} \leq \varepsilon \leq \varepsilon_{\max}
\end{aligned} \tag{1.1}$$

Where κ is the curvature along trajectory, w is the width of the deposited material filament, Q is the material flow rate that is affected by the environmental conditions: temperature T , humidity H and light intensity ε .

1.7 Thesis methodology

To solve the problematic of this thesis, the 3D printing process is divided into three stages: pre-printing, in-printing and post-printing stage, each stage is associated with a part of the thesis work. Through this methodology, the overall 3DCP process can be optimized.

Pre-printing is an offline stage concerning the following steps: shape design, robot workspace and trajectory generation, validation and emulated environment preparation. Shape design gives the overall geometry of the object structure, simple or complex. The trajectory generation step determines the positions, velocities and curvatures along the nozzle's trajectory. Finally, the external environment is emulated with a climate chamber, allowing performing the adaptive control of the printing robot machine during the In-printing stage.

In-printing refers to online printing stage, where the printing robot machine is guiding the recycled concrete material deposition continuously. Online methods should be applied in this stage, as it concerns various variables that can be measured directly or indirectly during the material deposition. The methods aim to solve two problems:

1. Automatic detection of filament width deviation.
2. Adaptive velocity compensation.

Post-printing stage focuses on the quality control of the printed structure. After the printing stage and the stability of the material, structural imperfections such as cracks can appear on concrete surfaces after long

time exposure to ambient environment. To guarantee the quality and maintenance of the printed furniture, a quality control method for automatic scanning and detection of the crack imperfection is proposed. This allows realizing local intervention method to repair this local defect.

1.8 Main contributions

Following the methodology in the previous section, the following contributions are discussed in this thesis:

- An offline approach to developing a simulation framework for 3D printing in construction, this involves the pre-printing stage and emulating the environment, facilitating the creation of a digital twin for the printing process.
- Development of an online detection and isolation method for filament width deviation [Yang 2022b], [Yang 2023a].
- Online adaptive velocity compensation during printing under various constraints [Yang 2023b].
- Offline method for detection and local intervention of concrete surface crack defects [Kahouadji 2021, Yang 2022a].

1.9 Contributions within CIRMAP framework

The thesis work contributed in the work packages WPT2 (Development of methodologies and process for the 3D printing of mortars containing RFA) and WPT3 (Industrial feasibility). WPT2 concerns the monitoring and control of the 3DCP process in order to improve printing quality in different conditions adaptively. WPT3 optimizes the solution of automation of printing process in order to facilitate the deployment and replicability of the solution towards industrials.

In the framework of CIRMAP project, University of Lille and CRISAL Lab contributed to the following deliverables:

- Automatic detection of filament width deviation based on AI. (WPT2, Deliverable 2.2)
- Adaptive compensation of material deposition in uncontrolled environment. (WPT2, Deliverable 2.3)
- Emulated environment for 3DCP. (WPT3)

- Pilots preparation (WPT3).

1.10 Disseminated results

Journals

- Xinrui Yang, Mouad Kahouadji, Othman Lakhall and Rochdi Merzouki (2022). Integrated design of an aerial soft-continuum manipulator for predictive maintenance. *Frontiers in Robotics and AI* (DOI: 10.3389/frobt.2022.980800).
- Xinrui Yang, Othman Lakhall, Abdelkader Belarouci and Rochdi Merzouki (2023). Automatic Detection and Isolation of Filament Width Deviation during 3D Printing of Recycled Construction Material. *IEEE/ASME Transactions on Mechatronics* (DOI: 10.1109/TMECH.2023.3313693)
- Xinrui Yang, Othman Lakhall, Abdelkader Belarouci, Sébastien Rémond and Rochdi Merzouki (2023). Emulated Environment for 3D Printing of Recycled Materials. *Automation in Construction* (Under review).

International conferences

- Mouad Kahouadji, Othman Lakhall, Xinrui Yang, Abdelkader Belarouci, Rochdi Merzouki (2021). System of Robotic Systems for Crack Predictive Maintenance. In 16th International Conference of System of Systems Engineering (SoSE). July 2021, Västerås, Sweden.
- Xinrui Yang, Othman Lakhall, Abdelkader Belarouci and Rochdi Merzouki (2022). Adaptive Deposit Compensation of Construction Materials in a 3D Printing Process. In 2022 IEEE/ASME International Conference on Advanced Intelligent Mechatronics (AIM), July 2022, Sapporo, Japan.
- Xinrui Yang, Othman Lakhall, Abdelkader Belarouci, Kamal Youcef-Toumi and Rochdi Merzouki (2023). Experimental Workflow Implementation for Automatic Detection of Filament Deviation in 3D Robotic Printing Process. In 2023 IEEE International Conference on Robotics and Automation (ICRA). June 2023, London, United Kingdom.
- Xinrui Yang, Othman Lakhall, Abdelkader Belarouci, Kamal Youcef-Toumi and Rochdi Merzouki (2023). Adaptive Estimation and Detection of Filament Width Deviation during 3D Robotic Printing of Construction Materials. In The 22nd World Congress of the International

Federation of Automatic Control (IFAC WC 2023). July 2023, Yokohama, Japan.

1.11 Thesis organization

This thesis manuscript is organized as follows:

- **Chapter 2: State of the art on 3D Concrete Printing.** A state of the art on 3D printing technologies in construction is presented. This state of art highlights the benefit of automated 3D printing process in construction based on recycled materials. The chapter explains the difference of 3D printing technologies and their performances in controlled and uncontrolled environments. It ends by introducing the main context of the thesis project and making a scientific positioning comparing to the literature in adapting the automation of 3D printing in construction to an uncontrolled environment.
- **Chapter 3: Pre-printing of 3DCP Process.** This chapter emphasizes the critical role of the pre-printing phase to ensure the success of 3D printing in construction. It highlights the significance of meticulous design of the printed shapes, including considerations on the proper scaling and the curvature. It reports how proper estimation of material quantity is essential for preparation. It explains how slicing the shape model and generating accurate toolpath through a robot kinematics is crucial for guiding the printer in depositing material layer by layer. Finally, it describes the emulated uncontrolled environment for 3D printing, allowing performing the process automation in different weather conditions.
- **Chapter 4: In-printing stage: Tracking of Filament Deposition.** This chapter addresses issues of monitoring and diagnosis of material deposition during in-printing stage. The material deposition is characterized by the filament width. The real-time tracking of filament width is realized through a Deep Learning based vision algorithm, allowing for detection of filament width deviation. Two diagnosis approaches (qualitative and quantitative) are then discussed for the isolation of filament width deviation. The chapter compares the two approaches through case studies on historical data of printing process under different conditions.
- **Chapter 5: In-printing stage: Adaptive estimation and compensation.** This chapter presents the real-time adaptive estimation and compensation of nozzle velocity during the 3D printing process. It uses a

neural network-based estimator trained on a diverse dataset to estimate optimal nozzle velocity based on printing conditions and filament width setting. The resulting velocity estimate is used to adjust the actual nozzle velocity through a proportional controller, thereby compensate for the filament width deviation. The real time tracking of filament width error is realized, when it exceeds a pre-defined threshold, the compensation mechanism is activated. This approach has been successfully tested under various temperature conditions, proving its efficacy in maintaining print quality in diverse environments.

- **Chapter 6: Post-printing stage: Preventive maintenance.** This chapter shifts the focus on preventive maintenance in the post-printing stage. It presents an innovative robotic system designed, used as 3D printing system for automatic detection and repair of structural cracks. The system is composed of a stationary UAV equipped with a soft-continuum arm used as a guide for material deposition. The system utilizes deep learning techniques for crack identification and localization, while the soft arm guides putty material deposition to fill the cracks. The UAV maintains contact with the wall via wheels, allowing the arm to operate without direct surface contact. A neural network model predicts the relationship between the bending tube length and input pressure, aiding in material deposition accuracy.
- **Chapter 7: General conclusions and perspectives.** This chapter concludes the main contributions to the CIRMAP project as well as the scientific contributions to the process automation of [3D Concrete Printing](#). In addition, perspective researches are discussed in this chapter.

State of the Art on 3D Printing in Construction

Contents

2.1	Introduction	12
2.2	3D Printing in Construction using Recycled Materials	13
2.2.1	Selection of Recycled Materials	15
2.2.2	3D Printing Process	16
2.2.3	Finishing and Detailing	21
2.2.4	Post-Printing Quality Inspection	22
2.2.5	Advantages of 3D Printing in Construction using Recycled Materials	23
2.3	3D printing with environmental conditions	24
2.3.1	Controlled Environmental Conditions	25
2.3.2	Uncontrolled Environmental Conditions	31
2.4	Comparative 3D printing processes	37
2.5	Conclusion	39

2.1 Introduction

The additive manufacturing (AM) in construction, also known as 3D printing in construction, has gained significant traction in recent times due to its potential for reduced expenses, a broad spectrum of printable materials, and innovative printing methodologies. This technique involves mold-free fabrication where materials are deposited layer by layer through a nozzle under computer control, ultimately achieving a pre-designed geometry. While there are now a plethora of cement-based materials suitable for printing, both for prototype creation and technology-integrable products, the nature of these

materials can be unstable. This instability can affect the quality of the structure during or post-printing, especially in unstructured or uncontrolled environments. Such environments make it essential to monitor print quality in real-time and inspect post-print for potential defects.

In practical scenarios, AM can be conducted in both controlled and uncontrolled environmental conditions, hinging on the technology, materials, and the specific application. Often, a blend of these environments is employed; for instance, prefabricated 3D-printed components might be created in a controlled factory ambiance and subsequently transported for assembly at the construction site. Additionally, the evolution of 3D printing has brought about diverse techniques and systems, many of which employ robotic systems like fixed manipulator robots, mobile robots, and occasionally, flying robots. The choice and integration of these systems depend on product requirements and contextual needs. This evolving landscape of AM practices and challenges underscores the importance of exploring automation processes in 3D printing in construction, especially within uncontrolled settings, as highlighted by our thesis work.

This state of art highlight the different practice of the AM according to the environmental conditions allowing to make the positioning of the thesis work in terms of automation process of 3D printing in construction under uncontrolled environment.

2.2 3D Printing in Construction using Recycled Materials

In the context of the CIRMAP project, 3D printing in construction with recycled materials emerges as an innovative, sustainable approach for the construction industry. This technique uses 3D printing technology to fabricate building components (e.g. public furniture), or even entire structures, using recycled materials as the primary substrate.

3D printing mortars are designed in order to exhibit very specific rheological behavior, to be printable, its properties are contradictory [Taleb 2023a]. In particular, cementitious inks are formulated in order to present a high structuration rate [Wangler 2016], allowing the progressive stiffening of the material during printing. Structuration rate is largely influenced by the temperature and printability, therefore strongly depends on the environmental conditions. Moreover, temperature and relative humidity could also have a strong influence on the drying rate and inter-layer bonding of the deposited material [Chen 2022]. [Nguyen-Van 2022] presented a perspective on material simulations in their study on 3DCP process modeling. They emphasize that

the buildability of the material is influenced by a combination of factors. This includes the intrinsic material properties (yield stress and structural build-up rate), as well as the structure dimensions and printing parameters (nozzle velocity and pumping flow rate etc.). A calibration step is therefore indispensable for determining optimal printing parameters that ensure consistent and stable material deposition. Consequently, it should be noted that the success of a certain 3DCP process, calibrated with specific parameter configurations within a particular environment, cannot be guaranteed under different environmental conditions.

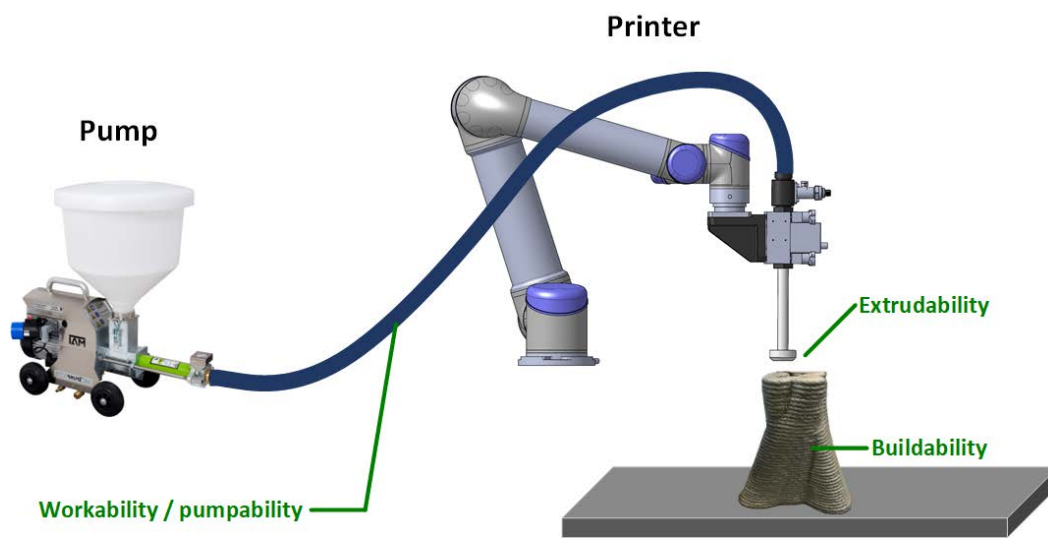


Figure 2.1: Fresh state properties of 3DCP materials.

The formulation, or mixing proportion of the printable materials is crucial, as they need to possess sufficient fluidity for extrusion. Additionally, the material must also have the necessary strength to bear its own weight. Hence, printable materials must meet the following requirements of characteristics [Xiao 2021, Kaliyavaradhan 2022]:

- **Pumpability:** Pumpability refers to how effortlessly the fresh mixture is transferred from the pump to the extrusion nozzle. The flowability of the concrete and pumping parameters must be tuned to guarantee sufficient and unobstructed supply of concrete. Different testing procedures have been explored to confirm that the concrete can be sufficiently supplied to the printhead without any blockages.
- **Extrudability:** The concrete must be extruded consistently at a specified rate to meet the efficiency and productivity demands during con-

struction. The printing process can be impacted by the rheological properties of the material as well as the extrusion system itself.

- **Buildability:** Following the delivery and extrusion of concrete, it's vital to ensure buildability to prevent any deformations in the deposited material. Buildability refers to the material's ability to maintain its shape during the extrusion process and progressively harden. This characteristic is essential to support the material as its weight increases with the addition of each new layer.

In order to meet these standards, the rheological characteristics of fresh printable concrete should differ from those of traditional concrete. It is necessary for printable concrete to demonstrate superior flowability and an extended setting period during the stages of concrete storage, pumping, and extrusion. Conversely, after deposition, it should exhibit reduced flowability, enhanced green strength, and a rapid setting rate [Malaeb 2019, Rahul 2019].

2.2.1 Selection of Recycled Materials

The use of recycled materials for 3D printing, especially in the field of concrete construction, is an emerging field with potential ecological benefits. Various research efforts have delved into the environmental impact and practicality of utilizing recycled components in 3D printing technology.

In a study by [Alhumayani 2020], the environmental effects of large-scale 3D printing with concrete and cob were analyzed. This research found that 3D printed concrete, while having a broader environmental footprint than cob, was less detrimental in aspects like marine eutrophication, land usage, and mineral resource scarcity. The research emphasized that tapping into renewable energy and breakthroughs in material science could amplify the benefits of both materials in construction.

By utilizing recycled materials such as tire rubber and PLA, the construction industry can reduce waste and promote a circular economy. Furthermore, understanding the mechanical properties of recycled materials and optimizing the printing process can contribute to the development of sustainable and environmentally friendly construction practices. [Laoutid 2021] attempts to use waste tire rubber for 3D printing of ABS and TPO composites, aiming to promote a circular economy in the automotive industry. Their findings highlight the capabilities of recycled tire rubber in producing filaments with significant mechanical properties.

The role of concrete's consistency in 3D printing is essential. [Jeong 2019] introduced an algorithm to determine the initial stress and hardening parameters of freshly mixed concrete suitable for 3D printing, with their model's

accuracy being affirmed through computational fluid dynamics. Concurrently, [Wu 2021b] studies the viscosity and workability of 3D printed concrete infused with recycled aggregates, emphasizing that a profound understanding of concrete's fluid properties and blend refinement is vital for its successful application in 3D printing.

From an environmental perspective, [Yao 2020] conducted an early life cycle assessment of three-dimensionally printed geopolymer concrete. While this technology reduces the carbon footprint, challenges remain in areas such as resource depletion and stratospheric ozone depletion. They propose mitigation measures such as limiting the silicate content of geopolymer mixtures.

Essentially, these works highlight the potential of using recycled materials in 3D printed concrete buildings. Through careful material optimization, understanding of fluid properties, and ecological assessment, the construction industry can move towards a more sustainable path. After recycling materials are conditioned for 3D printing, there are numerous variables to contemplate. The first is the mechanical integrity of the printed item. The study in [Anderson 2017] indicates that the mechanical properties of the printed parts are not significantly affected by the recycling process.

For 3D printed concrete, the interval between layers can potentially impact the bond robustness [Tay 2019a]. Fine-tuning the printing specifications is essential to ensure seamless layer bonding and improve the structural integrity of the 3D printed concrete. [Kumar 2021] studied the rheological, mechanical, and structural aspects of waste polymer-based filament designed for 3D printing. The incorporation of reinforcing materials such as iron powder enhances the mechanical properties, especially in terms of resilience and toughness.

Environmental and cost evaluations of 3D printed infrastructures using recycled concrete have been conducted [Han 2021]. Such appraisals explore the sustainability and cost viability of integrating recycled ingredients in construction endeavors.

In summary, The process of refining recycled materials for 3-D printing includes reflections on mechanical integrity, filament composition, recyclability, and concrete layer bonding, as well as the environmental and economic considerations of integrating recycled components into buildings. The research work discussed provides insight into the multifaceted dynamics of preparing recycled materials for 3-D printing.

2.2.2 3D Printing Process

Most of the extrusion-based 3DCP tasks follow a similar process, whether performed in a controlled or uncontrolled environment, which is illustrated in Fig.2.2. The process can be divided into three key stages: tool path genera-

tion, material preparation and material deposition (i.e. printing).

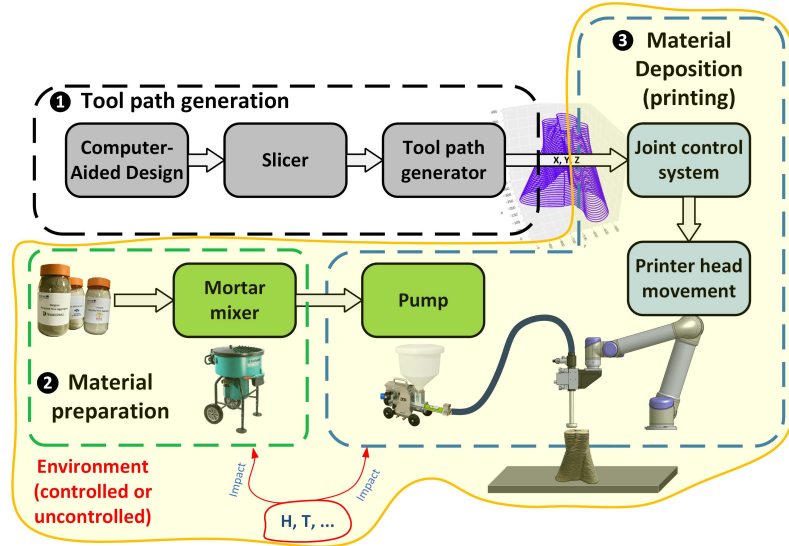


Figure 2.2: A typical process of 3D concrete printing in controlled or uncontrolled environment consisting of 3 stages. The environmental parameters (T: temperature, H: humidity, etc.) can affect the mixing (step 2) and deposition of material (step 3).

The creation of a tool path is essential, as it defines the trajectory that the 3D printer will follow for material deposition, ultimately influencing the precision and quality of the final printed item. Several algorithms and optimization techniques have been developed to refine tool paths and enhance printing efficiency [Fok 2019, Tan 2020]. For instance, researchers have introduced an ant colony optimization (ACO)-based tool path optimizer to expedite the printing process and enhance the visual appeal of the printed objects [Fok 2018].

Material preparation stands as another integral facet of the 3D printing process. A range of materials, such as plastics, metals, ceramics, and composites, can be utilized in 3D printing applications [Ngo 2018]. The choice of material depends on the desired properties of the print object. To illustrate, thermoplastic polyurethane (TPU) materials have been scrutinized for the creation of non-pneumatic tires via 3D printing, with researchers determining the optimal printing temperature through tensile testing and SEM observation [Wang 2020]. Additionally, exploratory work has been conducted on the application of conductive materials like silver nano-particles in 3D printing for electronic devices [Kim 2017].

Once the tool path is established and the materials are primed, the actual printing commences with material deposition. Layer by layer, the material is deposited according to the designated tool path, gradually constructing the

object [Lian 2019]. Critical factors in determining the mechanical properties of the final product include printing parameters like layer thickness and printing temperature [Kuznetsov 2018, Lian 2019]. For example, extensive investigations into the tensile properties of 3D printed components have revealed that the type and density of infill can impact the ultimate tensile strength of the printed object [Pandzic 2019].

In the context of 3D printing, the tool path generation process commences with the creation of a design using Computer-Aided Design (CAD) software. Commonly employed CAD software for this purpose includes Rhino and Onshape [Ahmed 2021]. Rhino offers a wide range of functions for constructing intricate NURBS surfaces, while Onshape provides additional capabilities for generating and manipulating T-spline surfaces [Hsu 2015]. This design is subsequently used as the foundation for defining the tool path. Slicing software also plays an important role. Two prominent slicing software tools within this domain are SlicerXL and Grasshopper 3D [Hong 2022]. SlicerXL is a user-friendly 5-axis 3D printing and conformal slicing software primarily used for numerical computation and toolpath generation. On the other hand, Grasshopper 3D serves as a visual scripting extension for 3D modeling software, such as Rhinoceros, enabling researchers to craft parametric models and enhance the design process. These slicing software tools have been applied for various purposes, including predicting printed line widths in different layer heights for precision manufacturing [Jiang 2021]. Such predictions can be integrated into SlicerXL or Grasshopper 3D for optimal 3D model slicing. In architecture, Grasshopper for Rhino 3D is favored for creating parametric models quickly [Rakha 2023], and it is also utilized in structural design for parametric modeling and structural analysis [Dzwierzynska 2020]. Additionally, SlicerXL and Grasshopper 3D find application in material extrusion additive manufacturing for toolpath generation and deposition sequence optimization [Volpato 2019], thereby improving accuracy, quality, production time, and material usage [Jiang 2020]. Moreover, slicing software has been instrumental in the dental industry for generating precise complete-arch models using intraoral video scanners [Jeong 2016] and in veterinary medicine for rapid prototyping and experimental applications [Hespel 2014]. These software tools leverage the external surface of the CAD design to establish the basis for defining the 3D printer head's tool path. SlicerXL or Grasshopper 3D can be employed for generating the tool path, guiding the print head during the printing phase. Furthermore, a study by [Neto 2013] underscores the importance of CAD software in generating tool paths for robotic systems in rapid prototyping, which can be relevant to 3D printing tool path generation. Additionally, [Schafer 2005] provide an example of incremental forming, a metal sheet shaping process that utilizes robots and CAD for tool path generation,

demonstrating the integration of CAD and robots in the tool path generation process for various manufacturing applications [Breaz 2019]. Consequently, the X, Y, and Z coordinates of each point along the print head's tool path, as determined by slicing software, are crucial. These coordinates, coupled with the printer head's velocity, are subsequently translated into a programming language compatible with the employed robot. Prior to commencing the printing process, robot simulation software is employed to reconstruct and validate the feasibility of the printing tool path [Sharafeldin 2018]. This step is essential to ensure the success of the printing process and the accurate production of the desired object. It permits the identification and rectification of potential issues or errors before actual printing, resulting in time and resource savings. The use of robot simulation software is particularly valuable when fabricating intricate models with numerous way-points in the tool path [Dai 2020]. In this paper, the motion planning algorithms can be utilized to compute a smooth, collision-free trajectory for the robot, thereby enhancing the overall quality of the fabrication process. In order to ensure the accuracy and precision of the printing process, post processing and path optimization techniques can be employed [Fu 2020]. Post processing is essential for achieving precise printing, especially when using poly-articular industrial robots for 3D printing complex free-form surfaces. Nonlinear error, which is inevitable in poly-articular industrial robots due to the nonlinear motion of the rotational joint, can be addressed through post processing and path optimization techniques.

For material preparation, a concrete batching (i.e.the proportion of the mixture of materials) should be determined and strictly followed during the preparation. The printing quality is subject to the rheological properties of the material, so it is significantly important to conform the same batching throughout a single process[Le 2012]. Unlike plastic 3D printing, where the materials are ready to be heated to a controlled temperature at the nozzle, for the 3DCP process, the material should be prepared a short time before each print job. The dry material components such as sand and cement are stored separately, and they will be mixed inside a mortar mixer with other chemical agents such as superplasticizer and viscosity-modifying agent. Then, a specific amount of water will be added to activate the hydration reaction for generating fresh-state concrete material.

During the printing stage, the material fresh mixture is extruded through the nozzle that is following the tool path, forming the designed geometry. Tool path generation stage is unaffected by environmental conditions, on the contrary, the other two stages are highly dependent on environmental conditions, in particular temperature and humidity. Furthermore, the operation time window is limited as the fresh state properties of the material change

because of cement hydration reactions.

2.2.2.1 Layer-by-Layer Construction

3D printing in construction is typically an additive manufacturing process, where material is deposited layer by layer to gradually build up the structure. This makes a slow process, but it offers high precision and flexibility in complex design.



Figure 2.3: Building up a cylindrical structure layer by layer.

In a study by [Loflin 2019], the effect of print layer height on the assessment of 3D-printed orthodontic models was investigated. The researchers found that there were no statistically significant effects of print layer height on the scoring of the models for any of the grading metrics or total score. This suggests that the layer height used in 3D printing does not significantly impact the accuracy or quality of the printed models. This finding is important in the context of construction, as it indicates that the layer height can be adjusted based on other factors such as printing velocity or material properties without compromising the structural integrity of the printed objects. [Taleb 2023b] conducted nondestructive testings on printed structure, as results, it was found that the previously deposited layer is harder than the upper one. It is also found by [Perrot 2020] that the addition of fibers can enhance the strength and durability of printed concrete structures. However, there are still challenges and risks associated with 3D printing in construction, particularly related to material properties and process optimization [El-Sayegh 2020].

2.2.2.2 Continual Printing Process

The printer continues to add layers until the entire structure is complete. Depending on the size and complexity of the project, this could take hours or even days. It is important to consider the factors that can influence the duration of the 3D printing process in construction. Several studies have investigated the impact of project size and complexity on the printing time, shedding light on the potential timeframes involved.

Study in [Khoshnevis 2004] suggests that the size of the structure can significantly impact the duration of the printing process. Larger structures require more layers to be printed, which naturally increases the printing time.

For example, a small-scale residential building may take several hours to print, while a larger commercial building could take several days or even weeks. The complexity of the design also plays a role in the printing time. Intricate designs with intricate details and intricate geometries may require more time to print compared to simpler designs [Buswell 2018]. Printing failure prediction methods has also been studied to address the issue of two most common failures during printing: plastic collapse and elastic buckling [Diab 2023].

The printing velocity of the 3D printer is another crucial factor. Different printers have varying printing velocities, which can significantly impact the overall printing time[Le 2012]. Faster printers can complete the printing process more quickly, reducing the time required to add each layer. However, it is important to note that increasing the printing velocity may compromise the quality and accuracy of the printed structure. Therefore, finding the right balance between velocity and quality is essential.

Furthermore, material type is another factor that impacts printing time. Indeed, different materials have varying properties, such as viscosity and curing time, which can affect the velocity at which each layer is printed and solidified.

2.2.3 Finishing and Detailing

Once the printing process is complete, additional finishing and detailing steps may be necessary to ensure the durability and aesthetics of the printed structure [Lim 2012]. For example, finishing steps are sometimes required to achieve the desired surface quality and appearance. These steps may include smoothing rough surfaces, removing excess material, and refining the overall texture. Techniques such as sanding, grinding, or polishing can be employed to achieve a smooth and uniform surface. Additionally, chemical treatments or coatings can be applied to enhance the aesthetics and protect the structure from environmental factors.

In some cases, additional detailing or repair steps may be necessary to address any imperfections or structural issues that may have occurred during the printing process. This can involve filling voids or gaps, reinforcing weak areas, or correcting any inaccuracies in the printed object. Techniques such as patching, grouting, or the addition of reinforcing elements can be utilized to ensure the structural integrity and functionality of the printed structure.

The durability of the printed structure has also been studied [Baz 2021], as it can be exposed to various weather conditions. [Moelich 2020, Zhao 2022] indicate that plastic shrinkage cracking can occur to concrete printed structures. Indeed, external environmental factors such as wind and higher temperature can increase rate of the hydration reaction, which is a reason for plastic shrink-

age cracking[Alanazi 2022]. This raises the necessity of the automatic crack repair process for concrete surfaces as well as post-printing quality monitoring methods.

2.2.4 Post-Printing Quality Inspection

Offline quality inspection methods have long been utilized in cement-based material 3D printing researches. In the post-printing phase, the mechanical properties of the solidified printed structure can be examined using destructive methods, for instance, cutting into the structure to study its cross-section. Additionally, the finite element method (FEM) has also been used in several works for simulating the geometrical accuracy and mechanical properties of the printed material [Breseghello 2021, Perrot 2021, Reinold 2022]. Nevertheless, considering the rapid construction speed of 3DCP, rapid and non-destructive or non-contact quality inspection methods are indispensable to fulfill the requirement of closed-loop control and full automation in the printing process.

In this context, Computer Vision (CV) and Deep Learning (DL) methods have been utilized to avoid destructive/contact-required or manual measurement of filament size. These visual based inspection methods have been widely applied and reported in various fields including medical science [Anantharaman 2018], agriculture [Hameed 2022, Jia 2020, Yu 2019] and structural health monitoring (SHM) in construction [Kahouadji 2021, Yao 2019, Dorafshan 2018b, Dorafshan 2018a].

In the construction industry, structured light scanning and 3D laser scanning are commonly used for structural assessments[Buswell 2020, Aryan 2021, Akinci 2006], enabling the identification of structural deformations. Another method, photogrammetry, has also been explored, facilitating 3D reconstruction of manufactured structures. These approach are usually more costly [Buswell 2020]. Other methods such as acoustic, electrical, and electromagnetic methods have been utilized for detecting surface defects like cracks, voids, and areas of increased porosity[Hoła 2015, Ma 2019], yet they often fall short in accuracy compared to visual-based techniques.

Visual-based offline methodologies have been developed for post-printing quality inspection in 3DCP. In [Lakhal 2019], a hyper-redundant robot system was developed for visual quality inspection of printed objects using embedded camera, as shown in Figure 2.8. This work provides a proof of concept benefiting from a soft arm that allows the camera to scan both the external and internal surface of the printed piece.

A post-printing inspection process combining DL and CV was developed in [Davtalab 2020] for the detection of layer deformation from side-view in a contour crafting-like process. As demonstrated in Figure 2.4, in this work,

the printed object is extracted as a whole by a DL semantic segmentation model, following this, a CV based method combining edge detection and line detection is applied to detect the deformation of layers such as bending. This method necessitates rigorous image pre-processing and parameter adjustments for the computer vision model under specific conditions.

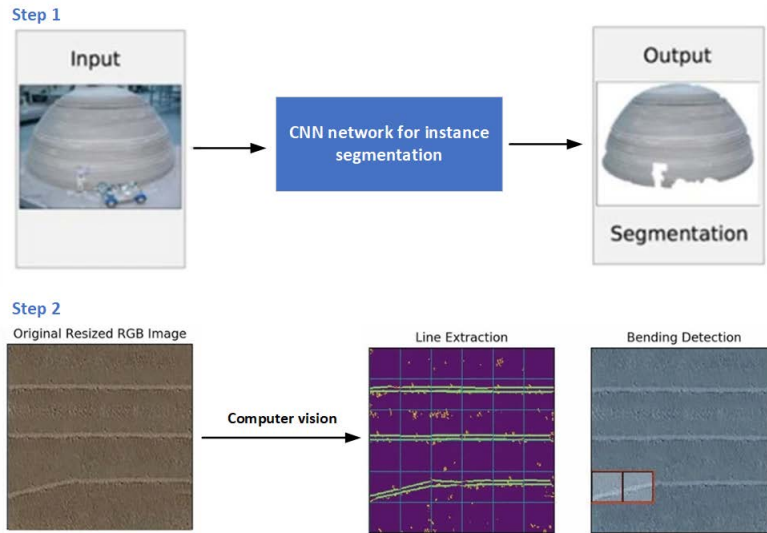


Figure 2.4: A post-printing offline layer deformation method combining DL and CV [Davtalab 2020].

The methods mentioned above enable offline post-printing quality inspections of the printed object. However, for achieving closed-loop control of printing quality during the actual printing stage, a real-time online quality monitoring approach is essential.

2.2.5 Advantages of 3D Printing in Construction using Recycled Materials

3D printing in construction using recycled materials offers several advantages. One of the key benefits is the realization of a circular economy, where 3D printed waste plastics can be reprocessed and recycled multiple times [Zhu 2021]. This recycling approach allows for the efficient utilization of 3D printing waste, reducing resource waste and promoting sustainability. Additionally, the use of recycled materials, such as recycled tire rubber, as additives in 3D printing can contribute to the production of thermoplastic composite materials [Laoutid 2021]. This not only helps in reducing waste but also provides an opportunity to repurpose materials that would otherwise end up in landfills.

Another advantage of 3D printing in construction using recycled materials is the positive environmental impact. A study comparing the environmental footprint of a 3D-printed house to a conventionally constructed house found that the 3D printing method had lower impacts in terms of global warming potential, non-carcinogenic toxicity, and water consumption [Abdalla 2021]. This indicates that 3D printing with recycled materials can contribute to reducing carbon emissions and minimizing resource consumption.

Furthermore, 3D printing in construction using recycled materials can also offer economic benefits. The same study mentioned above found that the 3D-printed house had a 78% reduction in overall capital costs compared to conventional construction methods [Abdalla 2021]. This cost reduction can make construction more affordable and accessible, especially in areas with limited resources or in disaster-stricken regions where quick and cost-effective housing solutions are needed. Using recycled materials and localized 3D printing can also reduce transportation emissions associated with traditional construction.

In addition to the environmental and economic advantages, 3D printing in construction using recycled materials also provides design freedom and higher efficiency. The technology allows for the creation of complex shapes and structures that may be difficult or costly to achieve with traditional construction methods (Guimarães et al., 2021). This flexibility in design opens up new possibilities for architectural innovation and customization. Moreover, 3D printing can save time and increase productivity in the construction process [Guimarães 2021]. The ability to rapidly fabricate components on-site can streamline construction timelines and reduce labor costs.

2.3 3D printing with environmental conditions

The 3D printing process for construction is significantly influenced by temperature and humidity. There are many studies showcasing the effects of temperature on this process. For instance, [Guessasma 2019] delved into how printing temperature impacted the microstructure and mechanical attributes of 3D printed wood-PLA/PHA via fused deposition modeling. [Jeon 2020] explored how nozzle temperature variations influenced the emission rate of ultrafine particles during the printing. [Iancu 2018] emphasized the role of printing temperature in determining the tensile strength of 3D printed PLA components.

Humidity, too, plays a critical role. [Perrot 2018] evaluated the adaptability of 3D printing with an extrusion deposit method for these materials. Their findings stressed the importance of understanding the rheological behavior of earth-based materials, particularly how humidity can modulate their flow and

workability during printing. [Tappa 2017] pointed out that humidity levels during printing can potentially affect the quality of 3D printed medicinal implants and devices.

In another study, [Alhumayani 2020] performed an environmental evaluation of large-scale 3D printing in the construction sector using concrete and cob. While the primary aim was to compare environmental impacts between 3D printing and traditional construction techniques, their research indirectly inferred that factors like temperature and humidity can alter the properties and printing process of concrete. [Joh 2020] dived deep into the buildability and mechanical attributes of 3D printed concrete. They defined buildability as the capability of freshly deposited concrete to resist deformation and to maintain its extruded form during construction. This crucial aspect can be influenced by elements like temperature and humidity, which, in turn, impact the workability and flow of concrete during its printing phase.

Lastly, the research by [Zareiyan 2017] offers insights into the role of interlocking in determining interlayer adhesion and overall structural strength in 3D printed concrete. The bonding between printed layers and the subsequent curing process can be influenced by environmental factors. Here again, temperature and humidity emerge as significant parameters, affecting the structural integrity and strength of 3D printed structures. Collectively, these studies underscore the intricate interplay between temperature, humidity, and the efficiency and quality of 3D printing in construction.

In summary, for construction-related 3D printing, it's vital to consider both temperature and humidity. While the former can influence mechanical properties and emission rates, the latter can affect material behavior and the quality of the end product. Proper management of these factors is essential for optimal 3D printing outcomes in construction scenarios.

2.3.1 Controlled Environmental Conditions

Nowadays, numerous approaches and technologies have been designed to make the 3D concrete printing process more efficient. A significant portion of these technologies is performed under controlled environment.

2.3.1.1 Factory Setting

In most of cases, 3D printing for construction takes place in controlled factory settings [Jagoda 2020]. The controlled factory settings for 3D printing in construction are necessary due to the limitations of the current 3D printing processes. These processes are known to be costly and unsuited to large-scale products and conventional design approaches [El-Sayegh 2020]. In 3D

printing, the challenges of the complete process are governed by the materials, machine, and the part of the design [Rahmat 2023]. Therefore, it is important to have controlled factory settings to ensure the proper functioning of the 3D printing process. The controlled environment allows for precise control over factors such as temperature, humidity, and other variables that can affect the quality and accuracy of the printed objects [Jagoda 2020]. Furthermore, the use of 3D printing in construction is still in its infancy, and there are challenges that need to be addressed. These challenges include the lack of large-scale implementation, the development of building information modeling, the requirements of mass customization, and the life cycle cost of the technology [Wu 2016]. Therefore, conducting 3D printing for construction in controlled factory settings allows for better research, development, and optimization of the technology before it is implemented on a larger scale.

Indeed, robotic systems play a significant role in executing tasks associated with 3D Concrete Printing (3DCP), i.e. guiding the nozzle during the material deposition phase. A variety of robotics, such as Cartesian robots, manipulators, and mobile robots, have been adopted in this field.

As an instance of static printer, in 2016, the Swiss company Sika¹, known for its specialization in chemistry, established a 3D automation center for construction in Widen, Switzerland. Their 3D printing gantry can craft modules spanning 4 meters in width, 3 meters in length, and reaching up to 6 meters in height, as seen in Figure 2.5. This process enables uninterrupted printing in factory environment for hours. It uses cement-based material to create unique and intricate concrete designs layer-by-layer. The machine boasts rapid print velocities due to its Sika Pulsment system and Sika MiniShot extruder, capable of depositing material at 1 m/sec and handling up to 4 tons of material hourly.

Mobile robots for 3D printing merge the strengths of gantry systems and manipulator robots, allowing an extension of the printer's workspace.

The Dutch construction firm CyBe², known for its expertise in 3D concrete printing, introduced a mobile concrete printer named RC 3Dp, as shown in Figure 2.6. This machine offers ease of site movement. It prints at an average pace of 200 mm/sec and can peak at 600 mm/sec. The device can craft objects up to 4.5 m tall, facilitated by two cylinders attached to its mobile base.

The Russian company Apis Cor³ has developed a transportable printer, seen in Figure 2.7, that can print within buildings during construction. This compact cylindrical manipulator has a hydraulic elevation system and doesn't need anchoring to the ground due to its stabilization system. The machine

¹<https://www.sika.com/>

²<https://cybe.eu/>

³<https://apis-cor.com/>

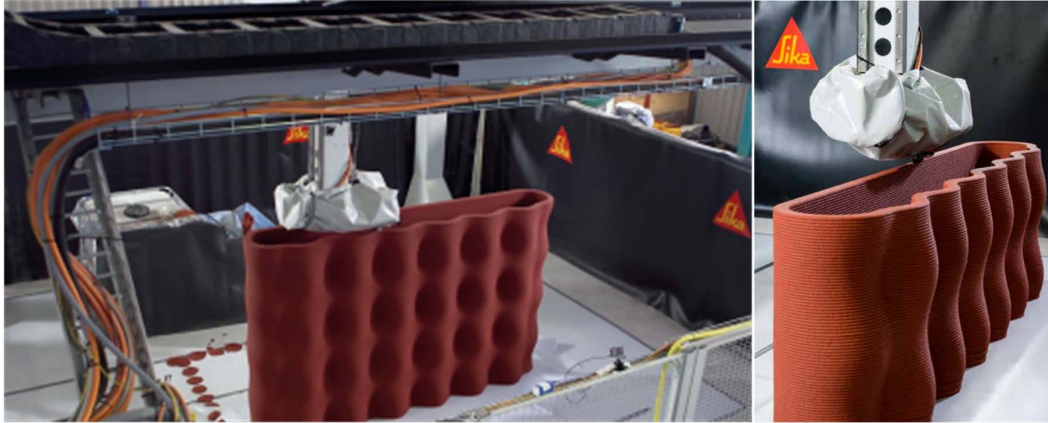


Figure 2.5: Sika 3D printing gantry.



Figure 2.6: CyBe mobile 3D printer.

has a print coverage of around 132 m^2 .

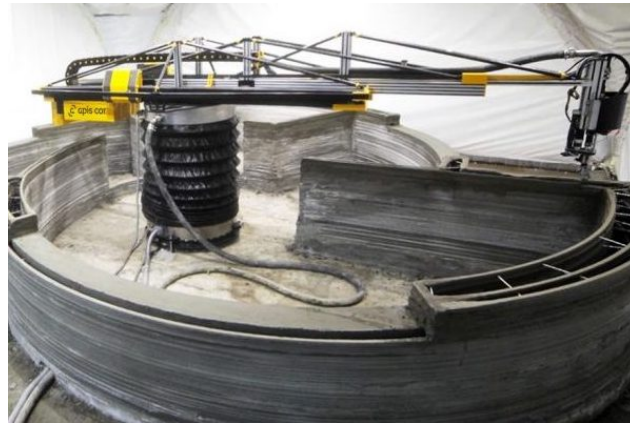


Figure 2.7: Apis Cor 3D printer machine.

In France, a mobile 3D concrete printing robotic system was developed in the University of Lille within framework of MATRICE project [Lakhal 2018, Lakhal 2019, Lakhal 2020]. This platform combines a KUKA manipulator and a mobile platform with four holonomic wheels, allowing for printing tasks in the laboratory or on-site without overall process control. Furthermore, by replacing the printer nozzle with a soft arm named CBHA equipped with a camera, visual-based post-printing product quality inspection can be realized.

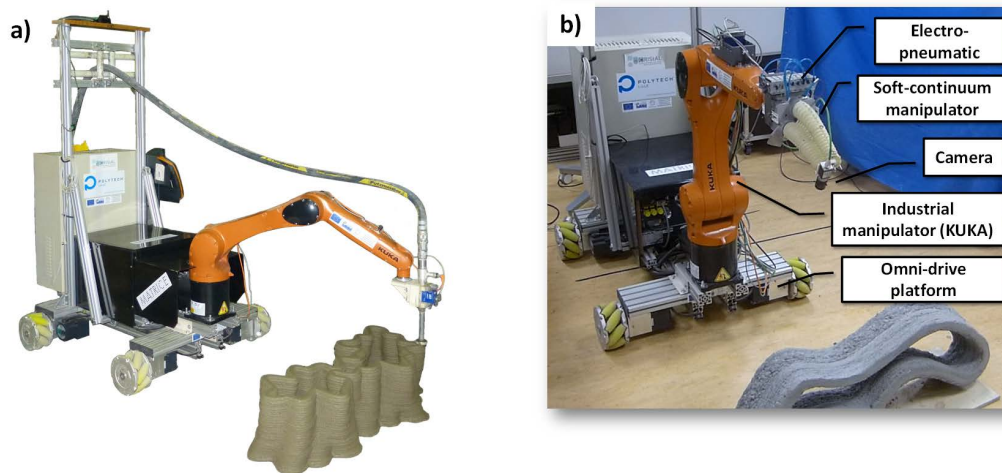


Figure 2.8: MATRICE [Lakhal 2018] mobile 3D concrete printer. a) Application in printing process. b) Quality inspection of printed structures, the printer nozzle is replaced by a soft arm equipped with visual sensors.

In another case, the Nantes Digital Sciences Laboratory LS2N at the Uni-

versity of Nantes in France has developed a distinctive additive manufacturing technology named BatiPrint3D⁴, illustrated in Figure 2.9. This system features an industrial manipulator arm mounted on a lifting truck, controlled by a supervisory system. A laser sensor guides the robot's tip, tracing a digital habitat blueprint on the ground.



Figure 2.9: BatiPrint3D developed by University of Nantes.

Although mobile printing platform provides the possibility for on-site printing task, most of the processes still operate or have been tested in controlled environment, which requires establishment of a relatively closed environment on-site.

2.3.1.2 Prefabrication

Another common practice involves the prefabrication of building components in a controlled environment. These components are then transported to the construction site for assembly.

The company Winsun⁵ has innovatively employed additive manufacturing technology to construct homes using Cartesian robot fixed on the ground. This approach involves bringing together prefabricated components at the construction site using traditional building materials [Hager 2016]. The printing device they utilize stands at 6.6 meters tall, spans 10 meters in width, and extends 150 meters in length, as showcased in Figure 2.10. This groundbreaking printer significantly augments production capacity by a factor of ten. Yet, most printed designs adopt conventional architectural forms given the challenges in printing complex geometric designs with Cartesian equipment.

⁴<https://www.batiprint3d.com/en>

⁵<http://www.winsun3d.com>

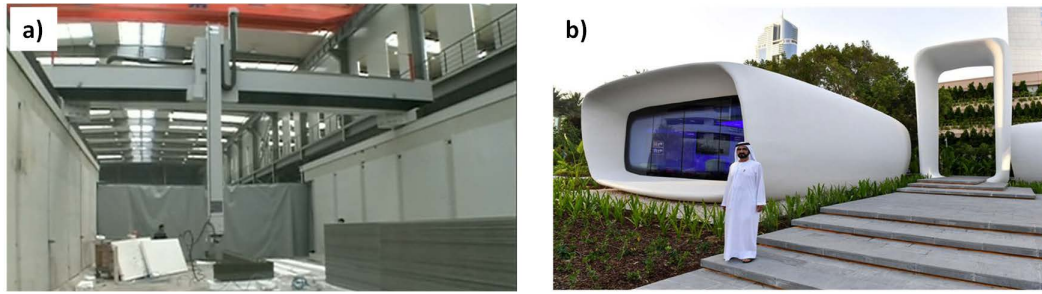


Figure 2.10: a) Winsun's concrete printing machine. b) Winsun's 3D printed office for Dubai Future Foundation.

The French company XtreeE⁶ utilized an ABB industrial robot to produce ultra-high-performance concrete architectural components with biomimetic designs, as seen in Figure 2.11. These structures, inspired by natural forms such as the shape of a coffee bean, are developed using the Dassault System's 3D Experience platform. They are printed modularly, allowing varied configurations when assembling multiple pavilions. XtreeE incorporates an experimental cement from Lafarge-Holcim in its creations.



Figure 2.11: The printer developed by XtreeE using an ABB industrial manipulator.

On the one hand, this process operated under a controlled environment ensures consistent quality and reduces the susceptibility to external factors like weather, on the other hand, it risks of increasing transportation and logistics costs. In term of sustainability, while transporting materials to a fabrication facility and then to the construction site, there could be a higher carbon footprint than sourcing materials locally for on-site construction.

⁶<https://www.xtreee.eu/>

2.3.2 Uncontrolled Environmental Conditions

Printing under uncontrolled environmental conditions face the challenge of unstable material rheology properties due to especially under unpredictable environmental factors like temperature and humidity. As a result, additional effort is needed to maintain deposit quality. Much of the research directly related to the challenges of printing under uncontrolled environment primarily focuses on simulating and modeling material properties. This involves examining materials from their foundational characteristics to understanding their behavior during the printing process[Khan 2022, Rizzieri 2023, Reinold 2022]. However, simulations that encompass a broader spectrum of materials or take into account varied environmental conditions remain relatively less. Two scenarios can represent the challenges of printing under uncontrolled environments: on-site printing and printing in remote settings.

2.3.2.1 On-Site Printing

In some instances, additive manufacturing is used directly on the construction site, which means it operates in less controlled environmental conditions. This approach requires adaptations to account for factors like weather, dust, and temperature variations. Most on-site printing endeavors predominantly focus on large-scale projects, such as walls or entire houses, typically characterized by simple and straightforward geometries. Conversely, on-site printing for mid-scale and smaller projects is less frequently encountered.

A variety of strategies have been considered to maintain printing quality. Specifically, online printing quality monitoring methods is indispensable. One technique is the real-time assessment of surface quality, as studied by [Lishchenko 2022], which aids in early error detection linked to surface texture, ensuring deposit consistency. Trials on different real time printing quality monitoring methods has been conducted in [Kazemian 2021], in this work, the authors investigated and evaluated four different inspection approaches, each concerning the monitoring of a specific parameter including power consumption measurements for the agitator motor, extrusion pressure measurements, electrical resistivity measurements, and computer vision. It is concluded that Computer vision seems to be the most reliable extrusion monitoring technique among the four. Another approach to realize feedback control of printing process is reported in [Panda 2017], in which the time-varying shear strength of the material was measured. For the most part, when looking at the CV methods developed for this specific purpose, they rely heavily on using images or visual information. These methods typically make use of tools from computer vision (CV) or they incorporate deep learning (DL) techniques to analyze the visual data. A few methods incorporate the monitoring of material flow rate

or pumping pressure to enhance the process.

In the literature, the deformation of the material deposition filament has generally been used as a criterion for evaluating the quality of printing, as it intuitively reflects the deterioration of the quality of the object to be printed, regardless of the stability assumed during the design phase. Indeed, compared to filament height, the filament width is more likely to deviate and the deformation is more evident, as in many cases the nozzle trajectory layer height is less than the nozzle diameter [Bos 2016], so that the filament height is almost equal to the layer height. Also, Material formulations are designed to minimize deformation of the substrate layer thickness (i.e., layer height) under the load of subsequent layers. Thus, in the context of this work, the width of printing filament is adopted as the primary criterion for evaluating real-time printing quality.

Online printing quality monitoring methodologies using conventional CV methods, particularly edge detectors, based on top view filament images have been reported in generic AM quality monitoring and control studies. For instance, in [Wu 2021a], edge detector have been applied to the binary mask of the material filament obtained by thresholding, in order to measure the width of the filament for the extrusion control in AM of polymer material . In food material AM, [Ma 2023] employed edge detectors to determine filament width and used the pixel difference between frames to calculate the extrusion rate. For these material cases, the printing platform, serving as a background, can be kept clean to ensure high contrast between the material filament and the print bed, as these printers provide a clean and highly controlled environment.

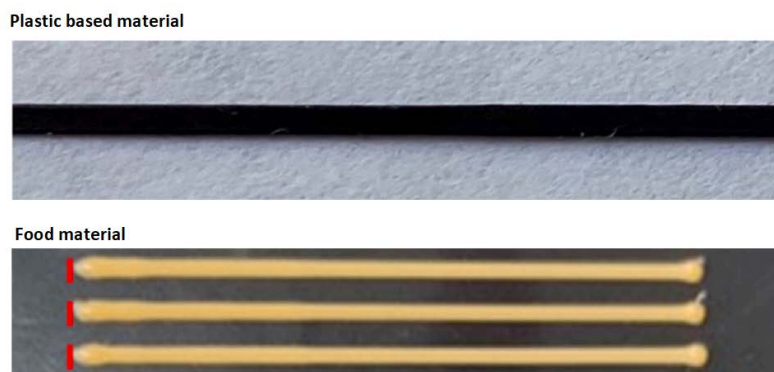


Figure 2.12: Conventional CV edge detectors have been used to determine filament size in AM of plastic based material [Wu 2021a] and food material [Ma 2023].

Conventional CV edge detectors were also employed to identify printed filament in AM of concrete materials for the purpose of online quality monitoring

and control via feedback from a vision-based filament measurement system. In [Kazemian 2019], as depicted in Figure 2.13a, the material filament was extruded onto a white print bed to maximize contrast. Subsequently, Otsu’s binarization was employed to distinguish the background (printing bed) from the foreground (filament) using a thresholding procedure. The width of the segmented filament served as feedback for modulating the material extrusion rate. This method was evaluated in a contour crafting process. Similarly, another work in [Barjuei 2022] employed edge detection to differentiate the filament margin from the print bed. Measurements of the identified filament were then used to adjust the nozzle velocity, ensuring consistent filament dimensions. As illustrated in Figure 2.13b, this technique was tested on a process similar to contour crafting, where both the nozzle and filament have a rectangular shape. Notably, both methods were exclusively trialed on straight line segments of substrate filaments.

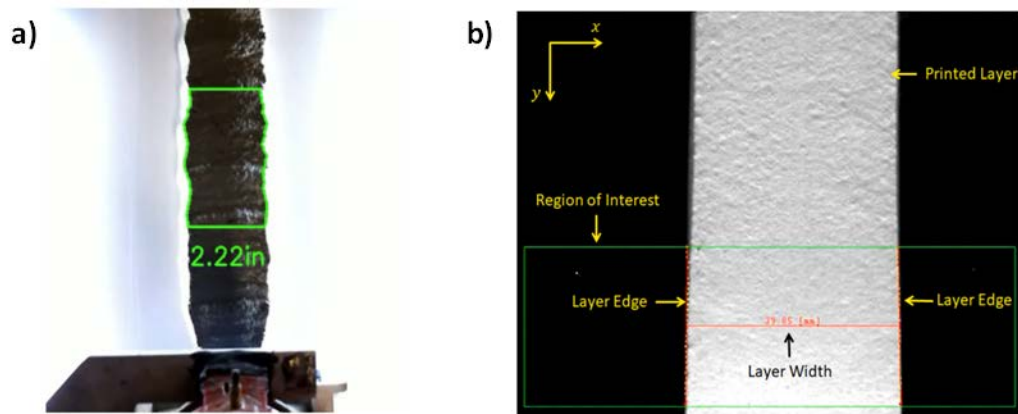


Figure 2.13: Conventional CV methods used in concrete 3D printing quality control. a) Otsu’s binarization is used to distinguish filament, the material extrusion rate is regulated in case of anomaly [Kazemian 2019]. b) Edge detector is used to distinguish filament, nozzle velocity is regulated in case of anomaly [Barjuei 2022].

However, for larger-scale AM of concrete material, especially for outdoor print jobs, cleanliness of the print bed can’t always be guaranteed due to residual materials generated during necessary calibration steps. In some cases the materials are to be deposited directly on the ground, therefore the color of the print bed can not be guaranteed. Furthermore, consistent lighting conditions and contrast can’t be ensured. The performance of CV methods highly depends on lighting conditions and a clean background, and its determined parameters are not always suitable for various conditions, which makes parameter tuning a time consuming task. In this regard, DL instance segmentation

models demonstrate more robust performance in dealing with different lighting conditions, backgrounds, and shape complexities. This approach, however, hasn't been extensively employed for identifying material filaments during the printing process. In [Rill-García 2022], a DL segmentation model was used to identify the lines between two layers from side-view, allowing the estimation of filament height. Subsequently, gray-level co-occurrence matrices (GLCMs) and local binary patterns (LBP) were applied for the analysis of filament surface texture features, followed by a Convolutional Neural Networks (CNN) based classification.

While monitoring holds significance, adjusting printing variables is equally critical. The influence of printing temperatures on the attributes of the printed items has been highlighted by [Coppola 2018]. Their insights guide practitioners towards pinpointing the ideal temperature spectrum to yield top-tier deposits. On the same note, [Kwon 2020] emphasize the potential challenges posed by humidity on the 3D printer's filament supply system. Innovations like remote humidity monitoring and automatic control systems can foster consistent filament delivery and curtail issues like nozzle blockages.

Material considerations also occupy a pivotal role in ensuring superior deposit quality. For instance, when utilizing clay nanocomposites in 3D printing, it's vital to meticulously adjust the printing temperature to achieve the targeted attributes[Coppola 2018]. In another domain,[Muñoz 2020] have demonstrated the significance of material choice and optimized fabrication processes in crafting 3D-printed sensors for environmental contaminant tracking.

In summation, the quest for impeccable deposit quality in 3D printing under varying environmental parameters hinges on a blend of real-time monitoring, meticulous parameter tweaking, and astute material decisions. By leveraging these methodologies, professionals can fine-tune printing conditions, ensuring consistent quality and bolstering the efficacy of 3D-printed creations. Overall, additive manufacturing technologies have the potential to revolutionize various industries, but further research and development are needed to optimize the process parameters, improve the quality of printed objects, and explore new applications.

2.3.2.2 Remote or Challenging Environments

Additive manufacturing can be especially advantageous in remote or challenging environments where traditional construction methods may be impractical. For example, it can be used in disaster relief efforts or in locations with limited access to construction materials.

In particular, flying robots can be utilized in the application of additive

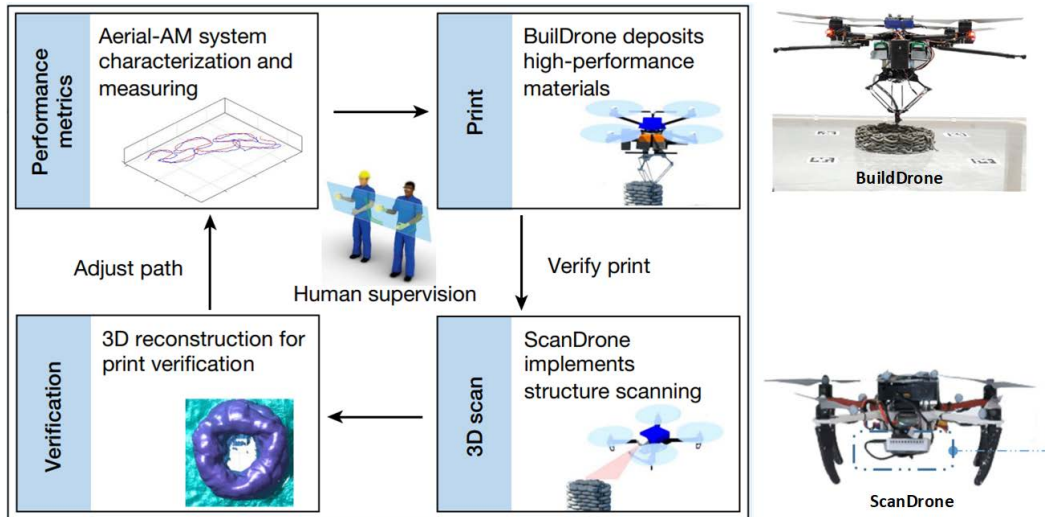


Figure 2.15: Printing process concept employing teams of aerial robots, developed by the Imperial College London [Zhang 2022].

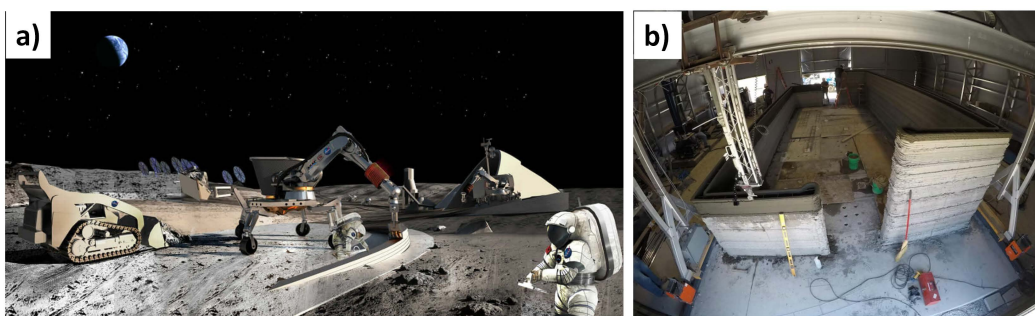


Figure 2.16: a) Concept of space construction through contour crafting by NASA. b) Automated Construction of Expeditionary Structures (ACES) by U.S. Army.

is important to select materials that are readily available locally, durable, and suitable for 3D printing. Local materials such as soil, sand, or regolith can be used as feedstock for 3D printing, reducing the need for transportation of construction materials. In remote environments, it is essential to have portable and robust 3D printing systems that can withstand harsh conditions and be easily transported. The equipment should be designed for easy setup, operation, and maintenance in challenging environments. Also, in remote environments, it may be difficult to access testing facilities and conduct quality control checks. Therefore, it is important to implement on-site quality control measures and develop non-destructive testing methods to assess the integrity and performance of the printed structures.

2.4 Comparative 3D printing processes

Tableref:table: printers gives a comparative study of existing architectural 3D printing techniques. Indeed, many of the processes, while mentioning uncontrolled environments, involve printing processes in controlled environments and then demonstrating the printed structures in uncontrolled environments to ensure the broad effectiveness and applicability of the technique and to assess the long-term resilience of the printed object. Although precise environmental conditions such as exact temperatures or humidity levels during these printings are often not specified, the indoor settings of these processes suggest they typically operate within standard room temperature and humidity ranges.

On the other hand, technological solutions specifically designed to address challenges posed by uncontrolled environments during the actual printing stage are comparatively scarce. The majority of research in this domain concentrates either on how varying environmental conditions impact the material properties directly or on the overall structural integrity. A few technologies, like BatiPrint3D, deploy insulating foam materials to create molds for concrete layers. While existing on-site printing projects often revolve around constructing large, simple geometric structures like houses, medium-scale, intricately designed furniture or artifacts using this technology are yet to be observed. Moreover, these on-site printing cases tend to compromise on printing speed and the resultant resolution of the printed item.

Date	Machine Developer	Type	Application	Operating / Testing Environment	Material	Country / Region
1998	Contour Crafting	Rail-gantry crane	Housing	Controlled	Fibrous concrete	USA
2003	D-shape	Gantry	Housing Prototyping	Controlled	Sand and binder	Italy
2004	Winsun	Gantry	Housing	Controlled	Fiber mortar	China
2007	Concrete printing	Gantry	Housing Prototyping	Controlled	Concrete	UK
2014	Totalkustom	Gantry	Housing Wall	Controlled	Concrete	USA
2015	XtreeE	Manipulator	Architecture Furniture	Controlled	Concrete	France
2016	Sika 3D	Gantry	Housing x Wall	Controlled	Concrete / Clay	Switzerland
2017	Apis Cor	Cylindrical manipulator	Housing	Controlled	Concrete	Russia
2016	ACES	Gantry	Housing	Controlled	Concrete	USA
2017	CyBe RC 3Dp	Mobile manipulator	Housing	Controlled	Concrete	Netherlands
2017	BatiPrint3D	Mobile manipulator	Housing	Uncontrolled	Insulating foam	France
2018	MATRICE	Mobile holonomic manipulator	Architecture Furniture	Controlled	Concrete/ Clay	France
2018	FlyElephant by Dedibot	Aerial robot	Concept	Unspecified	Unspecified	China
2020	Vertico	Manipulator on 6m track	Architecture Furniture	Controlled	Concrete	Netherlands
2020	BOD2 by COBOD	Mobile gantry	Housing	Uncontrolled	Concrete	Denmark
2021	Black Buffalo	Gantry	Housing	Controlled	Concrete	USA
2021	incremental3D	Manipulator	Furniture	Controlled	Concrete clay	Austria
2021	Concrenetics	Manipulator	Architecture Furniture	Controlled	Concrete	Belgium
2022	Aerial-AM by Imperial College London	Aerial robots team	Prototype	Controlled	Insulation foam / Cementitious	UK
2023	CIRMAP	Manipulator	Furniture	Uncontrolled	Concrete with recycled material	France

Table 2.1: Existing robot-based techniques for additive manufacturing in the construction

2.5 Conclusion

This state of art highlights the benefit of automated 3D printing process in construction. However, the replicability of the process depends on its robustness under different weather conditions, that can affect the printing materials. Nowadays, almost the technologies of 3D printing are utilized in controlled environment, thus limiting the conditions for printing. For that, the thesis position on performing the automation of the overall 3D printing process in uncontrolled environments to bring several significant benefits, especially in industries like construction, disaster relief, and remote infrastructure development. Uncontrolled environments present challenges like extreme temperatures, high humidity, or dust, where automated solutions proposed in this thesis can improve the overall 3D printing process and its deployment in these conditions, adapting to various environmental variables. Also, automated systems can often be remotely monitored and controlled. This allows for real-time adjustments, troubleshooting, and oversight by experts, even if they are not physically present at the construction site.

Pre-printing of 3DCP process

Contents

3.1	Introduction	40
3.2	Robot pre-preparation	41
3.2.1	Printing workspace	42
3.2.2	Trajectory Generation	49
3.2.3	Implementing in Robot Control	54
3.2.4	Executing the Trajectory	56
3.3	Shape Pre-preparation	59
3.3.1	Curvature limitation	60
3.3.2	Shape reconstruction from the 3D robot printing	61
3.4	Material Pre-preparation	66
3.4.1	Material mixing	66
3.4.2	Material Quantity Estimation	66
3.5	Emulated Uncontrolled Environment	68
3.6	Conclusion	72

3.1 Introduction

The pre-printing stage, called also Off-line step for 3D printing in construction involves several steps that prepare the construction site, materials, and equipment for the actual printing. This chapter is focusing on selection of 3D Printing Technology based on the project requirements. This includes choosing the type of 3D printer, as well as the type of material to be used. The chapter describes the 3D printing software in terms of setting the robot workspace, path planning, printing velocity, shape curvature, and other relevant parameters. The actual software represents a basis version for an extension to a digital twin of large scale 3D printing concept. The protocols and limitations of **pre-printing** stage of the **3DCP** process are discussed in this chapter.

3.2 Robot pre-preparation

The robot preparation step involves the shape design, slicing for path generation and the trajectory generation of the printing robot, as illustrated in Figure 3.1, this step defines the constraints that should be respected during the preparation stage.

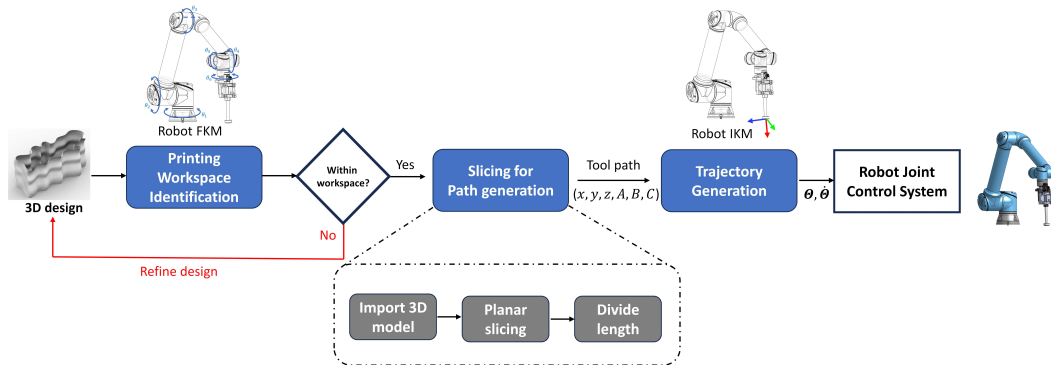


Figure 3.1: Robot preparation steps.

Starting from the 3D shape that needs to be replicated by depositing material, the process begins with a crucial accessibility check. This is carried out by employing the robot's direct geometric model while taking into account its articulation limitations. The aim is to ascertain whether the shape falls within the robot's workspace. Once this initial step is confirmed, the second phase, referred to as "slicing for path generation," unfolds in several distinct sub-stages. In the first sub-step, "Importing the 3D Model," the 3D model of the shape is digitally imported. Subsequently, the 3D shape is sliced into layers along the Z-axis. This slicing process is carried out based on the desired resolution and the robot's specifications. Each of these slices essentially represents a successive layer of material that will be deposited to form the final object. Finally, in the sub-step "Length Division," an optimal distance between points for each slice is determined. This determination is contingent upon the shape's geometry, desired resolution, and the robot's characteristics. Once these slicing operations are completed, we obtain a data-set of point clouds representing the coordinates of every point on the surface of the 3D shape, layer by layer. From these data, the robot's inverse model is then utilized to generate the precise trajectory the robot must follow. In other words, the robot's inverse model calculates the necessary joint coordinates for each moment during the manufacturing process to align with the shape of each individual slice of the 3D object. In the following sections, we will delve deeper into the specific methodologies and approaches for each step in the robot preparation process.

3.2.1 Printing workspace

The identification of the workspace of the printing system is essential in the preparation step. The workspace of a 3D printing robot refers to the geometric region within which the robot's end-effector (in this case, the print nozzle or extruder) can effectively operate or maneuver to deposit material. This workspace is determined by the forward kinematics of the robot under site-specific constraints.

Kinematic models concern the mathematical representation that describes how the movement of the robot's joints relates to the position and orientation of its end-effector in the task space. The **Forward Kinematic Model (FKM)** takes joint angles Θ as inputs and calculates the position and orientation of the end-effector \mathbf{X} :

$$\mathbf{X} = f(\Theta) \quad (3.1)$$

The following section describes the development of the kinematic model of the CIRMAP robot (cobot) to respect the condition of 3D printing in uncontrolled environment.

3.2.1.1 Forward Kinematic Model of CIRMAP cobot

In this section, we discuss the forward kinematic model of the selected robot in CIRMAP project, where its kinematics can be generalized to other types of serial arm manipulators. The Universal Robot UR10e is considered for this application of 3D printing in uncontrolled environment. It is a popular collaborative robot, also known as a cobot, used in the framework of CIRMAP project. It can handle objects weighing up to 10 kg (22 lbs). Its reach is approximately 1300 mm (1.3 meters), making it suitable for a wide range of tasks. The UR10e is designed to work alongside human operators without the need for extensive safety measures. It's equipped with force and torque sensors that allow it to detect and respond to contact with humans, ensuring safe and efficient collaboration. The UR10e is equipped with a range of safety features, including collision detection, velocity monitoring, and the ability to set safety zones, which further ensure safe collaboration with human workers. The UR10e is a six-joint robotic manipulator with a typical 6R (6 revolute joints) configuration. For the CIRMAP printing operations, we attach a nozzle with adjustable support to the cobot's end effector as illustrated in Figure 3.2.

The kinematics of this robot can be defined using the **DH** convention, which provides a systematic way to relate the joint angles to the position and orientation of the end-effector. As demonstrated in Figure 3.2, to determine the forward kinematics of the UR10e, we first specify its **DH** parameters. For

each joint i , the four defined parameters are: joint angle θ_i (rad), length offset d_i (mm), link twist α_i (rad) and link length a_i (mm).

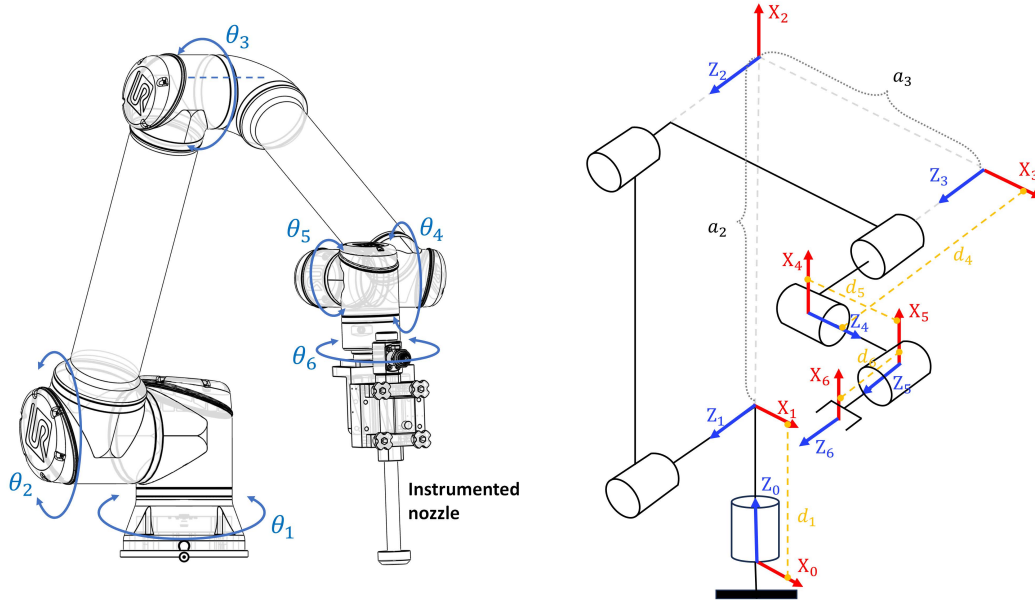


Figure 3.2: The Denavit-Hartenberg parameters and frame assignment of UR10e manipulator.

For UR10e, the parameters are given in Table 3.1.

Table 3.1: Denavit-Hartenberg parameters of UR10e manipulator.

<i>Joint</i>	θ_i	d_i	α_i	a_i
<i>Joint</i> ₁	θ_1	d_1	90°	0
<i>Joint</i> ₂	θ_2	0	0	a_2
<i>Joint</i> ₃	θ_3	0	0	a_3
<i>Joint</i> ₄	θ_4	d_4	90°	0
<i>Joint</i> ₅	θ_5	d_5	-90°	0
<i>Joint</i> ₆	θ_6	d_6	0	0

Given a serial manipulator with n links, with joint variables: $\Theta = [\theta_1, \theta_2, \dots, \theta_n]$, the transformation matrix from the base link to the end effector is given as

$${}^0_n\mathbf{T}(\Theta) = {}^0_1\mathbf{T}(\theta_1){}_2^1\mathbf{T}(\theta_2) \dots {}^{n-1}_n\mathbf{T}(\theta_n) = \begin{bmatrix} n_x & o_x & a_x & p_x \\ n_y & o_y & a_y & p_y \\ n_z & o_z & a_z & p_z \\ 0 & 0 & 0 & 1 \end{bmatrix} \quad (3.2)$$

where ${}^{i-1}_i\mathbf{T}(\theta_i)$ is the transformation matrix from link i to link $i - 1$ given by:

$${}^{i-1}_i\mathbf{T} = \begin{bmatrix} \cos(\theta_i) & -\sin(\theta_i) \cos(\alpha_i) & \sin(\theta_i) \sin(\alpha_i) & a_i \cos(\theta_i) \\ \sin(\theta_i) & \cos(\theta_i) \cos(\alpha_i) & -\cos(\theta_i) \sin(\alpha_i) & a_i \sin(\theta_i) \\ 0 & \sin(\alpha_i) & \cos(\alpha_i) & d_i \\ 0 & 0 & 0 & 1 \end{bmatrix} \quad (3.3)$$

the orientation of the end effector is then given by the rotation matrix:

$$\mathbf{R} = \begin{bmatrix} n_x & o_x & a_x \\ n_y & o_y & a_y \\ n_z & o_z & a_z \end{bmatrix} \quad (3.4)$$

the position of the end effector is given by the translation vector:

$$\mathbf{p} = \begin{bmatrix} p_x \\ p_y \\ p_z \end{bmatrix} \quad (3.5)$$

In the case of a UR10e, $n = 6$, therefore the orientation \mathbf{R}_{tip} and position \mathbf{p}_{tip} of the nozzle tip can be obtained by:

$${}^0_{tip}\mathbf{T} = {}^0_1\mathbf{T}_1\mathbf{T}_2\mathbf{T}_3\mathbf{T}_4\mathbf{T}_5\mathbf{T}_6\mathbf{T}_{tip} = \begin{bmatrix} \mathbf{R}_{\text{tip}} & \mathbf{p}_{\text{tip}} \\ \mathbf{0}_{1 \times 3} & 1 \end{bmatrix} \quad (3.6)$$

where ${}^6_{tip}\mathbf{T}$ is the transformation matrix from the tool center point of the end effector to the tip of the nozzle.

3.2.1.2 3DCP workspace limitation

The workspace of the 3DCP process is a key factor to consider while designing a shape. The final process workspace is based on the global workspace of the operating robot. In our case, the workspace of the UR10e robot can be calculated with its FKM.

The mechanical design of the UR10e robot in itself allows a rotation range of 360° for each joint, therefore, its reachable workspace is a spherical area. However, it is required that during material deposition, only translation movement of the nozzle is allowed and rotation should be avoided, also, the nozzle

is expected to be perpendicular to the print bed, thus, two constraints are imposed: $\theta_6 = 0^\circ, \theta_5 = -90^\circ$. Furthermore, the positioning of both the robot's control box and the robot itself on the ground introduces additional constraints. We operate under the assumption that the robot's working area is limited to one side of it. As a result, the subsequent constraints define a specific sub-workspace of the UR10e robot for the printing task:

$$\begin{cases} -90^\circ \leq \theta_1 \leq 90^\circ \\ -30^\circ \leq \theta_2 \leq -120^\circ \\ 30^\circ < \theta_3 \leq 150^\circ \\ -180^\circ \leq \theta_4 \leq -50^\circ \\ \theta_5 = -90^\circ \\ \theta_6 = 0^\circ \end{cases} \quad (3.7)$$

Based on Equation (3.3) and the D-H parameters given in Table 3.1, the following transformation matrices of successive frames can be obtained:

$${}^0_1\mathbf{T} = \begin{bmatrix} \cos(\theta_1) & 0 & \sin(\theta_1) & 0 \\ \sin(\theta_1) & 0 & -\cos(\theta_1) & 0 \\ 0 & 1 & 0 & d_1 \\ 0 & 0 & 0 & 1 \end{bmatrix} \quad (3.8)$$

$${}^1_2\mathbf{T} = \begin{bmatrix} \cos(\theta_2) & -\sin(\theta_2) & 0 & a_2 \cos(\theta_2) \\ \sin(\theta_2) & \cos(\theta_2) & 0 & a_2 \sin(\theta_2) \\ 0 & 0 & 1 & 0 \\ 0 & 0 & 0 & 1 \end{bmatrix} \quad (3.9)$$

$${}^2_3\mathbf{T} = \begin{bmatrix} \cos(\theta_3) & -\sin(\theta_3) & 0 & a_3 \cos(\theta_3) \\ \sin(\theta_3) & \cos(\theta_3) & 0 & a_3 \sin(\theta_3) \\ 0 & 0 & 1 & 0 \\ 0 & 0 & 0 & 1 \end{bmatrix} \quad (3.10)$$

$${}^3_4\mathbf{T} = \begin{bmatrix} \cos(\theta_4) & 0 & \sin(\theta_4) & 0 \\ \sin(\theta_4) & 0 & -\cos(\theta_4) & 0 \\ 0 & 1 & 0 & d_4 \\ 0 & 0 & 0 & 1 \end{bmatrix} \quad (3.11)$$

$${}^4_5\mathbf{T} = \begin{bmatrix} \cos(\theta_i) & 0 & -\sin(\theta_i) & a_i \cos(\theta_i) \\ \sin(\theta_i) & 0 & \cos(\theta_i) & a_i \sin(\theta_i) \\ 0 & -1 & 0 & d_i \\ 0 & 0 & 0 & 1 \end{bmatrix} \quad (3.12)$$

$${}^5_6\mathbf{T} = \begin{bmatrix} \cos(\theta_i) & -\sin(\theta_i) & 0 & a_i \cos(\theta_i) \\ \sin(\theta_i) & \cos(\theta_i) & 0 & a_i \sin(\theta_i) \\ 0 & 0 & 1 & d_i \\ 0 & 0 & 0 & 1 \end{bmatrix} \quad (3.13)$$

$${}^6_{tip}\mathbf{T} = \begin{bmatrix} 1 & 0 & 0 & 0 \\ 0 & 1 & 0 & a_7 \\ 0 & 0 & 1 & l_{nozzle} \\ 0 & 0 & 0 & 1 \end{bmatrix} \quad (3.14)$$

where l_{nozzle} and a_7 denote the nozzle's length and the offset of the nozzle tip with respect to the tool center point of end effector. Finally, the FKM is given by the equations derived from the matrix ${}^0_{tip}\mathbf{T}$, allowing to determine the position (p_x, p_y, p_z) of the nozzle tip:

$$\begin{cases} p_x = -C_1C_{234}S_5d_6 + C_5S_1d_6 + C_1S_{234}d_5 + S_1d_4 + C_1C_23a_3 + C_1C_2a_2 \\ p_y = -C_{234}S_1S_5d_6 - C_1C_5d_6 + S_1S_{234}d_5 - C_1d_4 + C_{23}S_1a_3 + C_2S_1a_2 + a_7 \\ p_z = -S_{234}S_5d_6 - C_{234}d_5 + S_{23}a_3 + S_2a_2 + d_1 - l_7 \end{cases} \quad (3.15)$$

Its orientation is given by the rotation matrix as presented by equation 3.4, where the elements are:

$$\begin{cases} n_x = C_1C_{234}C_5C_6 + C_6S_1S_5 - C_1S_{234}S_6 \\ n_y = C_{234}C_5C_6S_1 - C_1C_6S_5 - S_1S_{234}S_6 \\ n_z = C_5C_6S_{234} + C_{234}S_6 \\ o_x = -C_1C_{234}C_5C_6 - S_1S_5S_6 - C_1C_6S_{234} \\ o_y = -C_{234}C_5C_6S_1 + C_5S_5S_6 - C_6S_1S_{234} \\ o_z = -C_5C_6S_{234} + C_{234}C_6 \\ a_x = -C_1C_{234}S_5 + C_5S_1 \\ a_y = -C_{234}S_1S_5 - C_1C_5 \\ a_z = -S_{234}S_5 \end{cases} \quad (3.16)$$

Note that S_i and C_i denote $\sin(\theta_i)$ and $\cos(\theta_i)$ respectively, S_{234} and C_{234} denote $\sin(\theta_1 + \theta_2 + \theta_3)$ and $\cos(\theta_1 + \theta_2 + \theta_3)$ respectively. From the FKM, the sub-workspace under joint constraints for 3DCP can be calculated, as shown in Figure 3.3, the space represented by the blue dots is the global spherical workspace of the UR10e robot without constraints, while the red-dot space is the sub-workspace under the constraints given in Equation (3.7). Figure 3.4 demonstrates the sub workspace allowing for a printing process in top view and side view.

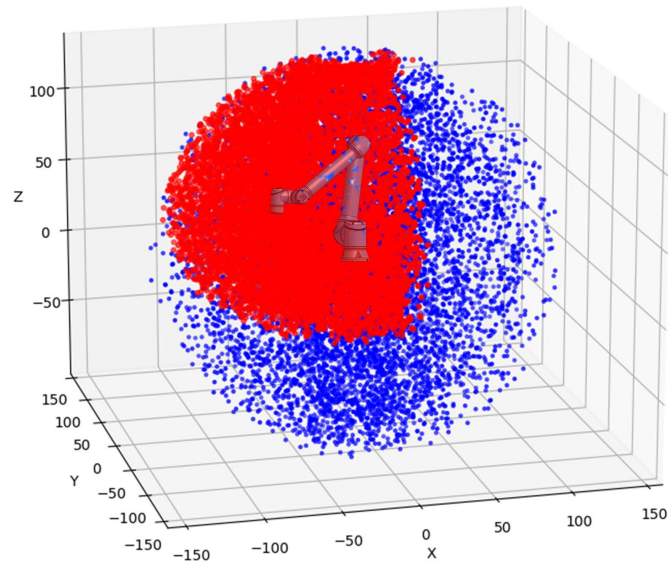


Figure 3.3: The global workspace of the UR10e robot without constraints (blue) and the sub workspace (red) under constraints for 3DCP.

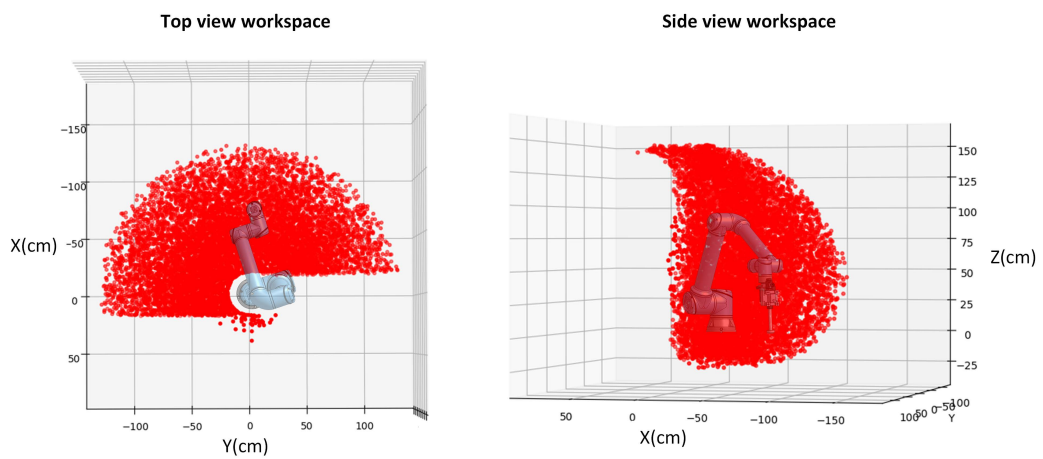


Figure 3.4: The sub workspace under constraints.

Therefore, the final safe workspace of the 3DCP process can be determined by a combination of the following criteria:

- A sub-workspace of the robot's reachable workspace can be calculated from its FKM, with limitations applied for certain joints.
- The printing system configuration: such as placement of equipment (robot, pump, hose, control box, etc.), length of the nozzle, etc. applies additional limitations to the workspace.
- Environmental Constraints: especially relevant for indoor printing, the available area can significantly limit the manipulator's operational scope. Walls, ceilings, and other obstructions need to be factored in when determining the workspace.
- Print Bed Requirement: Often, a print bed is used to facilitate the transport of printed structures. The inclusion of print bed can introduce additional constraints to the workspace.

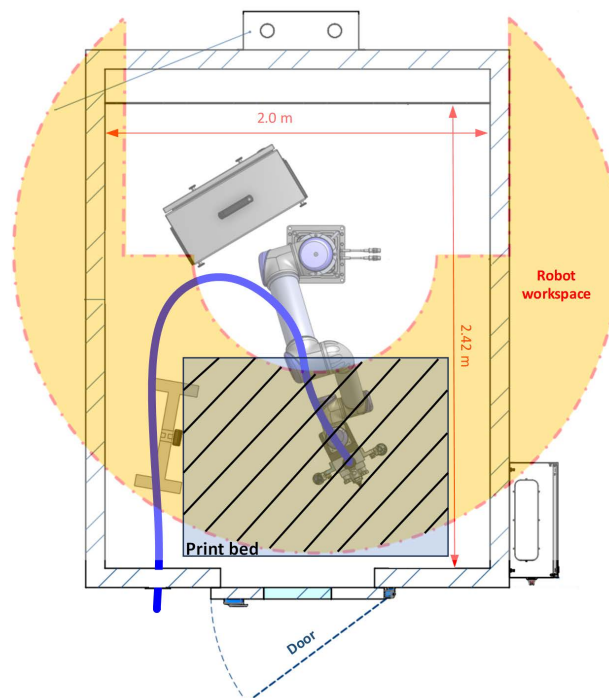


Figure 3.5: 3DCP process workspace limitation: the final workspace is represented by the shadowed area.

Taking all these factors into account, the final workspace of a printing system is essentially the intersection of these various limitations, an example

case is illustrated in Figure 3.5 where the printing system is placed inside a climatic chamber and a print bed is placed in front of the robot. The intersection of all the limitations gives the final workspace in the shadowed area. It's crucial that the shape design respects these boundaries to ensure the printing process.

3.2.2 Trajectory Generation

Trajectory generation for a robot arm in 3D printing involves planning a path that guides the end-effector (or tool) of the robot to trace out the desired shape or structure. This process is crucial in 3D printing to ensure accurate and efficient deposition of material. The following steps are required for the trajectory generation:

3.2.2.1 Define the Desired 3D Shape

The first step is to have a digital representation of the 3D object or structure that needs to be printed. A 3D designed shape can be represented in the form of vertex $V_i = (x_i, y_i, z_i)$ which is a point in the 3D coordinates and faces $F = (V_i, V_j, V_k)$ which is a flat surface (triangle) that connects three vertices. Thus, a vertex matrix and face matrix can describe the overall 3D shape.

3.2.2.2 Discretization of the Path

The continuous 3D shape needs to be discretized into a series of smaller segments or points. This is done to make it manageable for the robot to follow. Let's denote these points as $P_i = (x_i, y_i, z_i)$.

3.2.2.3 Trajectory Planning

Trajectory planning involves determining the specific path that the robot arm will follow to move from one point to another. This can be done using techniques like linear interpolation or more advanced methods like spline interpolation for smoother paths [Clément Gosselin 2008].

- *Linear Interpolation:*

For linear interpolation between two points P_i and P_{i+1} , the trajectory can be represented by a parametric equation:

$$P(t) = (1 - t)P_i + tP_{i+1} \quad (3.17)$$

where t varies from 0 to 1.

- *Spline Interpolation:*

Spline interpolation uses piecewise polynomial functions to generate smooth curves between points. One common type is cubic splines.

$$P(t) = a(t - t_i)^3 + b(t - t_i)^2 + c(t - t_i) + P_i \quad (3.18)$$

where t varies between t_i and t_{i+1} , and a , b , c are coefficients determined by the conditions at the endpoints.

3.2.2.4 Velocity and Acceleration Profiles

The trajectory should be generated in a way that ensures smooth and controlled motion [Mark W. Spong 2006]. This involves considering velocity and acceleration profiles to avoid sudden changes in velocity or direction. They determine how the robot's velocity, and acceleration change over time as it moves along a specific path.

- *Velocity Profile*

The velocity profile is calculated by determining the rate at which the robot should move along the path. This is influenced by factors like the desired velocity, the distance between waypoints, and any constraints on the robot's maximum velocity.

- *Acceleration Profile*

The acceleration profile is derived from the velocity profile. It indicates how quickly the robot changes its velocity. For instance, a high acceleration means the robot can change its velocity rapidly.

3.2.2.5 Slicing for path planning

Automatic slicing is a crucial step in the 3D printing process that involves breaking down a complex 3D model into thin, horizontal layers (slices) that can be printed one on top of the other. This is particularly important in construction, where large and intricate structures are built layer by layer [Zeng 704]. This step is necessary to convert the digital model into a format that can be understood by the 3D printer. The slicing process determines the thickness of each layer and the path that the printer will follow to deposit the concrete material [Panda 2017]. Slicing is a rich area of research in itself, as it involves a variety of factors such as material properties, structural integrity and stability, etc. To optimize this step, several key points need to be

considered including determining the distance between adjacent points, the velocity of nozzle and geometry of model. For example, simple geometries, such as cylinders and cubes, are suitable for optimizing the slicing parameters in extrusion-based 3D printing processes [Guo 2019], these basic shapes can be used to test and refine the parameters and ink formulas. For slicing a complex geometry, reducing the distance between adjacent points on curves of large curvature is recommended to assure accurate tracking of the designed shape.

The automatic slicing process follows the following steps:

- **Importing the 3D model**

The process begins with importing the designed 3D model of the construction project into a slicing program. The slicing allows users to prepare the model for the printing process. The STL (Stereolithography) format is an standard for 3D printing due to its compatibility. To bring the 3D shape into the robot’s base coordinate system and workspace and also ensure its correct orientation, geometric transformations needs to be applied:

$$\mathbf{p}^{\text{new}} = \mathbf{R}(s\mathbf{p}) + \mathbf{l} \quad (3.19)$$

where \mathbf{p}^{new} is the new position, \mathbf{p} is the original position, \mathbf{R} the rotation matrix and \mathbf{l} the translation vector. Specifically, s is a scaling factor that can be used to tune the volume size of the shape, to better fit in to the robot’s workspace.

- **Setting Printing Parameters**

Operators configure various printing parameters in the slicing software. In general 3D printing: this includes settings like layer height (the thickness of each slice), print velocity, material and print bed temperature, material flow rate, etc. These settings are critical for achieving the desired print quality. In the case of on-site 3DCP, the primary considerations are the layer height and print speed, given that material properties are beyond control in many cases. The layer height determines the thickness of each concrete layer, it also determines the resolution of the structure surface, this parameter often ranges between a few millimeters to several centimeters, depending on the printer’s capabilities and the project’s requirements. In case of CIRMAP nozzle with a diameter of 2.5 cm, the layer height is fixed at 9 millimeters. The selection of nozzle velocity is considered an initial value that can be adjusted during the printing stage, however, it is usually ranged between 3 cm/s and 20 cm/s [Zhang 2023].

- **Automatic Slicing**

Also referred to as layer generation. Planar slicing is used in our case, where the model is sliced into a series of flat horizontal layers based on the specified layer height [Hu 2017]. Each layer represents a cross-section of the final object, it is the most straightforward method and computationally less demanding as well. This process involves creating a 2D representation of each layer, showing where material needs to be deposited. This step can be done through a contouring algorithm as it is shown in Figure 3.6. A slicing plane $Plane_z$ can be mathematically defined by:

$$Plane_z : z = z_{slicing} \quad (3.20)$$

where z_{slice} is the height at which the slice is to be taken. The contour is therefore the intersection of slicing plane and surfaces of the 3D geometry.

- **Generating Toolpaths**

For each generated layer, the implemented algorithm for trajectory generation computes the toolpath - the exact route the nozzle should follow and the material will be deposited. When generating toolpaths for the manipulator, the path is discretized into a finite number of waypoints or positions that the nozzle should pass through. Between these waypoints, the manipulator interpolates its motion. This step can be done by an algorithm for dividing the length. A diagram of the methodology of slicing and toolpath generation is shown in Figure 3.6. The issue arises

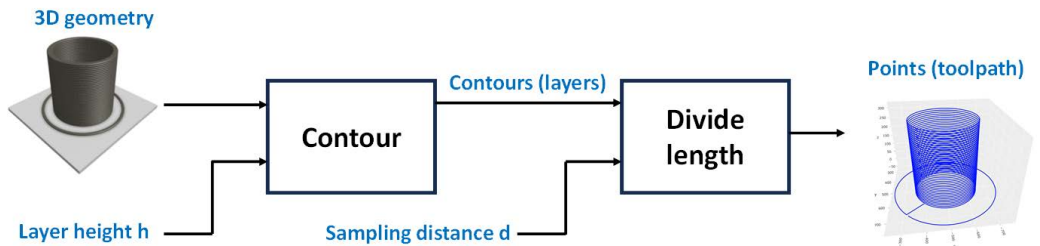


Figure 3.6: Slicing and tool path generation

when these waypoints are too far apart in high curvature areas, causing the interpolated path to potentially miss or cut across the desired curve. Therefore, a maximum distance between two adjacent points along the tool path (i.e. sampling distance) should be determined. This distance is significant because it not only affects the motion smoothness of the nozzle but also influences the accuracy of material deposition, as well as the consistency and quality of the printed structure.

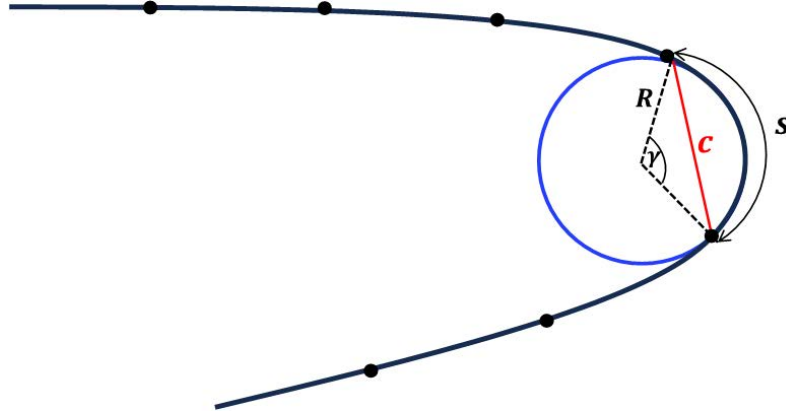


Figure 3.7: A curved region approximated as a segment of a circle.

Let's consider a high curvature region approximated as a segment of a circle with radius R , as illustrated in Figure 3.7. If we move a distance s along this circle, then the angle γ subtended by this segment at the circle's center is

$$\gamma = \frac{s}{r} = s\kappa \quad (3.21)$$

where κ is the curvature. For a given curve, if we set a maximum allowable deviation δ , the difference between the arc length d and chord length c is the deviation Δ :

$$\Delta = s - c \leq \delta \quad (3.22)$$

given that

$$c = 2R \sin\left(\frac{\gamma}{2}\right) \quad (3.23)$$

which derives

$$s - \frac{2}{\kappa} \sin\left(\frac{s\kappa}{2}\right) \leq \delta \quad (3.24)$$

Therefore, given the maximum curvature along the toolpath and a tolerance of deviation δ , a maximum sampling distance s can be calculated by the inequality 3.24. The δ can be selected and tuned according to the project requirement and the performance of robot motion.

- **G-Code Generation and Transfer to 3D Printer**

In generic 3D printing, the slicing software translates the toolpaths and printing instructions into G-code, which is a standard for CNC (computer numerical control) machining and has also found its way into the world of 3D printing. G-code provides a set of instructions for the machine to follow, determining the movements of the 3D printer, including

where and how it should move, the velocity and operation. In our case, as the G-code equivalent, the positions of the generated toolpath points expressed in (x, y, z) and the desired nozzle velocity are directly compiled into the cobot's specific programming language and sent to the cobot, then its *IKM* calculates the corresponding joint positions for each point to execute the trajectory.

Figure 3.8 gives an example of slicing for a complex shape with different parameter configurations, namely: distance between two successive layers h and distance between two adjacent points of the same layer d , the latter determines the number of points along the path of each layer. In our case, the layer height is fixed at 9 millimeters according to material test results. It can be seen that a smaller distance between adjacent points ensures that the generated toolpath respects the integrity of the designed shape.

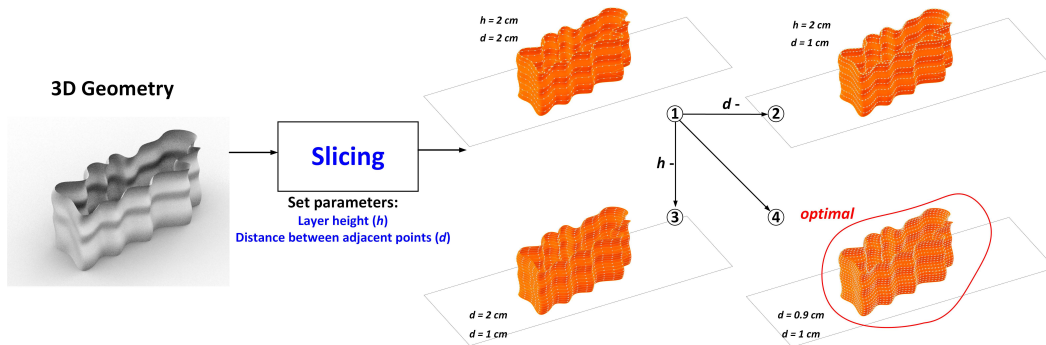


Figure 3.8: Slicing of a complex 3D shape for tool path planning of 3DCP process: 4 different selections of layer height and distance between points.

3.2.2.6 Time Parameterization

To execute the trajectory at a specific velocity, a time parameterization is applied. This involves dividing the path into discrete time steps and calculating the positions at each step based on the chosen velocity.

3.2.3 Implementing in Robot Control

The generated trajectory is then translated into the inverse kinematic model before implementing the robot-specific control commands, which dictate the joint angles or end-effector positions at each time step.

3.2.3.1 Inverse Kinematic Model for CIRMAP cobot

In contrast, the **Inverse Kinematic Model (IKM)** does the reverse: given a desired position and orientation \mathbf{X}_d for the end-effector, it computes the joint angles required Θ_d to achieve that pose:

$$\Theta_d = f^{-1}(\mathbf{X}_d) \quad (3.25)$$

For **IKM**, analytical and numerical solutions can be utilized according to the specific use case of the robot. Analytical solutions for inverse kinematics exist only for specific robot configurations, for most real-world robots, numerical methods (eg. Newton-Raphson method) are employed to solve the inverse kinematics problem. In the case of CIRMAP's 3D printing technology, the aim of **IKM** is to propose optimal kinematic postures of the cobot to track generated paths issued from the slicing process of the shapes to be printed. This allows detecting and avoiding singularity configurations of the printing robot.

For the CIRMAP cobot, an analytical **IKM** can be established based on the **FKM** equations given in Section 3.2.1.1. Figure 3.9 shows a list of robot configurations for the same end effector position. The **IKM** calculates not only the position but also the orientation of the nozzle tip. For maintaining printing quality, the nozzle should be perpendicular to the print bed, therefore, configuration 2 and 3 meets this requirement. Furthermore, to avoid collision between the robot arm and the print bed or other components of the printing platform, it's essential to choose the inverse kinematic solution according to the defined joint constraints for the 3D printing task. For example, in Figure 3.9, solution (3) is selected over solution (2) due to the constraint on joint angle θ_2 .

An analytical solution to the **IKM** of the CIRMAP cobot can be given as follows:

$$\left\{ \begin{array}{l} \theta_1 = \text{atan2}(A, B) - \text{atan2}(d_4, \pm \sqrt{A^2 + B^2 - d_4^2}) \\ \theta_2 = \text{atan2}\left(\frac{(a_3 C_3 + a_2)G - a_3 S_3 F}{a_2^2 + a_3^2 + 2a_2 a_3 C_3}, \frac{F + a_3 S_2 S_3}{a_3 C_3 + a_2}\right) \\ \theta_3 = \pm \arccos\left(\frac{F^2 + G^2 - a_2^2 - a_3^2}{2a_2 a_3}\right) \\ \theta_4 = \text{atan2}(-S_6(n_x C_1 + n_y S_1) - C_6(o_x C_1 + o_y S_1), o_z C_6 + n_z S_6) - \theta_2 - \theta_3 \\ \theta_5 = \pm \arccos(a_x S_1 - a_y C_1) \\ \theta_6 = \text{atan2}\left(\frac{D}{S_5}, \frac{E}{S_5}\right) \end{array} \right. \quad (3.26)$$

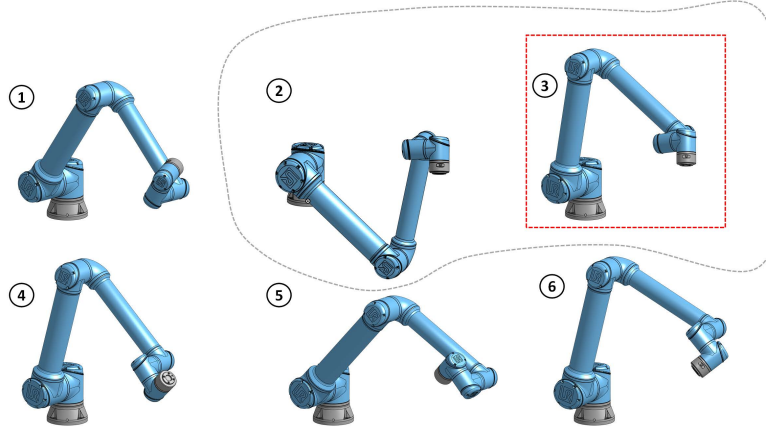


Figure 3.9: Different joint configurations for the same position: (1)-(6). (2) and (3) are two different configurations for the same position and orientation of end effector. (3) is the optimal configuration.

Note that this solution is calculated in the sequence of $\theta_1 \rightarrow \theta_5 \rightarrow \theta_6 \rightarrow \theta_3 \rightarrow \theta_2 \rightarrow \theta_4$, Where

$$\begin{cases} A = d_6 a_y - (p_y - a_7) \\ B = d_6 a_x - p_x \\ D = n_x S_1 - n_y C_1 \\ E = o_x S_1 - o_y C_1 \\ F = d_5 (S_6 (n_x C_1 + n_y S_1) + C_6 (o_x C_1 + o_y S_1)) - d_6 (a_x C_1 + a_y S_1) + p_x C_1 + (p_y - a_7) S_1 \\ G = p_z + l_7 - d_1 - a_z d_6 + d_5 (o_z C_6 + n_z S_6) \end{cases} \quad (3.27)$$

3.2.4 Executing the Trajectory

The robot arm is then commanded to follow the generated trajectory, moving from one point to the next in a controlled manner. The IKM of the robot enables the accurate and smooth tracking of the generated toolpath, an example is illustrated in Figure 3.10, given a sequence of nozzle tip poses, the corresponding robot joint configurations can be obtained thanks to the IKM. It should be noted that not every robot has analytical inverse kinematic solution, for more common cases or more complex robot design, numerical methods can be considered, although the latter are slower and more computationally expensive.

During the in-printing stage, the robot guides the nozzle to execute a pre-defined trajectory represented by a time history of the position, orientation and velocity of the nozzle tip, represented by $X = (x, y, z, R_x, R_y, R_z)$,

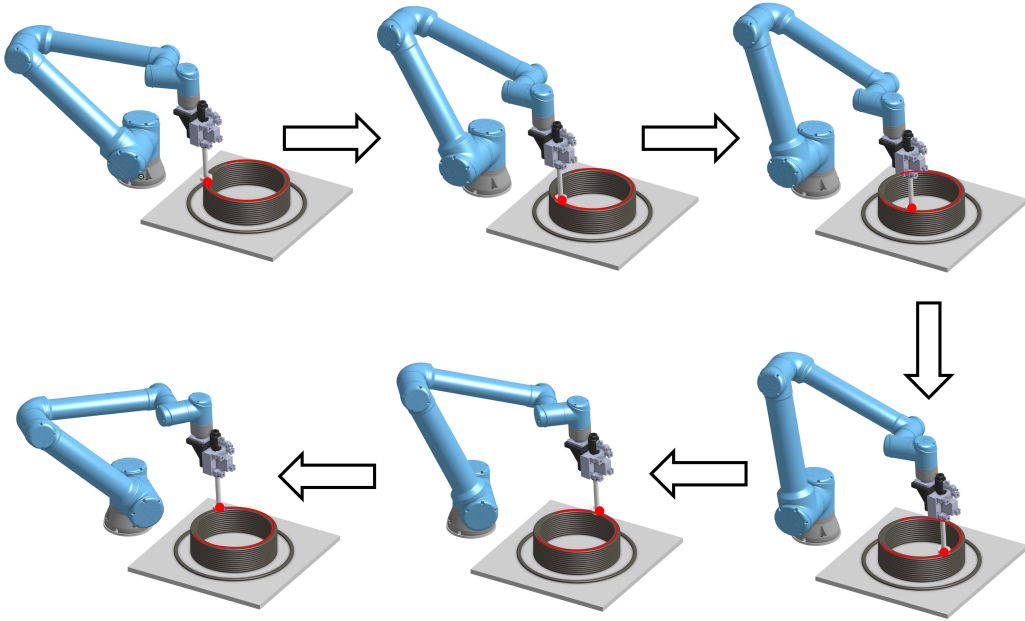


Figure 3.10: The sequence of poses of the nozzle tracking a circular toolpath.

$\dot{\mathbf{X}} = (\dot{x}, \dot{y}, \dot{z}, \dot{R}_x, \dot{R}_y, \dot{R}_z)$. To achieve this goal, a joint-based control scheme as shown in Figure 3.11 is widely used to track the trajectory for many robots nowadays[Craig 2006]. This approach is based on a trajectory conversion process that computes the joint trajectory: given the desired nozzle tip trajectory in Cartesian space, to compute the corresponding joint positions and velocities. The conversion is calculated based on the IKM of the robot.

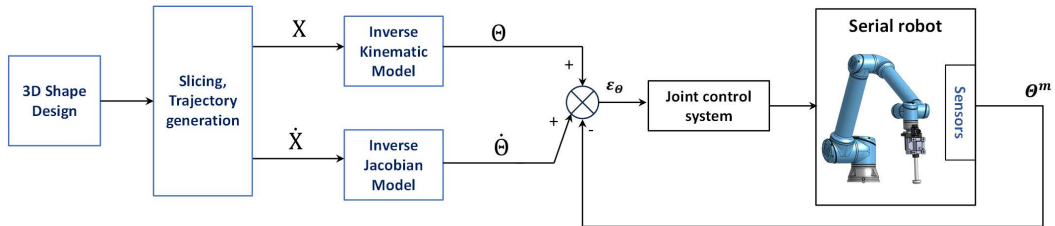


Figure 3.11: Nozzle pose and velocity control of robot.

For the robot, the differential kinematic is used for establishing the relationship between joint rate and end effector velocity. It is often expressed using the Jacobian matrix [Orin 1984, Renfrew 2004], denoted by \mathbf{J} , that effectively maps small displacement $\Delta\Theta$ in joint space to small displacement $\Delta\mathbf{X}$ in task (or Cartesian) space. In differential form:

$$\dot{\mathbf{X}}(t) = \mathbf{J}(\Theta)\dot{\Theta}(t) \quad (3.28)$$

where $\dot{\mathbf{X}}(t)$ is the end effector's velocity vector in task space (including linear and angular velocity), $\mathbf{J}(\Theta)$ is the Jacobian matrix that maps joint velocities $\dot{\Theta}(t)$ to end-effector velocities $\dot{\mathbf{X}}(t)$ in the robot's workspace.

For the CIRMAP cobot that has 6 degree of freedom, \mathbf{J} is a 6×6 matrix composed by the 3×6 linear velocity Jacobian \mathbf{J}_v and the 3×6 angular velocity Jacobian \mathbf{J}_ω :

$$\mathbf{J} = \begin{bmatrix} \mathbf{J}_v \\ \mathbf{J}_\omega \end{bmatrix} \quad (3.29)$$

In the case of 3D printing where the rotation of end effector is not concerned, the linear Jacobian is calculated as:

$$\mathbf{J}_v = \begin{bmatrix} \frac{\partial p_x}{\partial \theta_1} & \frac{\partial p_x}{\partial \theta_2} & \cdots & \frac{\partial p_x}{\partial \theta_6} \\ \frac{\partial p_y}{\partial \theta_1} & \frac{\partial p_y}{\partial \theta_2} & \cdots & \frac{\partial p_y}{\partial \theta_6} \\ \frac{\partial p_z}{\partial \theta_1} & \frac{\partial p_z}{\partial \theta_2} & \cdots & \frac{\partial p_z}{\partial \theta_6} \end{bmatrix} \quad (3.30)$$

For the CIRMAP cobot, the columns of linear Jacobian $J_{v_{\text{col}i}}$ are the following:

$$J_{v_{\text{col}1}} = \begin{bmatrix} -a_2 C_1 C_2 - a_3 C_1 C_{23} + d_4 S_1 - d_5 C_1 S_{234} + d_6 C_1 S_5 C_{234} + d_6 C_1 C_5 \\ a_2 C_1 C_2 + a_3 C_1 C_{23} + d_4 S_1 + d_5 C_1 S_{234} - d_6 S_1 C_5 + d_6 C_1 S_5 C_{234} \\ 0 \end{bmatrix} \quad (3.31)$$

$$J_{v_{\text{col}2}} = \begin{bmatrix} -a_2 S_2 C_1 - a_3 S_{23} C_1 + d_5 C_{234} C_1 + d_6 S_5 S_{234} C_1 \\ -a_2 S_1 S_2 - a_3 S_1 S_{23} + d_5 S_1 C_{234} + d_6 S_1 S_5 S_{234} \\ a_2 C_2 + a_3 C_{23} + d_5 S_{234} - d_6 S_5 C_{234} \end{bmatrix} \quad (3.32)$$

$$J_{v_{\text{col}3}} = \begin{bmatrix} -a_3 S_{23} C_1 + d_5 C_{234} C_1 + d_6 S_5 S_{234} C_1 \\ -a_3 S_1 S_{23} + d_5 S_1 C_{234} + d_6 S_1 S_5 S_{234} \\ a_3 C_{23} + d_5 S_{234} - d_6 S_5 C_{234} \end{bmatrix} \quad (3.33)$$

$$J_{v_{\text{col}4}} = \begin{bmatrix} d_5 C_1 C_{234} + d_6 S_5 S_{234} C_1 \\ d_5 S_1 C_{234} + d_6 S_1 S_5 S_{234} \\ d_5 S_{234} - d_6 S_5 C_{234} \end{bmatrix} \quad (3.34)$$

$$J_{v_{\text{col}5}} = \begin{bmatrix} -d_6 C_1 C_5 - d_6 S_1 S_5 C_{234} \\ d_6 S_1 C_5 - d_6 C_1 S_5 C_{234} \\ -d_6 S_5 S_{234} \end{bmatrix} \quad (3.35)$$

$$J_{v_{\text{col}6}} = \begin{bmatrix} 0 \\ 0 \\ 0 \end{bmatrix} \quad (3.36)$$

while the angular Jacobian J_ω is a 3×6 matrix, each column is the axis of rotation of the joint, expressed in the base frame of the robot. The columns of angular jacobian $J_{\omega_{\text{col}i}}$ are the following:

$$J_{\omega_{\text{col}1}} = \begin{bmatrix} 0 \\ 0 \\ 1 \end{bmatrix} \quad (3.37)$$

$$J_{\omega_{\text{col}2}} = \begin{bmatrix} S_1 \\ -C_1 \\ 0 \end{bmatrix} \quad (3.38)$$

$$J_{\omega_{\text{col}3}} = \begin{bmatrix} S_1 \\ -C_1 \\ 0 \end{bmatrix} \quad (3.39)$$

$$J_{\omega_{\text{col}4}} = \begin{bmatrix} S_1 \\ -C_1 \\ 0 \end{bmatrix} \quad (3.40)$$

$$J_{\omega_{\text{col}5}} = \begin{bmatrix} C_1 S_{234} \\ S_1 S_{234} \\ -C_{234} \end{bmatrix} \quad (3.41)$$

$$J_{\omega_{\text{col}6}} = \begin{bmatrix} S_1 C_5 - C_1 C_{234} S_5 \\ -C_1 C_5 - S_1 C_{234} S_5 \\ -S_{234} S_5 \end{bmatrix} \quad (3.42)$$

The inverse of this relationship (Equation 3.28) allows to determine the joint rates of the robot given a desired end effector velocity:

$$\dot{\Theta} = J^{-1} \dot{X} \quad (3.43)$$

where J^{-1} denotes the inverse Jacobian if J is square matrix and of full rank. In the case where J is not square or full rank, other techniques can be utilized such as the pseudo-inverse denoted by J^+ :

$$J^+ = J^T (J J^T)^{-1} \quad (3.44)$$

3.3 Shape Pre-preparation

Shape pre-preparation is a crucial step in 3D printing, especially in construction where large-scale objects are often printed. It involves preparing the design to ensure a successful printing process. The designed 3D model might

need to be scaled to fit the desired dimensions. Additionally, it's positioned within the 3D printing software to ensure it fits within the build volume and is correctly oriented for printing. Two main considerations should be considered are: the limitation of the curvature of the shape and the velocity control of the robot according to the curvature. This section develops analytically these two considerations.

3.3.1 Curvature limitation

One of the challenge for automation process of 3D printing in construction is the ability of the printing robot to follow generated shapes with complex curvatures (e.g. funicular shapes) during the step of slicing. In this section, we discuss the identification of the geometric shape constraints, knowing that not all the shapes can be realized by a unique robot kinematics. Let's assume a 3DCP process where the material flow rate Q at the nozzle outlet is constant. The overall structure shape is given by the design stage and the nozzle path is given by the slicer. In order to maintain a consistent desired width w^d of the deposited material filament, the nozzle traveling velocity (magnitude of velocity) is expected to be constant, noted by v^d .

The kinematic performance of a robot manipulator is limited due to its dynamic and structural constraints coming from the mechanical design and actuators. Specifically, when the trajectory involves sharp turns, maintaining a constant velocity or acceleration can be challenging due to the robot's constraints [Amersdorfer 2021].

For a plane curve $\gamma(\mathbf{s})$, where \mathbf{s} is the arc length, the local curvature at a point describes how quickly the tangent vector of the curve turns at this point. The curvature $\kappa(\mathbf{s})$ can be defined by the reciprocal of the radius of the osculating circle $R(\mathbf{s})$ at this point:

$$\kappa(\mathbf{s}) = \frac{1}{R(\mathbf{s})} \quad (3.45)$$

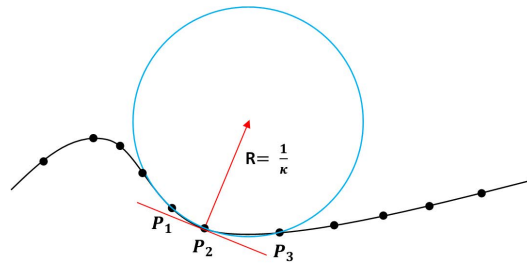


Figure 3.12: Curvature along trajectory

Assume that the constraints of a specific manipulator allow a maximum centripetal acceleration a_{cmax} for its end effector [Li 2018, Munasinghe 2002], in the case of desired nozzle velocity v^d ,

$$a_c = \frac{v^{d2}}{R} = \kappa v^{d2} \leq a_{cmax} \quad (3.46)$$

Therefore, during the material deposition along a designed trajectory:

$$v = \min(v^d, \sqrt{\frac{a_{cmax}}{\kappa}}) \quad (3.47)$$

Given a desired nozzle velocity v^d , the maximum trajectory curvature allowing keeping constant nozzle velocity is given by:

$$\kappa_{max} = \frac{a_{cmax}}{v^{d2}} \quad (3.48)$$

The maximum curvature is different for specific robot and nozzle velocity requirements. Although in many cases this limitation does not apply in order to achieve accurate deposition for complex shapes, this parameter can still be considered during the design or slicing phase to avoid disturbances to the material flow due to sudden changes in the direction of nozzle motion. There is a compromise between the accuracy and integrity of the shape and stability of nozzle velocity.

3.3.2 Shape reconstruction from the 3D robot printing

The process of printing a complex shape with variable curvature is considered in this study. The design of this shape is provided by the CIRMAP colleagues from the University of Liège. The layer height (i.e. distance between successive layers of tool path) is fixed at 9 millimeters. The tool path generated by the slicing step and the final printed shape are shown in Figure 3.13. For this printing task, the desired nozzle velocity is set constant at $v^d = 12 \text{ cm/s}$. The position sensors of the robot and its FKM developed in Section 3.2.1.1 allow the recording of the nozzle tip position at a rate of 20 Hz.

To study the impact of local curvature along toolpath on the nozzle velocity, an analysis of trajectory is performed on the time-stamped data of nozzle tip position. The actual nozzle velocity were calculated using 4th order central difference method for a more accurate approximation of v_x and v_y . The the (x, y, z) coordinates of nozzle tip were obtained with a sampling time $\Delta t = 50 \text{ ms}$. For a point $P_i(x_{t_i}, y_{t_i}, z_{t_i})$ on the nozzle's trajectory, the nozzle's velocity components along x, y direction when it travels through this point is

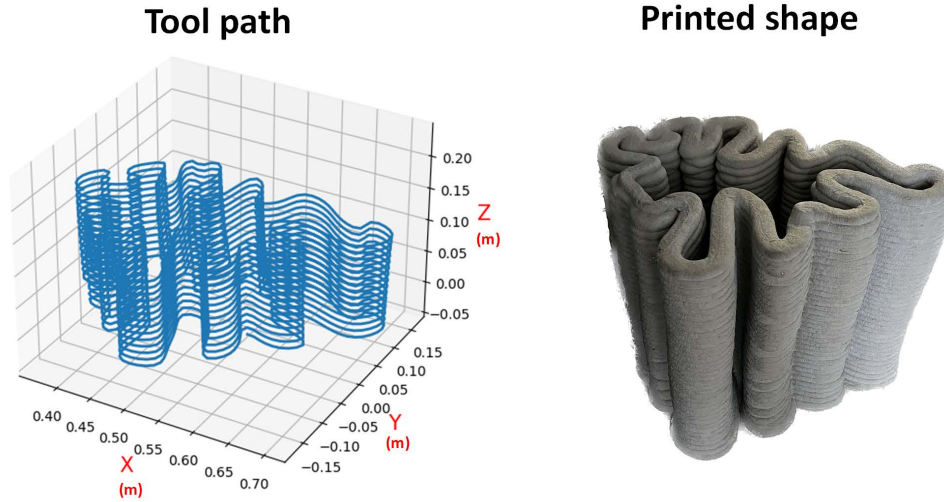


Figure 3.13: Printing a complex shape: toolpath generated by slicing and the final printed shape.

calculated as follows:

$$\begin{cases} v_{x_{t_i}} \approx \frac{x_{t_{i-2}} - 8x_{t_{i-1}} + 8x_{t_{i+1}} - x_{t_{i+2}}}{12\Delta t} \\ v_{y_{t_i}} \approx \frac{y_{t_{i-2}} - 8y_{t_{i-1}} + 8y_{t_{i+1}} - y_{t_{i+2}}}{12\Delta t} \end{cases} \quad (3.49)$$

Therefore, the scalar magnitude of the velocity, is given by:

$$v_{t_i} = \sqrt{v_{x_{t_i}}^2 + v_{y_{t_i}}^2} \quad (3.50)$$

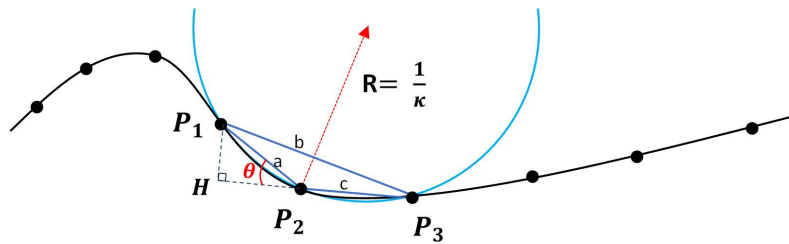


Figure 3.14: Circumcircle of $\triangle P_1P_2P_3$, the curvature at P_2 is given by the reciprocal of the circumradius.

The local curvatures of the trajectory are calculated by approximation at each point P_i . As illustrated in Figure 3.14, the approximation of the curvature at point P_2 can be given by the reciprocal of the circumradius of $\triangle P_1P_2P_3$. Let a, b and c denote the lengths of the triangle's three sides and A

denotes the triangle's area, the circumradius of the triangle is calculated as:

$$R = \frac{abc}{4A} \quad (3.51)$$

While this calculation is for a 2D representation, we utilize the cross product of vectors defined in 3D space, hence, the 2D vectors are treated as 3D vectors with a zero z-component. As demonstrated in the figure below, let the three points be $P_1(x_1, y_1, 0)$, $P_2(x_2, y_2, 0)$, $P_3(x_3, y_3, 0)$, the length of side P_1P_2 can be interpreted as the magnitude of difference between P_1 and P_2 denoted by $\|P_1 - P_2\|$, therefore:

$$abc = \|P_1 - P_2\| \|P_2 - P_3\| \|P_3 - P_1\| \quad (3.52)$$

According to the definition of cross product,

$$\begin{aligned} \|(P_1 - P_2) \times (P_2 - P_3)\| &= \|P_1 - P_2\| \|P_2 - P_3\| |\sin(\theta)| \\ &= \|P_1 - H\| \|P_2 - P_3\| = 2A \end{aligned} \quad (3.53)$$

Therefore,

$$R = \frac{abc}{4A} = \frac{\|P_1 - P_2\| \|P_2 - P_3\| \|P_3 - P_1\|}{2\|(P_1 - P_2) \times (P_2 - P_3)\|} = \frac{1}{\kappa} \quad (3.54)$$

Figure 3.15 corresponds to the nozzle's trajectory while executing a full single layer, with all points having the same z-coordinates, displaying the 2D trajectory in XOY plane and the magnitudes and directions of its local curvatures symbolized by the blue arrows.

The curvature and nozzle velocity along the traveled distance of the nozzle can then be represented in Figure 3.16. Indeed, when the nozzle pass through a point where the local curvature is greater, presenting a sharp turn, an error between the desired velocity v^d and the actual velocity v can be observed [Yang 2023a], namely a velocity error defined by:

$$\Delta v = v^d - v \quad (3.55)$$

A 3D representation demonstrated in Figure 3.17 shows this phenomenon by adopting vectors along Z-direction axis to represent the velocity error. It can be observed that greater velocity error occurs at sharp turns.

This fact can be explained by the maximum curvature limit for constant velocity tracking of the tool path given by equations (3.47) and (3.48). Figure (3.18) plots the curvature and velocity of the sampled points along a single layer, it can be seen that the distribution of the sampled points conforms to the given relation.

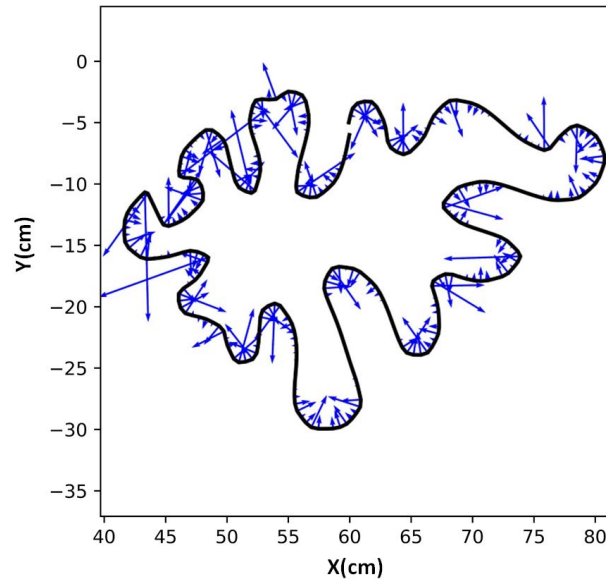


Figure 3.15: The curvature distribution along a single layer in XOY plane.

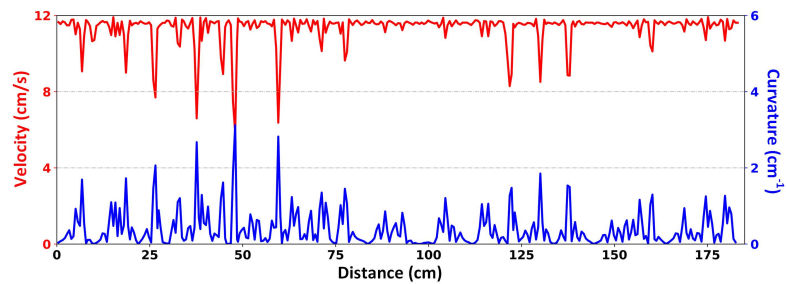


Figure 3.16: Nozzle velocity and curvature along traveled distance by nozzle.

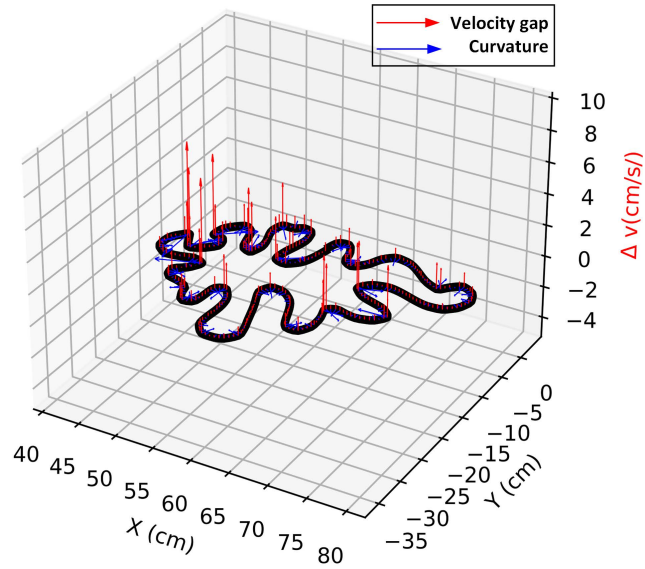


Figure 3.17: Representation in 3D, the blue arrows in XOY plane is the curvature, the red arrow along the third axis represents the velocity error Δv .

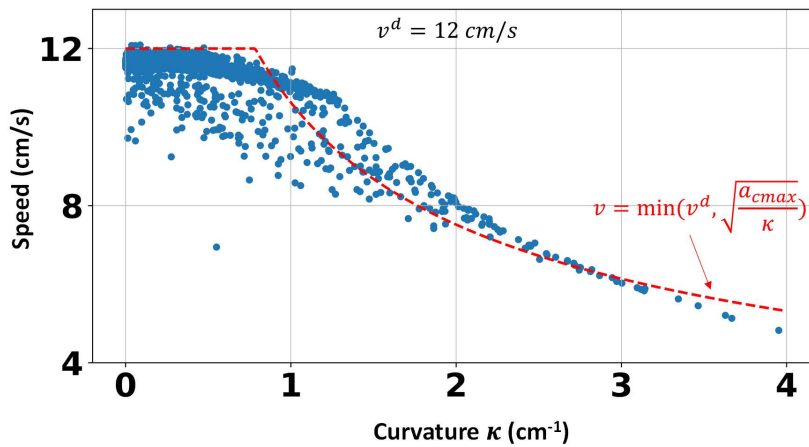


Figure 3.18: The relationship between local curvature κ and actual nozzle velocity v given a reference velocity $v^d = 12$ cm/s.

3.4 Material Pre-preparation

3.4.1 Material mixing

As mentioned in Chapter 2, Section 2.2, the material for 3DCP need to meet the requirements including pumpability, extrudability, buildability as well as workability. In the material preparation stage for 3D printing in construction with concrete, key components typically include cement, sand, water, and other additives to achieve desired rheology properties. Superplasticizers is added for lowering the yield stress of concrete, thereby improves its workability, Viscosity Modifying Agent is added to increases the plastic viscosity of concrete. The proportioning of these components is often determined based on empirical or computational models. The material components are mixed inside a mortar mixer. The mixing time is also a key point to decide whether the material is ready to be fed to the pump. The determination of the mixing time is also empirical, which depends on the mixer type and amount of materials. In order to determine this, in practical printing preparation, quality tests like slump flow test can be used to evaluate the workability of the fresh state concrete [Hynek 2022, Tay 2019b].

For example, one section of printing tests within CIRMAP project follows the the mixing proportion given in Table 3.2.

Table 3.2: Batching of Concrete Mix

Cement	35 kg
Recycled Sand	38.5 kg
Water	12.47 kg
Superplasticizer	700 g
Viscosity modifying agent (VMA)	70 g

3.4.2 Material Quantity Estimation

Given a specific shape design, an estimation of material quantity can help to avoid unnecessary material waste, this estimated quantity can help to determine the concrete batching quantity during the material preparation step. As discussed in Section 3.2.2, before executing the printing task, the 3D design shape is transformed into a sequence of discrete points within the robotic system's coordinate framework. This transformation is crucial in 3DCP)operations, as it ensures that the printing path aligns with the robot's



Figure 3.19: Flow table test to determine the workability of fresh concrete.

mechanical and operational capabilities. However, it is important to acknowledge that the trajectory ultimately executed by the robot may exhibit slight deviations from the originally intended design. These deviations are primarily attributable to the adjustments made to comply with the robot's kinematic constraints. Such modifications are necessary to ensure a feasible and physically realizable path, considering the inherent limitations of the robotic system.

Thus, based on the generated points (i.e. toolpath), the total travel distance of the nozzle can be calculated, which allows an estimation of the total volume and weight of the material.

Given all the points along the final generated toolpath: $(x_0, y_0, z_0), (x_1, y_1, z_1), \dots, (x_N, y_N, z_N)$, the cumulative travel length L_N for the nozzle can be computed as follows:

$$L = \sum_{i=1}^N \sqrt{(x_i - x_{i-1})^2 + (y_i - y_{i-1})^2 + (z_i - z_{i-1})^2} \quad (3.56)$$

Therefore, an estimated quantity of material weight can be calculated as:

$$M_{material}^{est} = Lhw^d\rho_{material} \quad (3.57)$$

where $h, w^d, \rho_{material}$ denotes the layer height, the designed width of material filament and the density of the fresh state material, respectively. This estimation allows to calculate the quantity of each mixing component (e.g. sand, cement, water, etc.) for material mixing.

3.5 Emulated Uncontrolled Environment

An emulated environment through a climate chamber has been developed in the framework of CIRMAP project. It aims at performing the automation of 3D printing in construction in uncontrolled environment, refers to a controlled setting designed to replicate specific environmental conditions that may not naturally occur at a construction site. This controlled environment is crucial for testing and validating 3D printing processes and materials under conditions that mimic real-world scenarios.

The walk-in climatic test chamber was installed and used to mimic different environmental conditions in which 3D concrete printing tests can be performed. The climate chamber of CIRMAP¹ measures 2.0 m × 2.42 m × 1.92 m. It integrates multiple components, including heating, cooling, drying, humidification and water supply/evacuation systems, enabling the control of temperature (T) and humidity (H) within the internal space of the chamber. Figure 3.20 and Figure 3.21 illustrates respectively the external configuration of the climate chamber, which accommodates the 3D printing robot while the material mixing and pumping system is positioned outside. The workspace of the robot enables the printing of objects up to a maximum size of 60 cm × 60 cm × 110 cm within the climate chamber.

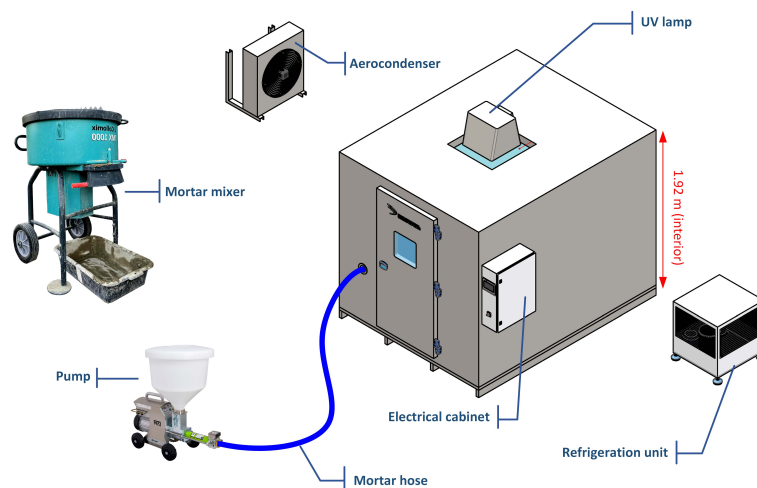


Figure 3.20: External configuration of the emulated environment.

The basic advantage of a climate chamber is its ability to simulate a wide range of weather conditions, from hot summers to cold winters. The purpose of this simulation is to mimic the various challenges that can be encountered on a construction site. One of the main reasons for this is the behavior of

¹<https://www.dycometal.com/en/>

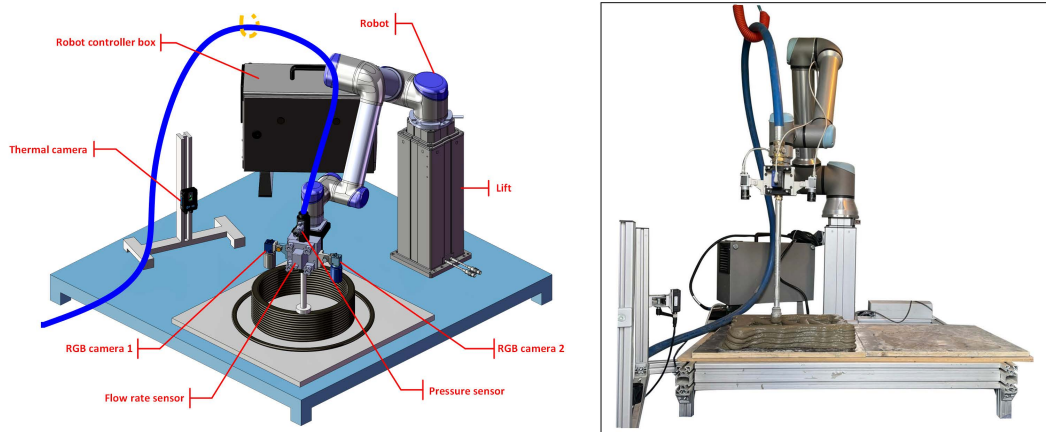


Figure 3.21: Internal configuration of the emulated environment.

construction materials at different temperatures. Temperature plays a decisive role in influencing material flow, curing times and overall print quality. In the CIRMAR climate chamber, the temperature can be finely adjusted within the range of 0°C to 50°C . Humidity is also a significant factor that impacts the material's behavior. Concrete is very sensitive to moisture content, so it's important to have a controlled environment that can simulate a variety of humidity levels to ensure material consistency during the printing process. In this chamber, humidity can be adjusted from 10% to 90% (non-condensing). The T and H profiles can be defined through scripts with the proprietary software (CID). The software also provides measurements of T and H of the internal environment at a defined frequency, with a minimum sampling time of 30 seconds, allowing monitoring and recording of the environmental conditions during printing tests. Figure 3.22 demonstrates the scenarios for the use of the climate chamber.

The chamber's capability to regulate temperature and humidity over a broad spectrum enhances its feasibility for diverse research applications. One of the utilization is its ability to simulate how specific concrete mixtures behave under a variety of environmental conditions. By allowing materials to print and cure in settings that mimic different temperature and humidity combinations, researchers can gain valuable insights into the properties and quality of the resulting structures.

It's worth noting that due to the spatial constraints within the climate chamber, the mortar mixer and pump are situated externally, potentially influencing the material's temperature. To mitigate this effect, the test protocol involving material handling requires a pre-conditioning step of storing raw materials—such as cement, sand, and water—inside the chamber at the

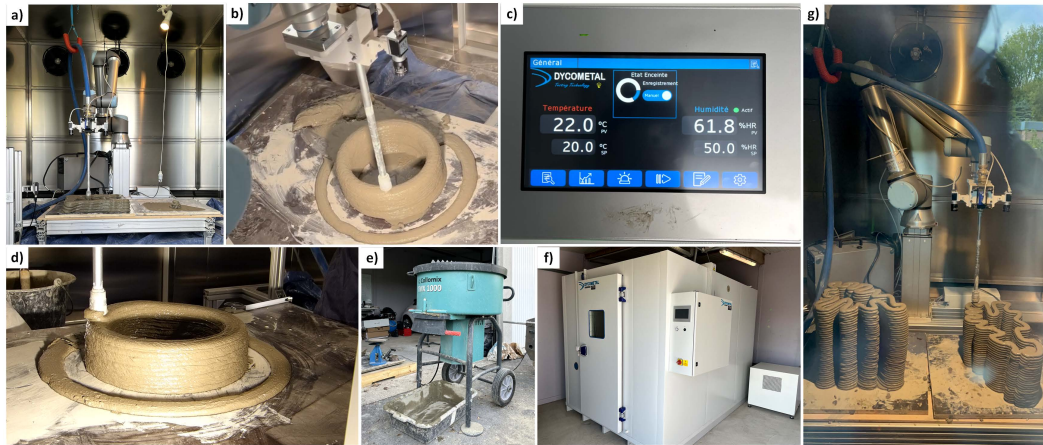


Figure 3.22: 3DCP tests conducted within the emulated environment. (a)(g) Printing objects of variable-curvature shape. (b)(d) Printing objects of constant-curvature (cylindrical) shape. (c) Control panel of the climatic chamber. e) Mortar mixer used for material preparation. f) The climate chamber.

set temperature and humidity. This precaution ensures that, at the commencement of the mixing process, the material's temperature aligns with the emulated environmental conditions. Additionally, it is important to note that the interval between the start of mixing of the material and its transportation through the hose is relatively brief, typically around 10 minutes, and the transportation is mainly inside the chamber as the hose is placed inside.

Other than material tests, printing parameters, including extrusion rates, nozzle temperature, and layer height, can be fine-tuned thanks to the emulated environment. This tuning, guided by data, can ensure that the end result matches the anticipated behavior at actual construction sites. Such detailed calibration helps to predict and prevent potential defects or inefficiencies in the process.

Moreover, the chamber's utility also benefits post-printing stage studies. After the initial construction, 3D printed structures can be subjected to comprehensive stress tests. These tests, which simulate adverse conditions like wind, rainfall, or extreme temperatures, are indispensable in evaluating the structural resilience and lifetime of the prints. Additionally, the chamber offers possibility into the study of thermal dynamics of printed structures. By monitoring the cooling phase under varied temperature conditions, it's possible to understand and potentially optimize the thermal properties of the construction material. For example, in collaboration with our project partners specializing in material research, a series of experiments have been conducted where cylindrical structures were 3D printed and subjected to varying cooling temperatures (details are given in Appendix A). Figure 3.23 illustrates

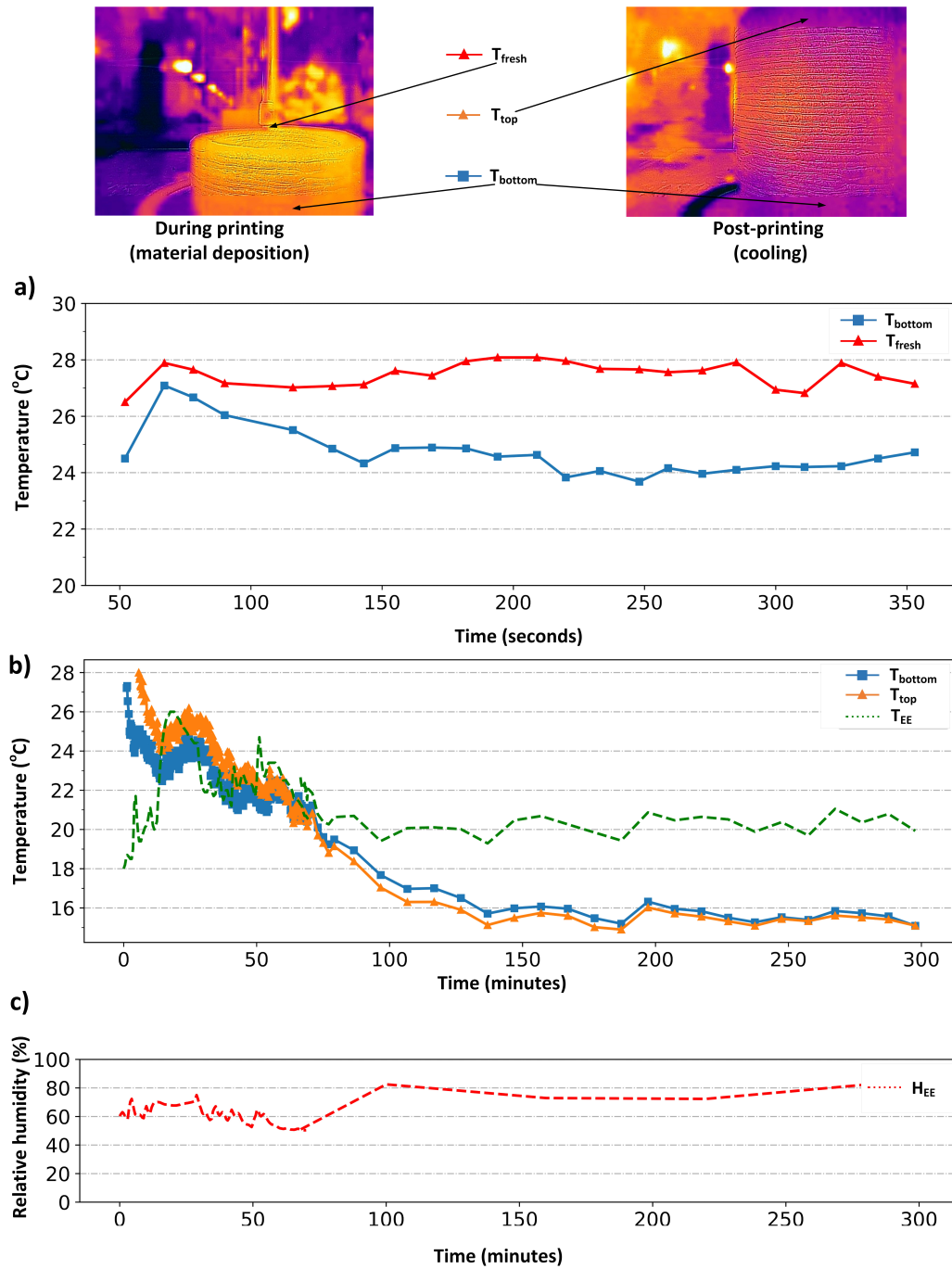


Figure 3.23: Test example: outdoor ambient temperature $T_{ambient} = 19^{\circ}C$. a) Temperature of newly extruded material T_{fresh} and deposited material at a specific point T_{bottom} measured during printing. b) The evolution of temperature at the top (T_{top}) and bottom (T_{bottom}) of the printed object and temperature inside the climate chamber measured during the material drying process. c) Humidity inside the climate chamber H_{EE} during the material drying process.

the monitoring of the surface's thermal behavior throughout the printing and subsequent drying processes. It can be observed that the surface temperature converges to around 15 °C, despite that the environmental temperature stays around 20 °C, which conforms to the behavior during evaporative cooling stage of concrete. Such tests are instrumental in understanding how the material properties respond to different environmental conditions. The results of tracking material surface temperature under other environmental conditions are given in Appendix A.

Conclusively, with the combined advantages offered by the chamber, it becomes significantly more straightforward to conduct research works linked to 3D printing in construction from a variety of aspects.

3.6 Conclusion

This chapter highlights the pre-printing phase, which plays in ensuring the success of 3D printing in construction. The significance of optimizing the shape design like proper scaling according to the shape curvature and velocity of the robot nozzle is explained. From the robot side, an identification of the workspace is provided from the forward kinematic model, while the trajectory generation is obtained from slicing the model and generating accurate tool-path for guiding the printer in depositing material layer by layer. The inverse kinematic model of the robot is developed to express the postures of the identified degree of freedom to track the trajectory inside the workspace without singularities. Finally, the pre-preparing phase of the material helps to estimate the needed quantity for the printed shape. The chapter also describes an emulated uncontrolled environment through a climate chamber, used for data collection and validating the 3D printing automation in various weather conditions.

In-printing stage: Tracking of Filament Deposition

Contents

4.1	Introduction	73
4.2	Problem Statement	74
4.2.1	Material deposition parameters	75
4.2.2	Assumptions	77
4.3	Deep Learning-based filament width estimation	77
4.3.1	Filament segmentation	78
4.3.2	Camera calibration	79
4.3.3	Filament width estimation	79
4.4	Qualitative diagnosis approach	84
4.4.1	Pattern recognition for system diagnosis	84
4.4.2	Case study: CIRMAP printing session	85
4.4.3	Results and discussion	91
4.5	Quantitative Diagnosis approach	99
4.5.1	Diagnosis based on Analytical Redundancy	99
4.5.2	Case study: CIRMAP printing session	100
4.5.3	Real-time diagnosis in controlled environment	107
4.5.4	Real-time diagnosis in uncontrolled environment	112
4.5.5	Comparison study	114
4.5.6	Conclusion	115

4.1 Introduction

The previous chapter discussed the preparatory aspects of the 3D Concrete Printing (3DCP) process, focusing on robot configuration, shape preparation,

and material preparation during the pre-printing stage. This chapter shifts the focus to the monitoring and diagnosis challenges encountered during the in-printing stage. The in-printing phase commences with the activation of the pump to initiate material flow, followed by the continuous deposition of fresh concrete through a nozzle. This nozzle is guided by a robotic arm that follows a predefined trajectory. Traditional 3DCP systems often require manual decision and adjustments of printing parameters by a human operator in the event of anomalies. One widely accepted criterion for online monitoring of material deposition quality is the geometric feature of the extruded filament, as it directly indicates any deformations and can be readily captured by visual sensors. To achieve full automation of the process, it is imperative to evaluate the quality of material deposition and implement robust monitoring and diagnostic methods that can provide real-time feedback for process adjustments [Xiao 2020]. Furthermore, in the event of an anomaly, it's essential to know which parameter is linked to this anomaly, as this enables us to select the parameter to be adjusted to compensate for the anomaly. In this context, this chapter focuses on a comparative study of two diagnostic approaches: a qualitative approach based on pattern recognition and a quantitative approach based on Analytical Redundancy Relation (ARR).

4.2 Problem Statement

The system that performs 3DCP process is a large-scale system that contains several parts involving different physical and dynamic behaviors. The complexity of the operation of 3DCP process can be highlighted by considering a System of Systems (SoS) consisting of three component systems $CS_{i,j}$ which are working in parallel and interactively, where i corresponds to the number of components at the same level of aggregation and j corresponds to the membership class [Khalil 2012] as follows: the material (including pumping), the robot and the shape. Figure 4.1 shows the architecture of the 3DCP SoS. The complexity also lies in the modeling of material behavior which is typically characterized by high levels of uncertainty and nonlinearity. This complexity is compounded by the dynamic nature of the materials used in 3D concrete printing, where properties such as setting time, flow characteristics, and mechanical strength can vary significantly based on environmental factors. Developing a comprehensive analytical model of material is out of the scope of this research work.

Our focus is primarily centered on the aspects of robotic control and the automation of the 3D printing process in uncontrolled environments. While acknowledging the complexity of material behavior modeling, we limit our

engagement with this aspect to the application of existing models and theories, rather than attempting to develop new analytical models from the ground up. This approach allows us to concentrate our efforts on the robotic and control aspects of 3D concrete printing, which align more closely with our field of expertise and the objectives of this research.

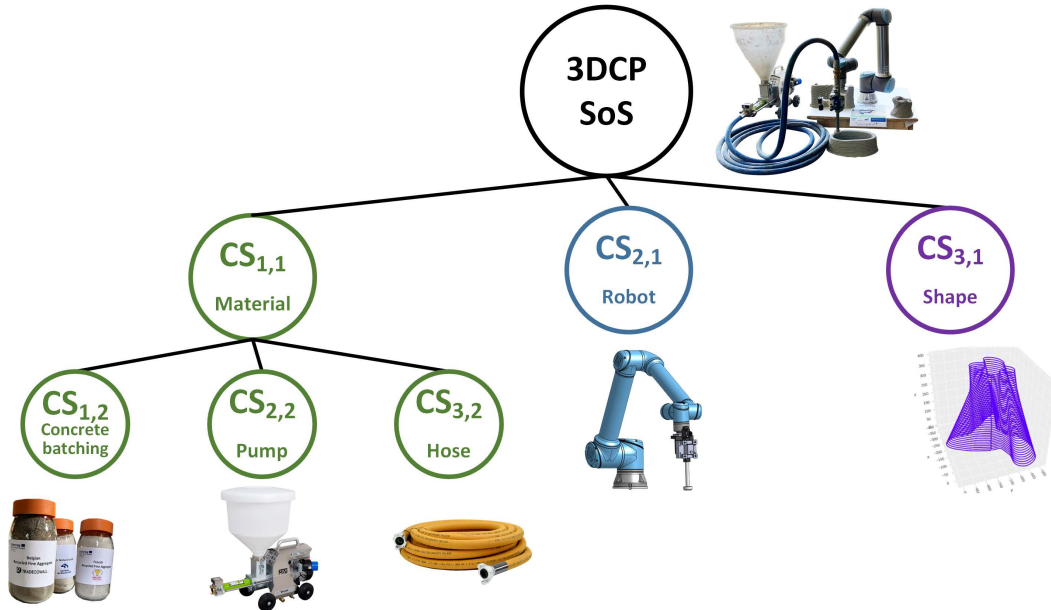


Figure 4.1: 3DCP SoS architecture

Thus, the in-printing stage of 3DCP process concerns the real-time collaboration between different component systems with heterogeneous dynamic behaviors including fluid (material), electro-mechanic (robot), electro-hydraulic (pump and hose), which are managerially and operationally independent, with presence of information exchange between each other. This complex interplay between two distinct dynamic systems (robotic arm and material pumping mechanism) poses challenge to the control of printing quality. Specifically, when anomaly occurs, it's imperative not only to identify the anomaly, identify which parameters are linked to the anomaly. This facilitates the accurate selection of parameters for regulatory adjustments to compensate for the disturbance.

4.2.1 Material deposition parameters

To recall, Figure 4.2 demonstrates the continuous material deposition during the in-printing stage. The parameters involved during material deposition are considered and listed in Table 4.1.

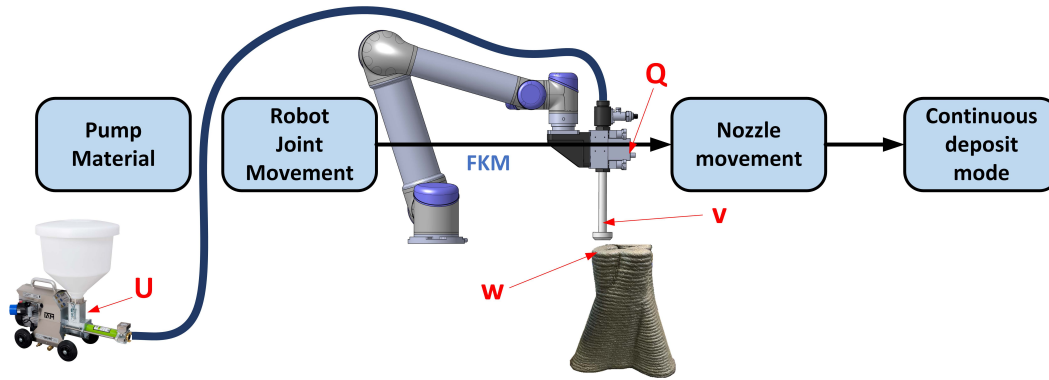


Figure 4.2: Continuous material deposition during in-printing stage.

Table 4.1: Description of Parameters

Parameter	Description	Unit
Q	Volumetric flow rate of material at the nozzle	cm^3/s
U	Pump voltage command	volt
w	Width of material deposit filament	cm
h	Height of material deposit filament	cm
v	Nozzle velocity	cm/s

4.2.2 Assumptions

Based on empirical data and the literature, certain parameters fall within a certain range during the operation. We have therefore adopted the following assumptions for the printing process throughout this study:

- **Nozzle velocity:** During the printing stage, the nozzle velocity is limited within the following range [Zhang 2023]:

$$3 \text{ cm/s} \leq v \leq 20 \text{ cm/s} \quad (4.1)$$

Indeed, the nozzle moving too slowly may lead to over deposit of material, on the contrary, if the nozzle moves too fast, the drying time of the deposited material is not sufficient for maintaining the structure, which affects the buildability.

- **Pump:** We assume that the relation between the material flow rate Q at steady stage and pump voltage command U is linear. The pump used in this work is a volumetric pump which means that the flow rate is proportional to the rotation velocity of the pump, and we assume that the rotation velocity and the voltage command conform to a linear relation within the range of 3DCP application. A continuous flow is generated by the pump.
- **Filament height:** In the slicing step, the height of each layer h is given by a fixed value (see Chapter 3). It is assumed that the deformation of material layer height can be neglected, therefore the layer height is identical to the tool path layer height.

4.3 Deep Learning-based filament width estimation

To assess the quality of the 3D printing, the filament width w serves as the chosen criterion. However, directly measuring w during the in-printing stage poses the risk of damaging the freshly-deposited concrete filament. As such, non-destructive methods are favored over direct measurement. Deep Learning (DL) techniques have gained traction in fault diagnosis and prognosis, particularly when visual sensors like cameras are used for monitoring the process [Qiu 2023]. Abnormal deposition events can manifest as deformations in the material filament, which we categorize as a geometric fault characterized by

width deviation. Given that we employ a visual sensor, this fault-like behavior can be detected at the pixel level. Consequently, a Deep Learning-based approach is utilized for estimating filament width [Yang 2022b].

The estimation approach is data-driven and adopted a Deep Learning instance segmentation model for the identification of freshly printed filament from an image taken by the visual sensor on the printer head. Then, the morphological medial axis transform is used to extract a center line from the identified filament segment and calculate the overall width of the filament segment in image frame, followed by a frame transformation to map the pixel width to millimeter. This approach allows to estimate the width of freshly deposited filament during the printing stage through a non-destructive method.

4.3.1 Filament segmentation

This part is realized by exploring the top-view images of freshly printed filaments provided by visual sensors (cameras). A review of the literature demonstrates that DL methods outperform conventional Computer Vision (CV) methods in terms of performance, generalization ability, and robustness to environmental noise [O'Mahony 2019]. We adopted a DL instance segmentation model, namely Mask RCNN [He 2017], to segment the filament in real-time. Mask RCNN has been implemented in other single-target-single-class instance segmentation tasks in multiple fields including medical science [Anantharaman 2018], agriculture [Hameed 2022, Jia 2020, Yu 2019] and structural health monitoring (SHM) [Kahouadji 2021], it has shown better performance compared to other models in term of efficiency and precision.

4.3.1.1 Instance segmentation model

A concrete filament image dataset is firstly collected for the training of the model. The dataset is divided into a training set containing 550 images and a validation set containing 150 images. All the images are taken from top-view, each image was captured during material deposit under different lighting conditions. To enhance the generalization and robustness of the instance segmentation model, data augmentation techniques were applied online during the training process. The considered augmentations included random flipping, as well as random adjustments to contrast and brightness to simulate wider range of lighting conditions and enrich the diversity of the dataset. The model's performance can be improved in handling a wider range of scenarios.

The architecture of the Mask RCNN implemented in this study is presented in Figure 4.3, the backbone of the network is composed of a ResNet50 and Feature Pyramid Network (FPN). By using a transfer learning approach,

a pre-trained model was fine tuned on the custom dataset on a DELL workstation with Intel[®] Core[™] i9-11950H CPU and NVIDIA RTX A3000 GPU. The trained model was tested on the validation set and has reached 87.6% average precision at 0.5 Intersection Over Union (IoU) and 78.8% average precision at 0.75 IoU.

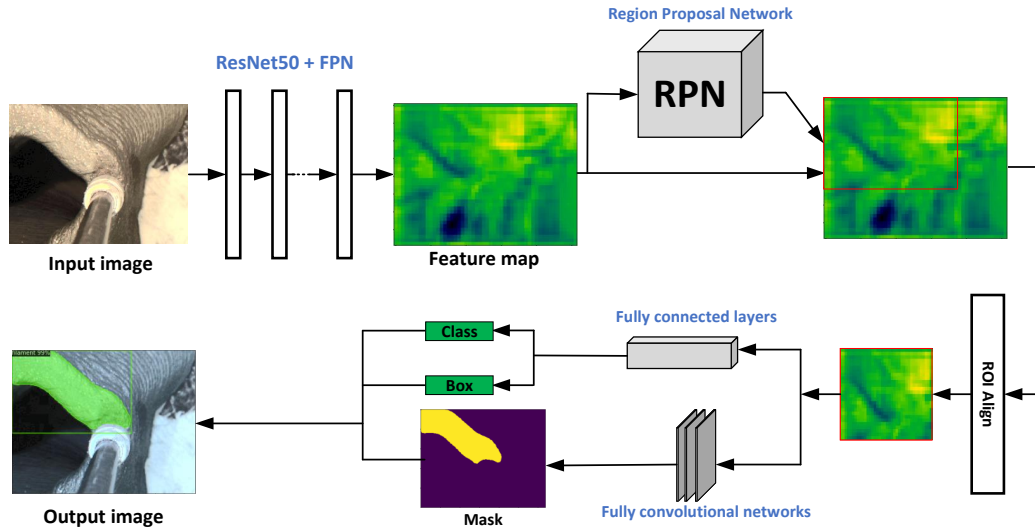


Figure 4.3: Architecture of Mask RCNN

As shown in Figure 4.3, the output of the model consists of a binary mask of the filament, a bounding box and an associated class. In the real-time implementation, we choose a smaller **Region of Interest (RoI)** according to the direction of nozzle velocity, so that the image contains a shorter segment of filament, which helps to improve the precision of width calculation.

4.3.2 Camera calibration

In order to eliminate the error caused by camera distortion when the detected target is close to the image edge, a calibration step is implemented before each print job with a chessboard using Zhang's method [Zhang 2000]. A $40\text{mm} \times 40\text{mm}$ ArUco marker is used to test the algorithm. As shown in Figure 4.4, the undistortion step significantly reduces the sum of squared errors (SSE) when calculating size of the four edges of the marker.

4.3.3 Filament width estimation

A morphology-based filament width estimation approach is developed. Based on the binary mask given by the instance segmentation model, we can compute the overall width of the freshly printed filament segment in millimeters.

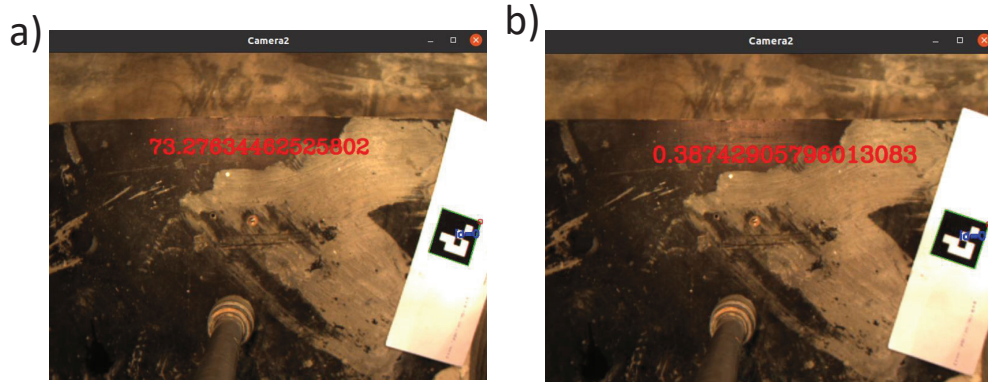


Figure 4.4: a) without undistortion step, $SSE \approx 73.3mm^2$; b) with undistortion step, $SSE \approx 0.39mm^2$

According to the assumptions given in Section 4.2.2, the nozzle moves at low velocity. In the implementation of the filament segmentation model, the sampling time (100 ms) of the cameras guarantees that no filament segments will be missed, therefore, we have a continuous record of material depositing during the process.

Since we apply a smaller RoI, a shorter segment of filament is considered in each estimation. The estimation of the overall width of a filament segment can be realized by two steps: center line extraction and image frame transformation. Firstly, we apply the morphological Media Axis Transform (MAT) on the binary mask of the filament to find the center line. Then, the distance map of the binary mask is computed by using Euclidean Distance Transform (EDT) [Maurer 2003]. As shown in Figure 4.5.a, let \mathcal{C} be the contour of the binary mask, \mathcal{D} is the binary mask and point $\mathbf{P} \in \mathcal{D}$, the value of distance map at \mathbf{P} , denoted by $DT(\mathbf{P})$, is given by:

$$DT(\mathbf{P}) = \min_{\mathbf{Q} \in \mathcal{C}} dist(\mathbf{P}, \mathbf{Q}) \quad (4.2)$$

Figure 4.5.b and 4.5.c present the distance map and the center line, respectively. The local width of the filament mask in pixels can be defined on each point on the center line \mathcal{M} of the binary mask:

$$w(\mathbf{P}) = 2DT(\mathbf{P}), \mathbf{P} \in \mathcal{M} \quad (4.3)$$

For a segment of filament, a set of local widths along its center line can be obtained. Figure 4.6 shows an example result of filament center line extraction in the image frame. It can be seen that the filament contour has an overall rectangle-like appearance, however, at the two ends ($E1$, $E2$) in green circle, the local widths along the center line don't match the actual width of the

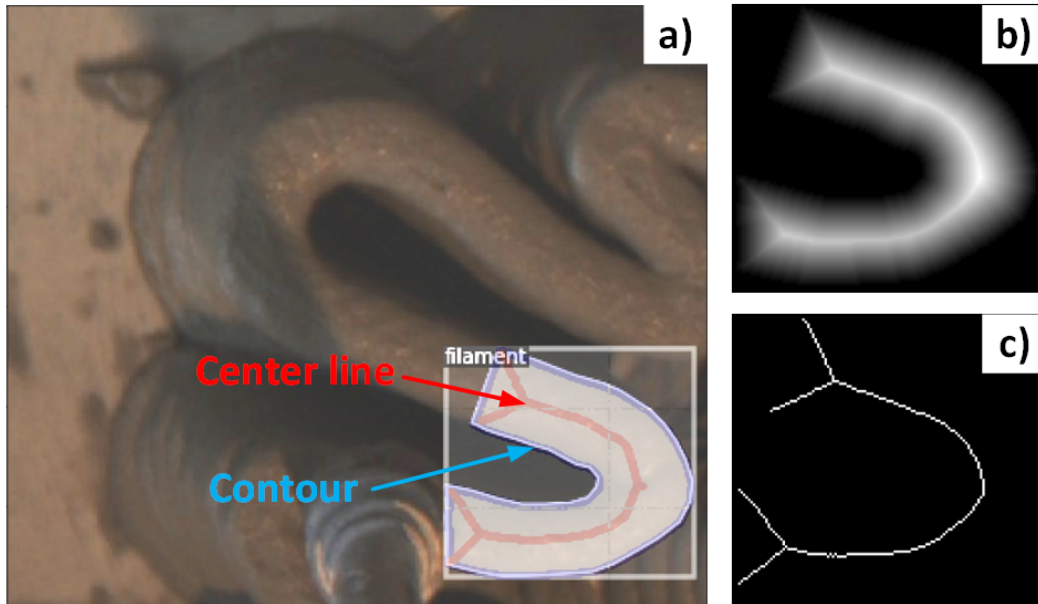


Figure 4.5: a) The contour and center line of the filament segment, extracted from the binary mask given by the instance segmentation model. b) The distance map of filament binary mask. c) The medial axis transform (MAT) of filament binary mask, defining the center line.

filament, thus, we consider only the local widths at the rest part of the center line. The distribution of local width values along the center line is calculated, as shown in Figure 4.7, the statistic mode of local width values can therefore represent the overall width value (in pixel unit) of the filament.

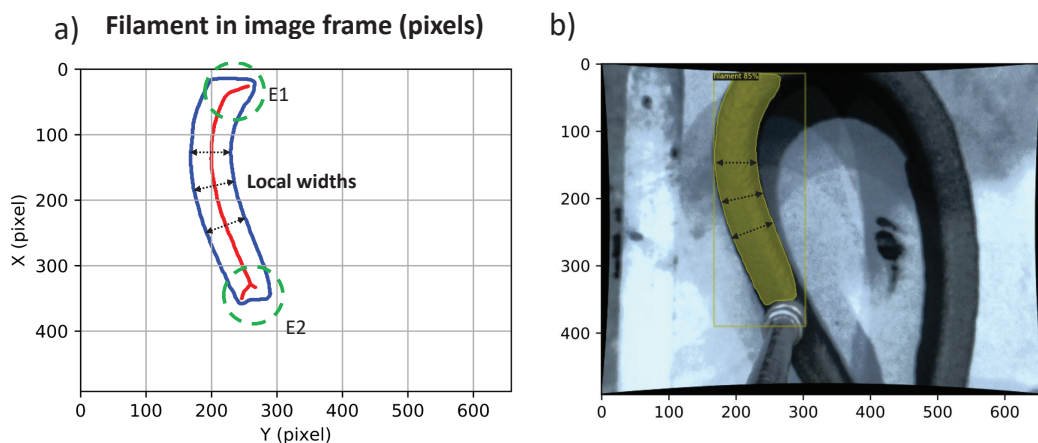


Figure 4.6: Filament center line in image frame. a). Local width values at two ends E1 and E2 should be ignored for width estimation. b). segmented filament from image captured by visual sensor.

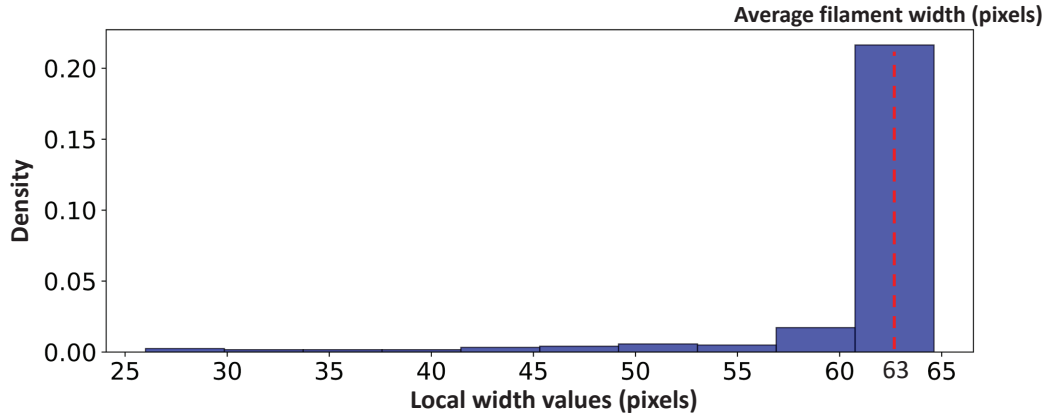


Figure 4.7: Local width value distribution (pixel unit)

When the overall width of filament is obtained in the image frame, the width in real dimension can be calculated by applying frame transformation. As the camera is fixed to the nozzle, the distance d from the lens to the freshly printed filament is fixed. The optical axis of the camera is orthogonal to the print bed, hence no rotation is considered. For a point $P_{image} = [m, n, 0]^T$ in the image frame, its coordinate $P_{world} = [x, y, z]^T$ in the world frame is given by:

$$P_{world} = R_{cam}^{-1}(M_{cam}^{-1}(d \cdot P_{image}) - Trans) \quad (4.4)$$

where:

- R_{cam} the rotation matrix of camera with respect to world frame, which can be substituted with identity matrix.
- M_{cam} the camera intrinsic matrix is obtained through camera calibration step.
- $Trans = [0, 0, d]^T$ the translation vector of camera with respect to the world frame, where d is the distance from the camera to the new filament surface.

Figure 4.8 showcases an example of the reconstruction of a filament segment in millimeters.

Figure 4.10 shows an example of result of filament segmentation and width calculation tested on a filament specimen of printed piece. The tolerance of the meter used for the measurement is $\pm 0.5\text{mm}$ with a value of 26mm (25.5 - 26.5mm), the measurement with the camera is 25.7mm i.e. a deviation of 0.3mm which represents 1.2% of the value. Measuring with the vision system gives sufficiently accurate values to ensure filament width tracking during printing. The workflow of the overall adaptive filament width estimation algorithm is shown in Figure 4.9.

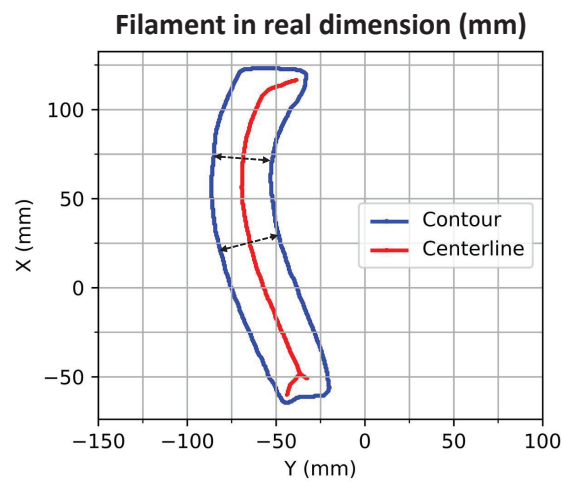


Figure 4.8: Overall filament width calculated in real dimension (35.5mm)

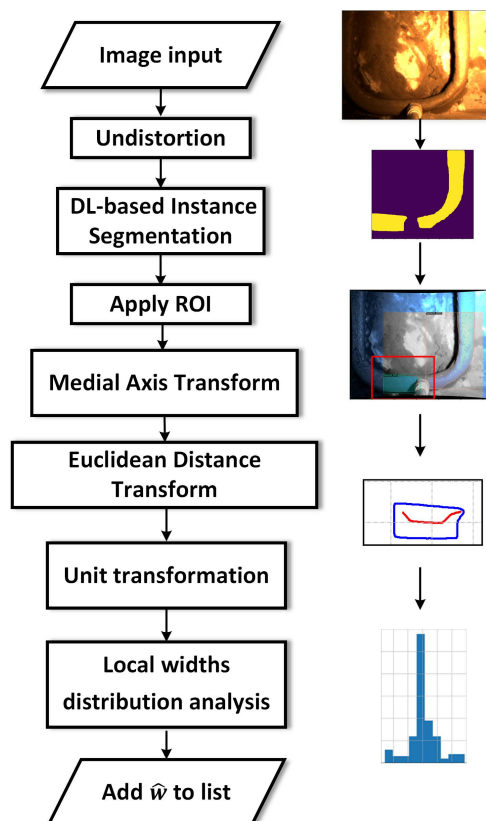


Figure 4.9: The overall workflow of filament width estimation algorithm.

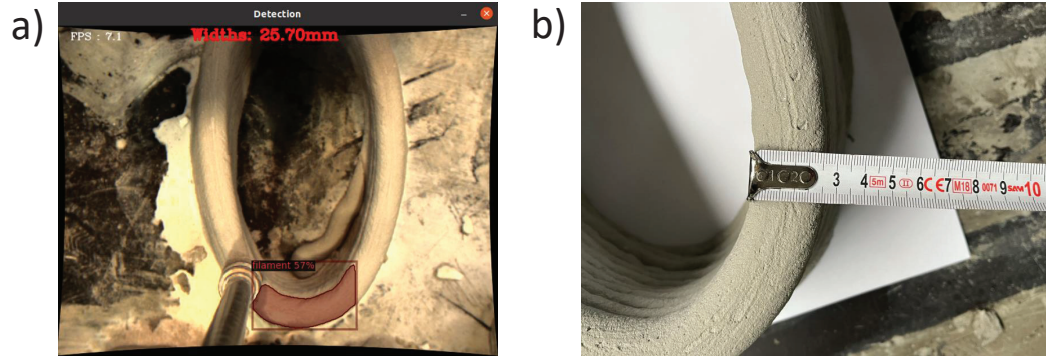


Figure 4.10: Results of an automatic filament segmentation and width calculation. a). Automatic calculated width during the printing stage: 25.7mm b). measured width in post printing stage: 26mm.

4.4 Qualitative diagnosis approach

4.4.1 Pattern recognition for system diagnosis

Pattern recognition serves as a qualitative approach for system diagnosis, particularly in systems that involve complex dynamic which makes it difficult to obtain an analytical model of the system. In this case, we can rely on data and expert knowledge on the system.

The operation mode, or status, of a system refers to the particular set of operational parameters and conditions under which it functions. These parameters could include various sensor readings, control inputs, or environmental factors that are crucial to the system's operation. In the context of a dynamic system, the system's state is often represented by a vector of measurements and observations, denoted as (x_1, x_2, \dots, x_n) . Each unique vector forms what we term an operation point, \mathcal{O} , situated in an n -dimensional feature space, \mathcal{P} :

$$\mathcal{O}(x_1, x_2, \dots, x_n) \in \mathcal{P}, \mathcal{P} \subseteq \mathbb{R}^n \quad (4.5)$$

The feature space serves as a high-dimensional landscape where each point encapsulates a specific operational scenario or condition for the system. Unfortunately, there is no systematic method for selecting the most appropriate parameters to solve a particular problem, so features can only be correctly selected if the problem to be solved is well understood.

The operation mode can be classified into different classes, including normal and various abnormal classes, each class occupies a region in the feature space. As illustrated in Figure 4.11, an operation point locates in a certain class of operation mode.

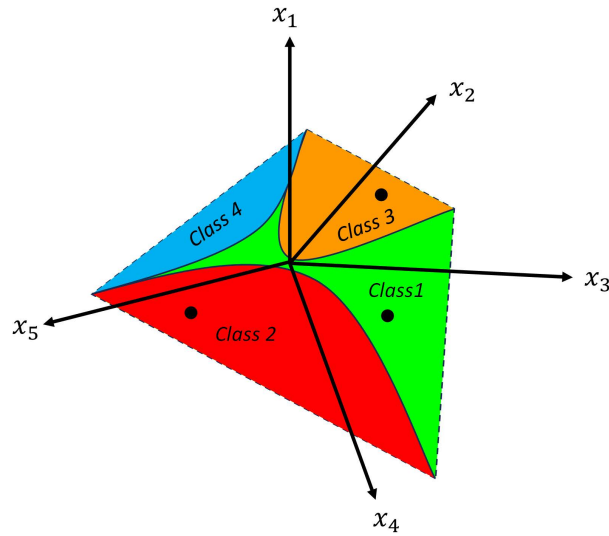


Figure 4.11: Classifications and observation points in the feature space.

The problem of determining the operation mode is therefore the problem of determining the boundaries between different classes in the feature space, so that given an operation point (the features), its classification can be determined automatically. This is crucial for the decision-making process concerning any necessary adjustments in real-time.

Various probabilistic and machine learning techniques, such as Support Vector Machines (SVM), Neural Networks, and Fuzzy Logic, can be employed for the classification task [Toscano 2005]. The choice of methodology often depends on the complexity of the feature space, the distribution of operation points, and the availability of labeled data.

In cases where data is sparse or imprecise, expert knowledge can provide invaluable insights into defining feature importance, interpreting ambiguous operation points, and fine-tuning class boundaries. Such human-in-the-loop involvement ensures a more robust and reliable diagnostic system.

4.4.2 Case study: CIRMAP printing session

In this case study, a comprehensive data set collected from multiple printing experiments serves as the basis for analyzing various operational modes ranging from normal to abnormal deposition. One critical aspect of automating the 3DCP process lies in the accurate identification of the material deposition's operational mode, as depicted in Figure 4.14. Detecting an abnormal mode is the first essential step and can be achieved through real-time filament width estimation given in the previous section. The subsequent crucial step is

the isolation of the abnormal mode to identify the specific parameter causing the anomaly, which could include variables like material flow rate and nozzle velocity. From a qualitative perspective, we utilized a pattern recognition-based approach for diagnosing the operational modes during the in-printing stage. This methodology is data-driven, drawing from an extensive set of experimental data to populate the feature space. The distribution of operation points within this space serves as a diagnostic tool, enabling us to isolate abnormal conditions effectively. This distribution also informs the selection of parameters for adjustments, thus facilitating compensation actions when deviations are observed.

4.4.2.1 Feature selection and classification based on Support Vector Machine (SVM)

- **Features**

To track the material deposition quality, as discussed before, the filament width is adopted as an evaluation criterion: given a specific desired filament width value w^d , the real width w is expected to closely match the desired width. Based on this expectation, we identify three classifications of operation modes, as shown in Figure 4.12. The Normal class is defined by scenarios where the actual filament width aligns with the desired value w^d . Conversely, Abnormal 1 denotes cases where the filament width exceeds w^d , resulting in over-deposition, while Abnormal 2 denotes cases of under-deposition, where the filament width falls below w^d .

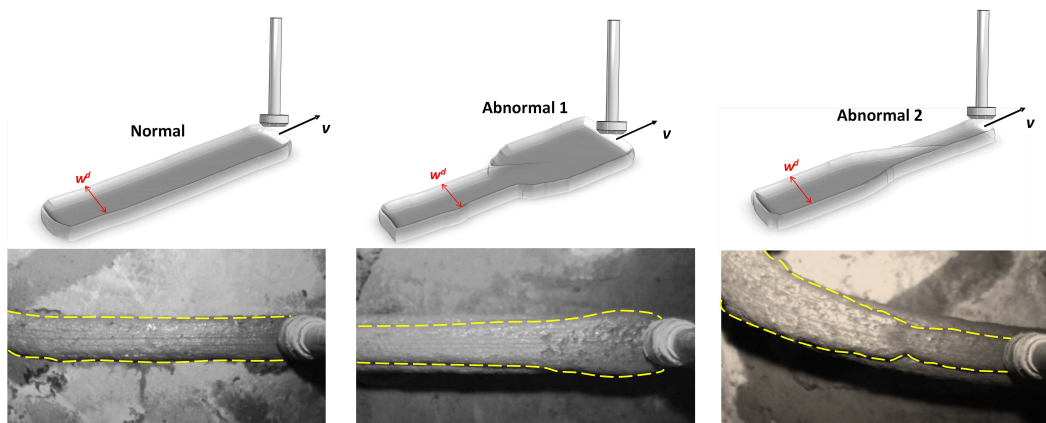


Figure 4.12: Continuous deposition operation points can be categorized into three classes. **Normal:** $w = w^d$; **Abnormal 1:** $w > w^d$; **Abnormal 2:** $w < w^d$.

Among the five parameters (Q, U, w, h, v) , three are selected to form a

three-dimensional feature space, as illustrated in Figure 4.13. During the in-printing stage, an operation point $\mathcal{O}' = (U, v, Q)$ in the feature space $\mathcal{P}' \subseteq \mathbb{R}^3$ is considered:

$$\mathcal{P}' = \{(U, v, Q) \in \mathbb{R}^3 : U_{\min} \leq U \leq U_{\max}, \quad v_{\min} \leq v \leq v_{\max}, \quad Q_{\min} \leq Q \leq Q_{\max}\} \quad (4.6)$$

where U, v, Q are limited within their minimum and maximum allowable values.

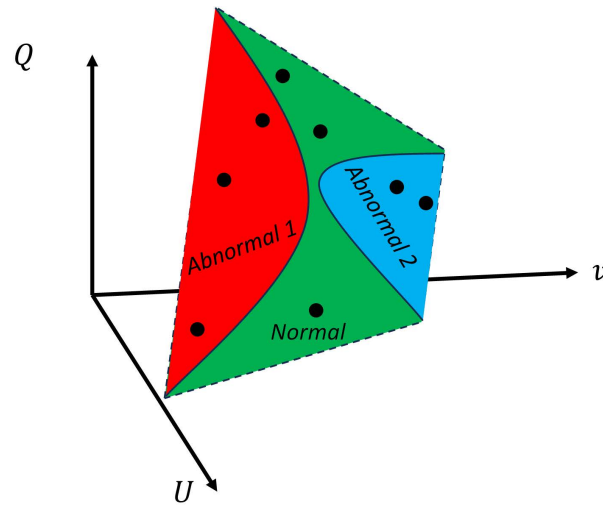


Figure 4.13: Three considered classes in the feature space formed by U , v , and Q .

In the complex system of 3DCP, understanding the behavior and relationships between variables is crucial. The choice of U , v and Q as features for pattern recognition is guided by their direct influence on the filament width w . These features are not only easy to measure but also include the controllable parameters (U, v) that can be adjusted in real-time to maintain print quality. Furthermore, focusing on these three parameters facilitates data visualization in a three-dimensional feature space \mathcal{P}' , offering an intuitive understanding of how these variables collectively contribute to different operational modes—Normal, Abnormal 1, and Abnormal 2. This visual perspective is instrumental in providing insights into the feature space and its relation to different classes, thereby aiding in more informed decision-making for real-time control and fault diagnosis.

Figure 4.14 illustrates the schematic framework for operational mode diagnosis within the 3D concrete printing process, based on pattern recognition

techniques. Subsequent to the real-time estimation of filament width, the focus shifts to pattern recognition for classifying distinct operational modes. Specifically, this involves learning the characteristic patterns associated with different classes of operational modes within the multi-dimensional feature space. This step is essential for the accurate diagnosis and isolation of both normal and abnormal operational states.

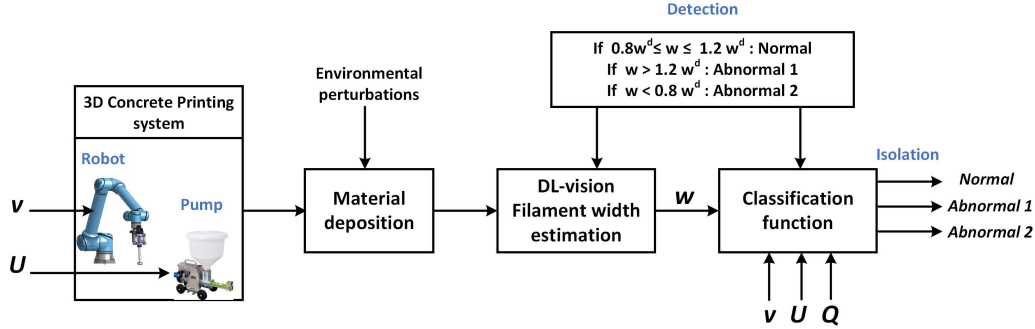


Figure 4.14: Qualitative diagnosis based on pattern recognition techniques.

- **Classification based on SVM**

To learn the boundaries between different classes of operation points in the feature space, we consider **Support Vector Machine (SVM)** approach. It has good performance in classification tasks, and is especially well suited for complex but smaller-sized or medium sized dataset[Bishop 2006]. The standard SVM deals with binary classification problem, as we have three features (U, v, Q), the training of the SVM classifier in our case follows the One-vs-One strategy, where an SVM is trained for every pair of classes, resulting in SVM models for a three-class problem (Normal vs Abnormal1, Normal vs Abnormal2, Abnormal1 vs Abnormal2).

For each pair of classes i and j , an SVM is trained. The decision function $f_{ij}(\mathbf{x})$ for each pair is:

$$f_{ij}(\mathbf{x}) = \mathbf{w}_{ij} \cdot \mathbf{x} + b_{ij} \tag{4.7}$$

where \mathbf{x} is the feature vector (U, v, Q) and \mathbf{w}_{ij} the normal vector of the hyperplane that separates the two classes in feature space.

The class that gets selected most often across all pairs is the predicted class:

$$\text{Predicted Class} = \arg \max_i \sum_j \mathbb{I}[f_{ij}(\mathbf{x}) > 0] \tag{4.8}$$

Here, \mathbb{I} is the indicator function, which is 1 if the condition inside is true and 0 otherwise. The optimization problem for each pair-wise SVM ij is:

$$\text{Minimize } f_{ij}(\mathbf{x}) = \frac{1}{2} \|\mathbf{w}_{ij}\|^2 \quad (4.9)$$

subject to:

$$y_{ij,k}(\mathbf{w}_{ij} \cdot \mathbf{x}_k + b_{ij}) \geq 1, \quad \forall k \quad (4.10)$$

Finally, three sets of classification models are trained, each model is trained based on a 3D printing dataset collected under a specific environmental condition (10, 20, 30 °C), therefore, each model account for the classification task under a specific temperature. The details of data collection and environment setting is given by the following sections.

4.4.2.2 Environmental condition and shape

The experiments were conducted within the climate chamber, as detailed in Chapter 3. The temperature settings are 10 °C, 20 °C and 30 °C, humidity setting is 50%. These settings were selected to cover the primary outdoor temperature conditions encountered in Lille throughout the year based on average monthly temperatures (7 °C in January and 25 °C in August in 2022).

The shapes selected for experimentation include a rounded rectangle, an ellipse, and a shape with zigzag features. The rounded rectangle serves as a benchmark for simple geometries, offering a mix of straight lines and smooth curves. This shape allows a constant velocity along each layer since its curvature doesn't exceeds the maximum allowed limit for a constant velocity (refer to Chapter 2).

The ellipse presents a continuous curvature towards more complex contours, therefore, given a constant reference velocity, this shape allows for a continuous change of curvature along each layer.

The zigzag shape exhibits sudden directional changes, reflecting conditions where intricate detailing or structural complexity might be required, this shape represents the case of non continuous velocity change at corners given a constant reference velocity.

The desired width of the material filament is set at $w^d = 3$ cm. The shape designs, layer numbers, environmental conditions as well as the estimated material volume (with 3 cm filament) are summarized in Figure 4.15. A threshold of 20% of w^d is used to decide normal and abnormal classes.

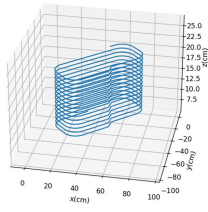
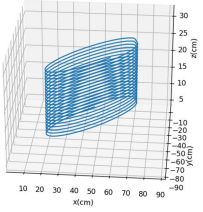
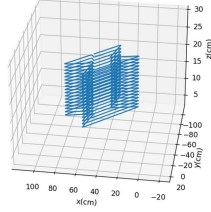
Shape			
Layers	20	20	20
Material volume (cm ³)	10300	10000	11000
Temperature Humidity	10 °C, 20 °C, 30°C 50%	10 °C, 20 °C, 30°C 50%	10 °C, 20 °C, 30°C 50%

Figure 4.15: Shape designs for printing test under different environments.

4.4.2.3 Data preparation

In order to collect a dataset containing all three classes of operation scenarios, the two controllable parameters of the printing system, the pump voltage U and the nozzle velocity v are adjusted to induce varying filament widths. By manipulating these parameters, we aim to simulate a range of operational scenarios that would produce a representative dataset facilitating diagnostic analysis. For achieving a realistic and practical data set, limitations on the feature ranges are imposed during the printing sessions to exclude extreme or impractical conditions. Specifically, the pump voltage U is varied within the range of 0.1 V to 5 V, and the nozzle velocity v is constrained between 3 cm/s and 20 cm/s. These bounds reflect real-world operating constraints. The data has been pre-processed by filtering and resampling for noise reduction and synchronization. Finally, the dataset contains 27000 operation points: 9000 points for each temperature.

Figure 4.16 illustrates a point cloud representing the distribution of operational points at 20 °C. The point cloud reveals distinct patterns based on velocity: the Abnormal 1 category predominantly occupies the lower velocity region of the feature space, whereas Abnormal 2 is concentrated in the higher velocity range. Despite these trends, a substantial number of points are dispersed throughout the space.

In the Figure 4.16 representation, we can observe three distinct points within the same range, indicating that they share identical parameters of temperature, velocity, flow rate, and pump control voltage. These points cor-

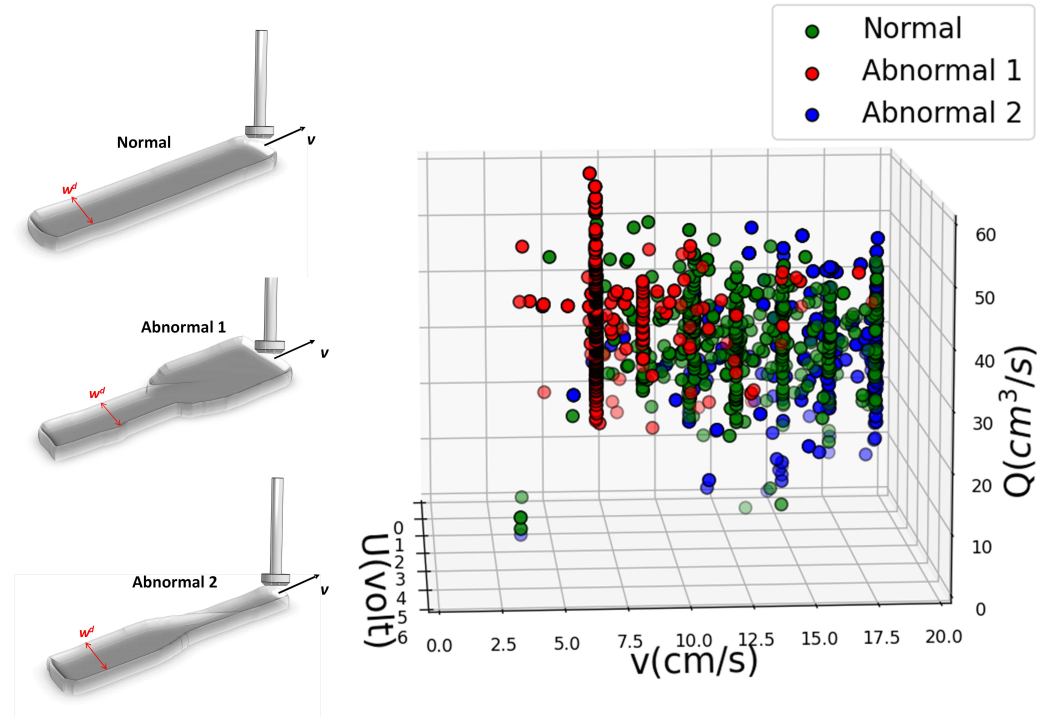


Figure 4.16: Cloud of operation points under 20°C.

respond, respectively, to a Normal condition, Abnormal 1, and Abnormal 2. It's essential to note that this figure does not account for several other phenomena, such as layer thickness, which we assume to be constant. Nevertheless, even a slight variation in the thickness of the initial layer can lead to a shift in layer height, altering the material extrusion configuration and resulting in more or less compressed layer widths. To mitigate this phenomenon, in the following section, we exclusively focus on layers where their height remains constant throughout the material deposition process.

4.4.3 Results and discussion

The three SVM classification models have been trained and tested on historical data under the three corresponding temperatures. The distributions of classified operation points in the (U, v, Q) feature space under three temperatures are demonstrated in Figure 4.17, 4.18 and 4.19 respectively.

- **Operation points of 3 classes under the same temperature**

For results under three temperatures, a similar distribution rule can be observed. A distinct concentration of operation points distribution is evident along the axis representing nozzle velocity. Specifically, the majority of the

Table 4.2: Range of features: Normal

Temperature	v (cm/s)	U (volt)	Q (cm ³ /s)
10 °C	7 – 17	0.5–2	15 – 55
20 °C	7 – 17	0.5–2	20 – 50
30 °C	7–12.5	0.5–2	20 – 45

Table 4.3: Range of features: Abnormal 1 (over deposition)

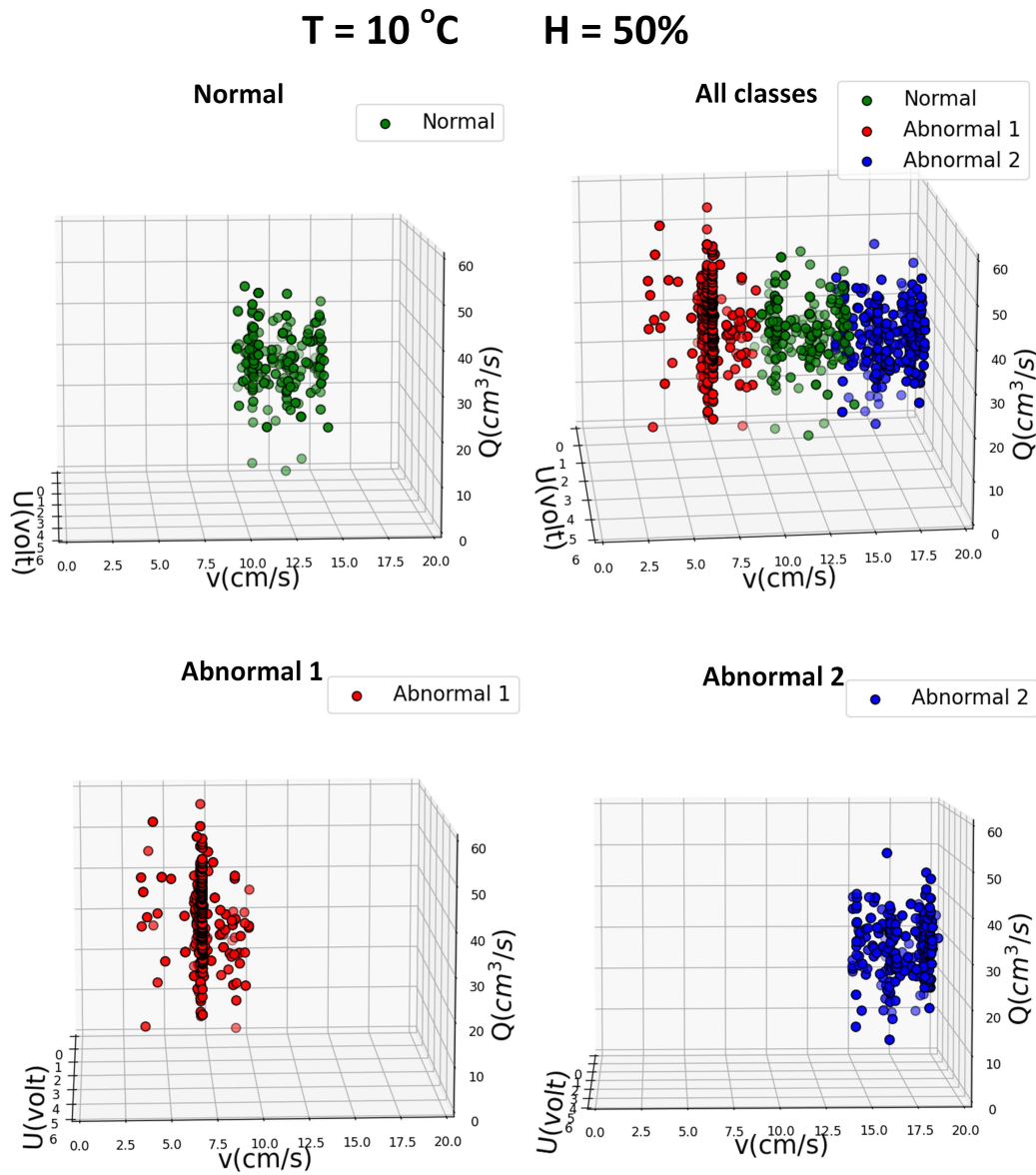
Temperature	v (cm/s)	U (volt)	Q (cm ³ /s)
10 °C	5 – 7	0.5–2	10 – 60
20 °C	5 – 7	0.5–2	20 – 60
30 °C	5 – 7	0.5–2	20 – 45

Table 4.4: Range of features: Abnormal 2 (under deposition)

Temperature	v (cm/s)	U (volt)	Q (cm ³ /s)
10 °C	17 – 20	0.5–2	10 – 40
20 °C	17 – 20	0.5–2	15 – 40
30 °C	12.5 – 20	0.5–2	20 – 45

points representing normal operation are found within the velocity range of $10 \text{ cm/s} \leq v \leq 15 \text{ cm/s}$. The concentration in this region reflects the usual choice of nozzle velocity in most practical scenarios. In contrast, operation points for the two abnormal classes (Abnormal 1 and Abnormal 2) are observed to deviate towards the extremes of the velocity axis. This distribution suggests that the likelihood of over-deposition (Abnormal 1) increases when velocity decreases to the range of $5 \text{ cm/s} \leq v \leq 10 \text{ cm/s}$, while under-deposition (Abnormal 2) becomes more probable when velocity increases to $15 \text{ cm/s} \leq v \leq 20 \text{ cm/s}$. This observation aligns with the physical intuition that at lower velocities, the material has more time to flow out, leading to over-deposition. Conversely, at higher velocities, the material has less time to flow, resulting in under-deposition. Therefore, to facilitate the classification, we establish velocity-based thresholds. Specifically, we consider the three velocity ranges: $5 \text{ cm/s} \leq v \leq 10 \text{ cm/s}$, $10 \text{ cm/s} \leq v \leq 15 \text{ cm/s}$, $15 \text{ cm/s} \leq v \leq 20 \text{ cm/s}$. These ranges are designed to segregate the operational points into categories that facilitate more nuanced analysis and control.

Regarding flow rate variations, it is observed that, for 10 °C and 20 °C, within the same temperature condition, the Abnormal 1 points reach to a higher flow rate compared to Abnormal 2. This observation confirms the understanding that higher flow rates are likely to produce over-deposition.

Figure 4.17: Classification of operating points under $T = 10\text{ }^{\circ}\text{C}$, $H = 50\%$.

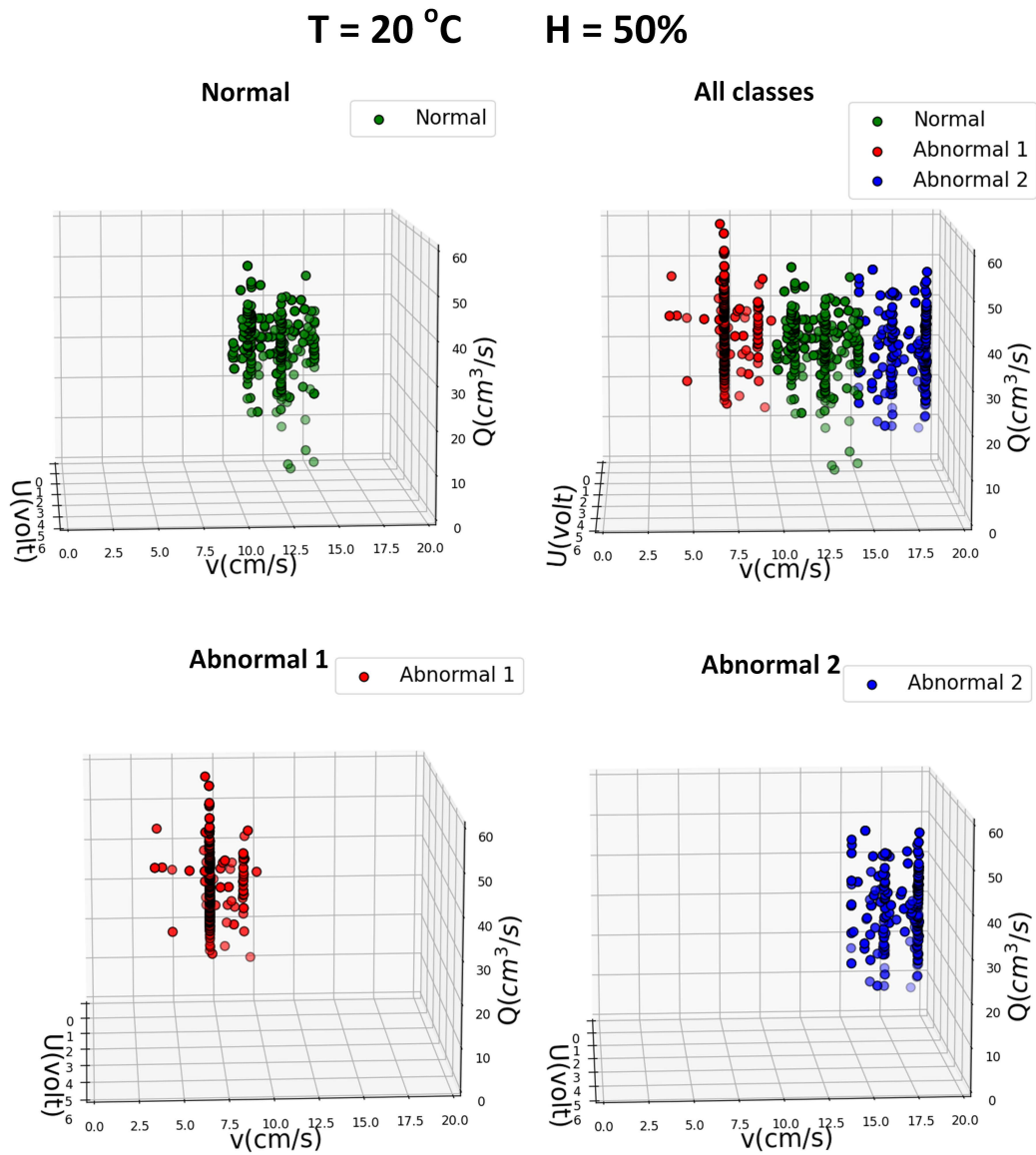
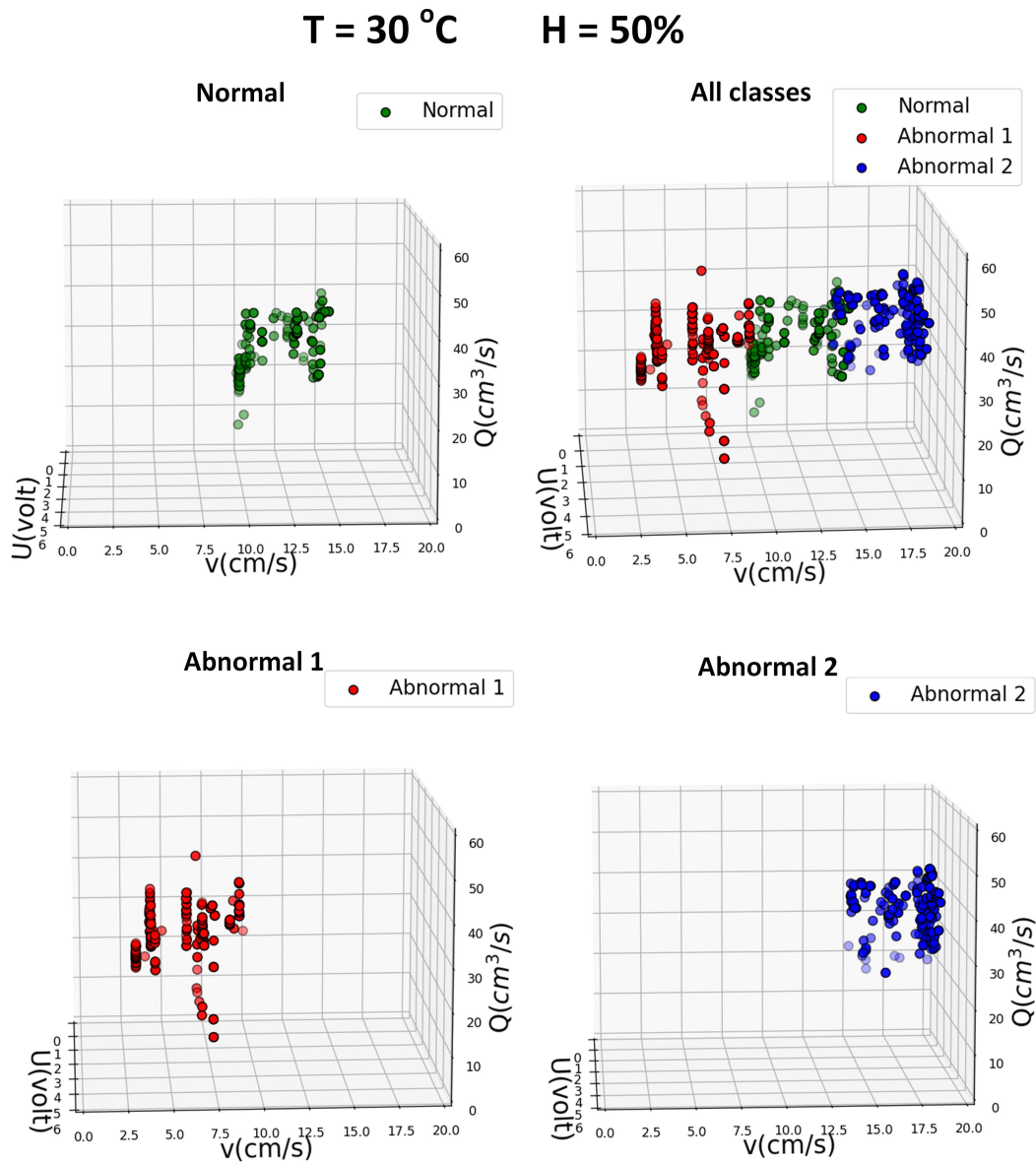


Figure 4.18: Classification of operating points under $T = 20 \text{ }^\circ\text{C}$, $H = 50\%$.

Figure 4.19: Classification of operating points under $T = 30\text{ }^{\circ}\text{C}$, $H = 50\%$.

The same is not observed under 30 °C, this could be attributed to the interplay of temperature with material properties and the pumping system. Also, at 30 °C, there's a higher likelihood to observe Abnormal 2 than Abnormal 1 . In fact, at elevated temperatures, the material viscosity may increase, leading to altered flow dynamics through the nozzle.

In general, operation points corresponding to normal conditions are predominantly located in the central region of the feature space, they exhibit median flow rates ($25 \text{ cm}^3/\text{s} \leq Q \leq 45 \text{ cm}^3/\text{s}$) and velocities ($7 \text{ cm/s} \leq v \leq 15 \text{ cm/s}$). If an operation point exhibits higher velocity coupled with a lower flow rate, it leans towards classification as Abnormal 2. Conversely, if it exhibits lower velocity and a higher flow rate, it leans towards Abnormal 1.

For a given flow rate range, the concentration distributions of all three classes tends to locate within three distinct ranges along the velocity axis. The transition between classes appears to be more sensitive to changes in nozzle velocity than to variations in flow rate. This phenomenon can be especially observed in Abnormal 1 that covers wide range of flow rate. This could suggest that nozzle velocity is a more critical feature in influencing the deposition quality under the examined conditions.

- **Operation points of each class under 3 temperatures**

The distributions of operation points for each class under temperatures of 10, 20 and 30 °C are shown in Figure 4.20, 4.21 and 4.22. For all three classes, it can be observed that compared to 10 and 20 °C, the variation of flow rate Q in 30 °C falls within a smaller range. Indeed, a higher environment temperature accelerates the hydration process of the fresh concrete material, therefore making it more viscous and subsequently increase its resistance to flow.

For normal class, the distribution region of normal operation under 30 °C is relatively more constrained compared to 10 and 20 °C. This indicates that the system's optimal working envelope is reduced at elevated temperatures, thereby making the 3D printing tasks more challenging in such conditions. Again, the constrained region may be attributed to the increased viscosity of the concrete material at higher temperatures, which impacts the flowability and deposition quality.

The number and density of operation points associated with Abnormal 1 class increases as temperature decreases. This suggests that within the range of 10 °C to 30 °C, the risk of over-deposition actually decreases as the temperature rises, because increased viscosity reduces its tendency to spread excessively, which consequently minimizes the occurrence of over-deposition.

It can be concluded that among the three studied temperatures, 20 °C appears to be the most suitable temperature for stable printing, which conforms

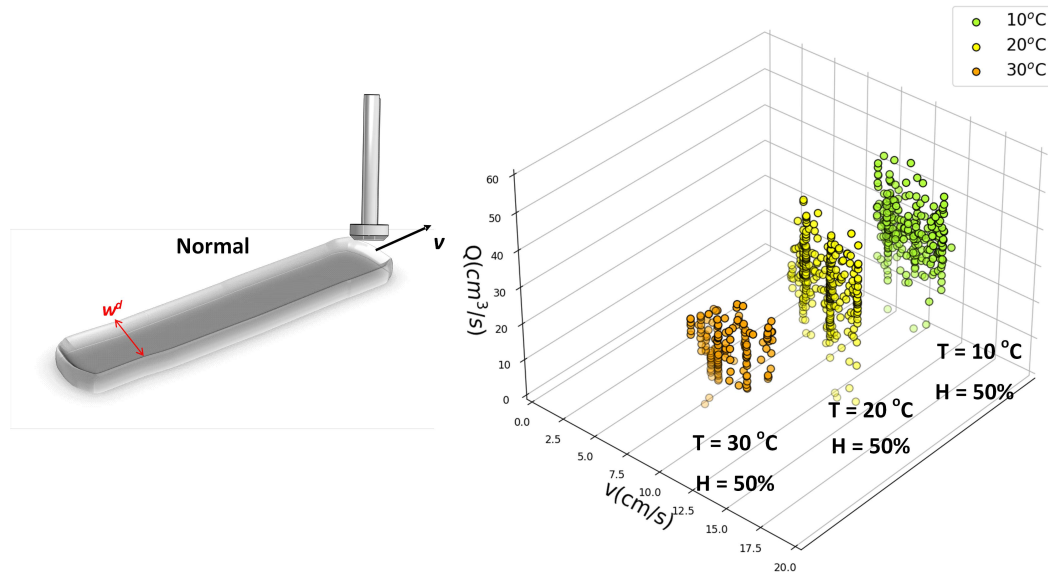


Figure 4.20: Operation points of Normal class under three temperatures.

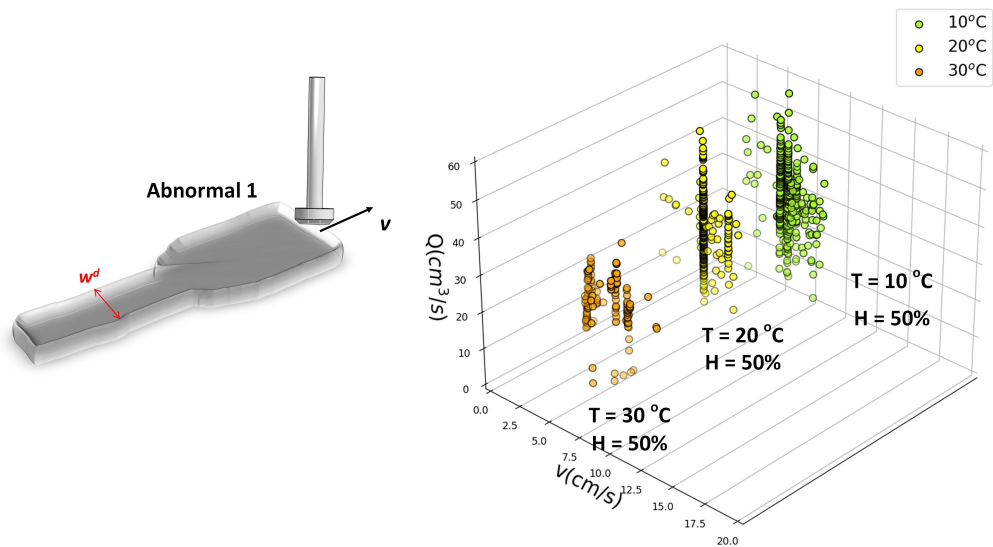


Figure 4.21: Operation points of Abnormal 1 class under three temperatures.

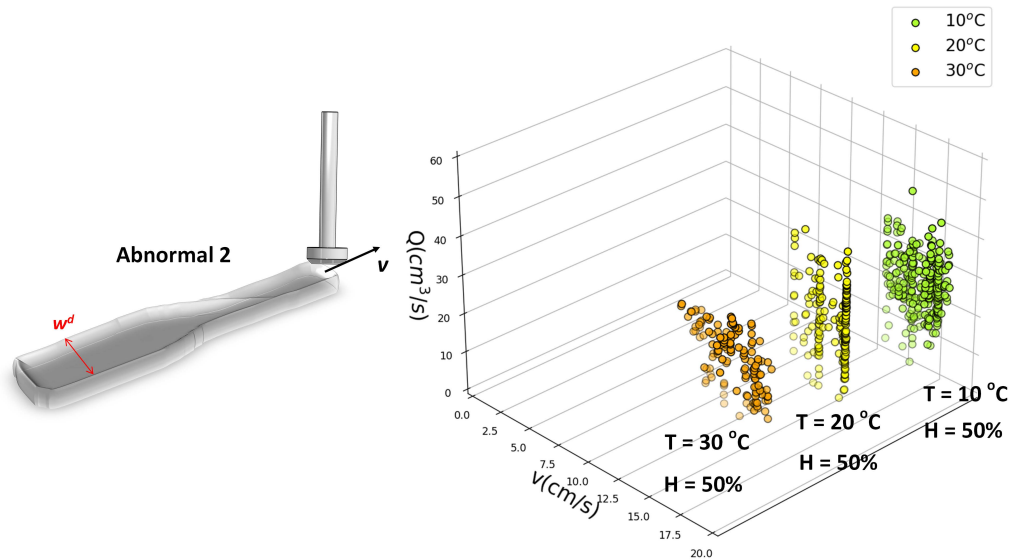


Figure 4.22: Operation points of Abnormal 2 class under three temperatures.

to practical experiences. Under low temperatures like 10 °C the material exhibits enhanced flowability, thereby increasing the flexibility in transition between different operational modes and contributing to higher occurrences of over deposition, particularly when operating at reduced velocities. Conversely, elevated temperatures like 30 °C make the material more viscous, thereby increasing pumping resistance and leading to a higher occurrence for under-deposition.

These observations underline the intricate relationship between material properties and environmental factors like temperature. They also signal that temperature can act as a modulating variable that alters the likelihood of encountering specific operational anomalies, such as over or under-deposition. This multi-variable complexity underscores the need for automated process control when 3D printing in uncontrolled environments. Specifically, in the event of an operational anomaly, the system should be capable of executing rapid and robust compensatory actions to maintain print quality.

Due to this complex correlation between the environment and the material property, it becomes imperative for a data-driven approach to go beyond system parameters. For a more generalized and accurate classification of operational modes, environmental variables such as temperature must be incorporated into the feature space

4.5 Quantitative Diagnosis approach

In Section 4.4, we focus on the classification of operational modes by identifying the boundaries that demarcate different classes within the feature space using pattern recognition for symptoms generation. In this section, we want to identify the symptoms of the system from multi-signal analysis of residuals using quantitative diagnosis approach. Thus, diagnosis based on Analytical Redundancy is a technique used in control engineering and control theory to detect and isolate faults or anomalies in a monolithic dynamic system¹. It relies on redundancy in sensor measurements and redundancy in system models to perform diagnostics. Analytical Redundancy uses mathematical models that describe the relationship between different system variables. These models are based on physics, engineering principles, or empirical data. The models predict the expected behavior of the system under normal operating conditions. **In the framework of the thesis work, the interest is not to diagnosis faults on dynamic systems such as the printing robot or the pump or the pipe, but the quality of the deposited filament of cement-based material [Yang 2023a].** The mathematical models can be interpreted as an Analytical Redundant Relation (ARR) and expressed through a set of functions or inequalities, denoted as \mathcal{F} , in case of faulty feature, as follows

$$\begin{cases} \text{ARR}_{normal} : \mathcal{F}(x_1, x_2, \dots, x_n) = 0 \\ \text{ARR}_{faulty} : \mathcal{F}(x_1, x_2, \dots, x_n) \neq 0 \end{cases} \quad (4.11)$$

4.5.1 Diagnosis based on Analytical Redundancy

FDI based on ARR aims to identify and isolate anomalies, malfunctions or irregularities within complex systems. In general, FDI is a two-stage process. The first stage, fault detection, concerns monitoring system variables and performance metrics to detect deviations from the expected behavior. The second stage, fault isolation, is executed once a fault has been detected. It aims to identify the specific component or subsystem within the complex system where the fault has occurred.

- **Fault detection**

¹A monolithic dynamic system refers to a single, integrated entity in which all components or elements work together as a unified whole to achieve a specific objective.

The fault detection stage usually involves two steps: residual generation and decision making. As mentioned before, the ARR is a mathematical model that describes the expected behavior of the system under normal operating conditions. It is formulated based on the system’s physical laws, empirical relationships, or data-driven models. In essence, the ARR serves as a reference model against which the real-time behavior of the system can be compared.

A residual signal $\mathbf{r}(t)$ is generated by evaluating the difference between measured or observed system behavior and the behavior predicted by the ARR:

$$\mathbf{r}(t) = \mathbf{y}_{measured}(t) - \mathbf{y}_{predicted}(t) \quad (4.12)$$

After the residual is detected, detection thresholds is determined to compare with residual signal, a fault is detected if:

$$\|\mathbf{r}(t)\| > \text{Threshold} \quad (4.13)$$

- **Fault isolation**

Once a fault is detected through a residual signal that crosses a pre-determined threshold, the next step is to identify which parameter of the system is responsible for the fault. This is crucial for the system reconfiguration. One of the common methods for fault isolation is to use a **Fault Signature Matrix (FSM)**, which is a binary matrix that indicates which residuals are sensitive to which faults. In a system with m residuals and n faults, the **FSM** will be an $m \times n$ matrix,

$$F = \begin{pmatrix} f_{11} & f_{12} & \dots & f_{1n} \\ f_{21} & f_{22} & \dots & f_{2n} \\ \vdots & \vdots & \ddots & \vdots \\ f_{m1} & f_{m2} & \dots & f_{mn} \end{pmatrix} \quad (4.14)$$

For each element f_{ij} , $f_{ij} = 1$ means that the i^{th} residual is sensitive to the j^{th} fault. When a fault occurs, it will cause certain residuals to become non-zero. By examining the pattern of affected residuals and consulting the **FSM**, it is possible to isolate which fault(s) have occurred.

4.5.2 Case study: CIRMAP printing session

We apply **FDI** methodology as a quantitative approach in the case of CIRMAP printing tasks. In this work, we extend the traditional definition of “system fault” to encompass the deformations observed in the material filament during

3D printing. Specifically, we treat these deformations as “fault-like” behaviors, manifesting as geometric deviations rather than physical malfunctions or breakdowns in the system.

- **Empirical redundancy relation** : ARR_1

An empirical linear model linking material flow rate Q to pump voltage command U was derived from large amount of experimental data gathered during printing processes using materials with the same mixing proportions.

In this system, the control of the pumping speed in an open-loop manner is achieved by means of voltage control. As shown in Figure 4.23, when a constant voltage control is applied to the pump, the accumulated material volume $\int Q(t)dt$ shows a quasi-linear relationship over time.

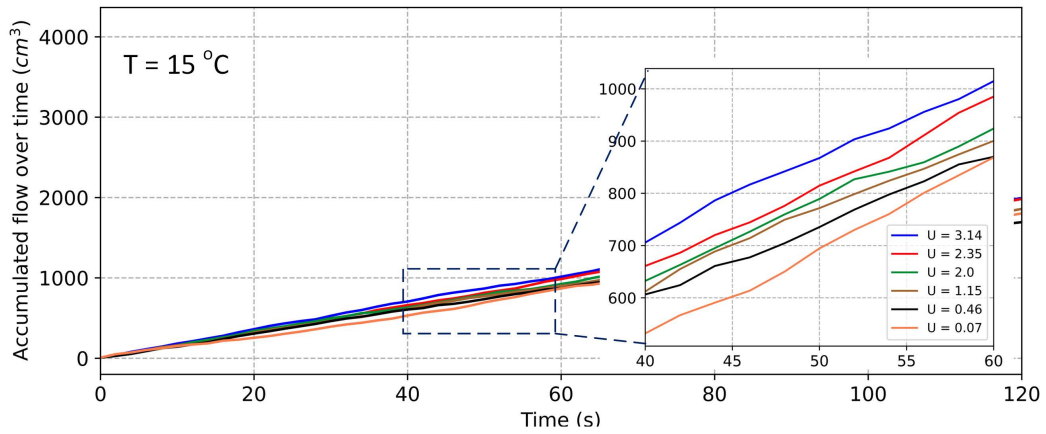


Figure 4.23: Accumulative flow (cm^3/s) under $T = 15^\circ\text{C}$ given different pump voltage control during the pumping of a same batch of material fresh mixture.

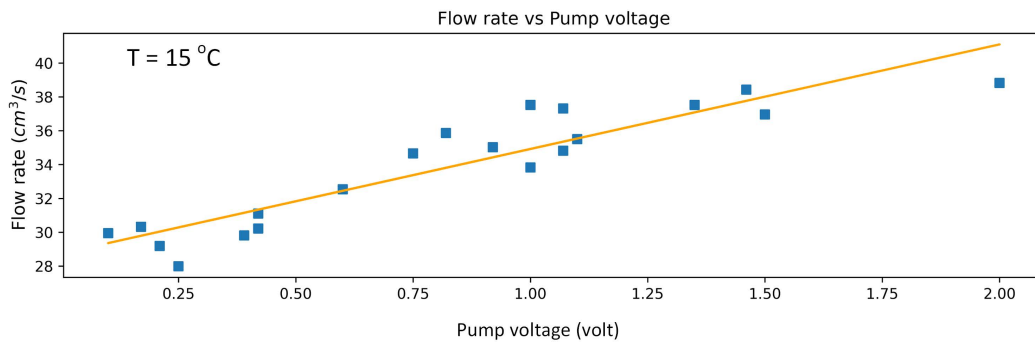


Figure 4.24: The flow rate Q and the pump voltage command conform to a linear relation under constant temperature $T = 15^\circ\text{C}$.

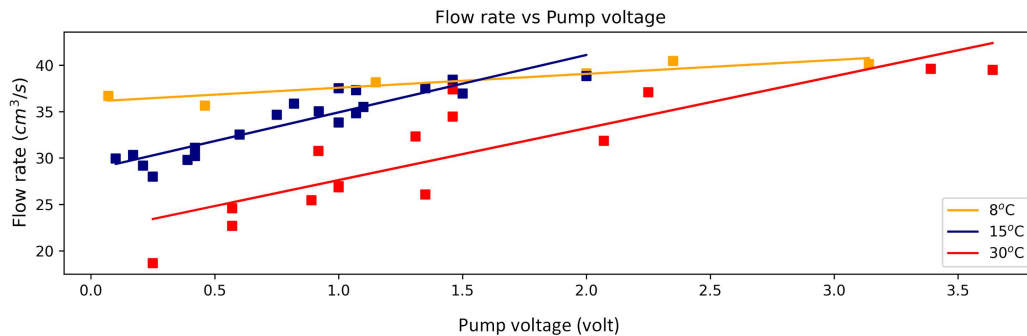


Figure 4.25: The flow rate Q and the pump voltage in different temperatures.

Furthermore, a linear relation between the pump voltage control U and the flow rate Q can be observed (Figure 4.24 and 4.25). This conforms to the assumption that a linear correlation exists between the voltage control and the pump rotation speed, and the used pump operates on a volumetric principle, whereby the flow rate in steady state should be directly proportional to the rotation speed of the pump.

As previously discussed, the pump employed in this research is a volumetric type, designed to transfer a fixed volume of fluid per pumping cycle. The rate of this pumping is governed by the applied voltage. Consequently, a theoretical linear relationship is posited between the pump voltage and the material flow rate. This relationship has been empirically confirmed, as evidenced in Figure 4.25, where printing sessions conducted under various environmental conditions have demonstrated its validity, particularly when a continuous material flow rate is achieved.

In practical 3DCP applications, the pump voltage is limited within a specific range during printing operations (typically between 1 to 4 volts). This linear correlation between voltage and flow rate is especially reliable when a steady flow of material is maintained, as observed during the printing stage. Prior to each printing session, this linear relationship is calibrated experimentally, involving extruding materials at different pump voltages to establish a baseline that represents the ideal flow behavior of the material under the initial environmental conditions.

Figure 4.25 show that the linear relation between the pump voltage and the flow rate changes with temperature. This change can be attributed to the influence of temperature on the rheological properties of fresh concrete [Link 2020], specifically its shear stress and kinematic viscosity. Indeed, elevated temperatures tend to accelerate the hydration process, thus altering the material's internal microstructure and increasing its viscosity. Conversely, lower temperatures slow down hydration, resulting in a more fluidic state for

the material. These temperature-induced changes in viscosity consequently affect the shear stress required to initiate flow and the material's resistance against flow, thereby modifying the the Q vs. U relationship. Subsequently, the change in material viscosity can be reflected by the deviation of its actual behavior from the learned expected behavior.

Therefore, for each print test, a data-driven linear relation between Q and U can be established by applying the ordinary least squares regression (OLSR). The following linear model is considered:

$$\hat{Q}(U) = \hat{\beta}_0 + \hat{\beta}_1 U \quad (4.15)$$

The intercept and slope (β_0, β_1) in Eq.(4.15) are determined by minimizing the mean squared error loss:

$$Loss_{MSE} = \frac{1}{n} \sum_{i=1}^n (Q_i - \hat{Q}_i(U_i))^2 = \sum_{i=1}^n (Q_i - \hat{\beta}_0 - \hat{\beta}_1 U_i)^2 \quad (4.16)$$

where \hat{Q}_i is the estimated flow rate value based on the voltage command U_i . Figure 4.26 shows the estimation of flow rate \hat{Q} based on U , the measured flow rate Q and the estimation error.

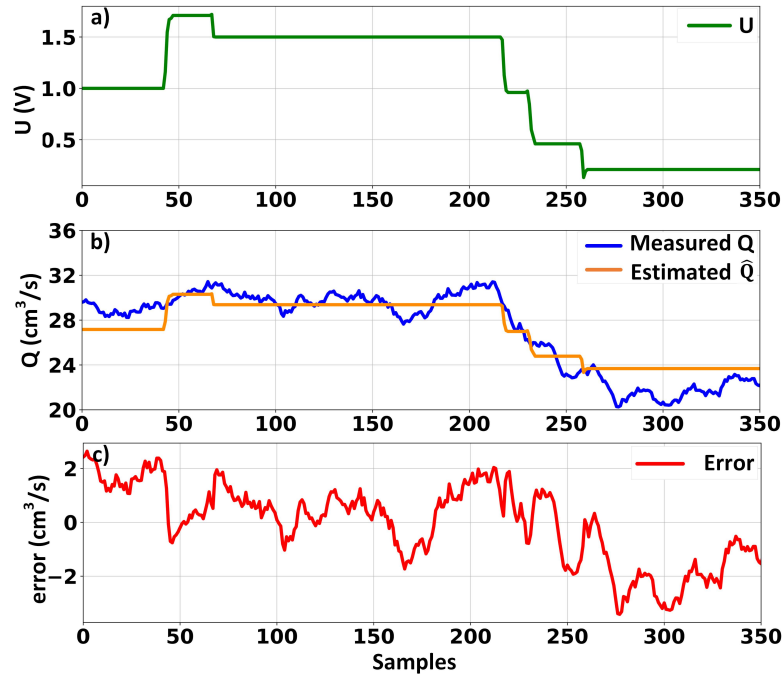


Figure 4.26: a) Pump voltage command U ; b) Estimated flow rate \hat{Q} based on U and measured flow rate Q ; c) Estimation error.

The fresh concrete mix is a non-Newtonian fluid which exhibits specific rheological properties. This means its flow behavior doesn't follow the linear relationship between shear stress and shear rate that's characteristic of Newtonian fluids (like water or oil). In particular, its viscosity changes under different shear stress levels during pumping. The error observed in Figure 4.26 is due to the thixotropic behavior of the concrete [Jiao 2021]. The pumping velocity is reduced from the 200th sample due to lower voltage command (around 0.3 volts), consequently, the material initially exhibits increased viscosity under lower shear stress, leading to an increase in resistance (internal friction) to flow. Notably, this is a reversible process. If the lower pumping velocity is maintained, the concrete will reach a new equilibrium state under this new condition, and the error will be smaller, as can be observed in the last 50 samples.

- **Analytical redundancy relation: ARR_2**

In the literature, a classic geometric model of the freshly printed filament is widely considered [Anton 2021, Yuan 2022]. During normal operation of the printing system, the filament is considered to be of a rectangular cuboid shape. We adopt this model to develop an analytical redundancy relation. According to the assumptions, the geometry of the freshly printed filament segment during a normal printing process can be modeled as shown in Figure 4.27.

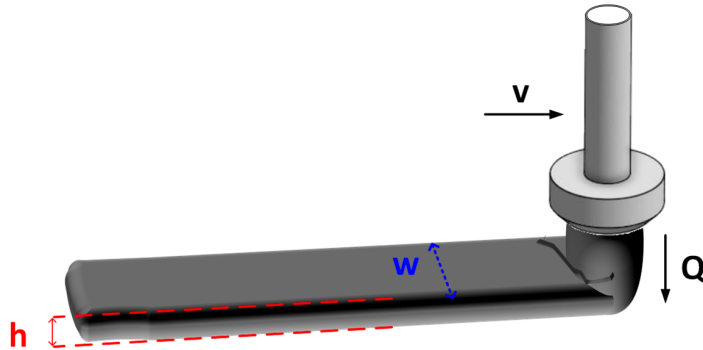


Figure 4.27: Geometric model of material deposit filament during a normal printing process.

Hence, the following relation of the material flow Q can be obtained:

$$ARR_2 : Q - whv = 0 \tag{4.17}$$

where: w represents the width of the filament, h the height of the filament and v the nozzle velocity.

In the context of this thesis, a key assumption is made regarding the height h (i.e., the thickness) of each deposited filament: it is considered to be constant and equivalent to the designed layer height, or the nozzle lift height, as outlined in [Zhang 2023]. This assumption is predicated on a well-acknowledged characteristic of the concrete mix used in 3D printing. Specifically, this mix is designed to exhibit a specific rheological behavior, characterized by a high structuration rate [Rubin 2023]. This implies that upon extrusion and deposition, the yield strength and cohesion of the concrete rapidly increase, resulting in a rapid decrease in workability and a transition towards greater rigidity. Such a property is crucial, as it ensures that the material, once deposited and in a static state, exhibits significant resistance to deformation, particularly in the vertical dimension.

This phenomenon is confirmed by findings in both [Comminal 2020] and [Reinold 2022], where the layer height is observed to be approximately equivalent to the print height (nozzle lift height between layers). Furthermore, [Reinold 2022] indicates that the printing height is the most appropriate metric for adjusting layer height.

Consistent with these findings, the experimental work undertaken in this thesis adheres to a uniform layer height of 9 millimeters. This consistency is maintained across all layers, from the base to the top of each printed structure. The adherence to this specified height has been empirically validated in our experiments, as illustrated in Figure 4.28.



Figure 4.28: Layer height considered constant across the printed shape.

- **Parametric Uncertainties and Adaptive thresholds**

Based on equations (4.15), (4.17), two ARRs can be derived. In real printing conditions, system uncertainties should be considered due to noises, stochastic error of measurements, environmental variations and linear regression procedure, etc.

For a parameter ξ , ξ_n denotes its nominal value, δ_ξ denotes the multiplicative uncertainty of ξ , while $\Delta\xi$ is its additive uncertainty, such that

$$\xi = \xi_n + \Delta\xi = \xi_n(1 + \delta_\xi) \quad (4.18)$$

In practical application of our case, the uncertainty is considered adaptive by using a rolling time window T_w :

$$\delta\xi(T_w) = \frac{\sqrt{\frac{1}{N} \sum_{i=t-T_w}^t (\xi(i) - \frac{1}{N} \sum_{i=t-T_w}^t \xi(i))^2}}{\frac{1}{N} \sum_{i=t-T_w}^t \xi(i)} \quad (4.19)$$

Therefore, the following uncertain ARRs are established, with the presence of parametric additive uncertainties:

$$\left\{ \begin{array}{l} ARR_1 : (Q_n + \Delta Q) - (\beta_{0n} + \Delta\beta_0) - (\beta_{1n} + \Delta\beta_1)U \\ \quad = Q_n - \beta_{0n} - \beta_{1n}U - (\beta_{0n}\delta_{\beta_0} + \beta_{1n}\delta_{\beta_1}U - Q_n\delta_Q) = 0 \\ ARR_2 : (Q_n + \Delta Q) - (w_n + \Delta w)h(v_n + \Delta v) \\ \quad = Q_n - w_nhv_n - (w_nhv_n\delta_v + w_nhv_n\delta_w \\ \quad + w_nhv_n\delta_w\delta_v - Q_n\delta_Q) = 0 \end{array} \right. \quad (4.20)$$

Each residual can be divided into two parts: 1) the nominal part r_i that generates the residual signal during the system operates, and 2) the uncertain part a_i for generating adaptive thresholds for residual r_i . Therefore:

$$\left\{ \begin{array}{l} r_1 = Q_n - \beta_{0n} - \beta_{1n}U \\ a_1 = |\beta_{0n}\delta_{\beta_0}| + |\beta_{1n}\delta_{\beta_1}U| + |Q_n\delta_Q| \end{array} \right. \quad (4.21)$$

$$\left\{ \begin{array}{l} r_2 = Q_n - w_nhv_n \\ a_2 = |w_nhv_n\delta_v| + |w_nhv_n\delta_w| \\ \quad + |w_nhv_n\delta_w\delta_v| + |Q_n\delta_Q| \end{array} \right. \quad (4.22)$$

As shown in Equation (4.21) and (4.22), a_i is the sum of the absolute values of several terms, making the upper threshold for r_i . A lower threshold is given by $-a_i$, as in normal case, the variation of the residual follows the variation of the uncertainties which can be positive or negative [Djeziri 2007, Djeziri 2009]. Thus, an envelope of adaptive thresholds is constituted, such that during normal operation of printing system:

$$-a_i \leq r_i \leq a_i \quad (4.23)$$

- **Fault Signature Matrix**

A Fault Signature Matrix (FSM) is a structured representation of fault patterns or signatures associated with the printing process. It is a valuable

tool in fault detection and diagnosis, where multiple components interact. It provides a structured way to assess the potential impact of an abnormal filament on the printing process. The FSM is deduced from the residuals obtained in the previous step. The proposed FSM is presented in Table 4.5. Two (2) generated residuals are included in the FSM ($r_{1,2}$). The binary elements of columns $r_{1,2}$ represent the sensitivity of the residuals to fault in each parameter of the printing system (1 if residual is sensitive to a parameter). The column of detectability D is defined as: a fault in certain parameter is detectable if the row corresponding to this parameter is not a zero-row, i.e. at least one residual is sensitive to this fault. The column of isolability I is defined as: a fault in certain parameter is isolable only if it's detectable and the row corresponding to this parameter is unique compared to other rows. In the case of 3DCP study, we are not focusing on physical faults in the system components, however, when anomaly occurs on the printing filament size, adopting the methodology of FDI system helps to indicate which control parameter (Q, U, v) is sensitive to this geometric fault.

Table 4.5: Fault Signature Matrix

	r_1	r_2	D	I
Q	1	1	1	1
U	1	0	1	1
v	0	1	1	1

Table 4.5 indicates that three (3) distinguishable signatures (r_1, r_2) are obtained. This facilitates understanding the origin of the geometric fault of the deposited filament. It can be origin from the pumping system control (U) with the signature ($r_1 = 1, r_2 = 0$); or the material (Q) with the signature ($r_1 = 1, r_2 = 1$); or the nozzle velocity (v) with the signature ($r_1 = 0, r_2 = 1$).

4.5.3 Real-time diagnosis in controlled environment

The quantitative diagnosis approach based on ARR can be implemented in real-time on 3D printing process.

In the following implementation, we want to demonstrate the automatic detection of the filament deviation, due to nozzle velocity changes. This helps to develop in *Chapter(5)* a strategy of adaptive velocity compensation. Compared to the deviation issued from the the flow Q of the voltage U , the compensation of the nozzle velocity v is faster due to the rapid dynamic of the

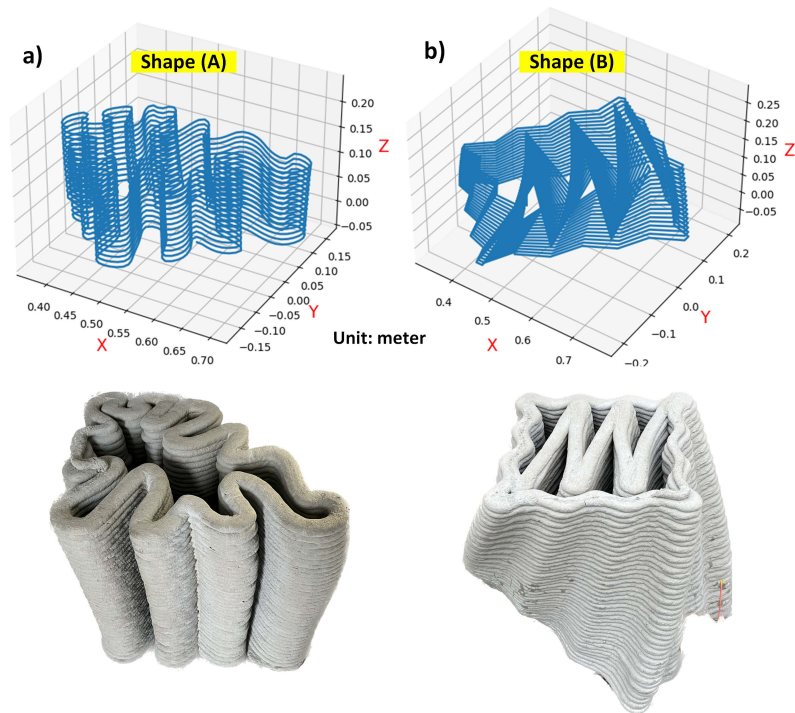


Figure 4.29: Complex shapes with variable curvature: nozzle paths given by slicing and final printed shapes. a) The toolpath and printed structure of Shape (A). b) The toolpath and printed structure of Shape (B).

robot. The velocity v varies when there is a complex curvature on the printing shape. In this case, two shapes exhibiting variable and larger range of curvatures are considered, as shown in Figure 4.29. The desired value of the nozzle velocity is fixed initially constant as: $v^d = 12$ cm/s. Fig. 4.30 and Fig. 4.31 shows the residuals r_1 , r_2 generated during the printing stage, as well as the monitoring of filament width error w , nozzle velocity v and path curvature κ .

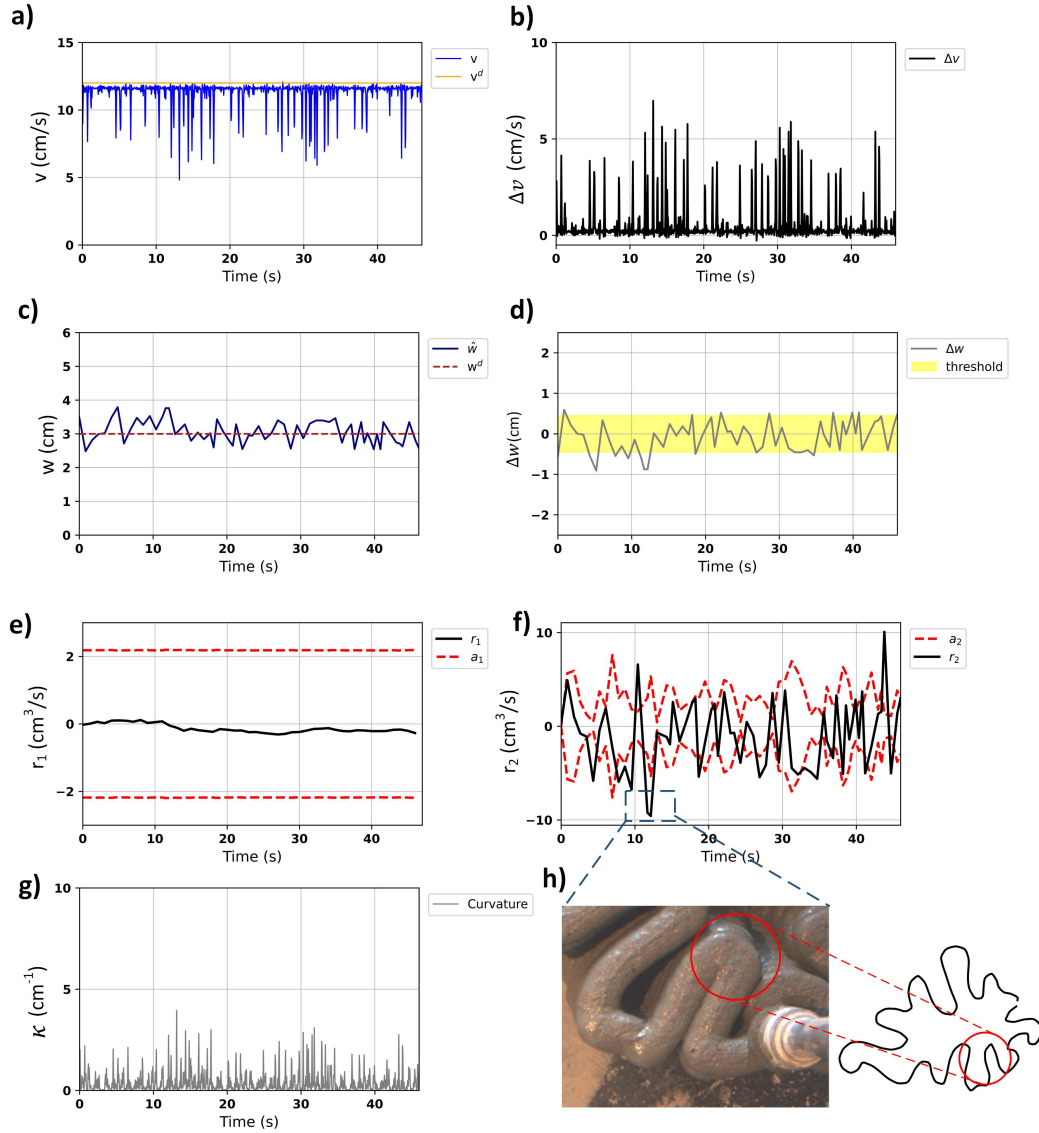


Figure 4.30: Tracking of a layer of Shape (A). a) Nozzle velocity v . b) Nozzle velocity error Δv . c) Filament width w . d) Filament width error Δw . e) Residual r_1 . f) Residual r_2 . g) Path curvature. h) Sharp turn with large curvature.

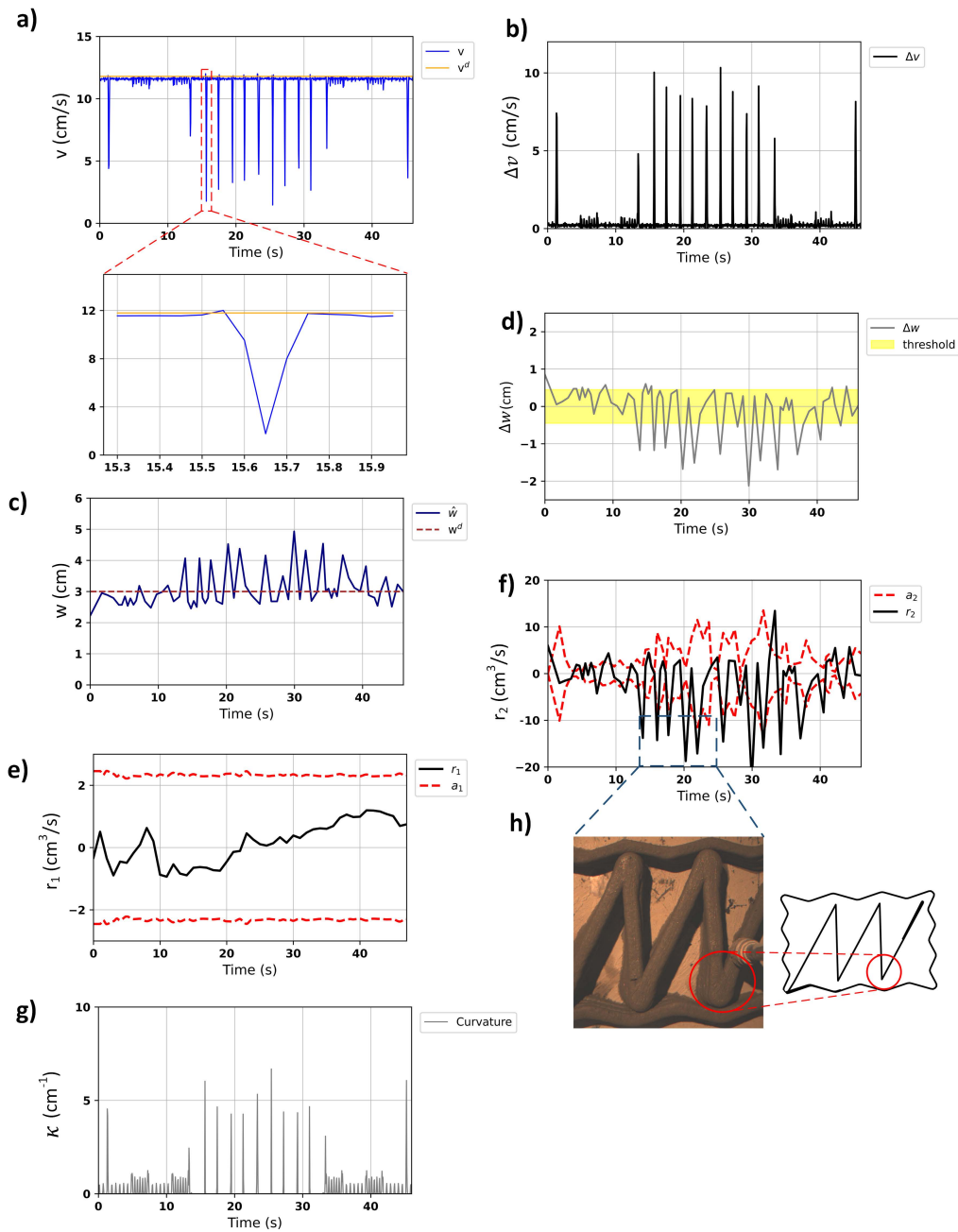


Figure 4.31: Tracking of a layer of Shape (B). a) Nozzle velocity v . b) Nozzle velocity error Δv . c) Filament width w . d) Filament width error Δw . e) Residual r_1 . f) Residual r_2 . g) Path curvature. h) Sharp turn with large curvature.

The tests were conducted under 20°C and the material was prepared according to predetermined mixing proportion (Chapter 3). The desired width of the filament is fixed to $w^d = 3$ cm of Fig. 4.30–(c) and Fig. 4.31–(c), and the admissible threshold for the width quality is 6 mm more and less of its nominal value in Fig. 4.30–(d) and Fig. 4.31–(d). In controlled environment without material perturbations, the change of rheological properties of the material at static state are relatively small and can be neglected. Consequently, the residual r_1 stays within its adaptive threshold envelop under constant pumping velocity. However, it is observed that the residual r_2 contains more fluctuations and has a fault-like behavior along the path. At certain instants, the residual r_2 exceeds its threshold boundary. This phenomenon describes a geometric fault detection of the deposited filament, localized when the continuous deposition of the material reaches the curved places of the targeted shape. It is noticed that the measured nozzle velocity profile fluctuates, this is due of the shape curvature changes Fig. 4.30–(a) and Fig. 4.31–(a), inversely proportional to the curvature variation Fig. 4.30–(g) and 4.31–(g) respectively.

The signature of the residuals ($r_1 = 0, r_2 = 1$) indicates that this fault-like behavior is originally due to the nozzle velocity v suddenly reduced with the increase of the curvature. The velocity error of shape (B) in 4.31–(b) is greater than the velocity error in shape (A) in 4.30–(b), similarly, the width error Δw of shape (A) in 4.30–(d) is greater than Δw of shape (B) in 4.31–(d). Such error of velocity is due to the curvature of the nozzle tool path. Thus, we can conclude that the velocity of the robot (Nozzle), although it was considered constant, however it adaptively changes according to the increase of the curvature of the shape. This protects the joints of the robot to structural damage in passing through curved trajectories. **The variation of the nozzle velocity (Figure 4.31-(a)) depends on the shape profile represented by the curvature (Figure 4.31-(g)), we can notice that when the curvature increases, the velocity decreases.**

Considering a scenario of printing a complex shape with variable large curvature turns, in which the desired of pumping velocity and nozzle travel velocity are fixed to constant values. When the nozzle reaches a sharp corner at the tool path, the instantaneous change of the direction of motion velocity while keeping a constant velocity is impossible to realize, because it requires a rapid acceleration, therefore, in order to realize the change of motion direction and follow the tool path, the joint actuators decelerate and then accelerate. Consequently, a reduction of actual travel velocity is inevitable, resulting in the velocity error observed in the tracking of Δv , which conforms to the results in Chapter 3 Section 3.3.1. If the pumping flow of material remains constant, this reduction of velocity will cause extra deposition of material at turning

corners with large curvatures.

4.5.4 Real-time diagnosis in uncontrolled environment

The quantitative approach has been employed in the same printing tests as outlined in 4.4.2.2, conducted under three varying temperatures: 10 °C, 20 °C, and 30 °C. The target filament width for these tests was set at $w^d = 3$ cm. Previous results highlighted geometric faults triggered by abrupt changes in direction, causing velocity errors. Subsequent findings provide examples of width deviation occurring on less complex geometries, characterized by smaller curvature and smoother paths.

Figures 4.32, 4.33, and 4.34 show cases of width deviation under 10 °C, 20 °C, and 30 °C, respectively. In each case, the residual r_2 , associated with velocity, plays a crucial role in detecting the deviation. For instance, in the 20 °C case, alarms for over-deposition are detected by r_2 at specific times, namely $t = 0, 31, 70$ s. At 30 °C, both over and under deposition were detected by r_2 at $t = 19$ s and $t = 52$ s, respectively. Across all scenarios, the fault signature indicates that deviations are velocity-related, necessitating velocity regulation for proper compensation.

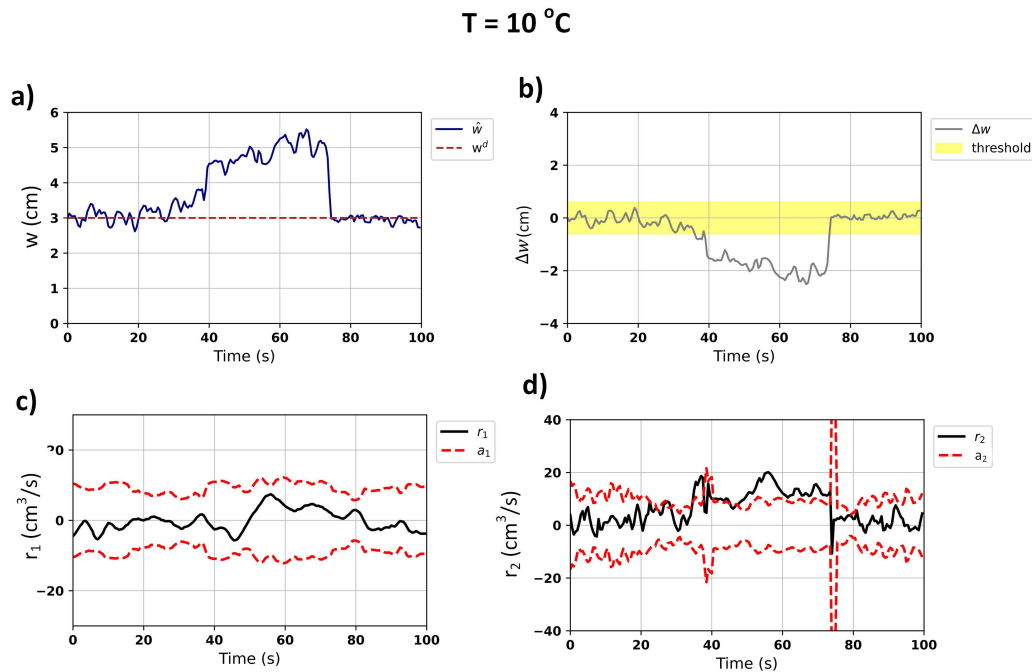


Figure 4.32: $T = 10$ °C, detection of an over deposition (Abnormal 1). a) Filament width. b) Filament width error. c) d) Residuals r_1 and r_2 .

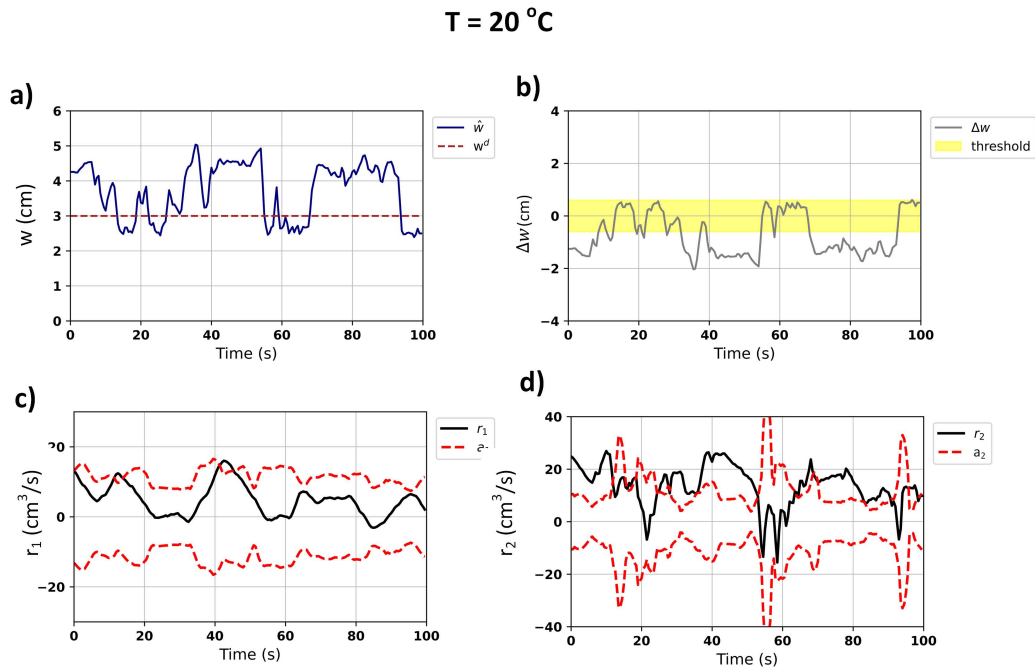


Figure 4.33: $T = 20\text{ }^{\circ}\text{C}$, detection of over depositions (Abnormal 1). a) Filament width. b) Filament width error. c) d) Residuals r_1 and r_2 .

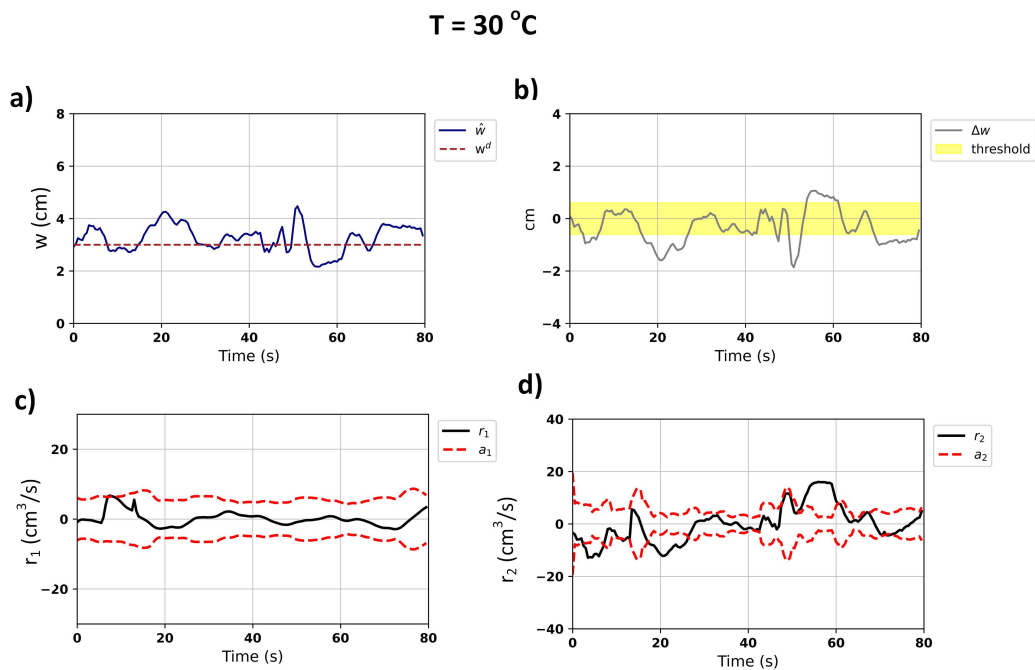


Figure 4.34: $T = 30\text{ }^{\circ}\text{C}$, detection of over deposition (Abnormal 1) and under deposition (Abnormal 2). a) Filament width. b) Filament width error. c) d) Residuals r_1 and r_2 .

One noteworthy aspect affecting detection performance is the uncertainty in setting the thresholds, which are constructed based on various uncertainties, including material flow. The material is pumped in discrete packs and controlled in an open loop. The presence of air packs could lead to instantaneous drops in the flow rate, particularly under elevated temperatures, thus adding noise to flow rate measurements. To mitigate this, one could consider implementing proper filtering techniques to reduce the incidence of false alarms related to this phenomenon. Furthermore, while false alarms tend to occur during sharp turns, the system's robustness is evidenced by its ability to detect deviations that stays outside the adaptive threshold envelope continuously.

4.5.5 Comparison study

The previous results on both qualitative (based on pattern recognition) and quantitative (based on analytical redundancies) diagnosis approaches allow a comparison between their performances for 3DCP process across three key aspects: detection of deviation, isolation of deviation, and the underlying decision-making mechanism. A summary is given in Table 4.6.

For detection, pattern recognition approach (qualitative) can process a vast amount of data quickly, identifying patterns within each class, thereby segmenting the feature space. As such, it diminishes the reliance on human subjectivity, promising a uniformity in assessment. This automates the detection of quality issues in 3DCP. However, it heavily leans on the quality and quantity of the training data obtained during the 3D printing process for pattern learning. Thus, its capacity is limited to recognizing patterns it has been trained on for a specific material. Conversely, analytical redundancy approach (quantitative) uses mathematical models to detect deviations from expected behavior of filament, which does not rely heavily on large amount of data, which sometimes are not easy to collect. However, an accurate mathematical model is complex to develop in applications such as 3DCP, as in transient stage, the dynamic material behavior inside the pump and hose is hard to predict. Consequently, the results issued by the analytical redundancy method is sensitive to the assumptions adopted in establishing the analytical models.

Regarding isolation, the qualitative approach offers the advantage of visually examining historical data within the feature space, thereby elucidating the factors contributing to each classification as well as the sensitivity to each feature when transition between classes. For instance, discussion in Section 4.4.3 indicates that the transitions between classes are notably influenced by changes in velocity compared to changes in flow rate. It is also helpful in

analysing the effects of environmental factors on the printing process. Specifically, it enables the visualization of how the regions representing each class in the feature space shift due to changing environmental conditions. This insight allows for a comprehensive understanding of the system's performance under different environmental conditions. When classification is well done, it is able to identify even minor deviations or defects and ensure consistent evaluation across assessments. However, the selection of Machine Learning classifier requires performance comparison across various techniques. Another issue is the potential over-fitting in the training of models. The quantitative approach, mathematically isolates the parameters linked to deviations, offering a more direct isolation technique. Same as detection, it relies on predefined models and assumptions which may not cover all possible material deposit behaviors. Also, non linear material behaviors raise more complexities.

For decision-making, the data collected to develop pattern recognition-based approach is used to enhance the 3DCP process. It offers the advantage of allowing for the anticipation of an optimal pilot region for the printing system settings, a priori. For instance, given the current temperature of the environment in which the printing operates, an optimal region concerning nozzle velocity and material flow rate as well as pump voltage can be determined, as indicated in Figure 4.20. This enables the prediction of specific parameters that can prevent deviations, making it particularly useful for planning printing tasks and calibrating the system while taking environmental conditions into account. The disadvantage lies in the lack of interpretability in case of utilization of Deep Learning models. In contrast, the quantitative approach operates on a reactive basis, responding to real-time data during the operation. It provides a clear rationale for detected faults thanks to the analytical models. It may however have difficulties dealing with defects that cannot be expressed by the chosen model such as discontinuous filament.

4.5.6 Conclusion

In this chapter, a methodology for evaluating the 3D printing quality is developed. For this purpose, the material filament width is considered as a criterion to evaluate the printing quality. Thus, a Deep Learning (DL) based filament width estimation algorithm is proposed. This algorithm uses an instance segmentation model from DL followed by morphological computations, allowing for real-time tracking of filament width. Two diagnostic methodologies are studied for operational diagnosis during the material deposition of the in-printing stage: a data-driven qualitative approach based on pattern recognition and a quantitative approach based on analytical redundancies. We categorize the printing operations into three classes: Normal, Abnormal

Table 4.6: Summary comparison between Pattern Recognition and Analytical Redundancy diagnosis approaches for 3DCP

	Diagnosis based on Pattern Recognition	Diagnosis based on Analytical Redundancy
Advantages		
Detection	<ul style="list-style-type: none"> • Automates detection of quality issues in 3D printing. • Processes a large number of parts quickly. • Reduces reliance on subjective human factors. 	<ul style="list-style-type: none"> • Uses mathematical models to detect deviations from expected behavior of filament. • Relies less on large amounts of training data.
Isolation	<ul style="list-style-type: none"> • Identifies even minor deviations or defects when the classification is well done. • Ensures consistent evaluation across assessments. 	<ul style="list-style-type: none"> • Utilizes known relationships between variables for fault isolation. • Identifies faults based on deviations from expected model behavior.
Decision-Making	<ul style="list-style-type: none"> • Data collected is used to enhance the 3D printing process. • Applies consistent criteria to every assessment. 	<ul style="list-style-type: none"> • Provides a clear rationale for detected faults based on analytical models.
Disadvantages		
Detection	<ul style="list-style-type: none"> • Relies heavily on the quality and quantity of training data during the 3D printing. • Recognizes only patterns it has been trained for a specific material. 	<ul style="list-style-type: none"> • Requires accurate mathematical models of the material behavior, which is complex to develop. • Results is sensitive to assumptions made in the considered analytical models.
Isolation	<ul style="list-style-type: none"> • Requires performance comparison in machine learning techniques. • Potential for over-tuning to the training data. 	<ul style="list-style-type: none"> • Relies on predefined models and assumptions, which may not cover all possible deposited filament quality. • Complexities arise nonlinear behavior of the deposited material.
Decision-Making	<ul style="list-style-type: none"> • Deep learning models may be challenging to interpret. 	<ul style="list-style-type: none"> • May have difficulty with defects that deviate from the chosen model such as the case of discontinuous filament.

1 (over deposition), and Abnormal 2 (under deposition). Both approaches aim to identify the underlying parameters contributing to abnormal behaviors, which in turn helps in pinpointing the origins of anomalies. Thus, both approaches have their strengths and weaknesses. Pattern recognition excels in automation and the ability to detect subtle defects such as width deviation. Analytical redundancy, on the other hand, relies on well-defined models and can be less data-dependent. The choice between them depends on factors like the availability of data, the complexity of the overall 3D printing system, and the level of certainty required in the diagnostic process. The combination of both approaches may provide the most robust solution for the 3D printing.

In-printing stage: Adaptive estimation and compensation

Contents

5.1	Introduction	118
5.2	Problem statement	119
5.3	Adaptive compensation based on velocity estimation	120
5.3.1	Neural network based velocity estimation	120
5.3.2	Adaptive velocity compensation	122
5.4	Results and discussion	123
5.4.1	Compensation of filament width deviations during the in-printing stage	123
5.4.2	Evaluation in large scale printing	126
5.5	Conclusion	139

5.1 Introduction

In the previous chapter, an integrated approach for real-time detection of printing filament width deviation is developed. During the printing stage, the aim is to maintain the width of the material deposit filament as close as possible to a desired value, while respecting the pre-defined trajectory. This desired width can be constant throughout the printing or can be variable according to the design and requirement. For instance, wider substrate layers can enhance the overall stability of the shape. In case of neighboring tool-paths, a less layer width helps to avoid layer intersections and can provide higher resolution as well. However, due to the variable material properties in uncontrolled environments, fluctuations in flow rate can lead to deviations in filament width. This chapter focuses on adaptive compensation strategies to mitigate such deviations.

5.2 Problem statement

As previously discussed, the 3DCP process or the 3DCP System-of-Systems (SoS) comprises three key components: the material system (responsible for pumping and extrusion), the robotic system, and the shape or structural design. Two controllable parameters exist in the process: robot velocity and pump voltage.

Theoretically, adaptive compensation for filament width deviation can be achieved in three ways: robot speed regulation, pump voltage regulation, or a combination of both. However, this process entails a trade-off between two disparate dynamics. On one hand, the material behavior itself and the material flow's reaction time to changes in pump voltage and pumping speed is relatively extended, which concerns a slow dynamic. This is due to the thixotropic of fresh concrete and length of the mortar hose as a flow conductor, indeed, this can be affected by various factors such as environment disturbances, hose length, etc. On the other hand, the robotic system exhibits rapid dynamic behavior, allowing for immediate adjustments in response to regulatory inputs. Given that the robotic system is generally better modeled and controlled compared to the complex material flow dynamics, this makes the compensation by robot velocity a more reliable choice for minimizing error. The optimization problem of kinetic energy cost can be therefore formulated as:

$$\begin{aligned}
 & \text{minimize } E_k(v, t) \\
 & \text{subject to :} \\
 & \quad w_{min} \leq w \leq w_{max}, \\
 & \quad v_{min} \leq v \leq v_{max}, \\
 & \quad Q_{min} \leq Q \leq Q_{max}, \\
 & \quad \kappa_{min} \leq \kappa \leq \kappa_{max} \\
 & \quad T_{min} \leq T \leq T_{max} \\
 & \quad H_{min} \leq H \leq H_{max}
 \end{aligned} \tag{5.1}$$

Where w is the filament width, w_{min} and w_{max} defines the acceptable range of filament width based on the desired width w^d . v , Q and κ denote the nozzle velocity, material flow rate and trajectory curvature, while T, H represents the environmental conditions: temperature and humidity.

5.3 Adaptive compensation based on velocity estimation

5.3.1 Neural network based velocity estimation

As mentioned above, to obtain a desired filament width, a velocity compensation strategy is considered. Given the complex interactions between the filament width, material flow rate, and the toolpath curvature, model-based strategy may struggle to provide the dynamism required for optimal print quality. Specifically in uncontrolled environment, fluctuations of material flow are usually unpredictable, also, the toolpath curvature may impact the actual velocity of the nozzle and cause deviation. To address this, we employ a data driven estimator based on [Artificial Neural Network \(ANN\)](#) to estimate an optimal nozzle velocity for a given width reference. **Actually, the measured velocity of the nozzle is the image of the geometric path and doesn't adapt to the material behavior. In this sub-section, we want to estimate an optimal velocity of the nozzle which consider the material behavior changes and can be used to elaborate the adaptive compensation of the robot velocity.** For this purpose, the designed neural network takes as its input a vector comprising the width of the filament, the material flow rate, and the curvature of the toolpath. The output, denoted as \hat{v} , represents the estimated nozzle velocity under which the desired width can be obtained. Even in case where variable desired width is required, the velocity estimation can account for this.

Throughout a series of printing sessions conducted within CIRMAP project, a [3DCP](#) data set is collected that covers a wide range of printing conditions, this includes the pump voltage, material flow rate, tool path curvature, nozzle velocity, as well as estimated filament width obtained by using the width estimation methodology given in the previous chapter. In the historical data, a wide range of velocities from 3 cm/s to 20 cm/s and flow rate from 10 cm³/s to 80 cm³/s are considered, which covers most of the practical printing scenarios.

A feed-forward neural network structure is adopted for the velocity estimation. The input feature is selected as $[w^d(t), Q(t), \kappa(t)]$, while the neural network maps from input features to velocity:

$$\hat{v} = f_{NN}(w^d, Q, \kappa; \phi) \quad (5.2)$$

where ϕ are the neural network parameters.

The network comprises multiple layers, starting with the input layer followed by hidden layers and finally the output layer. The transformation at

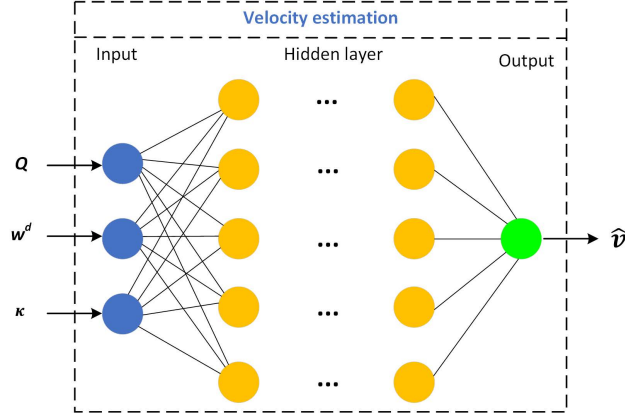


Figure 5.1: Neural network structure for velocity estimation.

each hidden layer can be represented as:

$$H^{(i)}(t) = f^{(i)}(W^{(i)} \cdot H^{(i-1)}(t) + b^{(i)}) \quad (5.3)$$

Here $H^{(i)}(t)$ is the output of the i -th hidden layer, $W^{(i)}$ is the weight matrix, $b^{(i)}$ is the bias vector, $f^{(i)}$ is the activation function at layer i . The output layer is defined as :

$$\hat{v}(t) = W^{out} \cdot H^{(2)}(t) + b^{out} \quad (5.4)$$

where W^{out} and b^{out} are the weight matrix and bias for the output layer. The activation function for the nodes is chosen based on the specific case of 3DCP. Generally, *ReLU* is a good first choice for hidden layers in regression tasks, but it's unbounded, making it less ideal for output layers when the output must be restricted. As in practices, the velocity should be bounded for safe and smooth operation. Thus, *Sigmoid* activation function is selected.

$$f(x) = \frac{1}{1 + e^{-x}} \quad (5.5)$$

The hyper-parameters of the neural network training is determined through grid search strategy. We use a **Mean Square Error (MSE)** loss function augmented with a penalty term for out-of-range velocity predictions:

$$Loss_{MSE} = \frac{1}{N} \sum_{i=1}^N (\hat{v}_i - v_i)^2 + \lambda \cdot B(\hat{v}_i) \quad (5.6)$$

The penalty term is defined by a barrier function:

$$B(\hat{v}_i) = \begin{cases} 0 & \text{if } v_{min} \leq \hat{v}_i \leq v_{max} \\ (\hat{v}_i - v_{min})^2 & \text{if } \hat{v}_i < v_{min} \\ (\hat{v}_i - v_{max})^2 & \text{if } \hat{v}_i > v_{max} \end{cases} \quad (5.7)$$

5.3.2 Adaptive velocity compensation

During the material deposition process, real-time tracking of the estimated filament width is accomplished, as detailed in Chapter 4. This enables the calculation of the width error Δw defined as:

$$\Delta w = w^d - \hat{w} \quad (5.8)$$

The real-time tracking of the width error Δw enables the system to determine whether the material deposition is proceeding normally or abnormally. In the case of abnormal deposition, the system is expected to adapt the nozzle velocity to compensate for the filament width deviation. This decision-making mechanism operates based on a pre-defined threshold for Δw . The selection of this threshold is case-specific and can impact the performance of the compensation. For example, in large-scale structural applications such as the production of walls and columns, a filament width deviation of up to 10 mm may be acceptable [Xu 2020]. In such cases, the system may be configured with a higher threshold for Δw , thereby reducing the frequency of adaptive interventions and conserving computational resources. Conversely, in some cases emphasizing aesthetics and for functional reasons [Xu 2017, Lim 2011], a lower threshold for Δw is considered, which can lead to more frequent activation of the adaptive compensation mechanisms. To ensure that the estimated nozzle velocity remains within a safe operating range, a velocity saturation function is applied. This function restricts the estimated velocity to fall within specified minimum and maximum bounds.

The tracking of difference between the estimated velocity and the measured velocity of the robot Δv is given by:

$$\Delta v = \hat{v} - v \quad (5.9)$$

During the in-printing stage, the robot guides the nozzle to follow a predefined trajectory, characterized by the time history of its poses and velocities, denoted by \mathbf{X} and $\dot{\mathbf{X}}$. In case of 3DCP, only linear velocity v without rotation is considered.

This trajectory is established in the pre-printing stage, as detailed in Chapter 3. To accurately track this trajectory, a commonly used joint-based control scheme is employed by industrial robots (see Figure 3.11, Chapter 3). The Δv is then used to form a kinematic adaptive control input $K\Delta v$, that adjusts

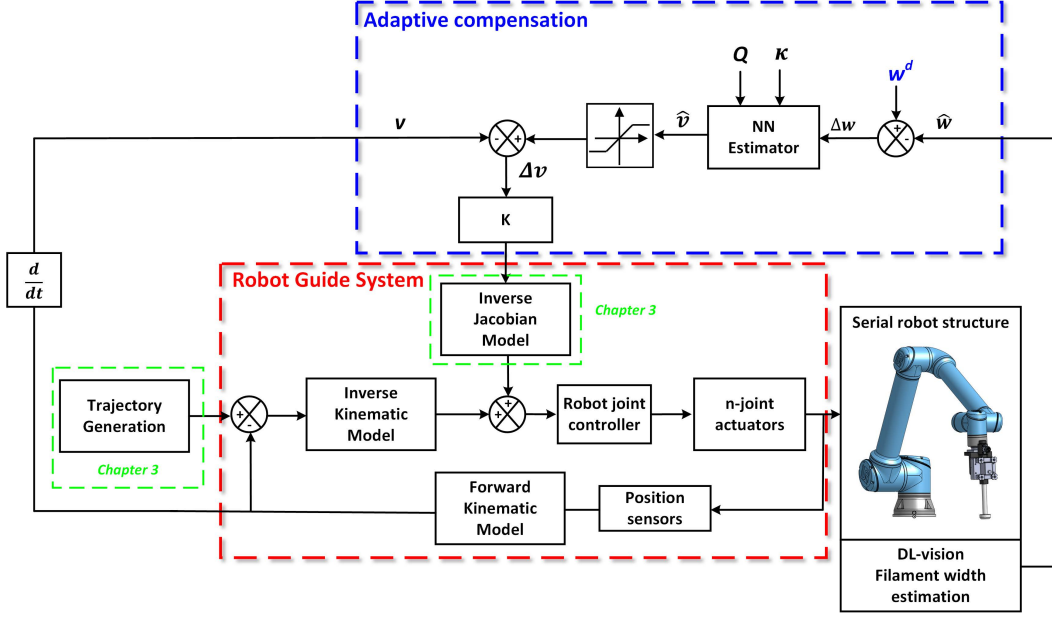


Figure 5.2: Adaptive compensation mechanism.

the joint velocity ($\Delta\dot{\Theta}$) in order to adapt the velocity in Cartesian space as follows:

$$\Delta\dot{\Theta} = J^{-1}(\Theta)K\Delta v \quad (5.10)$$

where:

$$K = \frac{G}{2}(1 + \text{sign}(|\Delta w| - th)) \quad (5.11)$$

The gain G is calculated from the curvature profile as discussed in Chapter 3. The threshold th represents the admissible threshold for control quality of the filament during printing. K expresses the implemented variable gain that is equal to 0 when the deviation Δw is encapsulated in the thresholds $(-th, th)$, and equal to 1 otherwise. This ensures that the adaptive velocity compensation is triggered only when the observed filament width falls outside of these admissible thresholds.

5.4 Results and discussion

5.4.1 Compensation of filament width deviations during the in-printing stage

The adaptive compensation algorithm was implemented through real-world printing sessions, conducted within the emulated environment described in

Chapter 3. These tests were performed under different temperature conditions of 10, 20, and 30 °C, while maintaining a consistent relative humidity level of 50%. The threshold of filament width error is set at 20% of the desired width w^d . The details of the printing system setup inside the climate chamber is given in Appendix A. In this study, the considered shapes are the rounded square and ellipse as depicted in Chapter 4 4.4.2.2.

Figures 5.3 and 5.4 shows the tracking of velocity and width errors, respectively, during a period in which deviations are detected and corrected under a temperature of $T=20$ °C. Peaks in velocity error correspond to moments when the compensation mechanism is activated. When a deviation is identified, the velocity error Δv shows a noticeable peak. Once the compensation is complete and the width error returns within the threshold envelope.

In real world experiment, the flow rate sensor measurement as well as the filament width estimation is subject to measurement noise and various uncertainties. These imperfections in data acquisition manifest themselves in the estimated velocity profile generated by the NN estimator. Note that the adaptive compensation mechanism is designed to activate only when the width error exceeds a predefined threshold. This design filters out minor fluctuations and sensor noise, thereby reducing unnecessary corrections and enhancing system stability. As a result, a more stable measured velocity profile is observed in comparison to the estimated velocity, as seen in Figure 5.3. **Indeed, we developed a data driven estimator of the velocity considering at the same time the curvature of shape and the material represented by its flow. The variation of the flow causes the variation of Δv .**

In the case presented in Figure 5.6, an Abnormal 2, indicating under-deposition, is detected at $t_{detection} = 13.2$ s. Compensation for this deviation is completed by approximately $t_{compensation} = 14.3$ s, therefore a total response time $t_r = 1.1$ s. This response time corresponds to a filament length of around 12 cm that features a deviated width. Quantifying the response time is crucial for identifying a response length, which denotes the filament length for which the width error deviates from the threshold envelope. This measurement serves as a valuable metric for evaluating the efficacy of the compensation strategy.

Compensated deviations for temperatures of 10 °C and 30 °C are provided in Figures (5.5, 5.6) and 5.7, respectively. The response length of the compensation are denoted at width error peaks. The compensation strategy has an average response time of 1.5 seconds across different temperature conditions. Considering the velocity limitations set during the printing process, this average response time results in a response length of filament between 8 cm and 20 cm. In the given examples, the average compensation response length is approximately 13 cm.

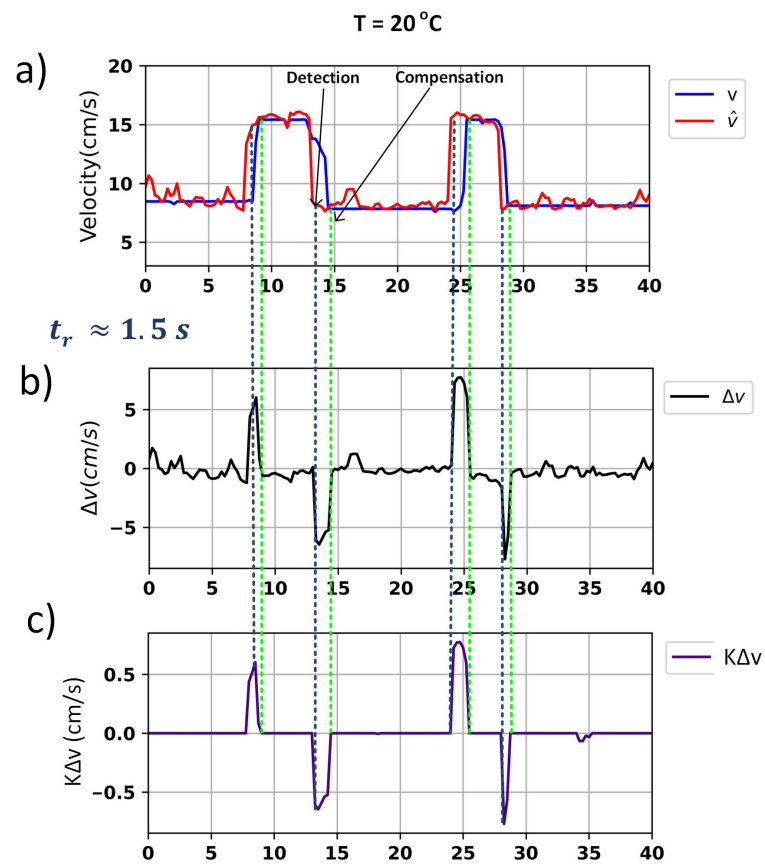


Figure 5.3: Compensation: $T = 20^\circ\text{C}$. a) Estimated velocity \hat{v} and real velocity v . b) Velocity error Δv . c) Control input $K\Delta v$.

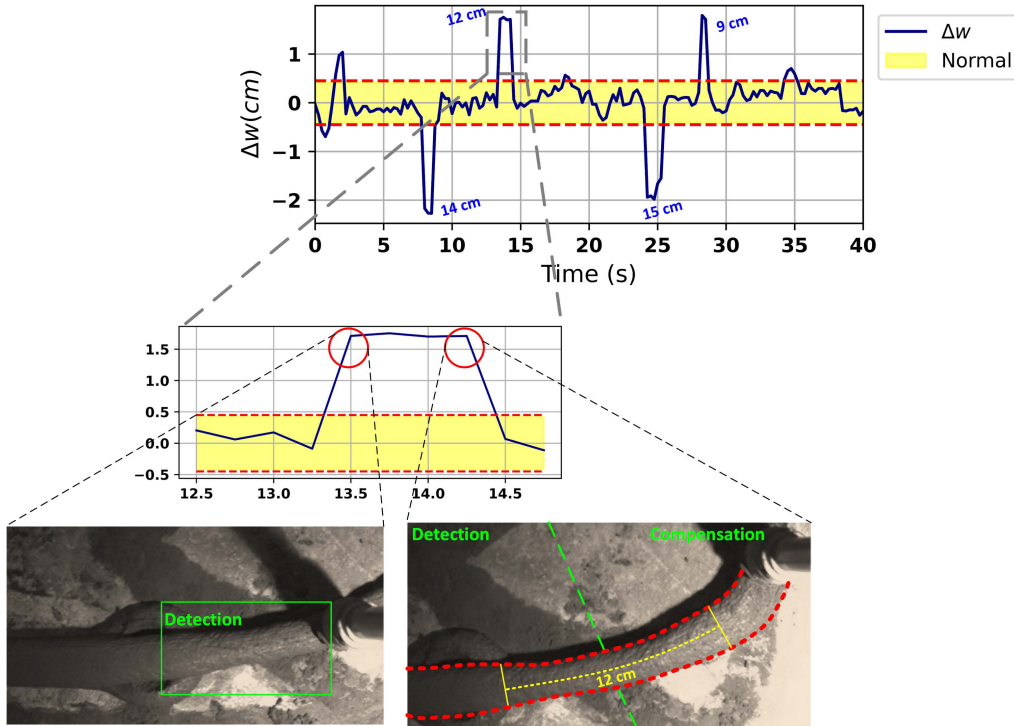


Figure 5.4: Compensation: tracking of filament width error, $T = 20 \text{ }^\circ\text{C}$.

5.4.2 Evaluation in large scale printing

The prior findings establish the effectiveness of the proposed adaptive compensation strategy for handling deviating filament segments during material deposition. To extend these results and evaluate how this strategy can improve overall printing quality in large-scale printing applications, we conducted additional printing tests under different of temperature conditions: 10, 20, and 30 $^\circ\text{C}$.

- **Test shape**

The selected shape for these tests is the zigzag shape with variable curvatures, as depicted in Figure 5.8. We completed the printing for a total of 21 layers. The total cumulative filament length (denoted by L_{total}) required to form this shape is 5040 cm (or 50.4 meters). This shape serves as a representative example for complex geometries in large-scale printing. The target filament width is set at $w^d = 3 \text{ cm}$ and the layer height at 0.9 cm. Therefore, the total estimated material quantity needed for printing this shape is approximately 14000 cm^3 (refer to Chapter 3, Section 3.4.2).

- **Test conditions and materials**

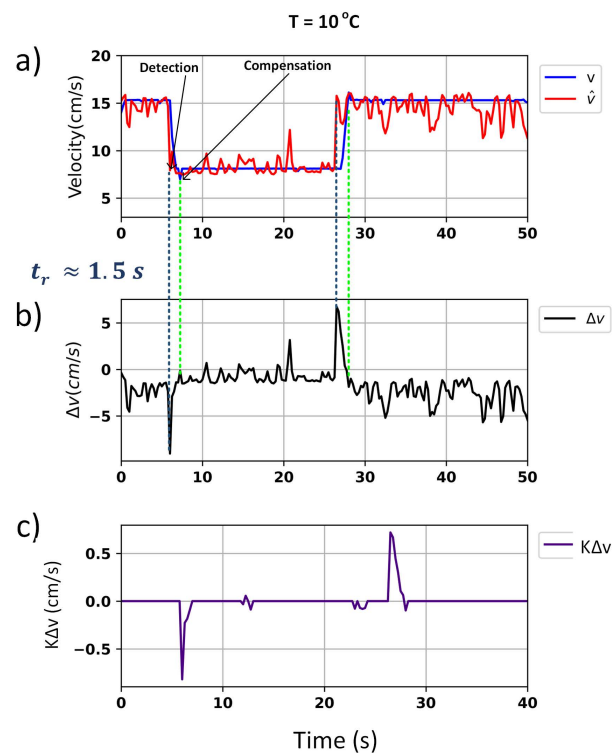


Figure 5.5: Compensation: $T = 10\text{ }^{\circ}\text{C}$. a) Estimated velocity \hat{v} and real velocity v . b) Velocity error Δv . c) Control input $K\Delta v$.

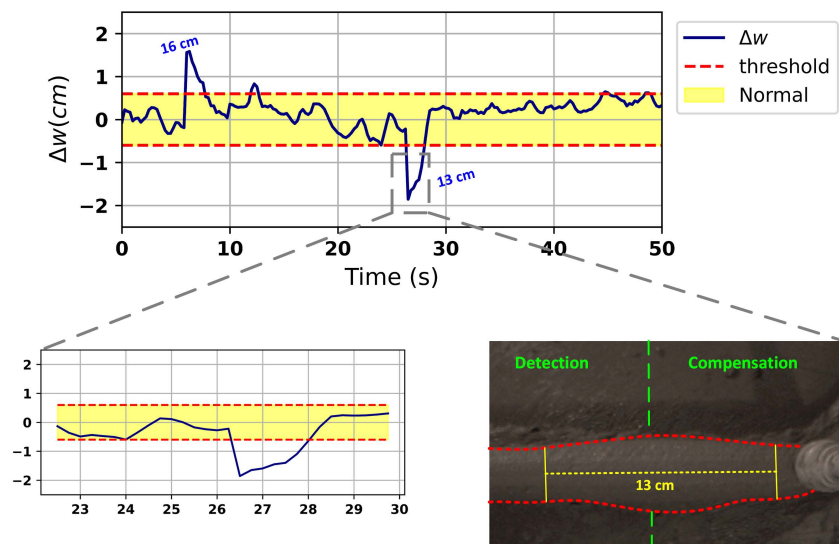


Figure 5.6: Compensation: tracking of filament width error, $T = 10\text{ }^{\circ}\text{C}$.

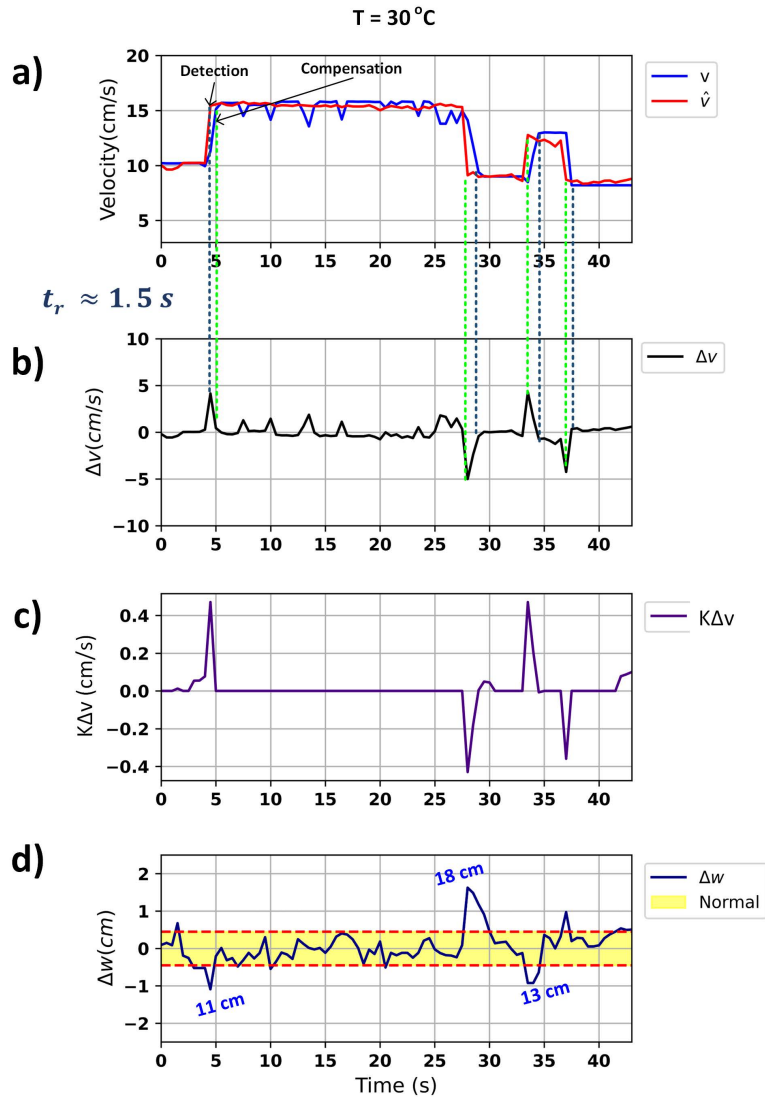


Figure 5.7: Compensation: T = 30 °C. a) Estimated velocity \hat{v} and real velocity v . b) Velocity error Δv . c) Control input $K\Delta v$. d) Width error Δw .

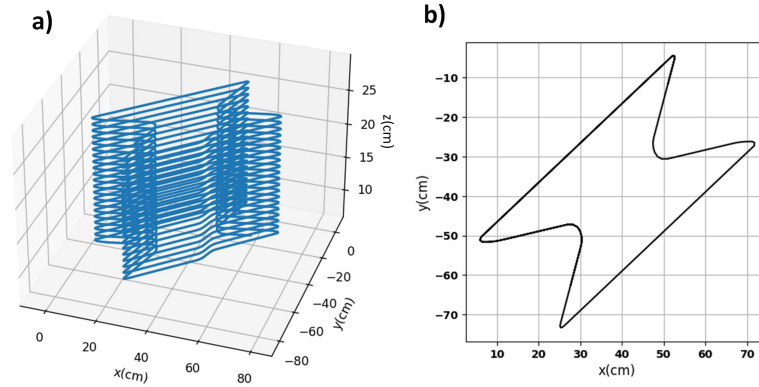


Figure 5.8: a) Test shape in 3D view. b) Test shape view in XOY plane.

Several tests were conducted within the climate chamber at temperatures of 10, 20, and 30 °C, each at a constant humidity level of 50%. At each temperature setting, three separate print runs were performed: one without compensation, one with a 15% w^d threshold for compensation, and another with a 10% w^d threshold for compensation. Here, the percentage threshold refers to the percentage of the desired filament width w^d which is set at 3 cm.

Note that for comparative consistency, the pump voltage was held constant at 2 volts for all nine tests. In the tests without compensation, a uniform desired velocity of 12 cm/s was employed.

During the tests, we maintained consistent proportions and types of materials, including 17.5 kg of VICAT¹ brand cement, 6.25 kg of water, 19.5 kg of recycled fine aggregate from Tradecowall Belgium ², 0.035 kg of Tempo 100 superplasticizer, and 0.035 kg of chryso ³ viscosity modifier. For each distinct test, whether conducted in a controlled or uncontrolled environment, we divided this composition into three portions. The first portion remained unchanged, while the second and third portions were supplemented with 300 ml and 600 ml of water, respectively. These water additions were carried out with the aim of modifying the rheological properties of the material and, consequently, its behavior during pumping under stress.

Indeed, the rheology of materials used in 3D concrete printing (3DCP) can be modified by adjusting the water content [Zahabizadeh 2019]. The addition of water affects the flow rate and layer volume of the 3DCP material, which is directly related to its rheological properties [Lee 2021]. It is crucial to carefully control the rheology of the material to ensure it can be pumped through the extruder and maintain its shape after being extruded [Panda 2018]. The

¹<https://www.vicat.fr/>

²<https://www.tradecowall.be/>

³<https://www.chryso.fr/>

rheological properties of the material should be balanced to achieve optimal fresh properties and printability [Fonseca 2023].

Given that changes can occur over extended periods, especially in an uncontrolled environment, such as due to gradual temperature variations, this modification is crucial. To quickly observe results on small and middle-scale shapes, the addition of water allowed us to simulate environmental disturbances like increased humidity or higher temperatures, as they might occur in real-world conditions. The rheological properties of 3DCP materials can change over time after mixing, resulting in a decrease in flow rate and layer volume [Lee 2021]. However, it's important to note that for tests conducted at low temperatures, the materials were stored in the climate chamber at 10°C for an extended period, approximately 10 hours. This condition was maintained to investigate the material's behavior in cold environments and gain a better understanding of its adaptation to such conditions.

• **Results and discussion**

Figure 5.9a shows the evolution of material flow rate over time, under a constant pump voltage of 2 volts, in $T = 20\text{ }^\circ\text{C}$. It can be seen that the addition of water significantly affects the material flow rate, evident fluctuations can be observed, which can cause filament width deviation as seen in Figure 5.9c. In this test, the threshold to trigger compensation is set at 10% of w^d . It can be seen from Figure 5.9b and 5.9c that in a duration of 350 seconds, the nozzle velocity is adapted according to the width tracking, as a result, a consistent filament width within tolerance range is maintained. The corresponding velocity error Δv and control signal $K\Delta v$ during this operation are given in Figure 5.10 a, b respectively.

In the context of large-scale printing, to assess the effectiveness of the adaptive compensation strategy, we introduce a metric called **deviation length percentage**, denoted by $d\%$. This metric quantifies the cumulative length of filament where the width deviates from the desired value by more than a specified threshold. Therefore, the deviation length percentage is given by:

$$d\% = \frac{L_{deviation}}{L_{total}} \times 100\% \tag{5.12}$$

Where L_{total} is the total filament length forming the shape. For the evaluation, we selected thresholds of 15% w^d and 10% w^d (equivalent to a deviation of $\pm 4.5\text{ mm}$ and $\pm 3\text{ mm}$ respectively) to calculate $d\%$ in each test.

The outcomes of this evaluation, carried out over nine tests, are summarized in Table 5.1. The corresponding histograms that detail the distribution of filament width error and the printed shapes from side-view are showcased

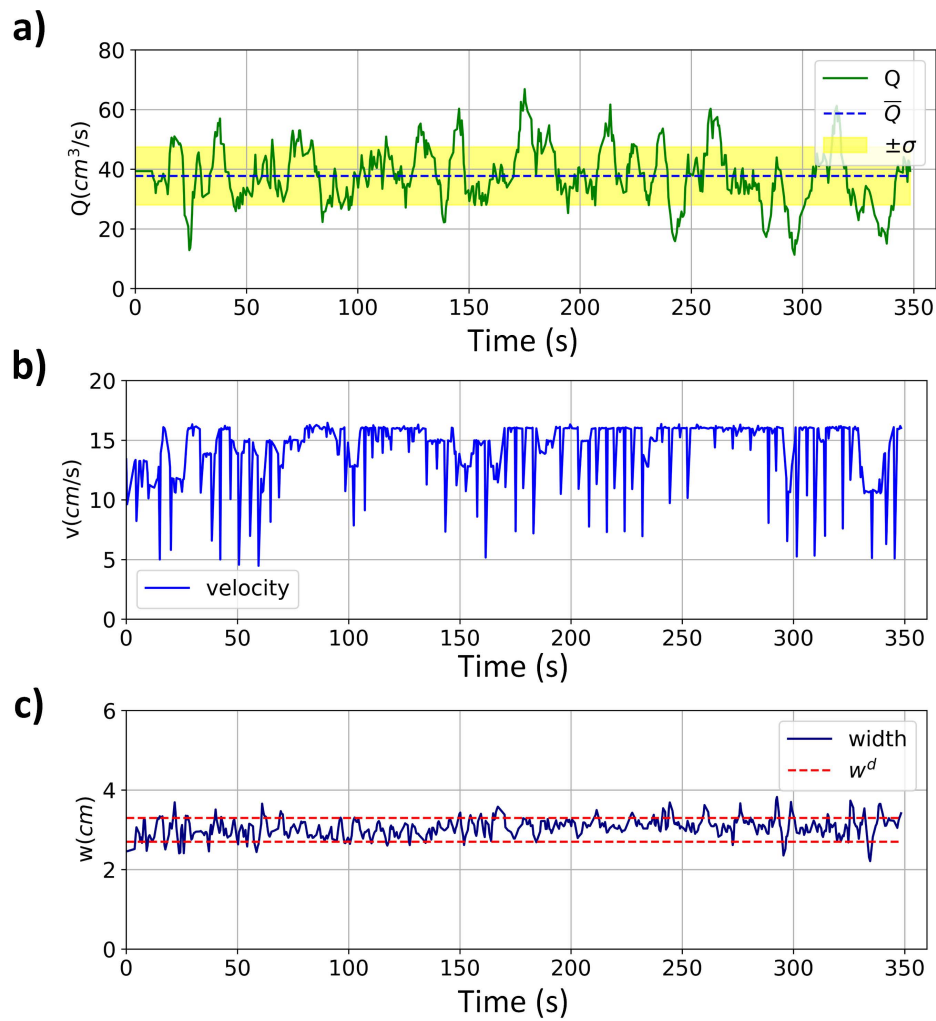


Figure 5.9: Test at $T=20^\circ\text{C}$, with compensation, compensation threshold is 10% of w^d . a) Material flow rate. b) Nozzle velocity measured during printing. c) Filament width.

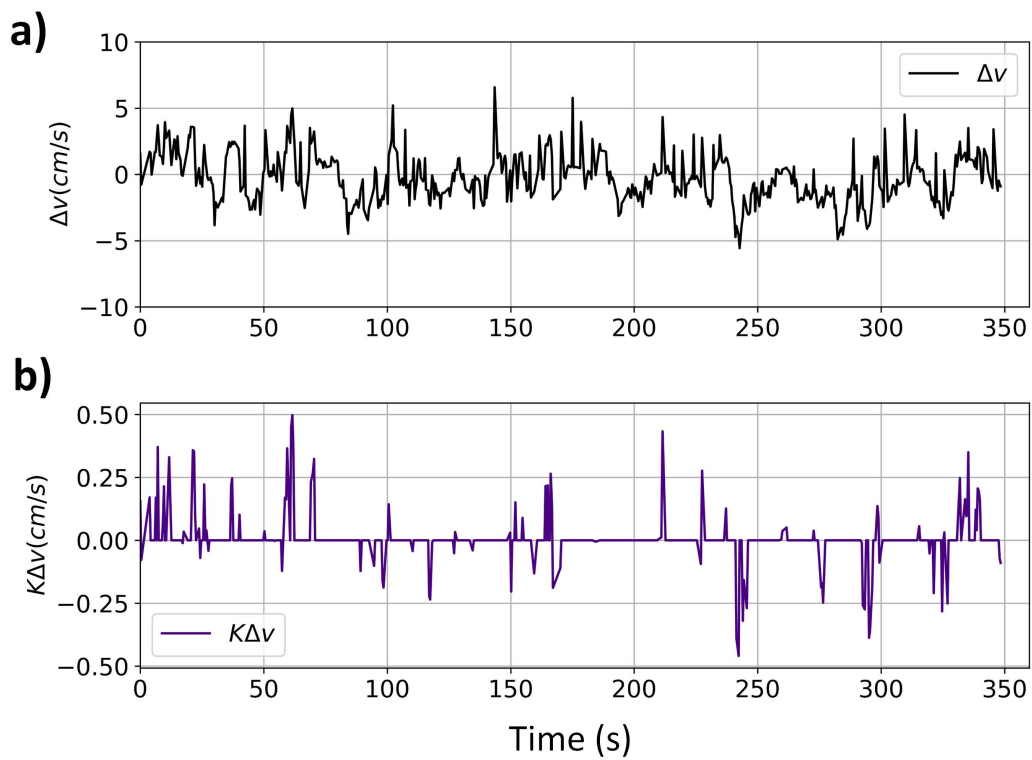


Figure 5.10: Test at $T=20^\circ\text{C}$, with compensation, compensation threshold is 10% of w^d . a) Tracking of velocity error $\Delta v = \hat{v} - v$. b) Tracking of control input $K\Delta v$.

in Figures 5.11 to 5.19. **Each histogram shows the width error distribution across all recorded sample points (denoted as operation points in feature space (U, Q, v, w)), during the printing process.** For the scope of these tests, the sampling time was 0.4 seconds.

The results show in the Table 5.1 that the compensation strategy is able to effectively reduce the deviation length percentage $d\%$. For the same temperature, the compensation strategy significantly decreases the percentage of width errors surpassing the acceptable threshold ($\pm 15\%$ and $\pm 10\%$ w^d). Specifically, $d\%$ is reduced by 18.2%, 14.7% and 20% for 10, 20 and 30 °C respectively given 15% threshold, by 24.8%, 24.5% and 24.1% for 10, 20 and 30 °C respectively given 10% threshold.

This enhancement is evident when comparing the width error histograms of tests with compensation to those without, across all temperature settings. Notably, histograms from compensated tests exhibit a higher concentration near zero, indicating fewer deviations that exceed threshold. This underscores the efficiency of the compensation strategy in reducing the deviation length percentage $d\%$ over a total filament length of 50.4 meters, thereby optimizing the overall print quality.

For example, Figures 5.11, 5.12 and 5.13 show that the width error histogram exhibits a broader spread in the case without compensation, primarily within the range of (-10 mm, 10 mm). When introducing compensation with thresholds of 15% and 10%, the histograms in Figures 5.12 and 5.13 display distributions more narrowly clustered around zero, specifically within the (-5 mm, 5 mm) range. This shows the effectiveness of the compensation strategy in mitigating width errors.

It is also noteworthy that the main peak (or statistical mode) of errors is biased towards negative values ($\Delta w < 0$). This predominance of negative errors suggests that there is more over-deposition than under-deposition. A plausible explanation for this trend is that the material perturbation comes from addition of extra water, this perturbation modifies the rheological properties of the material by reducing the viscosity, thus increasing the tendency for excessive flow, leading to more over deposition. The same phenomenon can be observed in 20 °C and 30 °C as well, from Figures 5.14 to 5.19.

In environments with elevated temperatures, such as 30 °C as shown in Figure 5.17, the characteristics and behavior of 3D printed concrete can change significantly. The distribution of width error in 30 °C is more dispersed than in 10 and 20 °C without compensation. Increased heat influences several aspects of the printing process. The first and most immediate is the concrete's curing process, which in turn impacts the overall performance of the printed structures. In addition, elevated temperatures can also affect interlayer adhesion and the ultimate hardened properties of the printed concrete. When

	15% threshold		10% threshold	
	Without Compensation	With Compensation	Without Compensation	With Compensation
T=10 °C	30.6%	12.4%	38.7%	13.9%
T=20 °C	25.8%	11.1%	35.0%	10.5%
T=30 °C	39.4%	19.4%	48.4%	24.3%

Table 5.1: The deviation length percentage (total print length $L_{total} = 50.4$ m) under different environment temperatures (T) given different threshold (15% and 10% of w^d).

T = 10 °C, without compensation

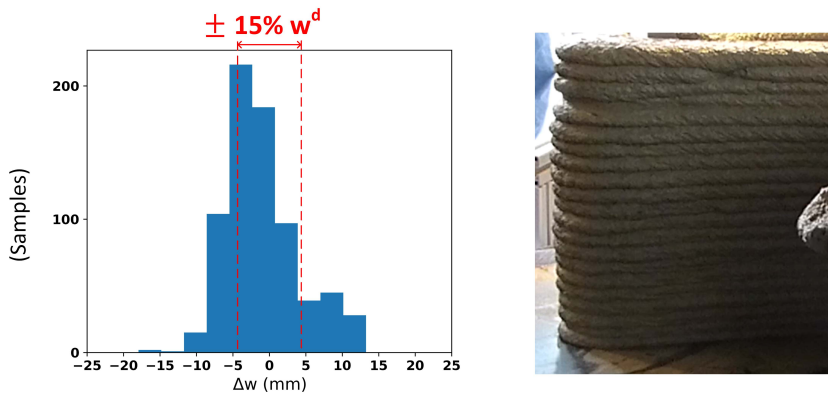


Figure 5.11: Histogram of filament width error and printed shape. T = 10 °C, without compensation.

T = 10 °C, with compensation (15 % threshold)

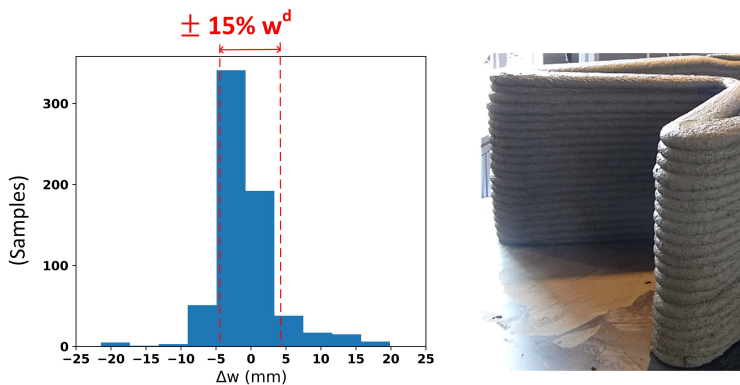


Figure 5.12: Histogram of filament width error and printed shape. T = 10 °C, with compensation given 15% of w^d as threshold.

T = 10 °C, with compensation (10 % threshold)

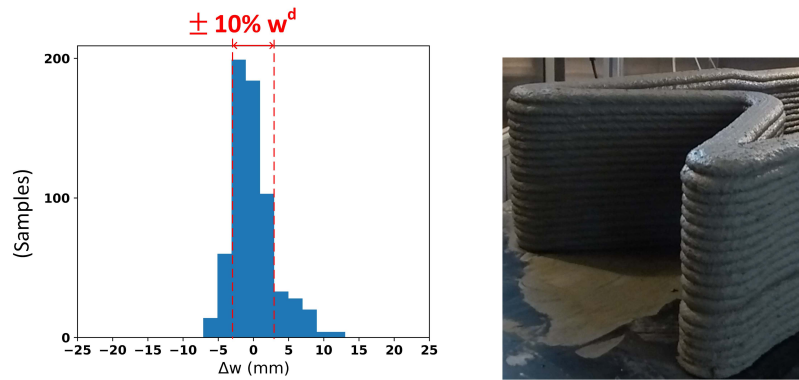


Figure 5.13: Histogram of filament width error and printed shape. $T = 10^\circ\text{C}$, with compensation given 10% of w^d as threshold.

T = 20 °C, without compensation

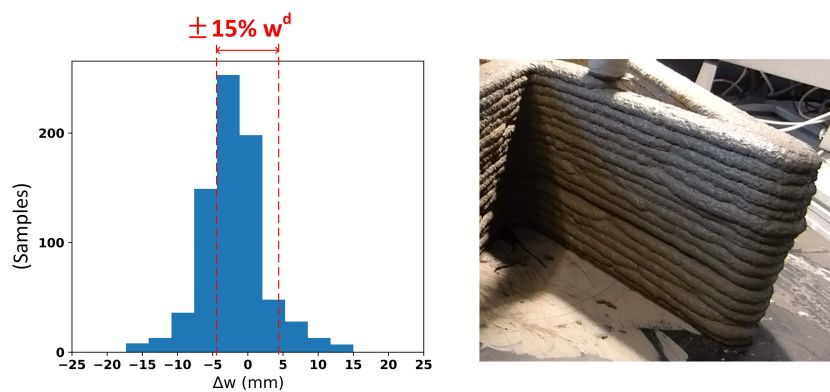


Figure 5.14: Histogram of filament width error and printed shape. $T = 20^\circ\text{C}$, without compensation.

T = 20 °C, with compensation (15 % threshold)

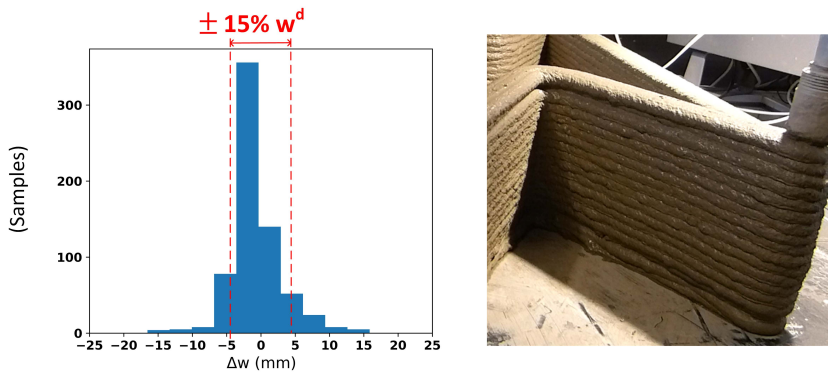


Figure 5.15: Histogram of filament width error and printed shape. T = 20 °C, with compensation given 15% of w^d as threshold.

T = 20 °C, with compensation (10 % threshold)

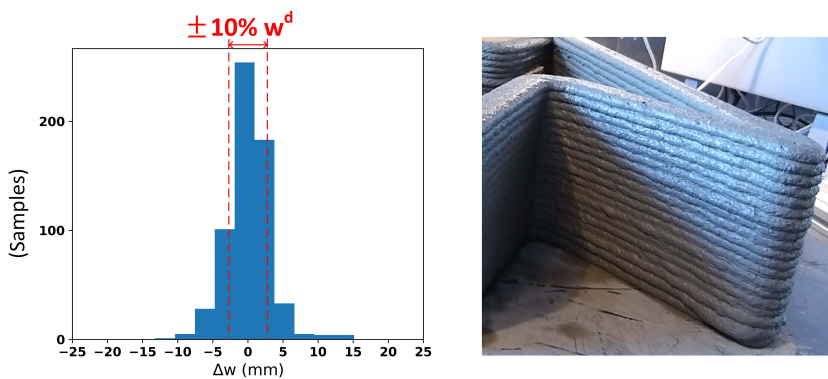


Figure 5.16: Histogram of filament width error and printed shape. T = 20 °C, with compensation given 10% of w^d as threshold.

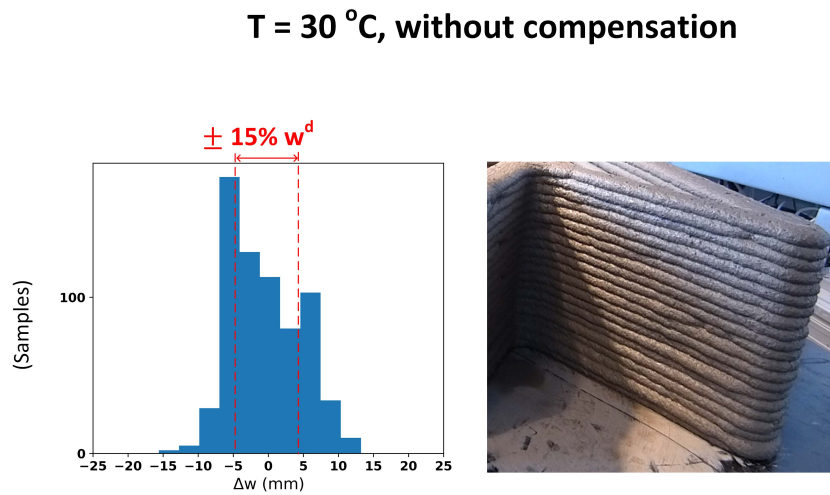


Figure 5.17: Histogram of filament width error and printed shape. $T = 30$ °C, without compensation.

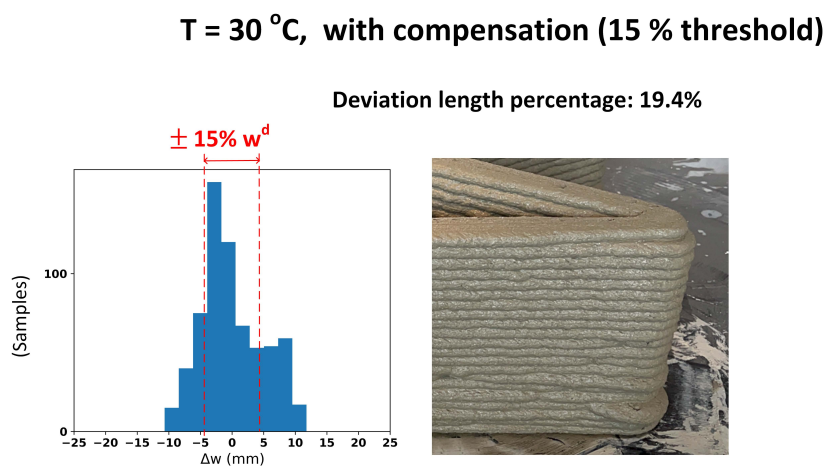


Figure 5.18: Histogram of filament width error and printed shape. $T = 30$ °C, with compensation given 15% of w^d as threshold.

T = 30 °C, with compensation (10 % threshold)

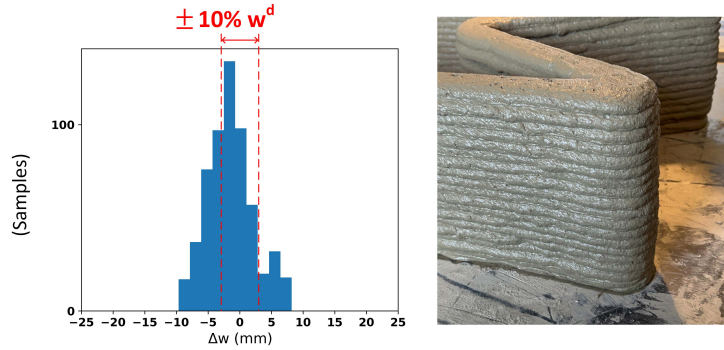


Figure 5.19: Histogram of filament width error and printed shape. T = 30 °C, with compensation given 10% of w^d as threshold.

compensation is applied, the peak of width error histogram falls within the range of (-5 mm, 5 mm), indicating that the width errors have been reduced.

In low-temperature environments, such as at 10 °C, the properties and behavior of concrete also undergoes significant changes. The decreased temperature affects two key areas: the curing process and the quality of material deposition. It is essential to consider the effects of low temperatures on the material's properties in its fresh state. This is because in a cold environment, the concrete curing process can be delayed, potentially leading to excessive material flow during deposition. Furthermore, when new layers are superimposed, there is a risk that they may cause the underlying layers to sag, compromising the integrity of the ongoing structure. However, these issues can be mitigated through velocity compensation adapting to variations in material viscosity caused by ambient temperature. Additionally, it's worth noting that during the material melting phase, the heat generated by this process can help warm up the building structure. This explains why, even in a low-temperature environment, material deposition can be controlled and maintain some level of consistency. Thus, the distribution of width errors in Figure 5.11 is less dispersed even without compensation, compared to 30 °C.

The obtained data demonstrates that in the range of 10°C – 30°C, the optimal printing environment, while adhering to material quantities, is at a temperature of around 20 °C, where the deviation length percentage is considerably lower compared to high or low-temperature printing. Figure 5.14 shows that even in the absence of compensation, the width error distribution exhibits limited dispersion, maintaining some level of consistency. Nonetheless, the implementation of the compensation strategy further constrains the

width errors to a narrower spectrum, thereby enhancing the overall printing quality. Indeed, as seen in the previous chapter, the range of robot parameter settings is more extensive at 20 °C, in contrast to 10 °C and 30 °C, which are more constrained. Maintaining a temperature around 20°C is crucial due to its ability to strike an ideal balance between several critical factors for successful 3D printing. At 20°C, the material is more likely to maintain stable rheological properties, facilitating consistent material deposition and reducing defects. Furthermore, this temperature allows the robot to operate within a broader parameter range, providing greater flexibility to achieve optimal outcomes. Thus, the data reveals that keeping the printing temperature around 20°C is a prudent choice to minimize defects during 3D printing while benefiting from a wider range of robot parameter adjustments, ultimately ensuring the quality of the final results.

5.5 Conclusion

This chapter focuses on the adaptive estimation and compensation of nozzle velocity during the in-printing stage. A neural network-based velocity estimator is developed using a dataset that encompasses various printing conditions. This allows for the real-time estimation of optimal nozzle velocity based on a given filament width setting. Leveraging the approach from Chapter 4, real-time tracking of the filament width error, denoted as Δw is made possible. This error, along with other critical parameters such as material flow and path curvature, serves as input to the estimator, which in turn outputs a nozzle velocity estimate. The resulting velocity error Δv multiplied by a variable gain G is then given to the nozzle-guidance robot control system to correct the velocity, thereby minimizing Δw , enabling consistent tracking of the reference width. The gain G is implemented so that compensation is triggered only when filament width deviation exceeds a pre-defined threshold. The methodology has been tested and validated in CIRMAP printing sessions at varying temperatures—10, 20, and 30 °C, demonstrating its robustness in maintaining print quality under diverse environmental conditions and constraints. Over the environmental conditions, the compensation strategy has an average response time of 1.5 seconds and an average deviated filament width of 13 cm. The compensation strategy was evaluated by conducting printing tests on a complex shape with a total filament length of 50.4 meters. These tests were performed under varying temperatures and accounted for changes in material properties. The results demonstrate that the compensation strategy substantially reduces the overall percentage of filament length that deviates from the target, thus confirming its efficacy in improving overall printing quality in un-

controlled environments. Furthermore, a temperature of 20 °C is found to be optimal for printing for a range from 10 to 30 °C, corroborating the findings presented in Chapter 4.

Post-printing stage: Preventive maintenance

Contents

6.1	Introduction	141
6.2	Predictive maintenance system	143
6.2.1	Description of the Flying 3D printing system	143
6.2.2	Operating principle description	145
6.3	Trajectory Generation : Crack Detection and Localization	145
6.3.1	Deep Learning for crack detection	145
6.3.2	Crack centerline extraction and localization	149
6.4	Model-based kinematic control of the soft arm	151
6.4.1	Modeling assumptions	152
6.4.2	Towards inverse kinematic model of the CBHA	154
6.4.3	Effort-based deformation of an inter-vertebra	159
6.5	Preventive maintenance: Crack repair	165
6.5.1	Soft-arm control strategy for crack repair	166
6.5.2	Relationship between material flow and input pressure	169
6.5.3	Experimental results	170
6.6	Discussion	171
6.7	Conclusion	173

6.1 Introduction

Additive manufacturing, which deposits materials layer by layer, including cement, has gained traction in the construction industry. A pivotal phase after material deposition in this domain is preventive maintenance. This is

essential as materials can elongate over time post-printing, leading to microscopic cracks. Indeed, the used materials (concrete, metal, wood ...) are subject to external conditions such as climate changes, humidity, etc. These cracks can compromise the material's mechanical properties, affecting tensile strength and fracture toughness, leading to fragile structures. While these micro-cracks are typically assessed by experts, complex surface structures can make certain areas inaccessible for both human and traditional rigid robots. Repairing these cracks at the first degradation stage is a subject of predictive maintenance. To address this challenge, this chapter introduces a novel integrated concept for automatic detection, localization and in-situ repair of microscopic cracks with a local intervention on the surface of the complex structures. This technology uses the principle of 3D printing of viscous material for crack repair. It focuses on a preliminary study for the utilization of soft-continuum robots to guide a nozzle mounted on an [Unmanned Aerial Vehicle \(UAV\)](#), to guide material deposit along a wall crack shape. The use of soft-continuum manipulators in the construction domain has garnered increasing interest in recent years. In the context of layer material deposition, the soft-continuum manipulators offer advantages such as enhanced dexterity, adaptability to various shapes, and the capability to deposit materials to areas that are inaccessible to traditional methods. The cooperation between an UAV and a flexible continuum arm makes it possible to scan a large area of the structure's surface and reach the location of microscopic cracks in less time, instead of using scaffolding for example. The drone can be controlled autonomously or with the operator in the loop. It is the latter option that is envisaged in this development, in order to take account of the safety requirements associated with using the drone in a confined space.

In this chapter, we will delve into our primary scientific contribution in the field of soft continuum hyper-redundant robots. The use of Hyper-redundant robots for guiding viscous material to be deposited inside cracks traces is justified by their ability to navigate through tight spaces and reach areas that may be inaccessible to humans or traditional robots. They can conform to complex and irregular surfaces and they can be equipped with various tools and instruments, allowing for a multi-modal approach to crack repair. Thus, the goal is to control the trajectory and the shape of these robots, which can reach a point in space while offering multiple possible configurations. The major challenge lies in solving the highly nonlinear equations governing this process while seeking a solution that optimizes energy expenditure during movement and while maintaining a constant velocity. More specifically, this chapter focuses on the kinematic modeling of a hyper-redundant system used in guiding tools for continuous material deposition along a crack. We will examine in detail both the control of nozzle movement and the continuous material depo-

sition process. Following this brief introduction, we provide a description of the experimental platform, consisting of a drone equipped with a flexible vacuum manipulator. Subsequently, the trajectory generation following the crack shape, derived from the detection and localization approach, is presented. The closed-loop control of the crack's path tracking is then introduced, focusing solely on the stationary phase. We will delve into the technical challenges, potential advantages, and the results of a real-time implementation.

6.2 Predictive maintenance system

In this section, a description of the predictive maintenance system is presented as a 3D printing mobile concept, followed by an explanation of the operating principles used to detect and repair microscopic cracks.

6.2.1 Description of the Flying 3D printing system

The experimental platform is a prototype for predictive maintenance against structural cracks on highest areas of infrastructures such as walls, bridges,... It is composed of an Unmanned Aerial Vehicle (UAV), a camera, and a soft arm, as shown in Figure 6.1. The idea is to design an industry-scale prototype that can automatically detect, locate and repair microscopic cracks by depositing continuously filament of material inside the cracks [Yang 2022a].

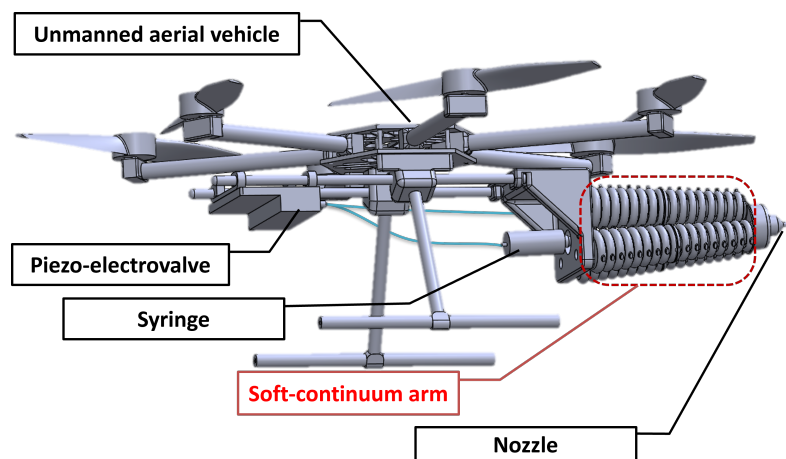


Figure 6.1: Predictive Maintenance Robot System

The **soft-continuum manipulator** studied in this research draws inspiration from the structure of an elephant's trunk (Figure 6.1), namely the compact bionic handling assistant (CBHA) [Lakhal 2018]. This soft arm is

employed to manipulate a nozzle for depositing materials onto intricate surfaces. Each flexible section of the CBHA consists of three tubes, controlled by electro-pneumatic actuators, as shown in the Figure 6.2. The electro-pneumatic controller uses the piezoelectric technology, which ensures a precise distribution. The system is equipped with a pressure sensor allowing a regulation of the output pressure. The position and orientation of each section are controlled by varying the pressure inside tubes. Six tubes can be loaded and unloaded with compressed air so that the structure can be moved in any desired direction.

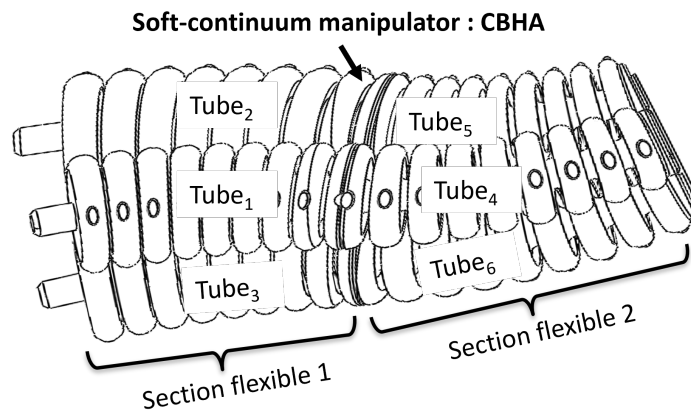


Figure 6.2: Description of the CBHA soft arm

Six wire potentiometer sensors are placed along each tube allowing to measure elongations of each tube. The voltages provided by wire-potentiometer sensors are proportional to the extension of each tube $l_{e,f}$, where $e = 1, \dots, 3$ and $f = 1, 2$ correspond to the wire-potentiometer and section flexible number, respectively.

The choice of a soft arm is justified by its ability to navigate through cluttered and confined environments due to its flexibility. Indeed, constrained areas may require complex movements from traditional rigid structures, potentially risking joint limitations. The use of flexible manipulators not only reduces inspection time but also minimizes energy consumption. The CBHA is used to guide a nozzle. The deposit system consists of a syringe. The syringe is connected to the electro-pneumatic by a pipe through the soft arm. The control of the material flow is done by air pressure.

In order for the system to detect and locate cracks, it is equipped with a sensor suite comprising a camera that captures image data, as well as ultrasonic sensors that provide distance data. The guidance system exchanges data with the onboard PC, facilitating efficient processing and accurate analysis of

6.3. Trajectory Generation : Crack Detection and Localization145

the gathered information. This synergy between the sensors and the onboard computer is crucial for ensuring the proper operation of the crack detection and localization system.

6.2.2 Operating principle description

The concept aims to automate the repair of cracks using specially designed robots and technologies. Achieving this goal involves several sequential steps, as illustrated in Figure 6.3. The initial step entails scanning the structures using a camera mounted on the drone, sending the images and the current system position to an embedded system for crack detection. Once a crack is detected, the vision system categorizes it into different classes. Based on the crack's size and location, a repair decision is made, and the system generates and transmits the crack's shape and central line information to the mobile platform and the flexible robot.

The subsequent phase involves calculating the coordinates of the crack within the drone's absolute frame of reference. This calculation allows the mobile platform to navigate to the crack's location. Once the mobile platform is in a stable position, the flexible arm guides the nozzle along the crack's central line while dispensing the repair material.

6.3 Trajectory Generation : Crack Detection and Localization

This section outlines a deep learning-based approach for detecting and locating cracks to generate a trajectory for tracking the crack shape. The approach explores images captured by the embedded visual sensor (camera) of the drone to detect existing cracks. Additionally, a central line (i.e., a skeleton) of the crack is extracted to generate a tool trajectory for the repair task. The crack's location in both the drone's frame and the global frame is then computed. A deep learning instance segmentation model is employed for crack detection, followed by a morphological transformation of the median axis for extracting the central line. Localization is achieved by applying the frame transformation to the previously calculated crack location.

6.3.1 Deep Learning for crack detection

The detection of an existing crack on a wall surface is an essential step for structural health monitoring and for the procedure of predictive maintenance.

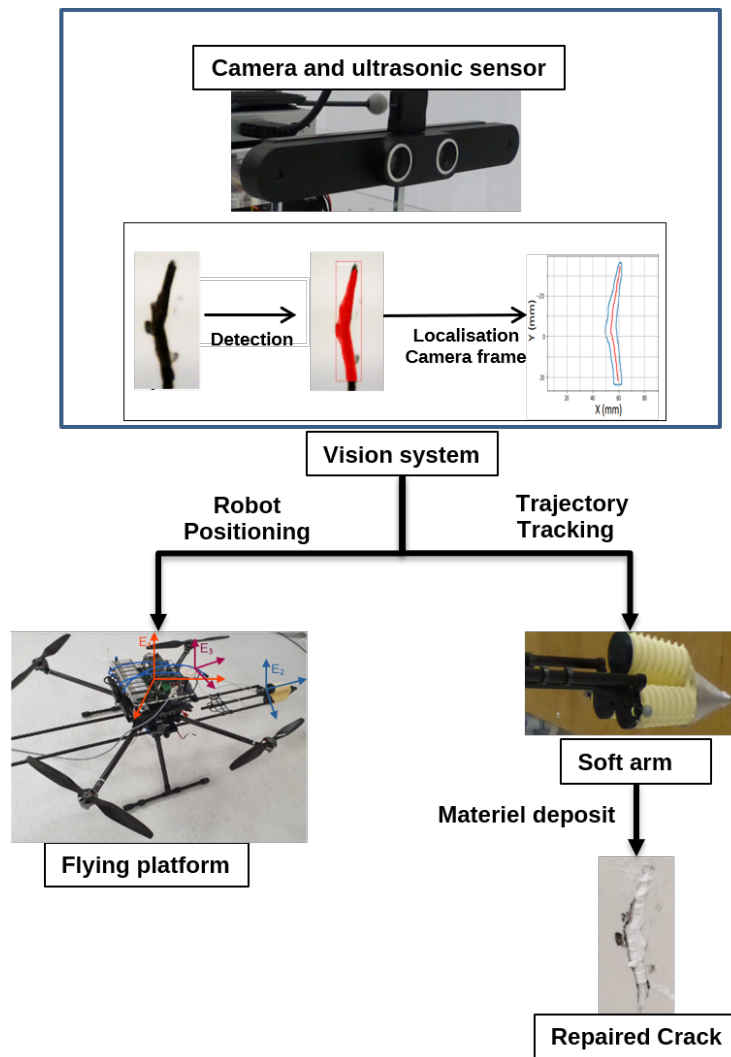


Figure 6.3: Functional scheme of automatic predictive maintenance for microscopic cracks

6.3. Trajectory Generation : Crack Detection and Localization 147

Visual-based Deep Learning models are a set of widely implemented methods for this task. Some research works have implemented image classification [Flah 2020] or object detection models [Park 2020] for the detection and localization of cracks or cracked area on concrete surfaces, however, those models don't meet our requirement for the purpose of automatic crack repair, because the tool path of the robot arm should overlap the structural shape of the crack. On the basis of the 2D image data available from visual sensors, we adopted the previously applied instance segmentation model Mask RCNN [He 2017] for the detection and segmentation of cracks. Given an image as input, the model is able to segment the crack area in pixel level in the image frame.

An image dataset is prepared based on two public concrete crack image datasets containing over 100,000 images totally [Özgenel 2017, Maguire 2018, Dorafshan 2018c]. The images in those datasets are classified into two categories according to the existence of cracks, but without annotation. Since we need to train an instance segmentation model, instead of using directly the datasets which are ready for training a binary classification model, we select certain images to create an annotated crack image dataset. When selecting the images to annotate, different environmental conditions are considered, such as shadows, the complexity of concrete background, etc., in order to improve the performance of the model.

The annotated dataset contains RGB images, each image contains between 0 and 4 cracks. With Computer Vision Annotation Tool (CVAT), we have annotated 300 images containing 493 crack instances and have split them into train (260 images) and validation (40 images) sets. For each image, a binary mask is created, in which the value 0 is assigned to background pixels and the value i is assigned to the pixels of the i -th crack. To enhance the diversity of the dataset, data augmentation methods are applied randomly, such as image flipping, blur and shadowing.

The transfer learning methodology is used in the training of the model. The model is developed based on a pre-trained instance segmentation model Mask R-CNN, which is trained on a large scale dataset, namely Microsoft COCO [Lin 2014]. As mentioned above, our annotated dataset is not a large one, while MS COCO contains over 200,000 annotated images. The pre-trained Mask R-CNN model is able to detect 80 different categories of objects, but cracks are not included. Thus, by applying transfer learning, we can train a model on our annotated crack dataset for crack detection, without losing the robustness of the model by fine-tuning the pre-trained one. The model is constructed upon ResNet50 with Feature Pyramid Network (FPN) as backbone. The model is flexible and has the ability to be generalised to other instance-level recognition tasks [Zhao 2019], which allows us to fine tune for crack detection. The multi-task loss function 6.1 is optimized during the

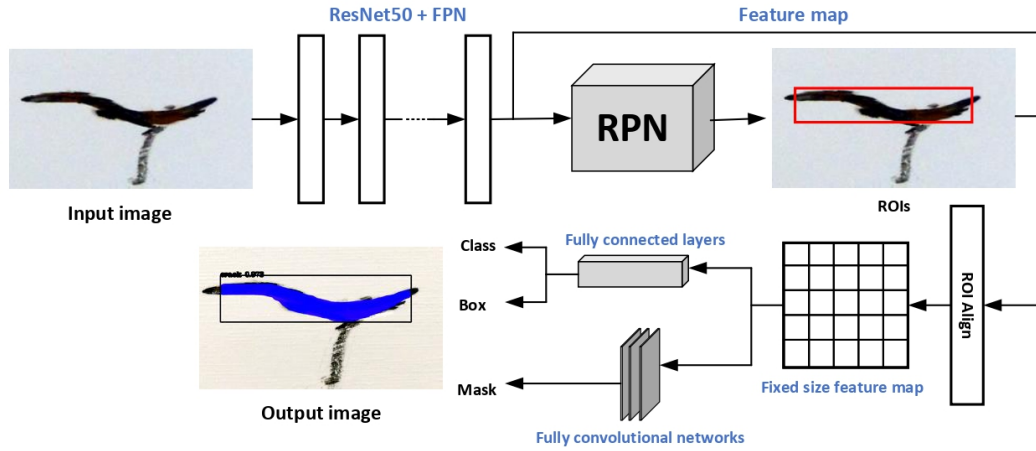


Figure 6.4: The architecture of Mask RCNN

training. The architecture of the adopted model is shown in Figure 6.4. The crack segmentation task is achieved in two stages: firstly, the input image is fed to the backbone networks for feature extraction and then Region Proposal Network (RPN) generates a number of Region of Interest (RoI) candidates in which an optimal one will be obtained through regression. Then the feature map and the chosen RoI are aligned and a fixed-size feature map is obtained, it is sent to two branches, one for classification and bounding box, the other generates a mask for pixel-level segmentation.

$$L_{Mask-RCNN} = L_{class} + L_{box} + L_{mask} \quad (6.1)$$

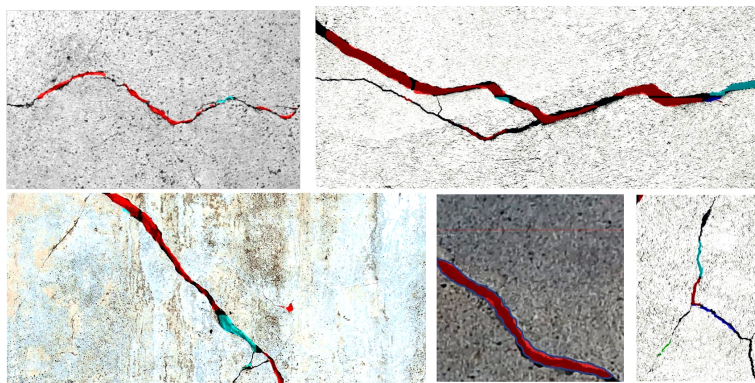


Figure 6.5: Results of the segmentation model applied on different images of cracks

The trained model [Yang 2022a] is tested on sample images with different sizes that are not contained in the training or validation dataset. Figure 6.6.

6.3. Trajectory Generation : Crack Detection and Localization 149

shows the bounding boxes and binary masks generated for detected crack instances. The shape of the crack can be reconstructed with its contour in the image coordinate system. The real time implementation of the model is also tested with the same graphic card on the video stream captured by a camera with a resolution of 640 x 480 pixels, it achieves 2 ~ 4 frames per second (FPS).

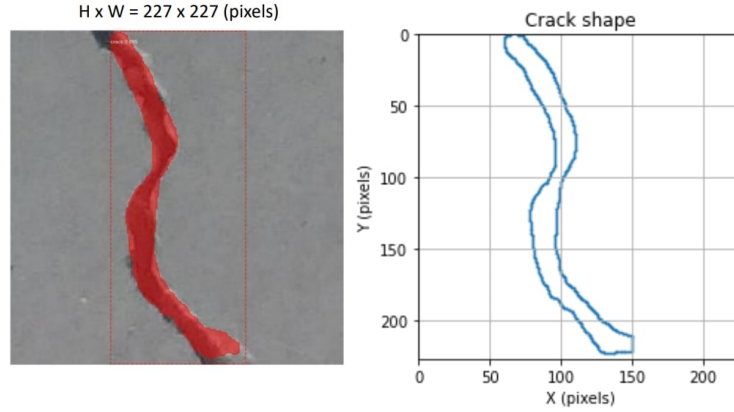


Figure 6.6: Crack shape reconstruction in image frame

6.3.2 Crack centerline extraction and localization

In order to allow the soft arm to access and follow the shape of the detected crack, the localization consists of two steps to be depicted in the following: centerline extraction and frame transformation.

Firstly, we extract the centerline of the crack in the image frame. The trajectory to be followed by the robot in the reparation system should represent the structural shape of the detected crack. In the image coordinate system, given S the set of points of the crack region bounded by C the contour of the crack shape, the centerline of the crack is the set of points $P \in S$ having more than one closest point on the contour C . As the output of the detection model contains a binary mask representing the crack, by applying the morphological **Media Axis Transform (MAT)** algorithm (refer to Chapter 4 Section 4.3.3) on the binary mask, we can obtain the coordinates of the points on the centerline in the image frame. Figure 6.7 shows an example of crack centerline extraction in the image frame. The medial axis transformation also gives the local widths of the crack at every point on the centerline, expressed in pixels unit.

A frame transformation is then applied to the points on the centerline in the image frame obtained from the previous step. In order that the soft arm

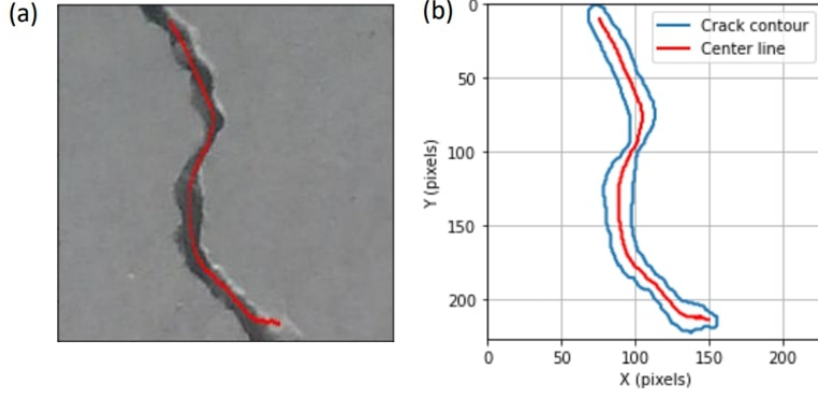


Figure 6.7: Extraction of crack centerline in image coordinate system. (a): Crack centerline; (b): reconstruction of crack and centerline in image coordinate system

can reach the detected crack, it is necessary to locate the centerline in the frame of soft arm as well as in the world frame.

Notably, the distance between the scanning system and the scanned surface is indispensable for accurate localization of the detected crack. For this purpose, the ultrasonic sensor embedded on the UAV is used for obtaining the distance between the camera and the scanned surface.

For the operation of predictive maintenance, the tool path for the end effector of the soft arm robot is identical to the crack centerline. The centerline is expressed as $[m \ n]$ in the pixel frame. In the frame of the scanned surface, the tool path of the end effector of the robot X_{ee} can be given by:

$$X_{ee} = R_{cam}^{-1}(M_{cam}^{-1}(dist \cdot C_{ee}) - Trans) \quad (6.2)$$

where

- R_{cam} is the rotation matrix of the camera fixed to the UAV.
- M_{cam} is the intrinsic matrix of the camera.
- $Trans = [g_1, g_2, g_3]^T$ is the translation vector of the camera with respect to the scanned surface frame.
- $dist = g_3$ is the depth value, as the UAV stabilises and is perpendicular to the scanned surface, it's equal to the distance.
- $C_{ee} = [m \ n \ 0]^T$ is the vector of the centerline in image frame.

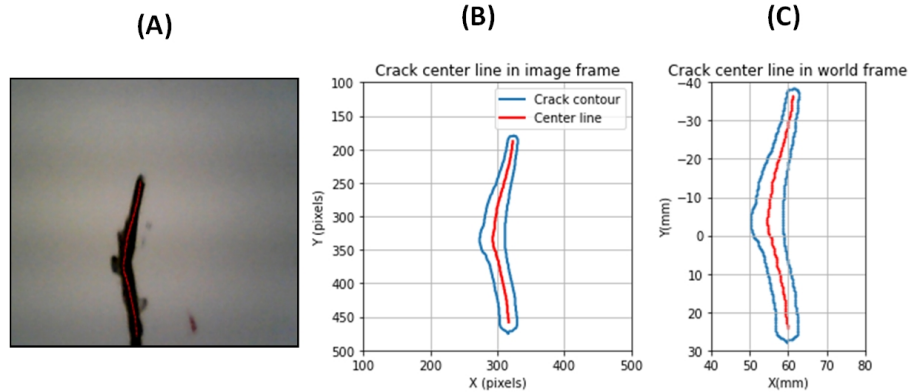


Figure 6.8: Crack centerline extraction and localization. **(A)**: Crack centerline in raw image; **(B)**: reconstruction of crack and centerline in image coordinate system (pixels); **(C)**: reconstruction of crack and centerline in real dimension (mm)

Figure 6.8 shows an example of localization of extracted centerline in real dimension. The unit of the obtained X_{ee} is in mm and will be sent to the controller of the soft arm robot to execute the maintenance procedure, the robot guides the tip of the nozzle to deposit material for repairing the localized crack in an injection way. The unit of the local widths of the crack is also transformed to mm after the localization step, this allows to classify the crack into microscopic, mesoscopic and macroscopic according to its size.

The overall processing time from the capture of an image to the calculation of the tool path takes around 0.3 s, allowing rapid execution of this visual-based approach.

6.4 Model-based kinematic control of the soft arm

The inverse kinematics involves determining the value to be applied to the actuators to obtain the desired position and orientation of the end effector. The model-based inverse kinematic control of soft arms is a topic of interest in the field of robotics. Soft robotics involves the use of flexible and compliant materials to create robots that can interact with their environment in a more natural and adaptable way. The model-based inverse kinematic control of soft arms is a complex and multidisciplinary research area. Several research papers have explored different approaches to model-based inverse kinematic control of soft arms. One such approach is the use of **Finite Element Method (FEM)**-based kinematic models which use finite element methods to design al-

gorithms for kinematic inversion and planning [Katzschmann 2019a]. Another approach is the use of Artificial Neural Network (ANN) for inverse kinematics. One paper presents a novel inverse kinematics solution for a robotic arm based on an ANN architecture [Almusawi 2016]. Additionally, multiple adaptive neuro-fuzzy inference systems have been used to solve the inverse kinematics problem of a robot arm trajectory [Refaai 2022]. Other papers have focused on the development of analytical solutions for inverse kinematics. For example, one paper presents a complete analytical solution to the inverse kinematics of a robotic arm, which allows for control of the arm to any reachable position in an unstructured environment [Gan 2005]. Model-based reinforcement learning has also been explored for closed-loop dynamic control of soft robotic manipulators [Thuruthel 2018]. This approach combines models of the robot's dynamics with reinforcement learning algorithms to improve control performance. Additionally, a model-based control method using a reduced order finite element model with a state observer has been developed for dynamically closed-loop controlled soft robotic arms [Katzschmann 2019b]. Furthermore, there are papers that discuss the kinematic modeling and control of multi-section continuum arms [Godage 2015], shape control of soft continuum finger robots using parametric curves [Mbakop 2021], and the control of soft robotic manipulators using visual servoing [Zhang 2017]. These papers highlight the importance of considering physical constraints, such as joint space limitations and actuator mechanics, in the kinematic models.

In our case, we can replicate the kinematic behaviors of the CBHA by making certain functional and structural assumptions. This category of manipulators pertains to soft-continuum manipulators, which are distinguished by their continuous property. These manipulators consist of interconnected elements configured in a continuous or uniform manner and are fabricated using 3D printing techniques and plastic-based materials. In this section, we focus on modeling and solving the kinematics of a specific type of hyper-redundant manipulators that exhibit soft-continuum characteristics. This process involves discretizing the soft-continuum manipulator into a series of parallel modules, ultimately reconstructing the overall kinematic features related to bending and shaping of the soft-continuum manipulator. In this section, the assumptions used in kinematic modeling is first presented. The kinematics of the CBHA is developed.

6.4.1 Modeling assumptions

In this work, the modeling approach was inspired from the modeling concept of parallel rigid manipulators. The mathematical model is obtained by considering the continuum manipulator as a concatenation of multiple parallel

robots.

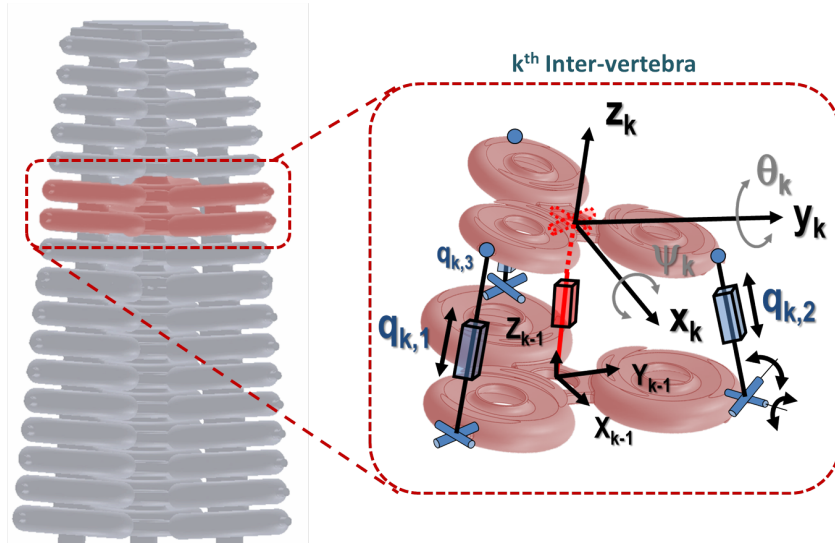


Figure 6.9: Schematic of an inter-vertebra modeled as parallel robot with 3 UPS-1 UP

The **Inverse Kinematic Model (IKM)** of the soft arm is developed under the following assumptions:

- The continuum manipulator is considered as a series of k^{th} vertebrae.
- An inter-vertebra is a flexible and non-deformable structure with a 3-DoF mobility. It is modeled with 3 UPS-1UP (3 Universal-Prismatic-Spheric - 1 Universal-Prismatic) joints.
- The manipulator yaw motion is not applicable with the existing mechanical links between the tubes.
- The UAV is considered stable and static in a reference position with contact to the wall, allowing the soft arm to operate autonomously without external disturbances.
- The interaction between the soft robot and the surface during material deposition is considered viscous, leading to a near-zero impact on the robot's dynamics

Based on these assumptions, the considered soft arm is composed of 16-vertebrae with 48-DoF in total. It consists of a lower and upper vertebra connected by three limbs with the same kinematic configuration, and a central leg. The limbs are modeled by a kinematic configuration of type UPS, in

which only the prismatic joints are active allowing to control the position and orientation of the upper vertebra relative to the lower vertebra. $q_{k,e}$ represents the variation of the length of the prismatic joint, where $e = 1, \dots, 3$ is the index of the active joint and k is the index of the frame. The central leg is modeled by a kinematic configuration of type UP located in the center of an intervertebra. It is considered as a passive joint.

6.4.2 Towards inverse kinematic model of the CBHA

In this section, the IKM of the CBHA is presented. As mentioned above, the entire CBHA is emulated by a series of parallel robots each comprising 3-DoF. The concatenation of intervertebral components transforms the overall system into an n-DoF system, introducing complexity into the model. The challenge arises from having knowledge solely of the final position $X_{arm} = \{x_{arm}, y_{arm}, z_{arm}\}$, representing the tip of the CBHA, corresponding to the crack's trajectory. This situation significantly complicates the calculation of the CBHA arm model, as the arm's end can reach its final position in various ways, presenting the challenge of multiple solutions within a limited framework of the inverse kinematic model. To address this issue, it is essential to establish an efficient selection criterion along with appropriate constraints to determine the optimal posture of the CBHA from the desired position. To do this, we generate a curve passing through the center of the CBHA, assuming constant curvature. In our approach, we also consider a uniform distribution of vertebrae along this curve. These assumptions not only help reduce calculation time but also lead to optimized results in terms of posture and energy consumption. The kinematic model allows for establishing the relationship between X_{arm} and the active prismatic joints denoted as $q_{k,e}$. In other words, it provides a representation that links the motion of X_{arm} to how the various prismatic joints behave and interact with each other. To gain a better understanding of the employed methodology and to follow the various steps, we have depicted the entire process in Figure 6.10.

6.4.2.1 Curve generation and frame placement

The Frenet-Serret frame placement method is commonly used to associate frames to a curve based on its tangent and orientation. However, when the curve involves direction changes, the Frenet-Serret frames can result in torsion. In the case of the bionic arm CBHA, which has frequent orientation changes without possible torsion, an alternative approach based on Bishop Frames is more suitable [Hu 2011, Khadem 2020]. Furthermore, the Bishop frame has been utilized in the modeling and control of continuum robots. Each section

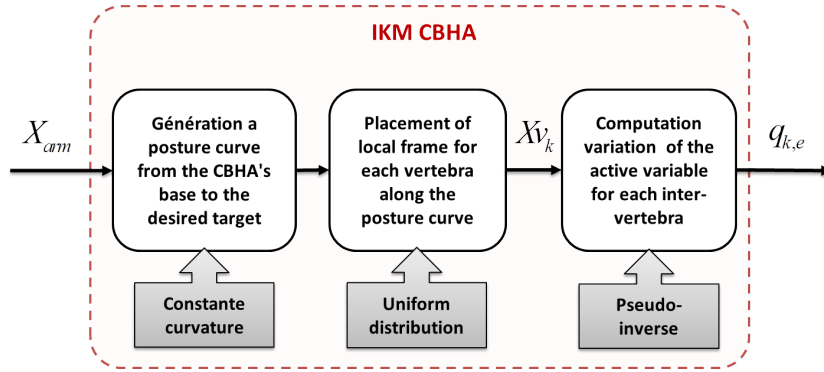


Figure 6.10: Calculation of the Inverse Kinematic Step for the CBHA

of a concentric tube robot was modelled as a deformable curve with a Bishop frame attached to each point along its length [Khadem 2020]. This approach allows for accurate control of the robot’s motion by considering the orientation of the Bishop frame. A Bishop frame has three orthonormal unit vectors: a tangent vector to the curve $T_1(k)$, a normal vector $N_1(k)$ and a binormal vector $N_2(k)$. Figure 6.11 shows various Bishop Frames ($O_k, N_{1k}, N_{2k}, T_{1k}$) along the central curve of the CBHA.

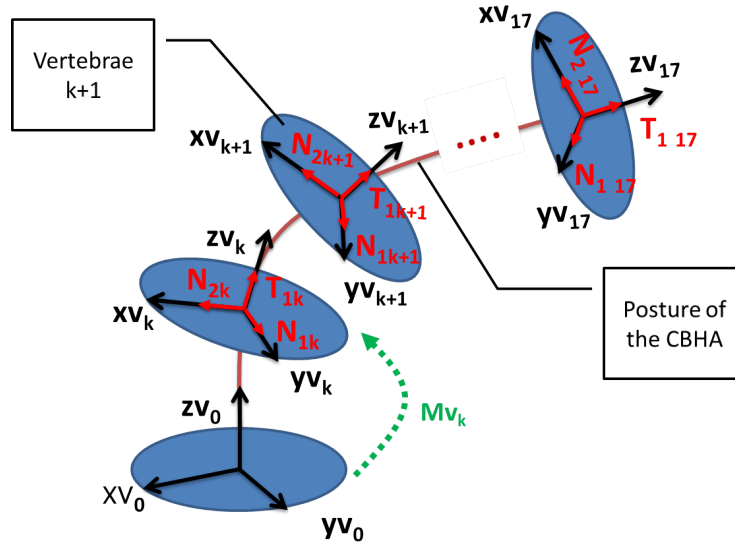


Figure 6.11: Placement of Bishop frames on the CBHA’s central curve

Then, the homogeneous transformation of equation (6.5) is obtained in function of the vector (6.3) and the matrix (6.4):

$$\mathbf{T}_v(k) = [xv(k) \ yv(k) \ zv(k)] \tag{6.3}$$

$$\mathbf{Rv}(k) = [\mathbf{T1}(k) \mathbf{N1}(k) \mathbf{N2}(k)] \quad (6.4)$$

$$\mathbf{Mv}_k(k) = \begin{pmatrix} \mathbf{Rv}(k) & \mathbf{Tv}(k) \\ 0 & 1 \end{pmatrix} \quad (6.5)$$

The obtained curve is parameterized by a vector $Tv \in \mathbb{R}^3$, where k is a variable parameter representing the length when crossing the curve and admits the following constraints:

- The constant curvature with a perfect arc of circle;
- The curve starts perpendicular to the horizontal plane.
- The frames placements are evenly spaced along the curve.

Once the vertebrae are positioned along the curve representing the overall CBHA posture, it is now possible to calculate the prismatic variations of each intervertebral joint since their position and orientation are obtained using the Mv_k matrix. The following section elaborates on the approach used to express the variables $q_{k,e}$ in terms of the position and orientation of the upper vertebra relative to the lower vertebra.

6.4.2.2 Kinematic modeling of a soft inter-vertebra

The task at hand is to discuss the Jacobian of a parallel robot. The Jacobian matrix is a fundamental tool in robotics that relates the velocities of the robot's end-effector to the velocities of its joints. It provides important information about the robot's kinematics and can be used for tasks such as inverse kinematics, trajectory planning, and control. In our case, the Inverse Kinematic Equation (IKEs) of an inter-vertebra of the soft continuum manipulator (Figure 6.9) are obtained by calculating the joint variables $\dot{q}_{k,e=1:3}$, corresponding to the pose (position and orientation) of the upper vertebra's center, relative to the lower vertebra frame. In the case of the considered soft arm, the inter-vertebra is considered as a 3-DoF parallel robot, because of movement constraints related to the passive kinematic chain Universal-Prismatic (UP). In fact, the rotation with respect to the z axis, denoted by $Rot(z, \phi_k)$, and the translations relative to the x and y axes denoted by $Trans(x, xv_k)$ and $Trans(y, yv_k)$, respectively, are not considered, because it does not exist a movement on these axis. Only the translation along the z axis is possible which is denoted by $Trans(z, zv_k)$. Hence, the IKEs can be formulated as follows:

$$q_{k,e} = f(zv_k, \psi_k, \theta_k) \quad (6.6)$$

where the angles θ_k and ψ_k indicate pitch and roll angles, respectively.

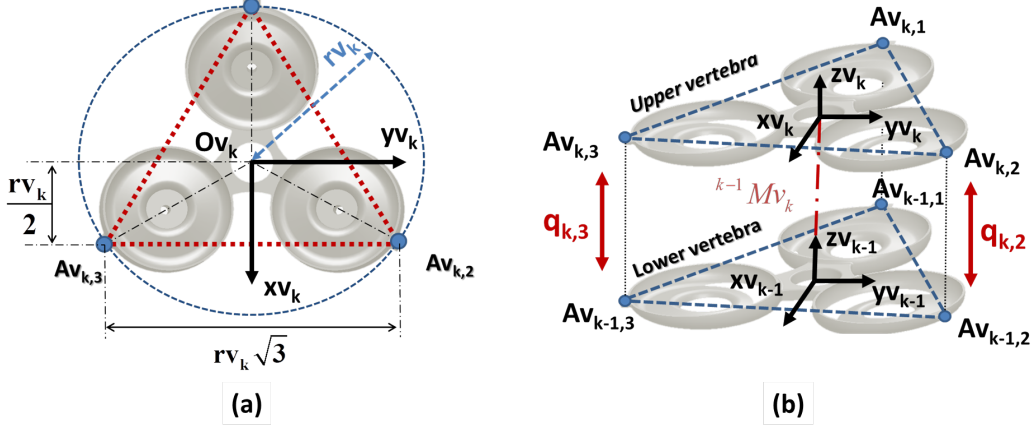


Figure 6.12: Geometric relationship of an inter-vertebra

$Av_{k,e}$ represents the connection point between the extensible driving leg $e = 1, \dots, 3$ and the vertebra k , as shown in Figure 6.12. For each vertebra, the points $Av_{k,1}Av_{k,2}Av_{k,3}$ form an equilateral triangle. The frame $Rv_{k-1}(Ov_{k-1}, xv_{k-1}, yv_{k-1}, zv_{k-1})$ is attached to the lower vertebra of origin Ov_{k-1} , center of the triangle $Av_{k-1,1}Av_{k-1,2}Av_{k-1,3}$ and the frame $Rv_k(Ov_k, xv_k, yv_k, zv_k)$ is attached to the upper vertebra of origin Ov_k , located at the center of the equilateral triangle $Av_{k,1}Av_{k,2}Av_{k,3}$. Knowing that the entire shape of the CBHA is conical, it is necessary to find the circumcircle radius rv_k of the considered vertebra, where $k = 1, \dots, N$ is the number of vertebrae. Let rv_{max} and rv_{min} , respectively the radius of the base and the apex of the backbone, the radius of each vertebra rv_k can be calculated by:

$$rv_k = \frac{k}{N}(rv_{min} - rv_{max}) + rv_{max}, \quad (6.7)$$

where N is the number of vertebrae. Consequently, we derive the equation that expresses the joint variables $q_{k,e}$ based on the position and orientation (Zv_k, θ_k, ψ_k) of the upper vertebra relative to the lower vertebra. For the k^{th} vertebra, this relationship is articulated as follows [Lakhal 2015]:

$$\begin{aligned}
q_{k,1}^2 &= zv_k^2 + 2rv_kzv_kS\theta_k - 2rv_{k-1}rv_kC\theta_k + rv_{k-1}^2 + rv_k^2 \\
q_{i,2}^2 &= zv_k^2 + zv_krv_k(\sqrt{3}C\theta_kS\psi_k - S\theta_k) - \\
&\quad rv_krv_{k-1}\left(\frac{\sqrt{3}}{2}S\theta_kS\psi_k + \frac{3}{2}C\psi_k + \frac{1}{2}C\theta_k\right) + rv_{k-1}^2 + rv_k^2 \\
q_{i,3}^2 &= zv_k^2 - zv_krv_k(\sqrt{3}C\theta_kS\psi_k + S\theta_k) + \\
&\quad rv_krv_{k-1}\left(\frac{\sqrt{3}}{2}S\theta_kS\psi_k - \frac{3}{2}C\psi_k - \frac{1}{2}C\theta_k\right) + rv_{k-1}^2 + rv_k^2
\end{aligned} \tag{6.8}$$

The notations C and S stand for the *cosine* and *sine* functions, respectively.

The primary objective when determining the inverse Jacobian matrix is to relate the linear velocities of the joint variables, denoted as $\dot{q}_{k,e}$, to the kinematics of the upper-vertebra. This relationship is systematically delineated in the equation (6.9):

$$\begin{bmatrix} \dot{q}_{k,1} \\ \dot{q}_{k,2} \\ \dot{q}_{k,3} \end{bmatrix} = Jcbha_k^{-1} \begin{bmatrix} V_{Ov_k} \\ \omega_{Ov_k} \end{bmatrix} \tag{6.9}$$

Here, V_{Ov_k} stands for the translation velocity, while ω_{Ov_k} signifies the angular velocity pertaining to the center of the k^{th} vertebra. To compute the inverse Jacobian matrix, represented as $Jcbha_k^{-1}$, it's essential to analyze the joint velocity $\dot{q}_{k,e}$ by referencing the subsequent equation:

$$\dot{q}_{k,e} = ui_{k,e}^T V_{A_{k,e}} \tag{6.10}$$

Where $ui_{k,e}$ denotes the unit vector connected with leg k and $V_{A_{k,e}}$ is the velocity of the connection point $A_{k,e}$ ($k = 1, \dots, 3$), as shown in the Figure 6.12.

The unit vector $ui_{k,e}$ is expressed as follows :

$$ui_{k,e} = \frac{Av_{k-1,e}Av_{k,e}}{\|Av_{k-1,e}Av_{k,e}\|} = \frac{Qv_{k,e}}{q_{k,e}} \tag{6.11}$$

The coordinates of the connection point $Av_{k,e}$ relative to the frame $Av_{k-1,e}$ are given as follows:

$$\begin{bmatrix} Qv_{k,e} \\ 1 \end{bmatrix} = {}^i T_{i-1} \begin{bmatrix} Av_{k,e} \\ 1 \end{bmatrix} - \begin{bmatrix} Av_{k-1,e} \\ 1 \end{bmatrix} \tag{6.12}$$

Where, ${}^i T_{i-1}$ is the transformation matrix of the upper vertebra frame relative to the lower vertebra, obtained in equation (6.5).

$${}^k Mv_{k-1} = \begin{pmatrix} C\theta_k & S\theta_kS\psi_k & S\theta_kC\psi_k & 0 \\ 0 & C\psi_k & -S\psi_k & 0 \\ -S\theta_k & S\psi_kC\theta_k & C\theta_kC\psi_k & zv_k \\ 0 & 0 & 0 & 1 \end{pmatrix}. \tag{6.13}$$

The notations C and S stand for the cosine and sine functions, respectively. The coordinates of the three connection points $A_{k,e}$ are given by the coordinates (6.14), relative to the centre of the k^{th} vertebra, as shown in Figure 6.12-a.

$$Av_{k,1} = \begin{bmatrix} -rv_k \\ 0 \\ 0 \end{bmatrix}; Av_{k,2} = \begin{bmatrix} \frac{1}{2}rv_k \\ \frac{\sqrt{3}}{2}rv_k \\ 0 \end{bmatrix}; Av_{k,3} = \begin{bmatrix} \frac{1}{2}rv_k \\ -\frac{\sqrt{3}}{2}rv_k \\ 0 \end{bmatrix}. \quad (6.14)$$

The velocity $V_{A_{k,e}}$ is given by the vector product below :

$$V_{Av_{k,e}} = V_{Ov_k} + Av_{k,e} \times \omega_{Ov_k} \quad (6.15)$$

By combining the relationships (6.15), (6.11) and (6.10), we obtain :

$$\dot{q}_{k,e} = \left(\frac{Qv_{k,e}}{q_{k,e}} \right)^T V_{Ov_k} + \left(\frac{Qv_{k,e}}{q_{k,e}} \times Av_{k,e} \right)^T \omega_{Ov_k} \quad (6.16)$$

Thus, from equation (6.16), the inverse Jacobian matrix $Jcbha_k^{-1}$ is obtained as follows:

$$Jcbha_k^{-1} = \begin{bmatrix} \frac{Qv_{k,1}}{q_{k,1}} & \frac{Qv_{k,1}}{q_{k,1}} \times A_{k,1} \\ \frac{Qv_{k,2}}{q_{k,2}} & \frac{Qv_{k,2}}{q_{k,2}} \times Av_{k,2} \\ \frac{Qv_{k,3}}{q_{k,3}} & \frac{Qv_{k,3}}{q_{k,3}} \times A_{k,3} \end{bmatrix} \quad (6.17)$$

The Jacobian provides us with a means to establish the relationship between joint variables and the position of the upper vertebrae relative to the lower vertebrae $\dot{X}v_k = J(q_{k,e})\dot{q}_{k,e}$. However, it's important to note that the joint variables $q_{k,e}$ vary depending on the pressure within the tube $Ps_{e,f}$, which induces deformation. The following section outlines the approach employed to determine the relationship between the variables $q_{k,e}$ and the pressures $Ps_{e,f}$.

6.4.3 Effort-based deformation of an inter-vertebra

In this section, an in-depth study is conducted on the deformation of a vertebra in response to the pressure effort, injected into the tubes. As mentioned earlier, the CBHA is actuated by a proportional piezo-pneumatic actuator. This actuator is capable of delivering adjustable pressure within a range of 0 to 1.5 bar.

The primary objective of this study is to establish the relationship between the pressure of each tube $Ps_{e,f}$, where $e = 1, \dots, 3$ and $f = 1, 2$ correspond to the tube number and flexible section number, respectively, applied by the

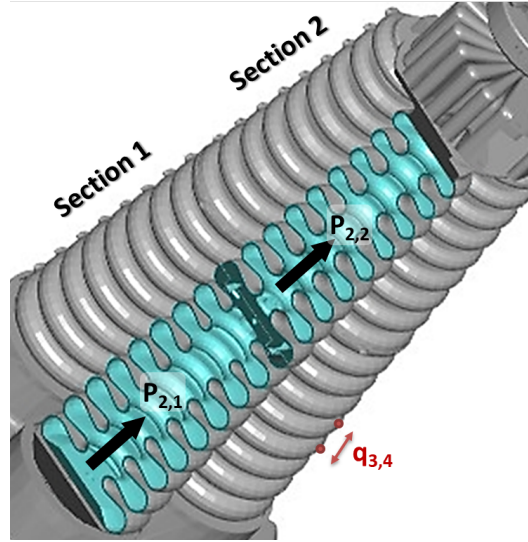


Figure 6.13: Cross-section of the pressure propagation in each CBHA's tube allowing deformation.

actuator and the variations in the elongations of the prismatic of the parallel robot $q_{k,e}$, as shown in Figure 6.13 . In other words, we aim to comprehend how the pressure applied in the pneumatic tubes of the CBHA impacts the microscopic deformations observed within a vertebra of the robot.

This investigation will enable us to gain better global control over the CBHA's behavior in different scenarios by adjusting the pressure accordingly. Additionally, it will provide us with essential insights to optimize the system's performance and ensure a precise and controlled response tailored to the specific needs of the application, which, in this case, involves material deposition.

In the context of our study, we begin with the assumption that the movements of the CBHA have a quasi-static behavior. As a result, the transmission of pressure through a tube can be considered nearly instantaneous. This implies that when we apply pressure at one end of the tube, this pressure rapidly propagates along the structure to induce motion, even if this movement is executed slowly. However, it is essential to note that this assumption of quasi-instantaneous remains valid only when the movements remain at significantly slower velocity compared to the dynamic characteristics of the system.

The analysis of deformations in an inter-vertebral component of the CBHA is conducted using a finite element method (FEM) and validated through ANSYS software, as shown in Figure 6.14. The Finite Element Method (FEM) is a numerical technique used to approximate the solutions of partial differential equations. When applied to model a soft inter-vertebra, it involves discretizing

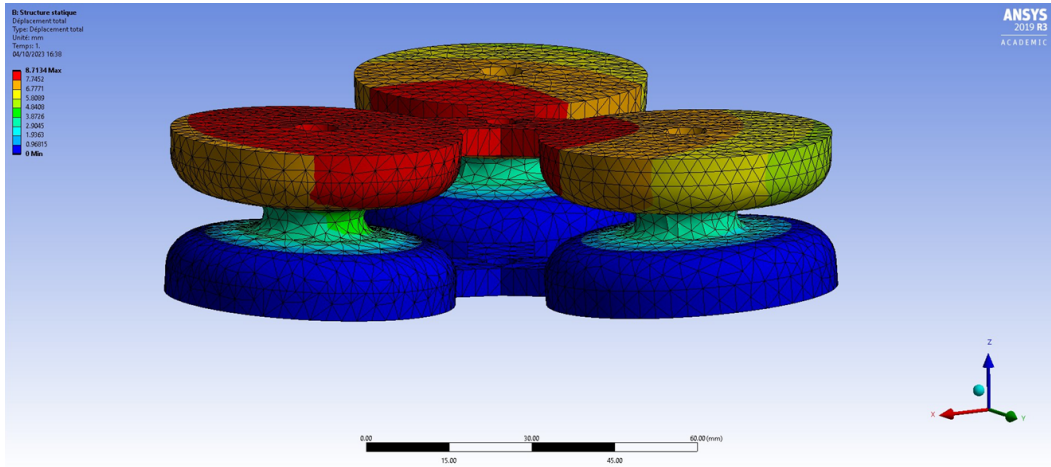


Figure 6.14: Finite Element Method (FEM) Simulation for Studying Microscopic Deformations and Mechanical Behavior of CBHA Using ANSYS.

the arm into smaller, finite elements to represent its behavior. Let's assume we are dealing with a one-dimensional a soft inter-vertebra. The latter can be represented by a series of connected elements, each with its own properties as follows:

- Divide the inter-vertebra into a series of discrete elements. For simplicity, let's assume we have n elements, denoted by e_1, e_2, \dots, e_n .
- At each node of an element, we define the variables of interest. For example, in an inter-vertebra, this might include displacement (u) and internal forces (F). These variables are typically expressed as functions of spatial coordinates and time. For element e_k , let u_k represent the displacement at the node associated with this element.
- $N_k(x)$ represents the shape function associated with element e_k . These functions determine how the displacement varies within the element. They are usually chosen based on the type of element (linear, quadratic, etc.) and the problem being modeled.
- For each element, we can express the equilibrium of forces:

$$\sum F_{ext} = \sum F_{int} \quad (6.18)$$

Here, F_{ext} represents external forces applied to the element, and F_{int} represents the internal forces.

- The strain (ε) is related to the displacement gradient (du/dx) through a material-specific constitutive equation. In soft materials, this relationship may be nonlinear.

$$\varepsilon = \frac{dx}{du} \quad (6.19)$$

- This equation relates the stress (σ) to the strain (ε). In soft materials, this relationship is often nonlinear.
- Define material properties like density, Young's modulus for the Polyamide 6 (PA6), constitutive material of the inter-vertebra. For polyamide PA6 typically falls within the range of 2.5 to 4.0 gigapascals (GPa).
- Assemble the equations from all the elements to create a global system of equations.
- Apply appropriate boundary conditions, which may include fixed displacements, applied forces, or other constraints.
- The resulting system of equations to obtain the displacement field ($u(x)$) and internal forces F_{int} .

The results generated by ANSYS, after model resolution, include information about deformations, stresses, and displacements, as illustrated in the Figure 6.15, Figure 6.16 and Figure 6.17. These findings facilitate a deeper understanding of the flexible structure's response to the specified loads and boundary conditions.

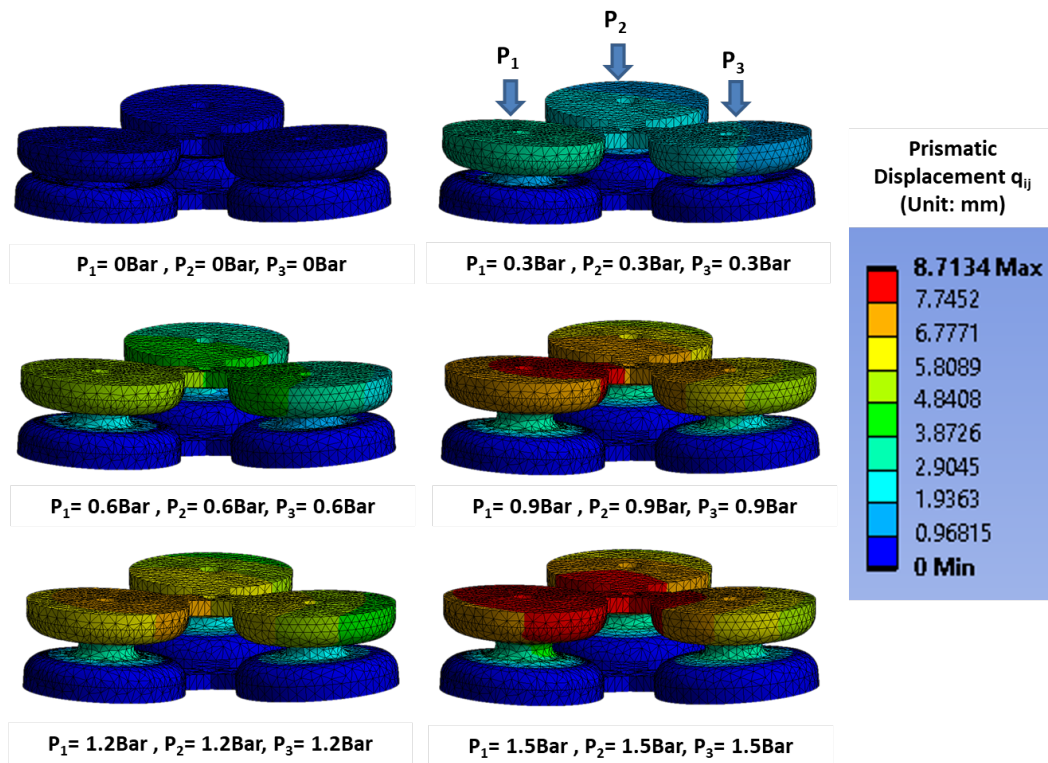


Figure 6.15: Results Generated by ANSYS for the Scenario Where All Tubes Are Simultaneously Supplied with the Same Pressure from 0 to 1.5 Bar

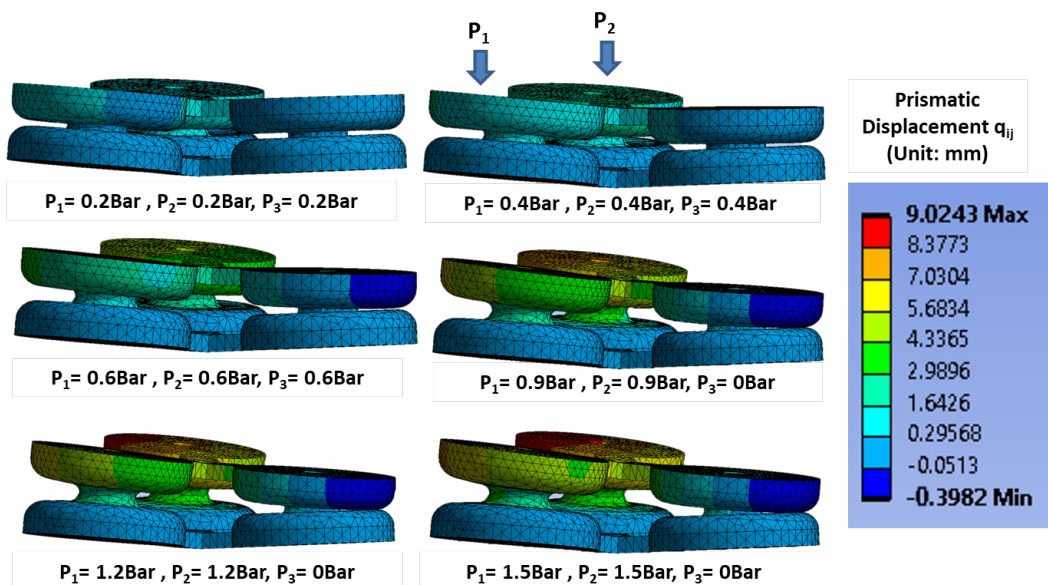


Figure 6.16: Results Generated by ANSYS for the Scenario with Simultaneous Pressurization of Two Tubes from 0 to 1.5 Bar

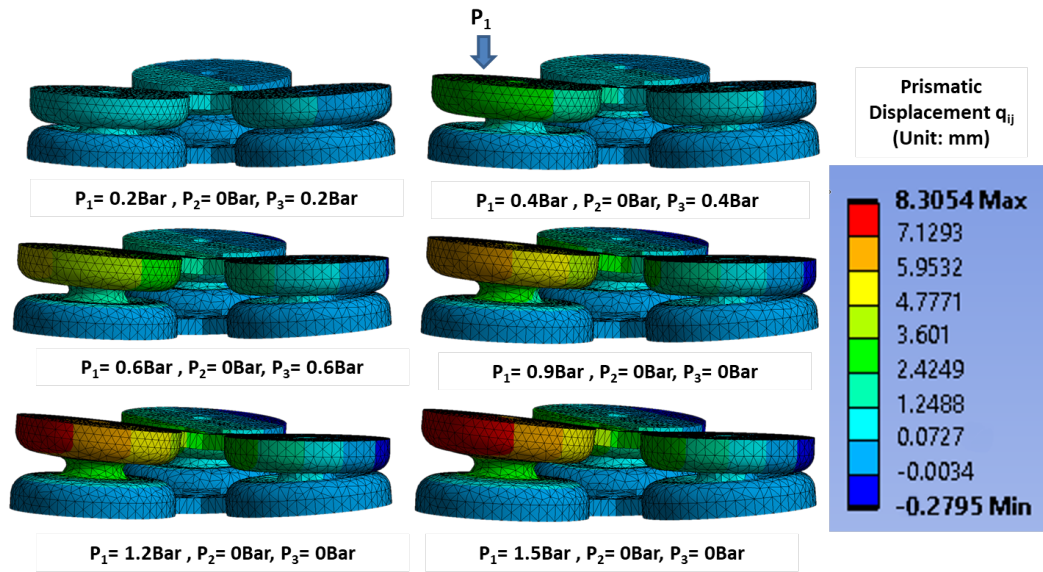


Figure 6.17: Results Generated by ANSYS for the Scenario with Only One Tube Supplied with Pressure from 0 to 1.5 Bar

The results obtained indicate that the variation in prismatic elongation, denoted as $q_{k,e}$, is not uniform and is closely related to the number of activated tubes. As shown in the figures, when pressure is applied to all three tubes simultaneously, the elongation varies in the range of 0 to 8.71 mm (Figure 6.15). However, if pressure is applied to a single tube, the elongation ranges from -0.30 mm to 8.30 mm (Figure 6.17), and when two tubes are activated, the variation in prismatic elongation extends from -0.4 to 9.02 mm (Figure 6.16).

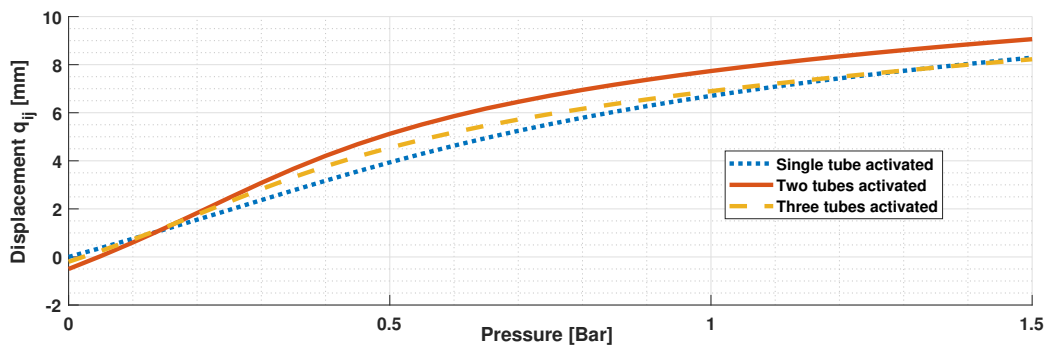


Figure 6.18: Comparative Analysis of Displacement Variation with Pressure Across Single, Double, and Triple Tubes

The Figure 6.18 illustrates the displacement variation in relation to pressure across three distinct scenarios: the activation of one tube, two tubes,

and three tubes. As pressure escalates, so does the elongation, which is an expected correlation. Notably, the displacement observed with three activated tubes significantly surpasses that of a single tube at the same pressure level. Furthermore, the displacement with two activated tubes stands out as the highest among the three scenarios at every pressure point. The slopes of these curves appear linear, hinting at an almost proportional relationship between pressure and displacement for an activated tube. However, this slope becomes steeper as more tubes are brought into action. In essence, engaging additional tubes results in a more pronounced increase in elongation for an equivalent pressure variation.

Based on the three curves representing different scenarios (Figure 6.18), we derive a third-degree polynomial trend-line of the form :

$$q_{k,e} = a_1 \cdot P s_{e,f}^2 + a_2 \cdot P s_{e,f} + a_3 \quad (6.20)$$

The coefficients corresponding to each scenario are identified in the Table 6.1.

Coefficient	a1	a2	a3
Single tube activated	-2.53	9.39	-0.14
Two tubes activated	-4.54	12.94	-0.46
Three tubes activated	-3.62	10.85	-0.16

Table 6.1: Polynomial trend-line coefficients for the three different scenarios

The trend curves allow us to estimate that from the pressures; however, we aim to derive pressure variations from the results of the inverse kinematic model, i.e., variations in $q_{k,e}$. Using Equation (6.20), there are two possible real solutions for each scenario due to the coefficients listed in the Table 6.1 and the quadratic nature of the equation. Nevertheless, in our specific situation, only the solution with positive pressure values is considered valid. Therefore, the solution takes on this particular form:

$$P s_{e,k} = \frac{-a_2 + \sqrt{a_2^2 - 4a_1(a_3 - q_{k,e})}}{2a_1} \quad (6.21)$$

Therefore, depending on the current position of the CBHA and the required pressure variation ($\Delta P s_{e,k}$) for motion and trajectory tracking, the coefficients will be chosen accordingly.

6.5 Preventive maintenance: Crack repair

In this section, we present the methodology of 3D printing solution for preventive maintenance in crack repair. This is based on kinematic-based control of

soft-continuum arm robot to guide a real-time material deposit inside cracks. In the upcoming sections, we will build upon the foundational assumptions established earlier. As a reminder, these assumptions include the UAV's stability and static positioning against the wall, which enables the soft arm to function autonomously without external disruptions. Additionally, we assume that the interaction between the soft robot and the surface during material deposition is viscous, resulting in minimal impact on the robot's dynamics. In the forthcoming sections it's worth noting that only the second flexible section of the CBHA is affixed to the drone, a decision driven by payload constraints. In this section, our primary objective is to showcase our control over material deposition using a soft-continuum arm robot. Firstly, we briefly recap the various steps in the 3D printing process, wherein a drone employs advanced vision systems to identify cracks, then accurately guides a nozzle using a soft-continuum arm, and finally deposits a repair material. We also describe the control of material deposition flow rate based on the continuum arm's movement velocity. Finally, we discuss experimental results concerning the accuracy of deposited material along the crack path.

6.5.1 Soft-arm control strategy for crack repair

The system architecture of the overall system is shown in Fig. 6.19. The different frames used to describe the kinematics of the system are shown in Fig. 6.20.

- The first frame $X_{UAV} = \{x_{UAV}, y_{UAV}, z_{UAV}\}$ is attached on the IMU of the UAV. The coordinates of the frame are given in a relative way to the world frame $X_{World} = \{x_{World}, y_{World}, z_{World}\}$.
- The second frame $X_b = \{x_b, y_b, z_b\}$ is attached to the base of the arm. The coordinates of the frame are given relatively to the UAV frame X_{UAV} .
- The third frame $X_{arm} = \{x_{arm}, y_{arm}, z_{arm}\}$ is attached to the tip of the arm. The coordinates of the frame are given relatively to the world frame X_{World} .
- The last frame $X_{crack} = \{x_{crack}, y_{crack}, z_{crack}\}$ is attached to the wall where the cracks are situated. The coordinates of the crack are given relatively to the world frame X_{World} .

The first step occurs with the vision system that performs the detection, classification and localization tasks. After receiving an image from the 2D camera, the system starts its detection task using the deep learning algorithm. Once

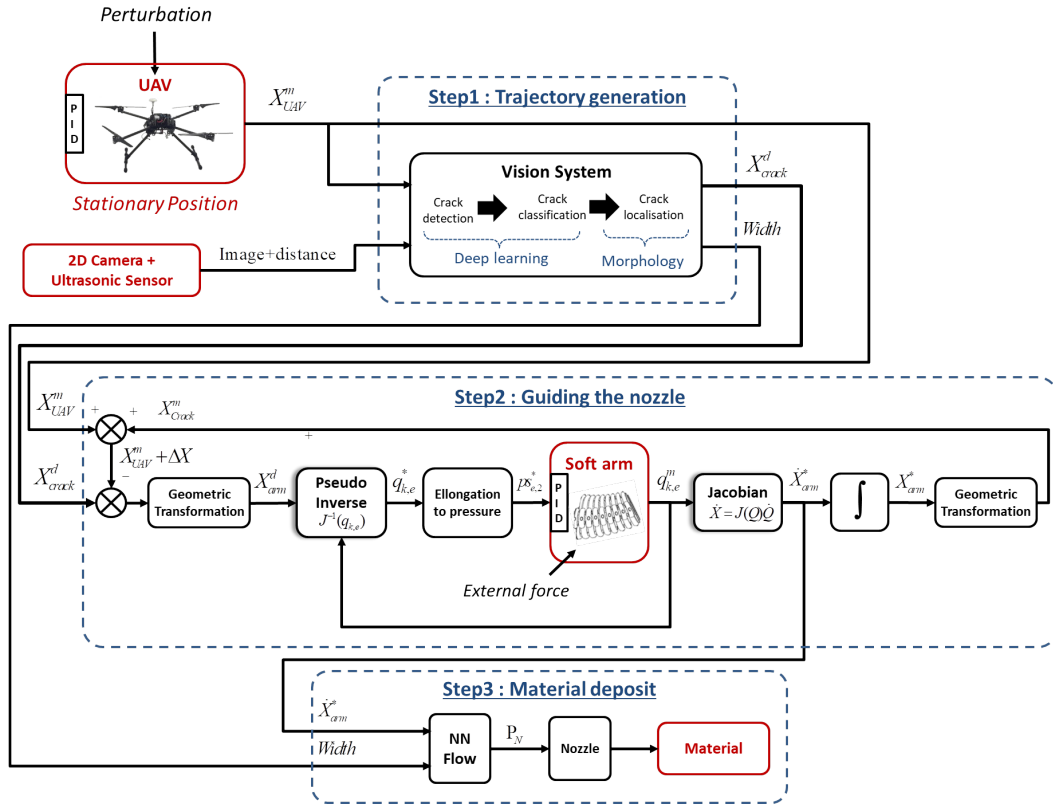


Figure 6.19: Predictive maintenance robot system control scheme for crack repair

the crack is detected, its width will be estimated and then the crack will be classified and a decision will be made according to the feasibility of reparation. The localization of the crack will be done using the image, the ultrasonic data and the IMU of the UAV X_{UAV}^m . The coordinates of the crack X_{Crack}^d relative to the world frame can be expressed by using the aforementioned data, thus, from the image obtained by the 2D camera, the vision system allows us to obtain the desired trajectory of the tool X_{Crack}^d relative to the world frame. The trajectories of the UAV X_{UAV}^d and soft arm X_{arm}^d are calculated from the desired trajectory X_{Crack}^d , in such a way that the crack is in the workspace of the soft arm, as represented in Fig. 6.21. Indeed, the set of points in the crack trajectory must be located inside the convex hull shown in red in the Fig. 6.21-b and Fig. 6.21-c.

The Fig. 6.21 represents the workspace of the soft arm, the blue point is given by the Opti-track system. Each position in the workspace of the arm corresponds to a combination $\{P_{s1,2}, P_{s2,2}, P_{s3,2}\}^d$.

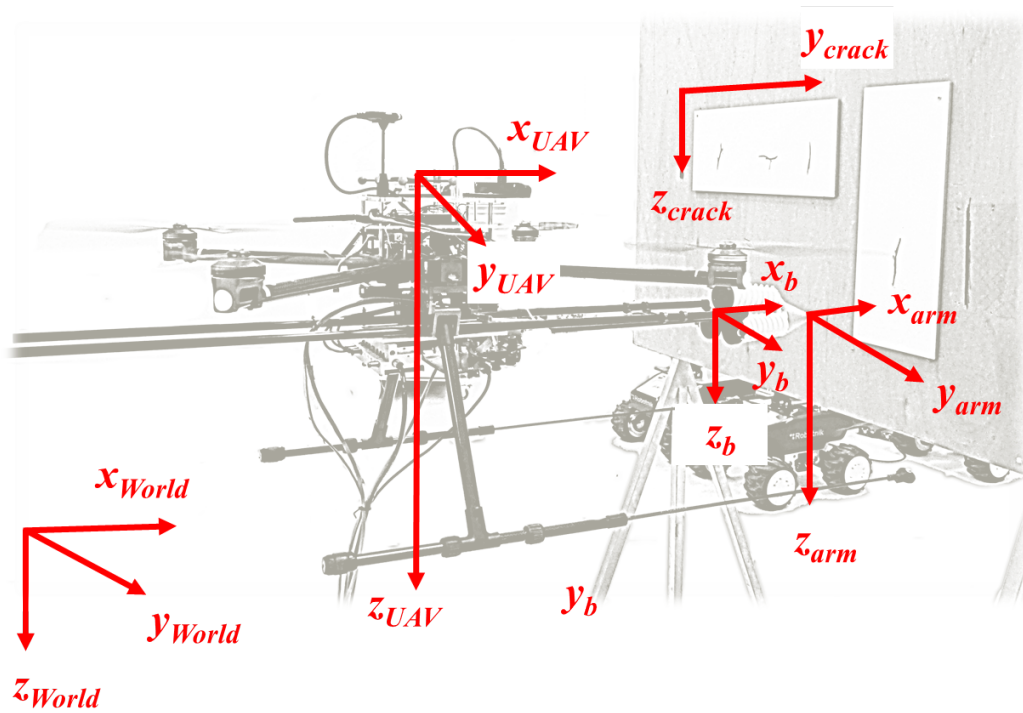


Figure 6.20: Associated frames of the robot system

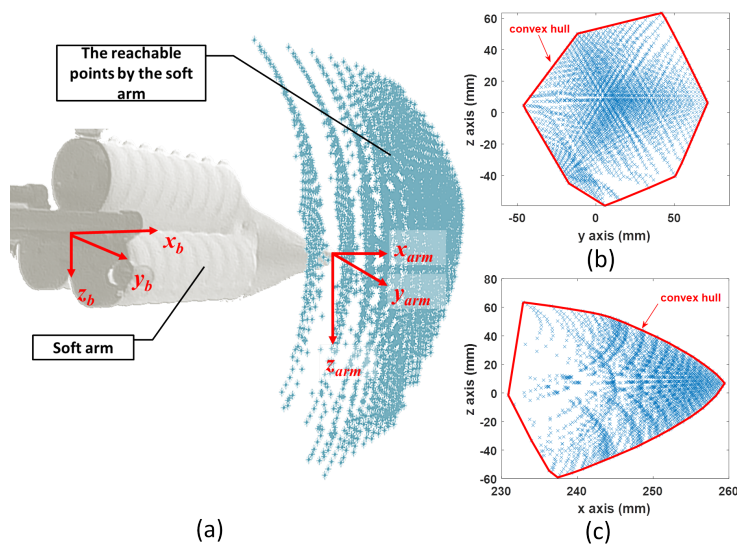


Figure 6.21: Workspace of the soft arm (a) perspective view (b) z-y view (c) z-x view

6.5.2 Relationship between material flow and input pressure

The system is equipped with a syringe containing material, which is operated using compressed air P_N , as shown in Figure 6.22. The compressed air propels the material through a flexible tube that extends through the flexible arm to a nozzle affixed at the end of the flexible arm. This solution serves to reduce the weight of the flexible arm and mitigate the risk of deforming the working space of the flexible arm.

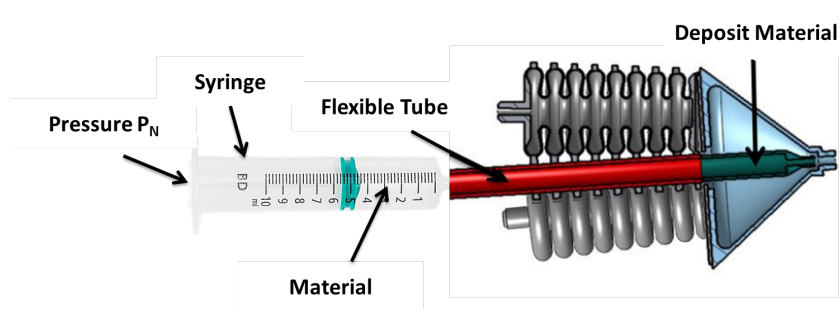


Figure 6.22: Material Delivery System with Syringe

To perform the quality of the deposit, the material characteristics are studied in order to estimate the control pressure through the nozzle. Indeed, the pressure controlling the flow rate at the nozzle outlet depends on the displacement velocity of the nozzle and the width of the crack. An industrial robot is used to characterise the size of the nozzle outlet cord according to the deposit velocity and the pressure applied on the tube, as shown in the Fig. 6.24. Thus, for the same formulation of the material, a nozzle velocity/flow rate correlation is obtained. The calibration and measurement steps must be carried out for each type of material. In our case, only the acrylic sealant material is considered. During the test, the value of the nozzle velocity varies between 4 mm/s and 18 mm/s with a step of 1. The pressure inside the tube is between 0.4 and 1.4 Bar with a step of 0.1. Thus, a learning base of 168 samples is obtained. The width of the cords are measured by a vernier caliper. This dataset is used to develop a neural network NN allowing to obtain an approximate pressure control value from the width of the crack and the deposit velocity of the material. In our case, the NN is obtained for a multi-layer perceptron architecture with 2 hidden layers with 5 neurons in each layer. The mean square error (MSE) result obtained on the tested samples is : 4.745×10^{-5} .

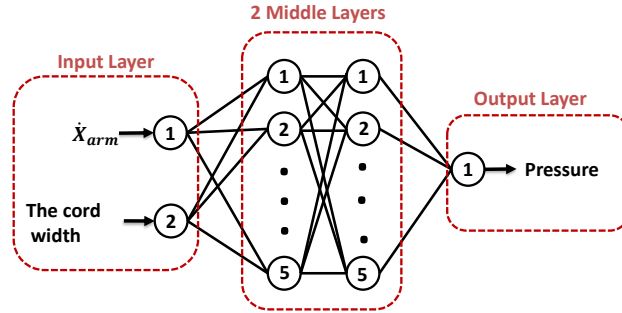


Figure 6.23: Neural Network architecture for modeling the material deposit pressure

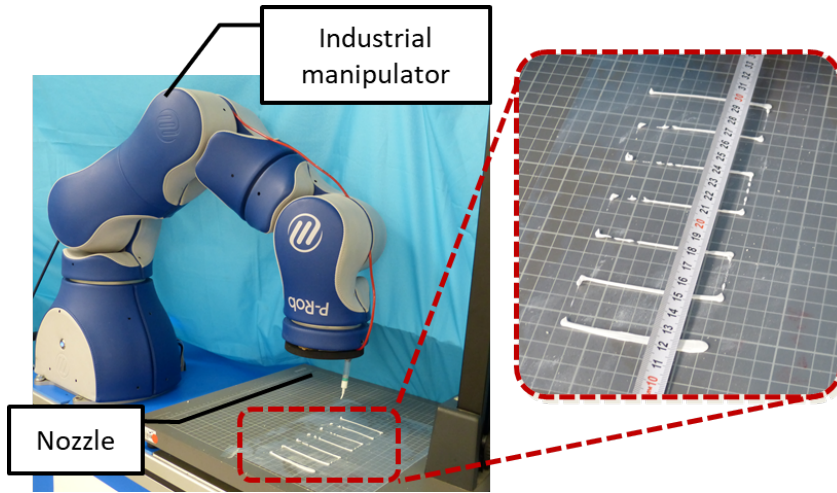


Figure 6.24: Rear and forward movements for pressure estimation of deposited material

6.5.3 Experimental results

Figure 6.25-a and 6.26-a show the trajectories of the tip of the arm (nozzle) during the deposit of putty materials on the crack 1 (vertical shape) and crack 2 (horizontal shape), respectively. The desired trajectories represent the center-lines of the reconstructed shapes of the cracks after crack detection and classification technique. The measured trajectory is issued from the Opti-track system and the estimated trajectory is generated from the inverse kinematic model of the soft arm. It is noticed from these experimental tests that the estimated kinematic model reconstruct globally the desired trajectory, while the measured trajectory based on the Opti-track vision capture is perhaps sensitive to micro-motion of the UAV in its stationary positioning. Figure 6.25-b, 6.25-b and 6.25-c represent the Euclidean errors along x, y and z axes for the crack 1. Whereas, Figure 6.26-b , 6.26-c and 6.26-d represent the the

Euclidean errors along x, y and z axes for the crack 2 It is noticed that the errors are less than 5 mm. However the error in z can be relatively higher than the others and can be explained by the gravity effect on the soft arm.

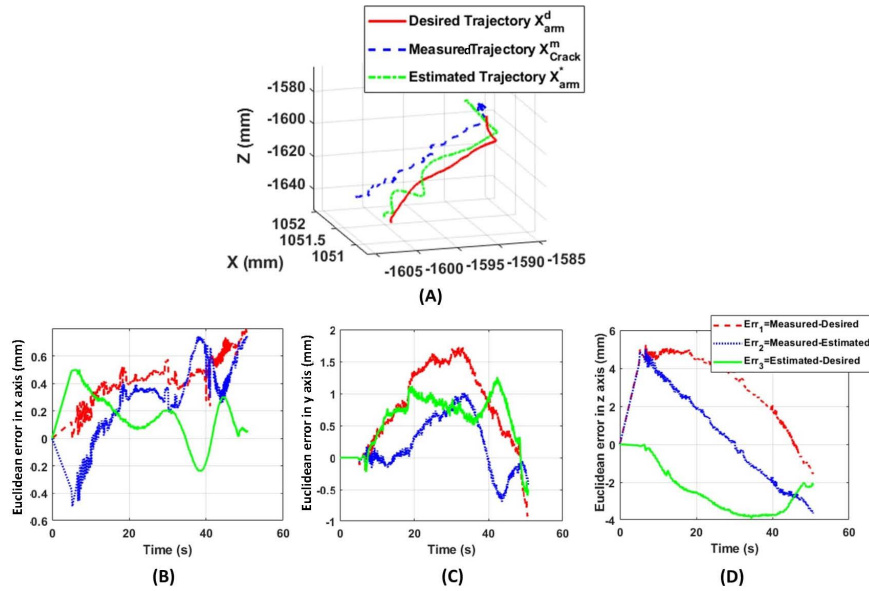


Figure 6.25: Trajectory of the tip of the arm during the reparation process of the crack 1. (A) 3D position tracking of the crack 1. (B) X-axis Error. (C) Y-axis Error. (D) Z-axis Error.

Euclidean Errors in Figure 6.25 and Figure 6.26 conclude that the proposed kinematics model is able to predict the position of the tip of nozzle with position errors less than 5 mm, where the nozzle diameter is about 5 mm.

In Figure 6.27, a sequential representation of the deposit material during the deposit of a putty material is shown. The accuracy of tracking tasks by the system is shown through in the video [Lakhal 2021], for online targets tracking.

Finally, based on the results of Figure 6.27 and the Euclidean errors in Figure 6.25, the performance of the microscopic crack detection and localization using deep learning technique is demonstrated.

6.6 Discussion

Artificial Intelligence based method using deep learning techniques has been developed to detect and repair cracks automatically. After applying the automatic detection algorithm on the wall surface, the classification of the cracks

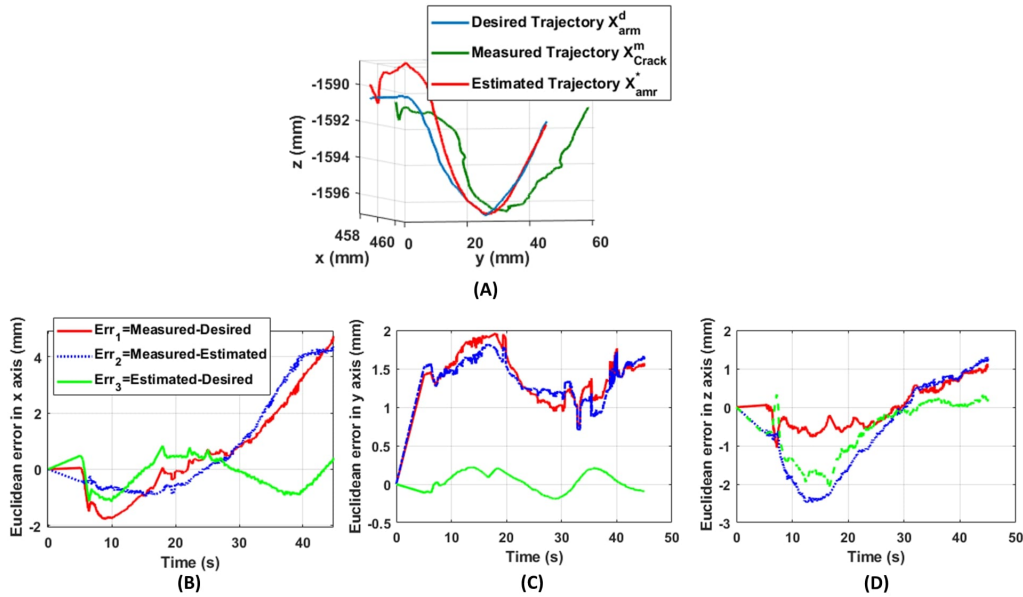


Figure 6.26: Trajectory of the tip of the arm during the reparation process of the crack 2. (A) 3D position tracking of the crack 2. (B) X-axis Error. (C) Y-axis Error. (D) Z-axis Error.

is obtained by dividing them according to their sizes into: microscopic (less than 5mm width), mesoscopic (in between 5 and 10mm width) and macroscopic (more than 10mm width). In this work, we focused on the microscopic cracks, where the preparation of the surface is not required, only the repair is needed. Then, the localization of the centerline of the crack shape is determined. Using the current position of the UAV, the ultrasonic sensor and the camera embedded on the robot give the measures for planning the trajectory to be followed by the tip of the soft continuum arm. The model-based control of the position of the arm tip is applied along the crack with various disturbances such as the not zero stability of the UAV but also the contact of the soft arm during the deposit the material. This is because errors are corrected by the soft arm, which has a faster and more accurate stability than the millimetre-scale drone. The stability of a UAV in flight is slightly more complex, especially for millimetre-scale movements. In our case study, the UAV is in a stationary position throughout the repair, which means that the sum of the opposing forces is zero and therefore the displacement of the system's centre of gravity is small due to the ground effect. In addition, when the soft arm comes into contact with the wall, it unloads to maintain a constant force when depositing the material, but also to avoid large disturbances on the movement of the drone that could involve a crash. Indeed, the combination of the soft arm capabilities and the flying mobile platform offers great

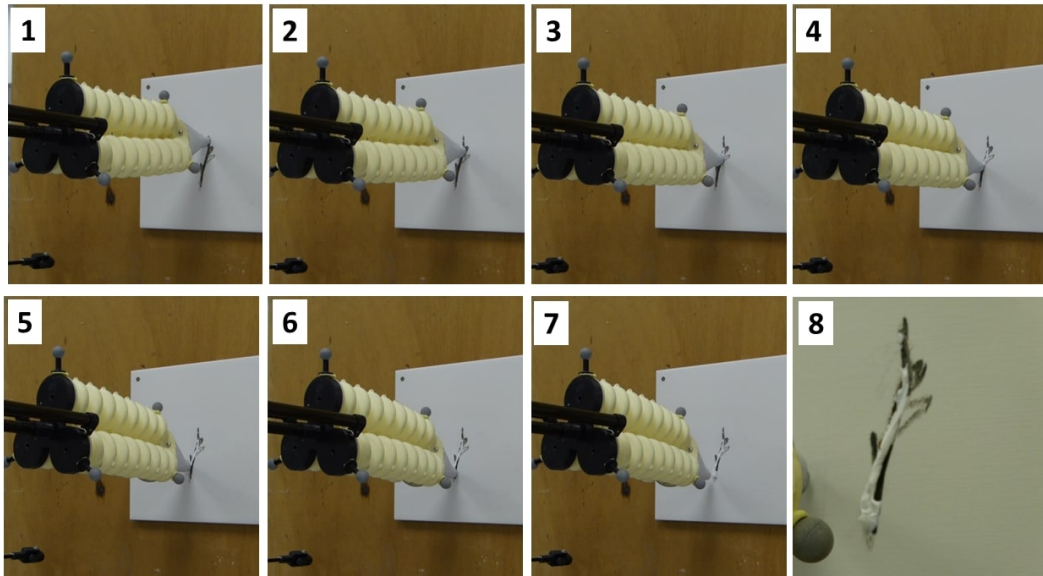


Figure 6.27: Repair steps for crack 1

cooperation to perform an operational task. The soft arm can reach complex position of the crack, while the UAV can guide and load the arm with different postures. In view of the results obtained, the proposed concept achieves promising performances in terms of precision and robustness for automatic detection and repairs in predictive construction maintenance. The accuracy is in the millimetre range. The trajectory tracking is well respected despite the total instability of the drone. However, as we can see from the curves, the intervention time is about 60 seconds for a crack of about 80mm in size. In fact, for precise control and optimal material deposition quality, it is preferable to work in quasi-static kinematics. If one wishes to increase the speed of loading and unloading of the pressure of the flexible arm, it is necessary to consider using other types of sensors than piezo. In Figure 6.27, the results are relatively satisfactory in terms of the quality of the material deposit. Indeed, a more or less identical contact force is obtained along the whole trajectory. Nevertheless, we have determined the gain A by assuming that the forces are exerted only on the z axis. However, curved trajectories require larger deformations of the flexible arm, which implies that the contact force is not only on the z -axis but on all three axes.

6.7 Conclusion

This work deals with an integrated robotic concept design for automatic crack detection and repair. This concept is composed of a stationary UAV and a

soft continuum arm. The latter is used to guide the putty material but also to reach complex shapes of microscopic cracks in flat and oblique surfaces of wall surfaces. The concept integrates the tasks of detection and localization of the crack shapes using deep learning techniques. The repair task is summarized by a continuous deposit of the material to fill the cracks. The stationary UAV is interacted with the wall surface using wheeled contact, while the soft arm is not directly in contact with the external surface. The methodology of the inverse kinematic control of the soft arm has been deployed. A neural network-based predictive model allows estimating the relationship between the bending tube' length and the input pressure. The experimental results show the performance of the kinematic control as a function of material deposition accuracy.

In future work, the objective is to implement a joint control on the robot position and the material deposition flow rate, as a function of the width and the deep of the crack, to improve the quality of the deposit.

Conclusion and Perspectives

Contents

7.1	General conclusions	175
7.2	Perspectives	178
7.2.1	Pre-printing	178
7.2.2	In-printing	179
7.2.3	Post-printing	181

7.1 General conclusions

This thesis work is part of a multidisciplinary collaborative project focused on construction 3D printing using recycled materials. On the contractual development side, the work involves the formulation of methodologies and processes for 3D printing of mortars containing **Recycled Fine Aggregates (RFA)**. An online monitoring system for the **3D Concrete Printing (3DCP)** process and an online quality control strategy have been developed. The industrial feasibility of the devised process has been validated through environmental emulation.

The primary aim of this thesis is to automate the entire **3DCP** process for 3D printing with recycled concrete material in uncontrolled environments. This process is divided into three stages: pre-printing, in-printing, and post-printing. Our methodology addresses all three phases to achieve comprehensive automation and optimization. Given the unstable properties of concrete material, which can be influenced by unpredictable environmental disturbances, an online compensation strategy is imperative for process automation. The printing system operates through the cooperation of two heterogeneous dynamic systems: a fast dynamic represented by the robot and a slow dynamic represented by material pumping. To realize fast reaction that accounts for high uncertainty from material pumping side, velocity-based compensation is employed. Therefore, the central research question is: How can the robot's printing velocity be adaptively adjusted along its trajectory to ensure consistent material deposition, while considering constraints such as trajectory

curvature, filament width, and material flow rate, and simultaneously adapting to external temperature and humidity variations.

The literature review reveals that existing 3D Concrete Printing technologies primarily operate in controlled environments. Most studies focusing on printing in uncontrolled settings tend to investigate specific components of the process, such as material properties or structural analysis during the post-printing cooling stage. There is a notable absence of comprehensive process control that encompasses all three stages: pre-printing, in-printing, and post-printing. The solutions proposed in this thesis aim to enhance the overall process by advancing towards automation, thereby enabling the system to adapt to extreme conditions, such as high or low temperatures.

The pre-printing phase, also known as the off-line stage, is critical for successful 3D printing in construction. From three point of view: machine, shape and material, Chapter 3 discusses the off-line preparation stage for the 3DCP process. In term of shape, the importance of optimizing shape design is discussed, emphasizing proper scaling in accordance with shape curvature and robot nozzle velocity. Indeed, the curvature of the designed shape can impact the nozzle velocity, for a point width greater curvature, the velocity is reduced when passing through this point. On the robotics front, the chapter outlines the identification of the workspace derived from the forward kinematic model. Trajectory generation for the nozzle path is achieved by slicing the 3D model and creating precise toolpath for layer-by-layer material deposition. The inverse kinematic model is employed to transform the nozzle path into robot's joint space configuration, enabling it to accurately track the generated trajectory within the workspace. The chapter also covers material preparation, estimating the required material quantities for the intended printed shape, this is essential for the process to avoid material and labor waste. Moreover, the chapter describes an emulated uncontrolled environment realized by a climate chamber, used for both data collection and validation of the 3D printing automation process under various weather conditions. The pre-printing stage provides all the necessary aspects before the launch of in-printing stage.

In the in-printing stage, the focus of automation shifts to online monitoring and diagnosis of material deposition, along with adaptive compensation for deviations. The selected criterion for evaluating print quality is the width of the deposited filament. For real-time tracking of this parameter, the use of a non-destructive method is crucial. To this end, a filament width estimation algorithm has been developed that combines a Deep Learning (DL)-based instance segmentation model with morphological computations. This algorithm enables real-time tracking of filament width, which is a fundamental step for detecting deviations and guiding subsequent diagnosis and compensation efforts.

Given a predetermined reference width, the deposited filament is expected to conform to this specification. When a width deviation is detected, it becomes important to examine the parameter associated with this deviation, thereby posing a diagnostic challenge. The underlying scientific issue, again, is that the system operates through the collaboration of two independent, heterogeneous systems with information exchange: a fast mechatronic dynamic system (robot), and a slow fluid dynamic system (material pumping). As such, it is crucial to identify which component system is responsible for the detected deviation.

We investigate two diagnostic methodologies for operational diagnosis for 3D printing process: a data-driven qualitative approach based on pattern recognition in feature space and a model-based quantitative approach based on analytical redundancies. The objective is to identify contributing factors to abnormalities such as over-deposition and under-deposition. Both of these diagnostic techniques present distinct pros and cons. The two methods have been empirically validated through CIRMAP printing tests under different environmental conditions. Each approach has its advantage and disadvantages. Based on the comparative study, pattern recognition approach offers the advantage of visualized feature-space analysis, which aids in predicting anomalies and anticipating optimal printing settings (nozzle velocity, pump voltage, material flow) in advance under specific environmental conditions. However, it relies on the quality of large amount of data for tuning model. Also, it only recognizes patterns it has been trained for a specific material. In contrast, the analytical redundancy approach uses known relationships and mathematical models for detection and isolation. This model-based approach does not acquire large dataset and can provide a clear rationale for detected faults based on analytical model. Nevertheless, it's sensitive to the assumptions made in considered analytical models. Also, in the context of 3DCP, it's difficult to establish accurate model for the complex dynamic behavior of the material.

A neural network is trained to act as a velocity estimator, capable of dynamically determining the optimal nozzle velocity based on the filament width, material flow rate and path curvature. Building upon methodologies introduced in Chapter 4, the system persistently monitors filament width error, denoted by Δw . The difference between estimated optimal velocity and the actual velocity, noted by velocity error Δv , is then directed to a variable gain, forming the control signal which corrects the velocity error Δv in order to eliminate Δw . The mechanism adjusts the nozzle velocity to effectively reduce Δw that exceeds admissible thresholds, thereby compensating for detected filament width deviation. This approach has been validated through printing tests conducted at various temperatures: 10, 20, and 30 °C, affirming its

effectiveness across diverse environmental conditions. Across the results, we obtained an average response time of 1.5 seconds and an average filament deviation length of 13 cm that corresponds to the detection-compensation duration. The compensation strategy has been evaluated through the printing of a complex shape corresponding to an overall filament length over 50 meters, in different environment temperatures, subject to material property variations. The results confirms its ability in significantly reducing the overall deviation percentage of the shape in different temperatures, thereby improving overall printing quality in uncontrolled environment. Furthermore, comparing results across different temperatures, 20 °C can be considered an optimal temperature for maintaining printing quality.

For the post-printing stage, we address the issue of preventive maintenance for cracks that appear on the concrete surface. We introduce an integrated robotic framework for automated detection and repair of cracks, featuring a stationary UAV and a soft continuum arm. The soft arm is used to guide the repair material, enabling tracking of complex crack geometries across flat and oblique wall surfaces. The system manages both the identification and localization of cracks through Deep Learning based vision system. Repair is carried out by continuously depositing filling material. An inverse kinematic control scheme for the soft arm is implemented, and a neural network model is used to predict the relationship between the arm's bending length and the applied pressure. Experimental data affirm the system's competence in achieving accurate material deposition.

7.2 Perspectives

Future extensions of this work will aim to broaden the scope of process automation and optimization in 3DCP. This research work has built a basis for further exploration in various aspects across the three stages of 3DCP process.

7.2.1 Pre-printing

Building upon the work presented in Chapter 3, our framework paves the way for creating a digital twin of the 3DCP process. This digital twin helps to fine-tune key parameters, such as printing velocity, layer settings, and material flow rate. Given a specific design shape, this advancement presents numerous benefits, particularly in optimizing the printing process from design to execution.

In order to create the digital twin, further enhancements could involve the printing system. By integrating components for more extensive measure-

ments of material characteristics — in addition to measuring material pressure and flow rate — we can assess the flow properties of the fresh concrete mix, including yield stress and plastic viscosity, under varied environmental conditions. A centralized data collection system would enable the gathering of a comprehensive dataset essential for 3DCP, as illustrated in Figure 7.1.



Figure 7.1: Online measurement and data collection system for creating digital twin for 3D concrete printing.

Moving away from complex mathematical models, a data-based digital twin, supported by AI models, could greatly assist in early-stage pre-printing validations. This includes assessing the feasibility of printing custom-designed shapes in particular environments and their replicability under varying conditions. Such a strategy could significantly optimize the printing process, minimizing the potential for failure and the time and efforts needed for extensive pre-printing validation trials. This comprehensive data set could benefit research in various fields related to 3D concrete printing. However, this will require a deeper understanding of the fluid state behavior of the material, influenced by mix proportions, environmental conditions, and pumping speed.

7.2.2 In-printing

The methodology for adaptive control of material filament deposition presented in this thesis is founded on a feedback mechanism that initially detects and subsequently reacts to compensate for deviations that occur. Regarding

this, the compensation strategy can be enhanced in two aspects. Firstly, a combined approach of adjusting both robot velocity and pump voltage should be considered. This integrated strategy could more effectively address the challenges encountered in printing complex shapes, where velocity regulation may be insufficient for compensation. Such an approach necessitates a more precise model of the pumping mechanism, acknowledging that the material flow rate at the nozzle is influenced by factors including pumping speed, material viscosity, hose length and diameter, and external environmental conditions. Also, given that material pumping concerns a slow dynamic behavior, the latency time in the flow rate control should be identified. Developing this model will be intricate, requiring a diverse and substantial dataset.

Secondly, expanding the range of material deposition defects under consideration is crucial. Specifically, issues like non-continuous deposition, often linked to high material viscosity, call for pump adjustments. Enhancing the detection mode will involve incorporating more image data from scenarios exhibiting these defects. For currently existing system, taking into account the pressure data during pumping could be helpful, as air bubbles inside the hose could be reflected by the pressure fluctuation.

However, a feedback mechanism inherently lacks the capacity to prevent defects. Therefore, a more ideal approach would be predictive control. By anticipating potential defects in the filament, a predictive strategy could avoid deviations or other defects, thereby achieving optimized printing quality surpassing that of the adaptive compensation strategy. This necessitates accounting for all measurable parameters associated with filament defects, measured before reaching the nozzle, particularly those indicative of material behavior: flow rate, pressure loss inside the hose, and the material's viscosity. Understanding the relationship between the material's temperature and its viscosity is of particular interest with our current system. Preliminary research in this area (see Appendix A) has begun, focusing on tracking the thermal evolution of the material during and after printing.

Given the variability in operational ranges across different environments, as discussed in Chapter 4, future work could delve deeper into analyzing these domains. A thorough study might identify specific toolpath points prone to anomalies, enabling predictive adjustments. Future research could also aim to acquire redundant pressure measurements at both the pump outlet and nozzle inlet. This data can aid in predicting fluctuations in material flow rate at the nozzle, a major contributor to filament width deviation. Leveraging this information could facilitate a shift from a feedback-based to a predictive, feed-forward compensation strategy. Moreover, the ongoing accumulation of data from each printing session is constructing a vast dataset that encapsulates a wide spectrum of environmental conditions, including temperature and

humidity. These elements could be integrated as features for optimal velocity estimation, further refining the system’s adaptability. Another avenue for future research is the development of an online material property characterization system. Such a system would enable real-time evaluations of material properties, significantly enhancing the adaptability of compensation strategies in uncontrolled environments.

7.2.3 Post-printing

Future work in concrete surface crack repair will focus on enhancing the quality of material deposition. This improvement can be achieved by fine-tuning the robot’s positioning and adjusting the material flow rate in accordance with the dimensions of the crack. Incorporating depth information into the vision system could significantly advance the estimation of the required material quantity, thereby improving the control over the integrated crack repair system. A viable method to estimate the depth—or the internal volume—of detected cracks is through the integration of a depth camera or a stereo vision system. Such systems are capable of providing a more accurate distance map of the scanned surface.

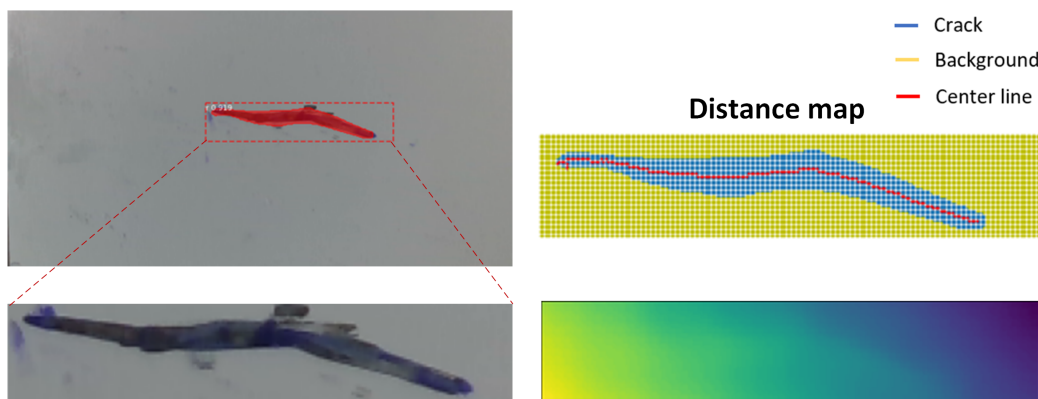


Figure 7.2: Estimation of crack depth with depth (RGB-D) camera.

As illustrated in Figure 7.2, the depth of a crack can be deduced by measuring the difference between the distance from the vision system to the background and the distance from the vision system to the crack’s central line (i.e., the medial axis). This depth information is crucial in estimating the crack’s volume and subsequently, the quantity of repair material needed. Additionally, understanding the depth distribution along the crack can assist in optimizing the pressure control during the material deposition stage, resulting in more precise material flow rate control, further enhancing the repair quality.

Appendices

APPENDIX A

CIRMAP printing system in emulated environment

A.1 CIARMAP printing system description

The printing system is installed inside the climate chamber detailed in Chapter 3. In order to obtain redundant measurements of different parameters of the printing system, additional sensors were fixed to the nozzle support. These sensors facilitate real-time monitoring of specific parameters throughout the printing phase. The printing system equipped with multiple sensors is depicted in Figure A.1.

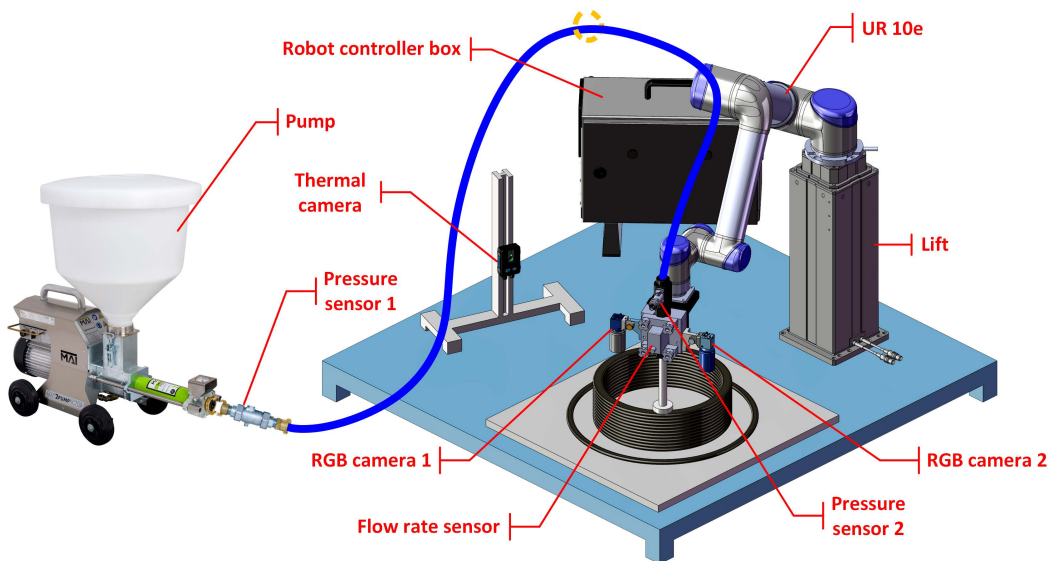


Figure A.1: 3D Concrete Printing system and available sensors.

The following sensors are available and used in this study:

- A SIKA VMZ 204 magnetic inductive flow sensor is installed at the inlet of the nozzle.

- Two MAI pressure sensor units are installed at the outlet of the pump and the inlet of the nozzle. The measurement of pressure at two sides provides redundant information of the material behavior, allowing for further analysis of material property.
- Two Basler industrial Gigabit Ethernet (GigE) cameras are fixed on both sides of the printer head, with their optical axes perpendicular to the print bed. The distance between the lenses and the tip of the nozzle is fixed at 480 mm. The cameras allow to obtain top-view images with 492×658 pixels, they are used for the estimation of the width of freshly deposited filament. The two cameras work alternately according to the direction of nozzle velocity, so that the captured images always contains the freshly printed filament rather than the filament from the previous layer.
- A FLIR AX8 thermal camera is positioned in front of the print bed to record the printed structure in thermal map, allowing for the tracking of surface temperature evolution of the structure.
- The temperature and humidity sensors integrated inside the climate chamber allows the tracking of ambient temperature and humidity evolution inside the chamber.

A.2 3D concrete printing dataset

A comprehensive 3DCP dataset is being constructed based on the data from the aforementioned sensors and the recorder of the climatic chamber. This dataset contains both time-stamped digital (available in CSV format) and image data (RGB image and thermal map) acquired during each printing test, and is being continuously enriched with every printing experiment. Table A.1 outlines the structure of the dataset.

Table A.1: 3DCP dataset

Type	Data	Description
Digital	Material flow rate	Measured at the nozzle.
	Pump voltage	Command issued by the master machine.
	Nozzle position	Given by internal position sensor of the robot.
	Nozzle speed	Calculated based on nozzle position data.
	Nozzle speed set value	Command issued by the master machine.
	Pressure	Measured at the inlet and outlet of the hose.
	Temperature	Printing environment temperature.
	Humidity	Printing environment humidity.
Image	RGB image (658×492 pixels)	Top-view images of freshly printed filaments.
	Thermal image	Front-view of the printed object, surface temperature can be extracted.



Figure A.2: Time-stamped image data sample captured during printing test under $T = 10^{\circ}\text{C}$. a) RGB images of freshly deposited filament from top-view captured by two cameras integrated on the nozzle. b) Thermal image captured by the thermal camera placed in front of the printed object.

During each printing, the RGB cameras and the thermal camera recorded the process at defined frequencies. Specifically, the RGB cameras captured images every 0.1 second in an alternating manner. As the temperature evolution is a slow process, the thermal camera captured images every 30 seconds during the printing process and every 15 minutes thereafter to optimize storage space. All images, including RGB and thermal images, were saved with a timestamp corresponding to the precise moment of capture. An example of the image data is demonstrated in Fig.A.2.

A.3 Printing tests in the emulated environment

A series of printing tests were conducted within the climate chamber located at the University of Lille campus over a duration of two days (19th - 20th July, 2022). During the tests, three different temperature set values were applied: 10°C, 20°C, and 30°C, while the humidity set value was maintained constant at 50%.

The environmental parameters inside the climate chamber, specifically temperature and humidity, presented during the testing procedures are illustrated in Figure A.3. The fluctuations in the temperature and humidity measurement profiles were caused by the significant difference between the outdoor ambient parameters and the inside-climate chamber parameters, this corresponded to the periods between two consecutive tests when the climatic chamber door was opened for cleaning.

The shape of the testing object was selected to be a cylinder with a fixed diameter of 30 cm, characterized by a constant curvature throughout. The cylindrical shape, as illustrated in Fig.A.4, comprises a total of 40 layers, with each layer having a height of 9 mm, therefore, the estimated height of the

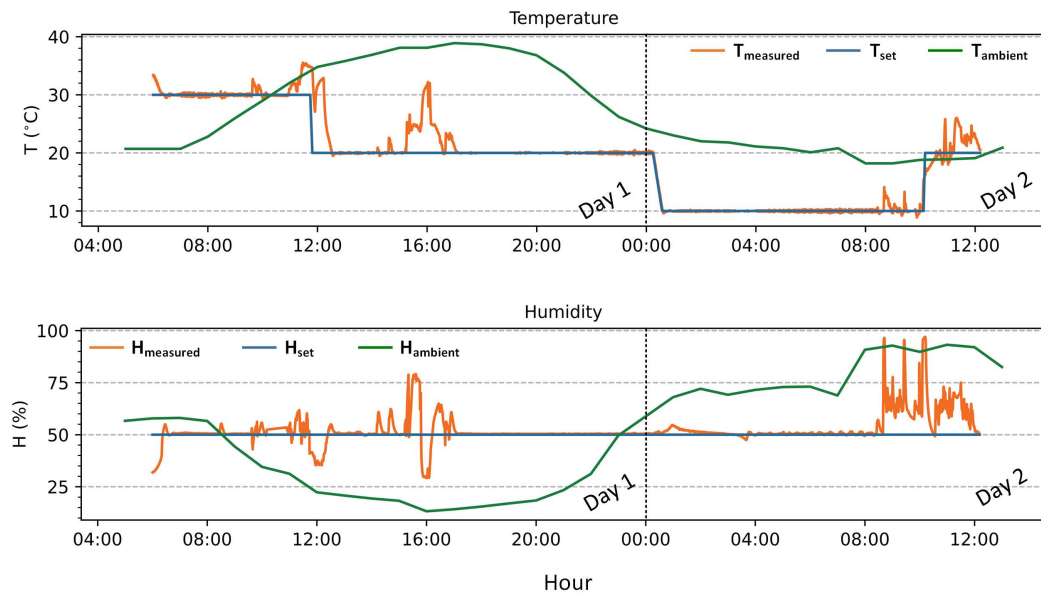


Figure A.3: Temperature and humidity set values and measured values inside climate chamber and outdoor ambient conditions in Lille, France during two testing days (19th - 20th July, 2022, these dates corresponded to an extreme heatwave in Lille, hence particularly high outdoor temperatures can be observed). The fluctuations were due to differences between outdoor ambient parameters and inside-climate chamber parameters when the door was opened.

Appendix A. CIRMAP printing system in emulated environment

cylindrical shape is 36 cm. In the first layer, a circle with a larger diameter of 45 cm was added to the tool path in order to facilitate the calibration of the system, i.e. the determination of printing parameters, namely, pump voltage and robot speed, which were to be kept constant throughout the printing of an object.

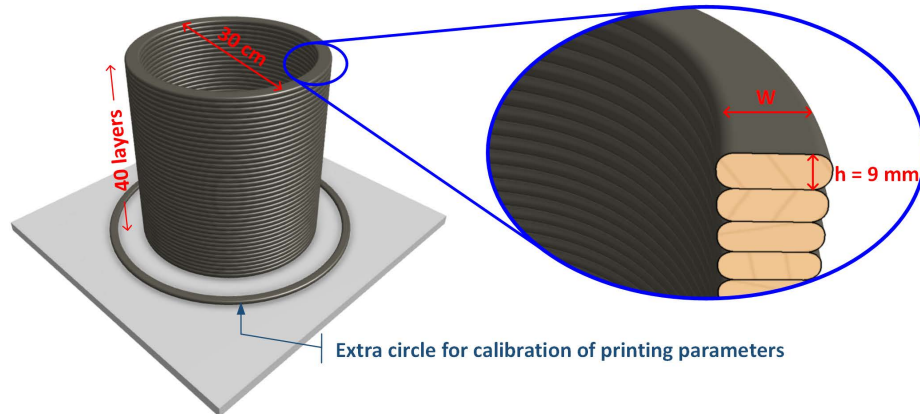


Figure A.4: The cylindrical shape with constant curvature designed for the printing test, the diameter is 30 cm.



Figure A.5: The first layer of the cylindrical shape designed for manual calibration of the printing system parameters based on the measurement of layer widths.

In the literature, the maximum layer number reached before failure (buckling or plastic collapse) for a fixed geometry could be used to characterize the buildability of a specific fresh mixture[Chen 2022], thus, for a given cylinder diameter in this case, the maximum number of layers reached before failure can be an indicator to evaluate the buildability of the fresh mixture and the replicability of this specific process under certain environmental conditions. The outcomes and details of the tests are summarized in Table.A.2.

Table A.2: Summary of results obtained through the printing tests.

The set value of relative humidity of the climate chamber is fixed at $H^{env} = 50\%$. $H_{ambient}$: outdoor ambient humidity, $T_{ambient}$: outdoor ambient temperature, T_{EE} : set value of temperature in climate chamber, T_{dry}^{mat} : temperature of dry materials before mixing, Δt_{mix} : duration between the start of material mixing and the beginning of printing, T_{mix}^{mat} : temperature of mixed material at the beginning of printing, D : diameter of flow table test, U^{pump} : pump voltage control, v^{nozzle} : nozzle motion speed, N : number of layers reached (maximum 40), W : average width of material deposit filament.

Tests	$H_{ambient}$ (%)	$T_{ambient}$ (°C)	T_{EE} (°C)	T_{dry}^{mat} (°C)	Δt_{mix} (minutes)	T_{mix}^{mat} (°C)	D (cm)	U^{pump} (volt)	W (mm)	N	Failure cause
Test 1	40	32	30	30	24	34	19.0	1.17	25	9	buckling
Test 2	30	32	30	30	30	34	17.0	1.17	32	23	buckling
Test 3	30	32	30	30	44	34	18.0	3.14	37	19	extrusion
Test 4	25	38	30	30	-	34	18.0	3.03	45	26	buckling
Test 5	25	38	20	30	29	38	15.5	2.5	45	17	plastic collapse
Test 6	25	39	20	30	37	38	16.5	2.5	47	20	extrusion
Test 7	78	21	20	20	13	25	17.5	2.5	45	40	-
Test 8	80	19	10	10	10	25	14.5	2.5	31	40	-
Test 9	80	19	10	10	-	22	14.5	3.03	40	40	-

Appendix A. CIRMAP printing system in emulated environment

The surface temperature of the printed object can be extracted from the thermal image, allowing to observe the material temperature during printing and long-term surface temperature evolution during the drying stage (Three examples are given in Figure A.6, Figure A.7 and Figure 3.23). The temperature difference between the deposited material at low level and the material just extruded through the nozzle during printing was also obtained.

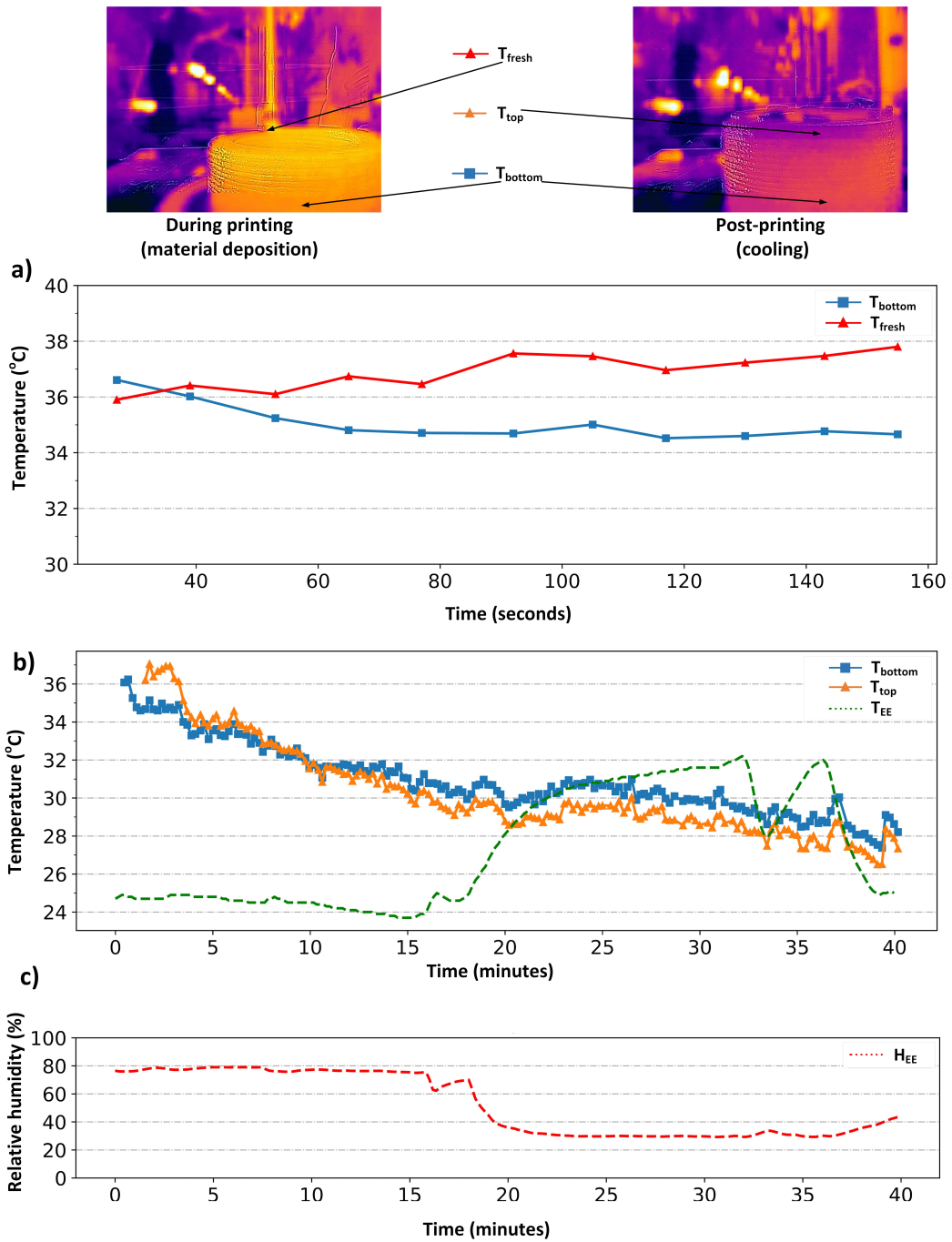


Figure A.6: Test example: outdoor ambient temperature $T_{ambient} = 39^{\circ}C$. a) Temperature of newly extruded material T_{fresh} and deposited material at a specific point T_{bottom} measured during printing. b) The evolution of temperature at the top (T_{top}) and bottom (T_{bottom}) of the printed object and temperature inside the climate chamber measured during the material drying process. c) Humidity inside the climate chamber H_{EE} during the material drying process.

Appendix A. CIRMAP printing system in emulated environment

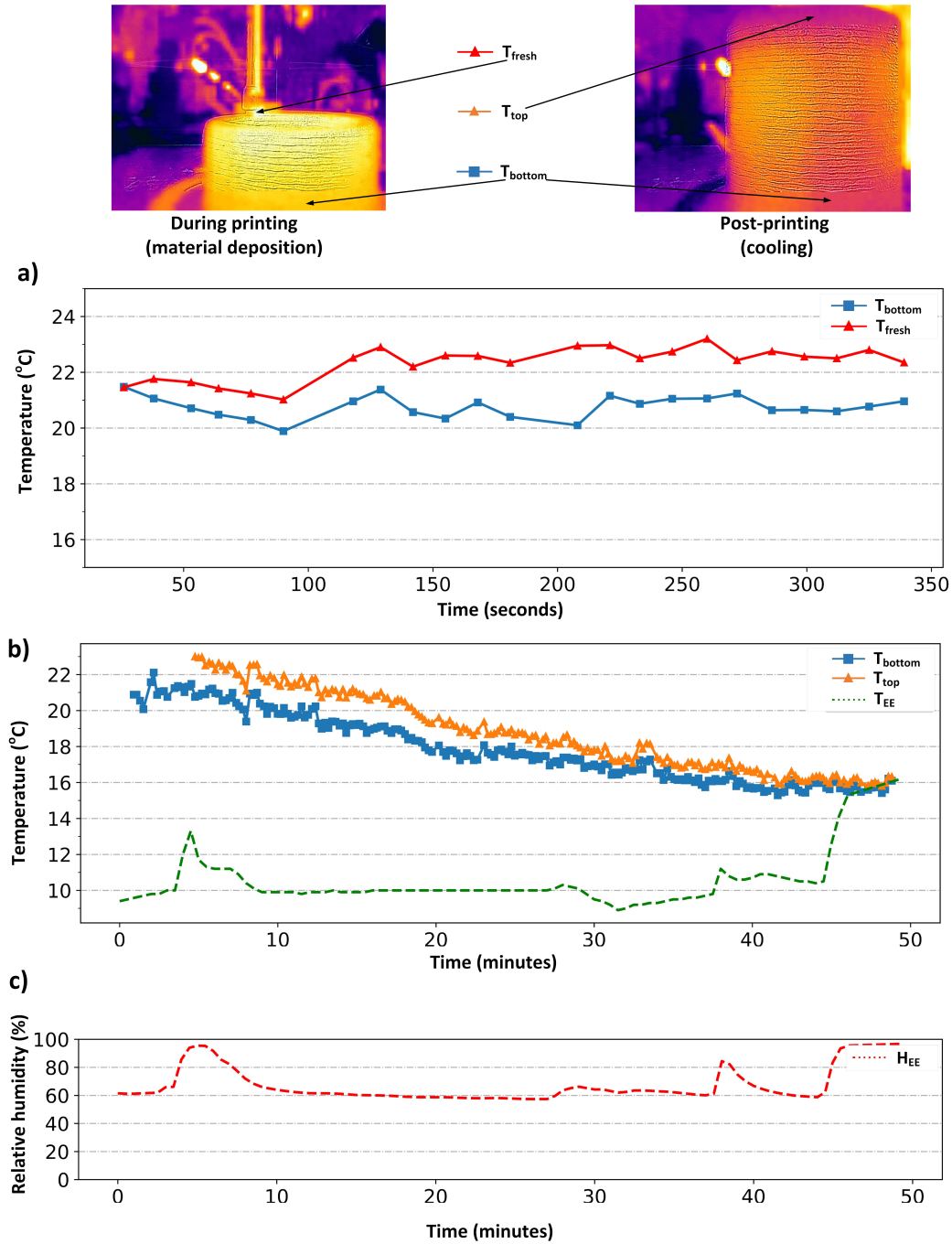


Figure A.7: Test example: outdoor ambient temperature $T_{ambient} = 21^{\circ}C$. a) Temperature of newly extruded material T_{fresh} and deposited material at a specific point T_{bottom} measured during printing. b) The evolution of temperature at the top (T_{top}) and bottom (T_{bottom}) of the printed object and temperature inside the climate chamber measured during the material drying process. c) Humidity inside the climate chamber H_{EE} during the material drying process.

3D shapes printed in CIRMAP project

B.1 CIRMAP 3D Printing Campaign at Polytech Lille, June 2023

A series of printing sessions within CIRMAP¹ framework was carried out at Polytech Lille between June 19 and June 30, 2023. The material used for these printings was a composite derived from recycled sand sourced from France, Germany, Belgium, and the Netherlands. Each participating country's team was responsible for designing the geometries of the printed structures.

The list of CIRMAP partners is given in Table B.1.

Table B.1: CIRMAP partners

Name	Country
Université de Lille	France
Manchester Metropolitan University	United Kingdom
Technische Universität Kaiserslautern	Germany
SAS NEO ECO DEVELOPPEMENT	France
Université de Liège	Belgium
Université d'Orléans	France
Heberger GmbH	Germany
VICAT	France
Gemeente Almere	Netherlands
Stadt Pirmasens	Germany

- Material

Recycled sand from different countries has been used throughout the printing session. The sources and associated producers are given in Table B.2.

- Printed Shapes

¹<https://www.nweurope.eu/projects/project-search/cirmap-circular-economy-via-customisable-furniture-with-recycled-materials-for-public-places/>

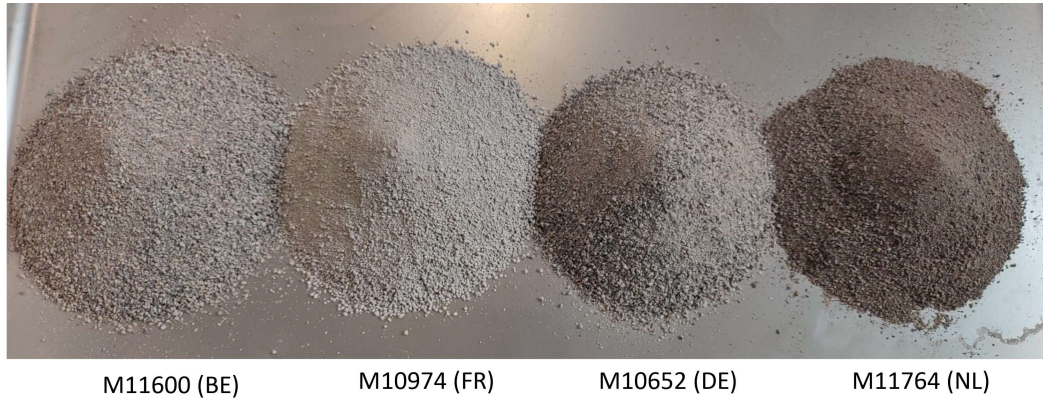


Figure B.1: Recycled sand sourced from different regions (Belgium, France, Germany, the Netherlands).

Country	France	Germany	Belgium	Netherlands
Sand	Helfaut	Heberger	Tradecowall	Cirwinn

Table B.2: Recycled sand from different countries.



Figure B.2: French design using French sand, 19-20 June, 2023.



Figure B.3: Dutch design using Dutch sand, 22-23 June, 2023.



Figure B.4: German design using German sand, 26-27 June, 2023.



Figure B.5: German design using German sand, 26-27 June, 2023.



Figure B.6: Belgian design using Belgian sand, 29-30 June, 2023.

B.2 Printing session at Orléans, September 2023

The CIRMAP 3D printing system from Polytech Lille was moved and set up at the University of Orléans for the purpose of printing experiments.

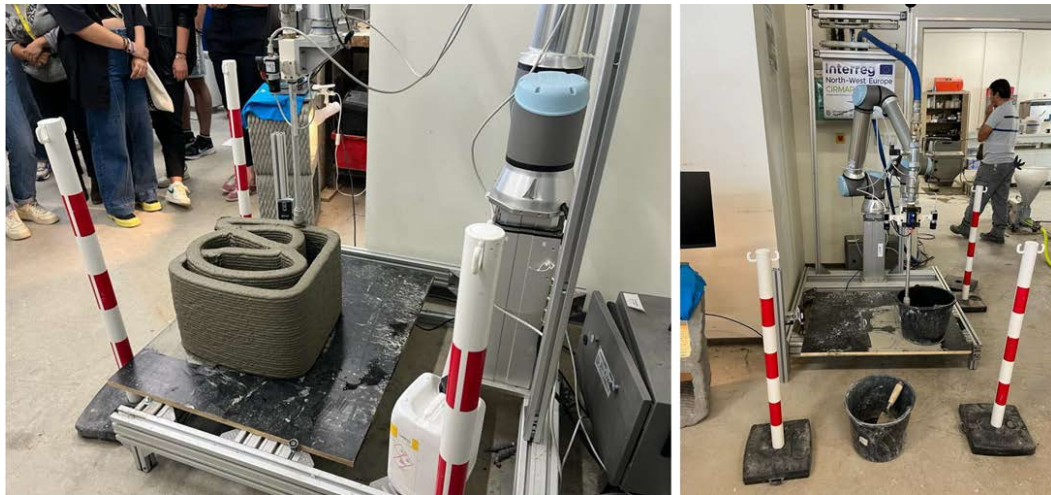


Figure B.7: Printing system setup, 27 September, 2023.



Figure B.8: Equipment installed in-situ, 27 September, 2023.

Acronyms

3DCP 3D Concrete Printing. ix, xvi, 1, 2, 5–8, 10, 11, 40, 44, 46–48, 51, 54, 60, 66, 73–75, 102, 114–116, 120–122, 175–179

AI Artificial Intelligence. 8, 179

AM Additive Manufacturing. viii, 12, 13, 32, 33, 38

ANN Artificial Neural Network. 120, 152

ARR Analytical Redundancy Relation. 74, 99, 107

CBHA Compact Bionic Handling Arm. 143

CIRMAP Circular economy via customizable furniture with Recycled Materials for public Places. 61

CV Computer Vision. 78

DH Denavit-Hartenberg. xvi, 42, 43

DL Deep Learning. 77, 78

EDT Euclidean Distance Transform. 80

FDI Fault Detection and Isolation. 99, 100

FEM Finite Element Method. 151

FKM Forward Kinematic Model. 42, 44, 46, 48, 55, 61

FPN Feature Pyramid Network. 147

FSM Fault Signature Matrix. 100

IKM Inverse Kinematic Model. 54–57, 153

MAT Media Axis Transform. 80, 149

MSE Mean Square Error. 121

NN Neural Network. 124

RFA Recycled Fine Aggregates. 2, 4, 6, 8, 175

RoI Region of Interest. 79, 80, 148

RPN Region Proposal Network. 148

SVM Support Vector Machine. 86, 88, 91

UAV Unmanned Aerial Vehicle. 142

UP niversal-Prismatic. 154

UPS niversal-Prismatic-Spheric. 153

Bibliography

- [Abdalla 2021] Hadeer Abdalla, Kazi Parvez Fattah, Mohamed Abdallah and Adil K Tamimi. Environmental footprint and economics of a full-scale 3D-printed house. *Sustainability*, vol. 13, no. 21, page 11978, 2021. (Cited on page 24.)
- [Ahmed 2021] Naseer Ahmed, Maria Shakoor Abbasi, Sara Haider, Nimra Ahmed, Syed Rashid Habib, Sara Altamash, Muhammad Sohail Zafar and Mohammad Khursheed Alam. Fit accuracy of removable partial denture frameworks fabricated with CAD/CAM, rapid prototyping, and conventional techniques: A systematic review. *BioMed research international*, vol. 2021, 2021. (Cited on page 18.)
- [Akinci 2006] Burcu Akinci, Frank Boukamp, Chris Gordon, Daniel Huber, Catherine Lyons and Kuhn Park. A formalism for utilization of sensor systems and integrated project models for active construction quality control. *Automation in construction*, vol. 15, no. 2, pages 124–138, 2006. (Cited on page 22.)
- [Alanazi 2022] N Alanazi, JT Kolawole, Richard Buswell and Luca Susmel. The Theory of Critical Distances to assess the effect of cracks/manufacturing defects on the static strength of 3D-printed concrete. *Engineering Fracture Mechanics*, vol. 269, page 108563, 2022. (Cited on page 22.)
- [Alhumayani 2020] Hashem Alhumayani, Mohamed Gomaa, Veronica Soebarto and Wassim Jabi. Environmental assessment of large-scale 3D printing in construction: A comparative study between cob and concrete. *Journal of Cleaner Production*, vol. 270, page 122463, 2020. (Cited on pages 15 and 25.)
- [Almusawi 2016] Ahmed RJ Almusawi, L Canan Dülger and Sadettin Kapucu. A new artificial neural network approach in solving inverse kinematics of robotic arm (Denso VP6242). *Computational intelligence and neuroscience*, vol. 2016, 2016. (Cited on page 152.)
- [Amersdorfer 2021] Manuel Amersdorfer and Thomas Meurer. Equidistant tool path and cartesian trajectory planning for robotic machining of curved freeform surfaces. *IEEE Transactions on Automation Science and Engineering*, vol. 19, no. 4, pages 3311–3323, 2021. (Cited on page 60.)

- [Anantharaman 2018] Rajaram Anantharaman, Matthew Velazquez and Yungyung Lee. Utilizing mask R-CNN for detection and segmentation of oral diseases. In 2018 IEEE international conference on bioinformatics and biomedicine (BIBM), pages 2197–2204. IEEE, 2018. (Cited on pages 22 and 78.)
- [Anderson 2017] Isabelle Anderson. Mechanical properties of specimens 3D printed with virgin and recycled polylactic acid. 3D Printing and Additive Manufacturing, vol. 4, no. 2, pages 110–115, 2017. (Cited on page 16.)
- [Anton 2021] Ana Anton, Lex Reiter, Timothy Wangler, Valens Frangez, Robert J Flatt and Benjamin Dillenburger. A 3D concrete printing prefabrication platform for bespoke columns. Automation in Construction, vol. 122, page 103467, 2021. (Cited on page 104.)
- [Arnaud Perrot 2017] Robby Caspeeel Arnaud Perrot Petr Kocáb. 3D Concrete Printing: Machine and Mix Design. Automation in Construction, vol. 79, 2017. (Cited on page 3.)
- [Aryan 2021] Afrooz Aryan, Frédéric Bosché and Pingbo Tang. Planning for terrestrial laser scanning in construction: A review. Automation in Construction, vol. 125, page 103551, 2021. (Cited on page 22.)
- [Barjuei 2022] E Shojaei Barjuei, E Courteille, D Rangeard, F Marie and A Perrot. Real-time vision-based control of industrial manipulators for layer-width setting in concrete 3D printing applications. Advances in Industrial and Manufacturing Engineering, page 100094, 2022. (Cited on pages viii and 33.)
- [Baz 2021] Bilal Baz, Georges Aouad, Joelle Kleib, David Bulteel and Sébastien Remond. Durability assessment and microstructural analysis of 3D printed concrete exposed to sulfuric acid environments. Construction and Building Materials, vol. 290, page 123220, 2021. (Cited on page 21.)
- [Bishop 2006] Christopher M Bishop and Nasser M Nasrabadi. Pattern recognition and machine learning, volume 4. Springer, 2006. (Cited on page 88.)
- [Bos 2016] Freek Bos, Rob Wolfs, Zeeshan Ahmed and Theo Salet. Additive manufacturing of concrete in construction: potentials and challenges of 3D concrete printing. Virtual and physical prototyping, vol. 11, no. 3, pages 209–225, 2016. (Cited on page 32.)

- [Breaz 2019] Radu Eugen Breaz and Sever Gabriel Racz. Considerations Regarding the Industrial Implementation of Incremental Forming Process. In *Materials Science Forum*, volume 957, pages 111–119. Trans Tech Publ, 2019. (Cited on page 19.)
- [Breseghello 2021] Luca Breseghello, Sandro Sanin and Roberto Naboni. Toolpath simulation, design and manipulation in robotic 3D concrete printing. In *The 26th Annual Conference of the Association for Computer-Aided Architectural Design Research in Asia, CAADRIA 2021*, pages 623–632. The Association for Computer-Aided Architectural Design Research in Asia . . . , 2021. (Cited on page 22.)
- [Buswell 2018] Richard A Buswell, WR Leal De Silva, Scott Z Jones and Justin Dirrenberger. 3D printing using concrete extrusion: A roadmap for research. *Cement and Concrete Research*, vol. 112, pages 37–49, 2018. (Cited on pages 1 and 21.)
- [Buswell 2020] Richard Buswell, Peter Kinnell, Jie Xu, Norman Hack, Harald Kloft, Mehdi Maboudi, Markus Gerke, Peter Massin, Georg Grasser, Rob Wolfset al. Inspection methods for 3D concrete printing. In *RILEM International Conference on Concrete and Digital Fabrication*, pages 790–803. Springer, 2020. (Cited on page 22.)
- [Chen 2022] Yu Chen, Shan He, Yidong Gan, Oğuzhan Çopuroğlu, Fred Veer and Erik Schlangen. A review of printing strategies, sustainable cementitious materials and characterization methods in the context of extrusion-based 3D concrete printing. *Journal of Building Engineering*, vol. 45, page 103599, 2022. (Cited on pages 13 and 188.)
- [Clément Gosselin 2008] Marc Gouttefarde Clément Gosselin. rajectory generation for automatic machines and robots. Springer, 2008. (Cited on page 49.)
- [Comminal 2020] Raphael Comminal, Wilson Ricardo Leal da Silva, Thomas Juul Andersen, Henrik Stang and Jon Spangenberg. Modelling of 3D concrete printing based on computational fluid dynamics. *Cement and Concrete Research*, vol. 138, page 106256, 2020. (Cited on page 105.)
- [Coppola 2018] Bartolomeo Coppola, Nicola Cappetti, Luciano Di Maio, Paola Scarfato and Loredana Incarnato. 3D printing of PLA/clay nanocomposites: Influence of printing temperature on printed samples properties. *Materials*, vol. 11, no. 10, page 1947, 2018. (Cited on page 34.)

- [Craig 2006] John J Craig. Introduction to robotics. Pearson Educacion, 2006. (Cited on page 57.)
- [Dai 2020] Chengkai Dai, Sylvain Lefebvre, Kai-Ming Yu, Jo MP Geraedts and Charlie CL Wang. Planning jerk-optimized trajectory with discrete time constraints for redundant robots. IEEE Transactions on Automation Science and Engineering, vol. 17, no. 4, pages 1711–1724, 2020. (Cited on page 19.)
- [Davtalab 2020] Omid Davtalab, Ali Kazemian, Xiao Yuan and Behrokh Khoshnevis. Automated inspection in robotic additive manufacturing using deep learning for layer deformation detection. Journal of Intelligent Manufacturing, pages 1–14, 2020. (Cited on pages viii, 22 and 23.)
- [Diab 2023] Zeinab Diab, Duc-Phi Do, Sébastien Rémond and Dashnor Hoxha. Probabilistic prediction of structural failure during 3D concrete printing processes. Materials and Structures, vol. 56, no. 4, page 73, 2023. (Cited on page 21.)
- [Ding 2020] Tao Ding, Jianzhuang Xiao, Shuai Zou and Yu Wang. Hardened properties of layered 3D printed concrete with recycled sand. Cement and Concrete Composites, vol. 113, page 103724, 2020. (Cited on page 2.)
- [Djeziri 2007] Mohand Arab Djeziri, Rochdi Merzouki, Belkacem Ould Bouamama and Genevieve Dauphin-Tanguy. Robust fault diagnosis by using bond graph approach. IEEE/ASME Transactions on Mechatronics, vol. 12, no. 6, pages 599–611, 2007. (Cited on page 106.)
- [Djeziri 2009] Mohand Arab Djeziri, Rochdi Merzouki and Belkacem Ould Bouamama. Robust monitoring of an electric vehicle with structured and unstructured uncertainties. IEEE transactions on vehicular technology, vol. 58, no. 9, pages 4710–4719, 2009. (Cited on page 106.)
- [Dorafshan 2018a] Sattar Dorafshan, Robert J Thomas, Calvin Coopmans and Marc Maguire. Deep learning neural networks for sUAS-assisted structural inspections: Feasibility and application. In 2018 International Conference on Unmanned Aircraft Systems (ICUAS), pages 874–882. IEEE, 2018. (Cited on page 22.)
- [Dorafshan 2018b] Sattar Dorafshan, Robert J Thomas and Marc Maguire. Comparison of deep convolutional neural networks and edge detectors

- for image-based crack detection in concrete. *Construction and Building Materials*, vol. 186, pages 1031–1045, 2018. (Cited on page 22.)
- [Dorafshan 2018c] Sattar Dorafshan, Robert J Thomas and Marc Maguire. SDNET2018: An annotated image dataset for non-contact concrete crack detection using deep convolutional neural networks. *Data in brief*, vol. 21, pages 1664–1668, 2018. (Cited on page 147.)
- [Dzwierzynska 2020] Jolanta Dzwierzynska. Multi-objective optimizing curvilinear steel bar structures of hyperbolic paraboloid canopy roofs. *Buildings*, vol. 10, no. 3, page 39, 2020. (Cited on page 18.)
- [El-Sayegh 2020] Sameh El-Sayegh, Lotfi Romdhane and Solair Manjikian. A critical review of 3D printing in construction: Benefits, challenges, and risks. *Archives of Civil and Mechanical Engineering*, vol. 20, pages 1–25, 2020. (Cited on pages 20 and 25.)
- [Flah 2020] Majdi Flah, Ahmed R Suleiman and Moncef L Nehdi. Classification and quantification of cracks in concrete structures using deep learning image-based techniques. *Cement and Concrete Composites*, vol. 114, page 103781, 2020. (Cited on page 147.)
- [Fok 2018] Kai-Yin Fok, Chi-Tsun Cheng, Nuwan Ganganath, Herbert Ho-Ching Iu and K Tse Chi. An ACO-based tool-path optimizer for 3-D printing applications. *IEEE Transactions on Industrial Informatics*, vol. 15, no. 4, pages 2277–2287, 2018. (Cited on page 17.)
- [Fok 2019] Kai-Yin Fok, Nuwan Ganganath, Chi-Tsun Cheng, Herbert Ho-Ching Iu and K Tse Chi. Tool-path optimization using neural networks. In *2019 IEEE International Symposium on Circuits and Systems (IS-CAS)*, pages 1–5. IEEE, 2019. (Cited on page 17.)
- [Fonseca 2023] Mariana Fonseca and Ana Mafalda Matos. 3D Construction Printing Standing for Sustainability and Circularity: Material-Level Opportunities. *Materials*, vol. 16, no. 6, page 2458, 2023. (Cited on page 130.)
- [Fu 2020] Guoqiang Fu, Tengda Gu, Hongli Gao and Caijiang Lu. A postprocessing and path optimization based on nonlinear error for multijoint industrial robot-based 3D printing. *International Journal of Advanced Robotic Systems*, vol. 17, no. 5, page 1729881420952249, 2020. (Cited on page 19.)

- [Gan 2005] John Q Gan, Eimei Oyama, Eric M Rosales and Huosheng Hu. A complete analytical solution to the inverse kinematics of the Pioneer 2 robotic arm. *Robotica*, vol. 23, no. 1, pages 123–129, 2005. (Cited on page 152.)
- [Godage 2015] Isuru S Godage, Gustavo A Medrano-Cerda, David T Branson, Emanuele Guglielmino and Darwin G Caldwell. Modal kinematics for multisection continuum arms. *Bioinspiration & biomimetics*, vol. 10, no. 3, page 035002, 2015. (Cited on page 152.)
- [Guessasma 2019] Sofiane Guessasma, Sofiane Belhabib and Hedi Nouri. Microstructure and mechanical performance of 3D printed wood-PLA/PHA using fused deposition modelling: Effect of printing temperature. *Polymers*, vol. 11, no. 11, page 1778, 2019. (Cited on page 24.)
- [Guimarães 2021] Ana S Guimarães, João MPQ Delgado and Sandra S Lucas. Advanced manufacturing in civil engineering. *Energies*, vol. 14, no. 15, page 4474, 2021. (Cited on page 24.)
- [Guo 2019] Chaofan Guo, Min Zhang and Bhesh Bhandari. Model building and slicing in food 3D printing processes: a review. *Comprehensive Reviews in Food Science and Food Safety*, vol. 18, no. 4, pages 1052–1069, 2019. (Cited on page 51.)
- [Hager 2016] Izabela Hager, Anna Golonka and Roman Putanowicz. 3D printing of buildings and building components as the future of sustainable construction? *Procedia Engineering*, vol. 151, pages 292–299, 2016. (Cited on page 29.)
- [Hameed 2022] Khurram Hameed, Douglas Chai and Alexander Rassau. Score-based mask edge improvement of Mask-RCNN for segmentation of fruit and vegetables. *Expert Systems with Applications*, vol. 190, page 116205, 2022. (Cited on pages 22 and 78.)
- [Han 2021] Yilong Han, Zhihan Yang, Tao Ding and Jianzhuang Xiao. Environmental and economic assessment on 3D printed buildings with recycled concrete. *Journal of Cleaner Production*, vol. 278, page 123884, 2021. (Cited on page 16.)
- [He 2017] Kaiming He, Georgia Gkioxari, Piotr Dollár and Ross Girshick. Mask r-cnn. In *Proceedings of the IEEE international conference on computer vision*, pages 2961–2969, 2017. (Cited on pages 78 and 147.)

- [Hespel 2014] Adrien-Maxence Hespel, Ray Wilhite and Judith Hudson. Invited review-applications for 3D printers in veterinary medicine. *Veterinary Radiology & Ultrasound*, vol. 55, no. 4, pages 347–358, 2014. (Cited on page 18.)
- [Hoła 2015] J Hoła, J Bień, K Schabowicz et al. Non-destructive and semi-destructive diagnostics of concrete structures in assessment of their durability. *Bulletin of the Polish Academy of Sciences. Technical Sciences*, vol. 63, no. 1, pages 87–96, 2015. (Cited on page 22.)
- [Hong 2022] Freddie Hong, Steve Hodges, Connor Myant and David E Boyle. Open5x: Accessible 5-axis 3D printing and conformal slicing. In *CHI Conference on Human Factors in Computing Systems Extended Abstracts*, pages 1–6, 2022. (Cited on page 18.)
- [Hossain 2020] Md Hossain, Altynay Zhumabekova, Suvash Chandra Paul, Jong Ryeol Kim et al. A Review of 3D Printing in Construction and its Impact on the Labor Market. *Sustainability*, vol. 12, no. 20, page 8492, 2020. (Cited on page 1.)
- [Hsu 2015] Ming-Chen Hsu, Chenglong Wang, Austin J Herrema, Dominik Schillinger, Anindya Ghoshal and Yuri Bazilevs. An interactive geometry modeling and parametric design platform for isogeometric analysis. *Computers & mathematics with applications*, vol. 70, no. 7, pages 1481–1500, 2015. (Cited on page 18.)
- [Hu 2011] Shuangwei Hu, Martin Lundgren and Antti J Niemi. Discrete Frenet frame, inflection point solitons, and curve visualization with applications to folded proteins. *Physical Review E*, vol. 83, no. 6, page 061908, 2011. (Cited on page 154.)
- [Hu 2017] Jing Hu. Study on STL-based slicing process for 3D printing. In *2017 International solid freeform fabrication symposium*. University of Texas at Austin, 2017. (Cited on page 52.)
- [Hynek 2022] Estelle Hynek, David Bulteel, Antoine Urquizar and Sébastien Remond. Formulation and Characterization of a Low Carbon Impact Cementitious Ink for 3D Printing. In *RILEM International Conference on Concrete and Digital Fabrication*, pages 99–104. Springer, 2022. (Cited on page 66.)
- [Iancu 2018] I Iancu and MG Ionita. A Case Study on the Effect of Printing Temperature on the Tensile Strength of 3D Printed Parts with PLA

- Material. The Scientific Bulletin of Electrical Engineering Faculty, vol. 21, no. 2, pages 49–52, 2018. (Cited on page 24.)
- [Jagoda 2020] Jeneé Jagoda, Brandy Diggs-McGee, Megan Kreiger and Steven Schuldt. The viability and simplicity of 3D-Printed construction: A military case study. *Infrastructures*, vol. 5, no. 4, page 35, 2020. (Cited on pages 25 and 26.)
- [Jeon 2020] Haejoon Jeon, Jihoon Park, Sunju Kim, Kyungho Park and Chungsik Yoon. Effect of nozzle temperature on the emission rate of ultrafine particles during 3D printing. *Indoor Air*, vol. 30, no. 2, pages 306–314, 2020. (Cited on page 24.)
- [Jeong 2016] Il-Do Jeong, Jae-Jun Lee, Jin-Hun Jeon, Ji-Hwan Kim, Hae-Young Kim and Woong-Chul Kim. Accuracy of complete-arch model using an intraoral video scanner: An in vitro study. *The Journal of prosthetic dentistry*, vol. 115, no. 6, pages 755–759, 2016. (Cited on page 18.)
- [Jeong 2019] Hoseong Jeong, Sun-Jin Han, Seung-Ho Choi, Yoon Jung Lee, Seong Tae Yi and Kang Su Kim. Rheological property criteria for buildable 3D printing concrete. *Materials*, vol. 12, no. 4, page 657, 2019. (Cited on page 15.)
- [Jia 2020] Weikuan Jia, Yuyu Tian, Rong Luo, Zhonghua Zhang, Jian Lian and Yuanjie Zheng. Detection and segmentation of overlapped fruits based on optimized mask R-CNN application in apple harvesting robot. *Computers and Electronics in Agriculture*, vol. 172, page 105380, 2020. (Cited on pages 22 and 78.)
- [Jiang 2020] Jingchao Jiang and Yongsheng Ma. Path planning strategies to optimize accuracy, quality, build time and material use in additive manufacturing: a review. *Micromachines*, vol. 11, no. 7, page 633, 2020. (Cited on page 18.)
- [Jiang 2021] JC Jiang, Xinghua Xu, Wanzhi Rui, Zhengrong Jia and Zuowei Ping. Line Width Mathematical Model in Fused Deposition Modelling for Precision Manufacturing. In *E3S Web of Conferences*, volume 231, page 03003. EDP Sciences, 2021. (Cited on page 18.)
- [Jiao 2021] Dengwu Jiao, Robin De Schryver, Caijun Shi and Geert De Schutter. Thixotropic structural build-up of cement-based materials: A state-of-the-art review. *Cement and Concrete Composites*, vol. 122, page 104152, 2021. (Cited on page 104.)

- [Joh 2020] Changbin Joh, Jungwoo Lee, The Quang Bui, Jihun Park and In-Hwan Yang. Buildability and mechanical properties of 3D printed concrete. *Materials*, vol. 13, no. 21, page 4919, 2020. (Cited on page 25.)
- [Kahouadji 2021] Mouad Kahouadji, Othman Lakhel, Xinrui Yang, Abdelkader Belarouci and Rochdi Merzouki. System of Robotic Systems for Crack Predictive Maintenance. In *2021 16th International Conference of System of Systems Engineering (SoSE)*, pages 197–202. IEEE, 2021. (Cited on pages 8, 22 and 78.)
- [Kaliyavaradhan 2022] Senthil Kumar Kaliyavaradhan, PS Ambily, Prabhath Ranjan Prem and Swapnil Balasaheb Ghodke. Test methods for 3D printable concrete. *Automation in Construction*, vol. 142, page 104529, 2022. (Cited on page 14.)
- [Katzschmann 2019a] Robert K Katzschmann, Cosimo Della Santina, Yasunori Toshimitsu, Antonio Bicchi and Daniela Rus. Dynamic motion control of multi-segment soft robots using piecewise constant curvature matched with an augmented rigid body model. In *2019 2nd IEEE International Conference on Soft Robotics (RoboSoft)*, pages 454–461. IEEE, 2019. (Cited on page 152.)
- [Katzschmann 2019b] Robert K Katzschmann, Maxime Thieffry, Olivier Goury, Alexandre Kruszewski, Thierry-Marie Guerra, Christian Duriez and Daniela Rus. Dynamically closed-loop controlled soft robotic arm using a reduced order finite element model with state observer. In *2019 2nd IEEE international conference on soft robotics (RoboSoft)*, pages 717–724. IEEE, 2019. (Cited on page 152.)
- [Kazemian 2019] Ali Kazemian, Xiao Yuan, Omid Davtalab and Behrokh Khoshnevis. Computer vision for real-time extrusion quality monitoring and control in robotic construction. *Automation in Construction*, vol. 101, pages 92–98, 2019. (Cited on pages viii and 33.)
- [Kazemian 2021] Ali Kazemian and Behrokh Khoshnevis. Real-time extrusion quality monitoring techniques for construction 3D printing. *Construction and Building Materials*, vol. 303, page 124520, 2021. (Cited on page 31.)
- [Khadem 2020] Mohsen Khadem, John O’Neill, Zisos Mitros, Lyndon Da Cruz and Christos Bergeles. Autonomous steering of concentric

- tube robots via nonlinear model predictive control. IEEE Transactions on Robotics, vol. 36, no. 5, pages 1595–1602, 2020. (Cited on pages 154 and 155.)
- [Khalil 2012] Wissam Khalil, Rochdi Merzouki, Belkacem Ould-Bouamama and Hafid Haffaf. Hypergraph Models for System of Systems Supervision Design. IEEE Transactions on Systems, Man, and Cybernetics - Part A: Systems and Humans, vol. 42, no. 4, pages 1005–1012, 2012. (Cited on page 74.)
- [Khan 2022] Shoukat Alim Khan and Muammer Koç. Numerical modelling and simulation for extrusion-based 3D concrete printing: The underlying physics, potential, and challenges. Results in Materials, vol. 16, page 100337, 2022. (Cited on page 31.)
- [Khoshnevis 2004] Behrokh Khoshnevis. Automated construction by contour crafting—related robotics and information technologies. Automation in construction, vol. 13, no. 1, pages 5–19, 2004. (Cited on page 20.)
- [Kim 2017] Kyuyoung Kim, Jaeho Park, Ji-hoon Suh, Minseong Kim, Yongrok Jeong and Inkyu Park. 3D printing of multiaxial force sensors using carbon nanotube (CNT)/thermoplastic polyurethane (TPU) filaments. Sensors and Actuators A: Physical, vol. 263, pages 493–500, 2017. (Cited on page 17.)
- [Kumar 2021] Sudhir Kumar, Rupinder Singh, TP Singh and Ajay Batish. On investigation of rheological, mechanical and morphological characteristics of waste polymer-based feedstock filament for 3D printing applications. Journal of Thermoplastic Composite Materials, vol. 34, no. 7, pages 902–928, 2021. (Cited on page 16.)
- [Kuznetsov 2018] Vladimir E Kuznetsov, Alexey N Solonin, Oleg D Urzhumtsev, Richard Schilling and Azamat G Tavitov. Strength of PLA components fabricated with fused deposition technology using a desktop 3D printer as a function of geometrical parameters of the process. Polymers, vol. 10, no. 3, page 313, 2018. (Cited on page 18.)
- [Kwon 2020] SoonWon Kwon, SeonWoo Lee, YongRae Kim, YoungChan Oh, SunKon Lee, JooHyung Kim and JangWoo Kwon. A Filament supply system capable of remote monitoring and automatic humidity control for 3D printer. Journal of Sensors, vol. 2020, pages 1–10, 2020. (Cited on page 34.)

- [Lakhal 2015] Othman Lakhal, Achille Melingui and Rochdi Merzouki. Hybrid approach for modeling and solving of kinematics of a compact bionic handling assistant manipulator. *IEEE/ASME Transactions on Mechatronics*, vol. 21, no. 3, pages 1326–1335, 2015. (Cited on page 157.)
- [Lakhal 2018] Othman Lakhal. Contribution to the modeling and control of hyper-redundant robots: application to additive manufacturing in the construction. PhD thesis, Université de Lille, CRISTAL UMR 9189, 2018. (Cited on pages viii, 28 and 143.)
- [Lakhal 2019] Othman Lakhal, Achille Melingui, Gerald Dherbomez and Rochdi Merzouki. Control of a hyper-redundant robot for quality inspection in additive manufacturing for construction. In *2019 2nd IEEE International Conference on Soft Robotics (RoboSoft)*, pages 448–453. IEEE, 2019. (Cited on pages 22 and 28.)
- [Lakhal 2020] Othman Lakhal, Taha Chettibi, Abdelkader Belarouci, Gerald Dherbomez and Rochdi Merzouki. Robotized additive manufacturing of funicular architectural geometries based on building materials. *IEEE/ASME Transactions on Mechatronics*, vol. 25, no. 5, pages 2387–2397, 2020. (Cited on pages 2 and 28.)
- [Lakhal 2021] Othman Lakhal, Mouad Kahouadji and Xinrui Yang. Detection and crack reparation with UAV. <https://drive.google.com/file/d/1AFDw5UIIs0tjcsSDvQApTC1wLDpGQSre/view?usp=sharing>, 2021. (Cited on page 171.)
- [Laoutid 2021] Fouad Laoutid, Soumaya Lafqir, Antoniya Toncheva and Philippe Dubois. Valorization of recycled tire rubber for 3D printing of ABS-and TPO-based composites. *Materials*, vol. 14, no. 19, page 5889, 2021. (Cited on pages 15 and 23.)
- [Le 2012] Thanh T Le, Simon A Austin, Sungwoo Lim, Richard A Buswell, R Law, Alistair GF Gibb and Tony Thorpe. Hardened properties of high-performance printing concrete. *Cement and Concrete Research*, vol. 42, no. 3, pages 558–566, 2012. (Cited on pages 19 and 21.)
- [Lee 2021] Hojae Lee, Eun-A Seo, Won-Woo Kim and Jae-Heum Moon. Experimental Study on Time-Dependent Changes in Rheological Properties and Flow Rate of 3D Concrete Printing Materials. *Materials*, vol. 14, no. 21, page 6278, 2021. (Cited on pages 129 and 130.)

- [Li 2018] Jincan Li, Mingyu Gao, Zhiwei He and Yuxiang Yang. Circular Trajectory Planning with Pose Control for Six-DOF Manipulator. In 2018 IEEE 4th Information Technology and Mechatronics Engineering Conference (ITOEC), pages 1950–1955. IEEE, 2018. (Cited on page 61.)
- [Li 2019] Minghao Li, Zeyu Chen, Jack C. P. Cheng, Xiangyu Wang and Guomin Zhang. 3D Printing of Buildings and Infrastructure: New Opportunities and Challenges for the Construction Industry. *Automation in Construction*, vol. 99, 2019. (Cited on page 3.)
- [Lian 2019] Qin Lian, Xiao Li, Dichen Li, Heng Gu, Weiguo Bian and Xiaoning He. Path planning method based on discontinuous grid partition algorithm of point cloud for in situ printing. *Rapid Prototyping Journal*, vol. 25, no. 3, pages 602–613, 2019. (Cited on page 18.)
- [Lim 2011] Sungwoo Lim, Richard A Buswell, Thanh T Le, Rene Wackrow, Simon A Austin, Alistair GF Gibb and Tony Thorpe. Development of a viable concrete printing process. 2011. (Cited on page 122.)
- [Lim 2012] Sungwoo Lim, Richard A Buswell, Thanh T Le, Simon A Austin, Alistair GF Gibb and Tony Thorpe. Developments in construction-scale additive manufacturing processes. *Automation in construction*, vol. 21, pages 262–268, 2012. (Cited on page 21.)
- [Lin 2014] Tsung-Yi Lin, Michael Maire, Serge Belongie, James Hays, Pietro Perona, Deva Ramanan, Piotr Dollár and C Lawrence Zitnick. Microsoft coco: Common objects in context. In *European conference on computer vision*, pages 740–755. Springer, 2014. (Cited on page 147.)
- [Link 2020] Julian Link, Thomas Sowoidnich, Christopher Pfitzner, Teba Gil-Diaz, Frank Heberling, Johannes Lützenkirchen, Thorsten Schäfer, Horst-Michael Ludwig and Michael Haist. The influences of cement hydration and temperature on the thixotropy of cement paste. *Materials*, vol. 13, no. 8, page 1853, 2020. (Cited on page 102.)
- [Lishchenko 2022] Natalia Lishchenko, Ján Pitel’ and Vasily Larshin. Online monitoring of surface quality for diagnostic features in 3d printing. *Machines*, vol. 10, no. 7, page 541, 2022. (Cited on page 31.)
- [Loflin 2019] Wyatt A Loflin, Jeryl D English, Catharine Borders, Lacey M Harris, Audrey Moon, J Nathaniel Holland and F Kurtis Kasper. Effect of print layer height on the assessment of 3D-printed models. *American*

- Journal of Orthodontics and Dentofacial Orthopedics, vol. 156, no. 2, pages 283–289, 2019. (Cited on page 20.)
- [Ma 2019] Guowei Ma, Zhijian Li, Li Wang, Fang Wang and Jay Sanjayan. Mechanical anisotropy of aligned fiber reinforced composite for extrusion-based 3D printing. Construction and Building Materials, vol. 202, pages 770–783, 2019. (Cited on page 22.)
- [Ma 2023] Yizhou Ma, Jelle Potappel, Aneesh Chauhan, Maarten AI Schutyser, Remko M Boom and Lu Zhang. Improving 3D food printing performance using computer vision and feedforward nozzle motion control. Journal of Food Engineering, vol. 339, page 111277, 2023. (Cited on pages viii and 32.)
- [Maguire 2018] Marc Maguire, Sattar Dorafshan and Robert J Thomas. SDNET2018: A concrete crack image dataset for machine learning applications. 2018. (Cited on page 147.)
- [Malaeb 2019] Zeina Malaeb, Fatima AlSakka and Farook Hamzeh. 3D concrete printing: machine design, mix proportioning, and mix comparison between different machine setups. In 3D Concrete printing technology, pages 115–136. Elsevier, 2019. (Cited on page 15.)
- [Mark W. Spong 2006] M. Vidyasagar Mark W. Spong Seth Hutchinson. Robot modeling and control. Wiley, 2006. (Cited on page 50.)
- [Maurer 2003] Calvin R Maurer, Rensheng Qi and Vijay Raghavan. A linear time algorithm for computing exact Euclidean distance transforms of binary images in arbitrary dimensions. IEEE Transactions on Pattern Analysis and Machine Intelligence, vol. 25, no. 2, pages 265–270, 2003. (Cited on page 80.)
- [Mbakop 2021] Steeve Mbakop, Gilles Tagne, Marc-Henri Frouin, Achille Melingui and Rochdi Merzouki. Inverse dynamics model-based shape control of soft continuum finger robot using parametric curve. IEEE Robotics and Automation Letters, vol. 6, no. 4, pages 8053–8060, 2021. (Cited on page 152.)
- [Moelich 2020] Gerrit M Moelich, Jacques Kruger and Riaan Combrinck. Plastic shrinkage cracking in 3D printed concrete. Composites Part B: Engineering, vol. 200, page 108313, 2020. (Cited on page 21.)
- [Munasinghe 2002] Sudath R Munasinghe and Masatoshi Nakamura. Determination of maximum tangential velocity at trajectory corners

- in robot manipulator operation under torque constraint. In *Proceedings of the 41st SICE Annual Conference. SICE 2002.*, volume 1, pages 396–401. IEEE, 2002. (Cited on page 61.)
- [Muñoz 2020] Jose Muñoz and Martin Pumera. Accounts in 3D-printed electrochemical sensors: towards monitoring of environmental pollutants. *ChemElectroChem*, vol. 7, no. 16, pages 3404–3413, 2020. (Cited on page 34.)
- [Neto 2013] Pedro Neto and Nuno Mendes. Direct off-line robot programming via a common CAD package. *Robotics and Autonomous Systems*, vol. 61, no. 8, pages 896–910, 2013. (Cited on page 18.)
- [Ngo 2018] Tuan D Ngo, Alireza Kashani, Gabriele Imbalzano, Kate TQ Nguyen and David Hui. Additive manufacturing (3D printing): A review of materials, methods, applications and challenges. *Composites Part B: Engineering*, vol. 143, pages 172–196, 2018. (Cited on page 17.)
- [Nguyen-Van 2022] Vuong Nguyen-Van, Shuai Li, Junli Liu, Kien Nguyen and Jonathan Phuong Tran. Modelling of 3D concrete printing process: A perspective on material and structural simulations. *Additive Manufacturing*, page 103333, 2022. (Cited on page 13.)
- [Orin 1984] David E Orin and William W Schrader. Efficient computation of the Jacobian for robot manipulators. *The International Journal of Robotics Research*, vol. 3, no. 4, pages 66–75, 1984. (Cited on page 57.)
- [Özgenel 2017] Çağlar Fırat Özgenel. Concrete crack images for classification. *Mendeley Data*, v1, 2017. (Cited on page 147.)
- [O’Mahony 2019] Niall O’Mahony, Sean Campbell, Anderson Carvalho, Suman Harapanahalli, Gustavo Velasco Hernandez, Lenka Krpalkova, Daniel Riordan and Joseph Walsh. Deep learning vs. traditional computer vision. In *Science and information conference*, pages 128–144. Springer, 2019. (Cited on page 78.)
- [Panda 2017] Biranchi Panda, Jian Hui Lim, Nisar Ahamed Noor Mohamed, Suvash Chandra Paul, Yi Wei Daniel Tay and Ming Jen Tan. Automation of robotic concrete printing using feedback control system. In *ISARC. Proceedings of the International Symposium on Automation and Robotics in Construction*, volume 34. IAARC Publications, 2017. (Cited on pages 31 and 50.)

- [Panda 2018] Biranchi Panda, Suvash Chandra Paul, Nisar Ahamed Noor Mohamed, Yi Wei Daniel Tay and Ming Jen Tan. Measurement of tensile bond strength of 3D printed geopolymers mortar. *Measurement*, vol. 113, pages 108–116, 2018. (Cited on page 129.)
- [Pandzic 2019] Adi Pandzic, Damir Hodzic and Aleksa Milovanovic. EFFECT OF INFILL TYPE AND DENSITY ON TENSILE PROPERTIES OF PLAMATERIAL FOR FDM PROCESS. *Annals of DAAAM & Proceedings*, vol. 30, 2019. (Cited on page 18.)
- [Park 2020] Song Ee Park, Seung-Hyun Eem and Haemin Jeon. Concrete crack detection and quantification using deep learning and structured light. *Construction and Building Materials*, vol. 252, page 119096, 2020. (Cited on page 147.)
- [Perrot 2018] Arnaud Perrot, Damien Rangeard and Eric Courteille. 3D printing of earth-based materials: Processing aspects. *Construction and Building Materials*, vol. 172, pages 670–676, 2018. (Cited on page 24.)
- [Perrot 2020] A Perrot, Y Jacquet, D Rangeard, E Courteille and M Sonebi. Nailing of layers: a promising way to reinforce concrete 3D printing structures. *Materials*, vol. 13, no. 7, page 1518, 2020. (Cited on page 20.)
- [Perrot 2021] A Perrot, A Pierre, VN Nerella, RJM Wolfs, E Keita, SAO Nair, N Neithalath, N Roussel and V Mechtcherine. From analytical methods to numerical simulations: A process engineering toolbox for 3D concrete printing. *Cement and Concrete Composites*, vol. 122, page 104164, 2021. (Cited on page 22.)
- [Qiu 2023] Shaohua Qiu, Xiaopeng Cui, Zuwei Ping, Nanliang Shan, Zhong Li, Xianqiang Bao and Xinghua Xu. Deep Learning Techniques in Intelligent Fault Diagnosis and Prognosis for Industrial Systems: A Review. *Sensors*, vol. 23, no. 3, page 1305, 2023. (Cited on page 77.)
- [Rahmat 2023] NF Rahmat, N Ali, SR Abdullah, NA Abdul Hamid, N Salleh and S Shahidan. Fresh properties and flexural strength of 3D printing sustainable concrete containing GGBS as partial cement replacement. In *IOP Conference Series: Earth and Environmental Science*, volume 1205, page 012042. IOP Publishing, 2023. (Cited on page 26.)

- [Rahul 2019] AV Rahul, Manu Santhanam, Hitesh Meena and Zimam Ghani. 3D printable concrete: Mixture design and test methods. *Cement and Concrete Composites*, vol. 97, pages 13–23, 2019. (Cited on page 15.)
- [Rakha 2023] Walaa Mahmoud Rakha, Ashraf Ali Nessim and Mostafa Refaat Ismail. RETROFITTING SHADING UNITS TO OPTIMIZE DAYLIGHTING IN THE GOVERNMENTAL SCHOOL BUILDING IN CAIRO. *Journal of Al-Azhar University Engineering Sector*, vol. 18, no. 66, pages 183–202, 2023. (Cited on page 18.)
- [Refaai 2022] Mohamad Reda A Refaai. An Improved Inverse Kinematics Solution for a Robot Arm Trajectory Using Multiple Adaptive Neuro-Fuzzy Inference Systems. *Advances in Materials Science & Engineering*, 2022. (Cited on page 152.)
- [Reinold 2022] Janis Reinold, Venkatesh Naidu Nerella, Viktor Mechtcherine and Günther Meschke. Extrusion process simulation and layer shape prediction during 3D-concrete-printing using the Particle Finite Element Method. *Automation in Construction*, vol. 136, page 104173, 2022. (Cited on pages 22, 31 and 105.)
- [Renfrew 2004] Alasdair Renfrew. Introduction to robotics: Mechanics and control. *International Journal of Electrical Engineering & Education*, vol. 41, no. 4, page 388, 2004. (Cited on page 57.)
- [Rill-García 2022] Rodrigo Rill-García, Eva Dokladalova, Petr Dokládál, Jean-François Caron, Romain Mesnil, Pierre Margerit and Malo Charrier. Inline monitoring of 3D concrete printing using computer vision. *Additive Manufacturing*, vol. 60, page 103175, 2022. (Cited on page 34.)
- [Rizzieri 2023] Giacomo Rizzieri, Liberato Ferrara and Massimiliano Cremonesi. Numerical simulation of the extrusion and layer deposition processes in 3D concrete printing with the Particle Finite Element Method. *Computational Mechanics*, pages 1–19, 2023. (Cited on page 31.)
- [Rubin 2023] Ariane Prevedello Rubin, Lucas Carvalho Quintanilha and Wellington Longuini Repette. Influence of structuration rate, with hydration accelerating admixture, on the physical and mechanical properties of concrete for 3D printing. *Construction and Building Materials*, vol. 363, page 129826, 2023. (Cited on page 105.)

- [Schafer 2005] Timo Schafer and Rolf Dieter Schraft. Incremental sheet metal forming by industrial robots. *Rapid Prototyping Journal*, vol. 11, no. 5, pages 278–286, 2005. (Cited on page 18.)
- [Schuldt 2021] Steven J Schuldt, Jeneé A Jagoda, Andrew J Hoisington and Justin D Delorit. A systematic review and analysis of the viability of 3D-printed construction in remote environments. *Automation in Construction*, vol. 125, page 103642, 2021. (Cited on page 35.)
- [Shahzad 2021] Qamar Shahzad, Junyi Shen, Rabia Naseem, Yonggang Yao, Saad Waqar and Wenqiang Liu. Influence of phase change material on concrete behavior for construction 3D printing. *Construction and Building Materials*, vol. 309, page 125121, 2021. (Cited on page 2.)
- [Sharafeldin 2018] Mohamed Sharafeldin, Abby Jones and James F Rusling. 3D-printed biosensor arrays for medical diagnostics. *Micromachines*, vol. 9, no. 8, page 394, 2018. (Cited on page 19.)
- [Souza 2020] Marcelo Tramontin Souza, Igor Maia Ferreira, Elisangela Guzi de Moraes, Luciano Senff and Antonio Pedro Novaes de Oliveira. 3D printed concrete for large-scale buildings: An overview of rheology, printing parameters, chemical admixtures, reinforcements, and economic and environmental prospects. *Journal of Building Engineering*, vol. 32, page 101833, 2020. (Cited on page 1.)
- [Taleb 2023a] M Taleb, D Bulteel, D Betrancourt, F Roudet, S Rémond, A Montagne and Didier Chicot. Multi-scale mechanical characterization of the interface in 3D printed concrete. *Materials and Structures*, vol. 56, no. 1, page 24, 2023. (Cited on page 13.)
- [Taleb 2023b] Maria Taleb, David Bulteel, Damien Betrancourt, Francine Roudet, Sébastien Rémond and Didier Chicot. Interfacial weakness criterion by indentation in 3D printed concrete. *3D Printing and Additive Manufacturing*, vol. 10, no. 2, pages 318–329, 2023. (Cited on page 20.)
- [Tan 2020] Lisa Jiaying Tan, Wei Zhu and Kun Zhou. Recent progress on polymer materials for additive manufacturing. *Advanced Functional Materials*, vol. 30, no. 43, page 2003062, 2020. (Cited on page 17.)
- [Tappa 2017] Karthik Tappa, Udayabhanu Jammalamadaka, David H Ballard, Todd Bruno, Marissa R Israel, Harika Vemula, J Mark Meacham, David K Mills, Pamela K Woodard and Jeffery A Weisman. Medication eluting devices for the field of OBGYN (MEDOBYN): 3D printed

- biodegradable hormone eluting constructs, a proof of concept study. PLoS One, vol. 12, no. 8, page e0182929, 2017. (Cited on page 25.)
- [Tay 2019a] Yi Wei Daniel Tay, Ming Yang Li and Ming Jen Tan. Effect of printing parameters in 3D concrete printing: Printing region and support structures. Journal of Materials Processing Technology, vol. 271, pages 261–270, 2019. (Cited on page 16.)
- [Tay 2019b] Yi Wei Daniel Tay, Ye Qian and Ming Jen Tan. Printability region for 3D concrete printing using slump and slump flow test. Composites Part B: Engineering, vol. 174, page 106968, 2019. (Cited on page 66.)
- [Thuruthel 2018] Thomas George Thuruthel, Egidio Falotico, Federico Renda and Cecilia Laschi. Model-based reinforcement learning for closed-loop dynamic control of soft robotic manipulators. IEEE Transactions on Robotics, vol. 35, no. 1, pages 124–134, 2018. (Cited on page 152.)
- [Toscano 2005] Rosario Toscano. Commande et diagnostic des systèmes dynamiques: modélisation, analyse, commande par pid et par retour d'état, diagnostic. ellipses, 2005. (Cited on page 85.)
- [Volpato 2019] Neri Volpato and Thiago Tavares Zanotto. Analysis of deposition sequence in tool-path optimization for low-cost material extrusion additive manufacturing. The International Journal of Advanced Manufacturing Technology, vol. 101, pages 1855–1863, 2019. (Cited on page 18.)
- [Wang 2020] Jun Wang, Bin Yang, Xiang Lin, Lei Gao, Tao Liu, Yonglai Lu and Runguo Wang. Research of TPU materials for 3D printing aiming at non-pneumatic tires by FDM method. Polymers, vol. 12, no. 11, page 2492, 2020. (Cited on page 17.)
- [Wangler 2016] Timothy Wangler, Ena Lloret, Lex Reiter, Norman Hack, Fabio Gramazio, Matthias Kohler, Mathias Bernhard, Benjamin Dillenburger, Jonas Buchli, Nicolas Rousselet al. Digital concrete: opportunities and challenges. RILEM Technical Letters, vol. 1, pages 67–75, 2016. (Cited on page 13.)
- [Wu 2016] Peng Wu, Jun Wang and Xiangyu Wang. A critical review of the use of 3-D printing in the construction industry. Automation in Construction, vol. 68, pages 21–31, 2016. (Cited on page 26.)

- [Wu 2021a] Pinyi Wu, Keval S Ramani and Chinedum E Okwudire. Accurate linear and nonlinear model-based feedforward deposition control for material extrusion additive manufacturing. *Additive Manufacturing*, vol. 48, page 102389, 2021. (Cited on pages [viii](#) and [32](#).)
- [Wu 2021b] Yiwen Wu, Chao Liu, Huawei Liu, Zhenzi Zhang, Chunhui He, Shuhua Liu, Rongfei Zhang, Youqiang Wang and Guoliang Bai. Study on the rheology and buildability of 3D printed concrete with recycled coarse aggregates. *Journal of Building Engineering*, vol. 42, page 103030, 2021. (Cited on page [16](#).)
- [Xiao 2020] Jianzhuang Xiao, Shuai Zou, Ying Yu, Yu Wang, Tao Ding, Ying Zhu, Jiangtao Yu, Shuaishuai Li, Zhenhua Duan, Yuching Wuet *al.* 3D recycled mortar printing: System development, process design, material properties and on-site printing. *Journal of Building Engineering*, vol. 32, page 101779, 2020. (Cited on page [74](#).)
- [Xiao 2021] Jianzhuang Xiao, Guangchao Ji, Yamei Zhang, Guowei Ma, Viktor Mechtcherine, Jinlong Pan, Li Wang, Tao Ding, Zhenhua Duan and Shupeng Du. Large-scale 3D printing concrete technology: Current status and future opportunities. *Cement and Concrete Composites*, vol. 122, page 104115, 2021. (Cited on page [14](#).)
- [Xu 2017] Jie Xu, Lieyun Ding and Peter ED Love. Digital reproduction of historical building ornamental components: From 3D scanning to 3D printing. *Automation in Construction*, vol. 76, pages 85–96, 2017. (Cited on page [122](#).)
- [Xu 2020] Jie Xu, Richard A Buswell, Peter Kinnell, Istvan Biro, John Hodgson, Nikolaos Konstantinidis and Lieyun Ding. Inspecting manufacturing precision of 3D printed concrete parts based on geometric dimensioning and tolerancing. *Automation in Construction*, vol. 117, page 103233, 2020. (Cited on page [122](#).)
- [Yang 2022a] Xinrui Yang, Mouad Kahouadji, Othman Lakhhal and Rochdi Merzouki. Integrated design of an aerial soft-continuum manipulator for predictive maintenance. *Frontiers in Robotics and AI*, vol. 9, page 980800, 2022. (Cited on pages [8](#), [143](#) and [148](#).)
- [Yang 2022b] Xinrui Yang, Othman Lakhhal, Abdelkader Belarouci and Rochdi Merzouki. Adaptive Deposit Compensation of Construction Materials in a 3D Printing Process. In *2022 IEEE/ASME International Conference on Advanced Intelligent Mechatronics (AIM)*, pages 658–663. IEEE, 2022. (Cited on pages [8](#) and [78](#).)

- [Yang 2023a] Xinrui Yang, Othman Lakhal, Abdelkader Belarouci and Rochdi Merzouki. Automatic Detection and Isolation of Filament Width Deviation During 3-D Printing of Recycled Construction Material. IEEE/ASME Transactions on Mechatronics, 2023. (Cited on pages 8, 63 and 99.)
- [Yang 2023b] Xinrui Yang, Othman Lakhal, Abdelkader Belarouci, Kamal Youcef-Toumi and Rochdi Merzouki. Experimental Workflow Implementation for Automatic Detection of Filament Deviation in 3D Robotic Printing Process. In 2023 IEEE International Conference on Robotics and Automation (ICRA), pages 12309–12315. IEEE, 2023. (Cited on page 8.)
- [Yao 2019] Gang Yao, Fujia Wei, Yang Yang and Yujia Sun. Deep-learning-based bughole detection for concrete surface image. Advances in Civil Engineering, vol. 2019, 2019. (Cited on page 22.)
- [Yao 2020] Yue Yao, Mingming Hu, Francesco Di Maio and Stefano Cucurachi. Life cycle assessment of 3D printing geo-polymer concrete: An ex-ante study. Journal of Industrial Ecology, vol. 24, no. 1, pages 116–127, 2020. (Cited on page 16.)
- [Yu 2019] Yang Yu, Kailiang Zhang, Li Yang and Dongxing Zhang. Fruit detection for strawberry harvesting robot in non-structural environment based on Mask-RCNN. Computers and Electronics in Agriculture, vol. 163, page 104846, 2019. (Cited on pages 22 and 78.)
- [Yuan 2022] Philip F Yuan, Qiang Zhan, Hao Wu, Hooi Shan Beh and Liming Zhang. Real-time toolpath planning and extrusion control (RTPEC) method for variable-width 3D concrete printing. Journal of Building Engineering, vol. 46, page 103716, 2022. (Cited on page 104.)
- [Zahabizadeh 2019] Behzad Zahabizadeh, Vitor MCF Cunha, João Pereira and Cláudia Gonçalves. Development of cement-based mortars for 3D printing through wet extrusion. 2019. (Cited on page 129.)
- [Zareiyani 2017] Babak Zareiyani and Behrokh Khoshnevis. Effects of interlocking on interlayer adhesion and strength of structures in 3D printing of concrete. Automation in Construction, vol. 83, pages 212–221, 2017. (Cited on page 25.)
- [Zeng 704] Feng Zeng. An area filling algorithm for 3D printing. In Proceedings of the 2017 5th International Conference on Frontiers of Manu-

- facturing Science and Measuring Technology (FMSMT 2017), pages 1269–1272. Atlantis Press, 2017/04. (Cited on page 50.)
- [Zhang 2000] Zhengyou Zhang. A flexible new technique for camera calibration. *IEEE Transactions on pattern analysis and machine intelligence*, vol. 22, no. 11, pages 1330–1334, 2000. (Cited on page 79.)
- [Zhang 2017] Zhongkai Zhang, Thor Morales Bieze, Jérémie Dequidt, Alexandre Kruszewski and Christian Duriez. Visual servoing control of soft robots based on finite element model. In *2017 IEEE/RSJ International Conference on Intelligent Robots and Systems (IROS)*, pages 2895–2901. IEEE, 2017. (Cited on page 152.)
- [Zhang 2022] Ketao Zhang, Pisak Chermprayong, Feng Xiao, Dimos Tzoumanikas, Barrie Dams, Sebastian Kay, Basaran Bahadir Kocer, Alec Burns, Lachlan Orr, Christopher Choiet al. Aerial additive manufacturing with multiple autonomous robots. *Nature*, vol. 609, no. 7928, pages 709–717, 2022. (Cited on pages viii, 35 and 36.)
- [Zhang 2023] Nan Zhang and Jay Sanjayan. Extrusion nozzle design and print parameter selections for 3D concrete printing. *Cement and Concrete Composites*, vol. 137, page 104939, 2023. (Cited on pages 51, 77 and 105.)
- [Zhao 2019] Zhong-Qiu Zhao, Peng Zheng, Shou-tao Xu and Xindong Wu. Object detection with deep learning: A review. *IEEE transactions on neural networks and learning systems*, vol. 30, no. 11, pages 3212–3232, 2019. (Cited on page 147.)
- [Zhao 2022] Yanhua Zhao, Wei Meng, Peifu Wang, Dongqing Qian, Wei Cheng and Zhongqing Jia. Research Progress of Concrete 3D Printing Technology and Its Equipment System, Material, and Molding Defect Control. *Journal of Engineering*, vol. 2022, 2022. (Cited on page 21.)
- [Zhu 2021] Caihan Zhu, Tianya Li, Mohamedazeem M Mohideen, Ping Hu, Ramesh Gupta, Seeram Ramakrishna and Yong Liu. Realization of circular economy of 3D printed plastics: A review. *Polymers*, vol. 13, no. 5, page 744, 2021. (Cited on page 23.)
- [Zou 2021] Shuai Zou, Jianzhuang Xiao, Tao Ding, Zhenhua Duan and Qingtian Zhang. Printability and advantages of 3D printing mortar with 100% recycled sand. *Construction and Building Materials*, vol. 273, page 121699, 2021. (Cited on page 2.)

Towards Automation Process of 3D Printing in Construction under Uncontrolled Environment

Abstract: Additive Manufacturing (AM) with concrete material, also known as 3D Concrete Printing (3DCP), has gained increasing attention in the construction industry as well as in academia across various research fields including material science, automatic control, and robotics. This technology enables the fabrication of designed 3D complex geometries in a layer-by-layer manner, using construction materials such as concrete that can come from recycled demolition wastes containing RFA (Recyclable Fine Aggregates). A robotic system guides a nozzle that deposits material along a defined trajectory. Most 3DCP technologies are performed under controlled environments without environmental disturbances. However, in uncontrolled environments, changes in temperature and humidity can significantly affect the rheological properties of the fresh concrete, thereby impacting print quality. Specifically, the material behavior changes, causing the width of the material filament to deviate from its desired value. To address the issue of printing process control under uncontrolled environments, this thesis work focuses on adaptive compensation for deviations in material filament width during deposition. The printing process involves a trade-off between two different dynamics: a rapid dynamic system, namely the robot, which is a mechatronic system, and a slow dynamic system, namely material pumping, which is a fluid mechanical system. Thus, the research question consists of: How to adapt the printing robot's velocity along the trajectory to maintain continuous and consistent material deposition, under the constraints of trajectory curvature, desired material filament width, and flow rate, while accounting for fluctuations in external temperature and humidity. For this purpose, an integrated approach has been proposed that covers the overall process: pre-printing, in-printing, and post-printing.

Keywords: Additive manufacturing, Adaptive estimation and compensation, Qualitative diagnosis, Serial robot, Uncontrolled environment, Quantitative diagnosis
